



University of Kentucky
UKnowledge

University of Kentucky Doctoral Dissertations

Graduate School

2008

CARBON NANOTUBE SUPPORTED METAL CATALYSTS FOR NO_x REDUCTION USING HYDROCARBON REDUCTANTS

Eduardo Santillan-Jimenez
University of Kentucky, esj102780@gmail.com

[Right click to open a feedback form in a new tab to let us know how this document benefits you.](#)

Recommended Citation

Santillan-Jimenez, Eduardo, "CARBON NANOTUBE SUPPORTED METAL CATALYSTS FOR NO_x REDUCTION USING HYDROCARBON REDUCTANTS" (2008). *University of Kentucky Doctoral Dissertations*. 672.
https://uknowledge.uky.edu/gradschool_diss/672

This Dissertation is brought to you for free and open access by the Graduate School at UKnowledge. It has been accepted for inclusion in University of Kentucky Doctoral Dissertations by an authorized administrator of UKnowledge. For more information, please contact UKnowledge@lsv.uky.edu.

ABSTRACT OF DISSERTATION

Eduardo Santillan-Jimenez

The Graduate School

University of Kentucky

2008

CARBON NANOTUBE SUPPORTED METAL CATALYSTS FOR NO_x
REDUCTION USING HYDROCARBON REDUCTANTS

ABSTRACT OF DISSERTATION

A dissertation submitted in partial fulfillment of the
requirements for the degree of Doctor of Philosophy in the
College of Arts and Sciences
at the University of Kentucky

By
Eduardo Santillan-Jimenez

Lexington, Kentucky

Co-Directors: Dr. Mark Crocker, Professor of Chemistry
and Dr. David Atwood, Professor of Chemistry

Lexington, Kentucky

2008

Copyright © Eduardo Santillan-Jimenez 2008

ABSTRACT OF DISSERTATION

CARBON NANOTUBE SUPPORTED METAL CATALYSTS FOR NO_x REDUCTION USING HYDROCARBON REDUCTANTS

Nitrogen oxides (NO_x) are atmospheric pollutants that pose a serious threat to both the environment and human health. Although catalytic deNO_x technologies for engines working under stoichiometric air-to-fuel ratios (i.e., most gasoline engines) are already available, their performance is unsatisfactory under excess air conditions like those under which diesel engines operate.

The selective catalytic reduction of NO_x with hydrocarbon reductants (HC-SCR) is a potential deNO_x solution for diesel engines, whose operating temperatures are 150-500 °C. Given that is unlikely for a single catalyst to show acceptable activity throughout this entire temperature span, the use of two catalysts is proposed in this dissertation. Whereas several catalysts active at high temperatures (>300 °C) are already available, a catalyst showing an acceptable performance at low temperatures (<300 °C) is yet to be found.

Platinum group metals (PGMs) supported on activated carbon have been identified as promising low temperature HC-SCR catalysts. However, these materials show three main drawbacks: 1) the propensity of the carbon support to undergo combustion in an oxidizing environment, 2) a narrow temperature window of operation; and 3) a high selectivity towards N₂O (as opposed to N₂).

To address the first limitation, the use of multi-walled carbon nanotubes (MWCNTs) as the support has been investigated and found to yield catalysts displaying a higher resistance to oxidation. Further, the acid activation of MWCNTs prior to their use as catalyst support has been explored, following reports that link carrier acidity with improved catalyst performance. In turn, the use of PGM alloys as the active phase has been examined as a means to improve catalyst activity and selectivity.

Additionally, kinetic, spectroscopic and mechanistic studies have been performed in an attempt to probe structure-activity relationships in the MWCNTs-based formulations showing the best deNO_x performance. The fundamental insights gained through these

studies may inform further improvements to HC-SCR catalysts. Finally, the synthesis of the most promising formulations has been scaled-up using commercial metal monoliths as the catalyst substrate and the resulting monolithic catalysts have been tested in a diesel engine for activity in the HC-SCR reaction.

KEYWORDS: NO_x, Selective Catalytic Reduction, Hydrocarbons, Platinum Group Metals, Multi-walled Carbon Nanotubes.

Eduardo Santillan-Jimenez

October 24th, 2008

CARBON NANOTUBE SUPPORTED METAL CATALYSTS FOR NO_x
REDUCTION USING HYDROCARBON REDUCTANTS

By

Eduardo Santillan-Jimenez

Dr. Mark Crocker
Co-Director of Dissertation

Dr. David Atwood
Co-Director of Dissertation

Dr. Robert Grossman
Director of Graduate Studies

October 24th, 2008

RULES FOR THE USE OF DISSERTATIONS

Unpublished dissertations submitted for the Doctor's degree and deposited in the University of Kentucky Library are as a rule open for inspection, but are to be used only with due regard to the rights of the authors.

Bibliographical references may be noted, but quotations or summaries of parts may be published only with the permission of the author, and with the usual scholarly acknowledgments.

Extensive copying or publication of the dissertation in whole or in part also requires the consent of the Dean of the Graduate School of the University of Kentucky.

A library that borrows this dissertation for use by its patrons is expected to secure the signature of each user.

Name

Date

DISSERTATION

Eduardo Santillan-Jimenez

The Graduate School
University of Kentucky

2008

CARBON NANOTUBE SUPPORTED METAL CATALYSTS FOR NO_x
REDUCTION USING HYDROCARBON REDUCTANTS

DISSERTATION

A dissertation submitted in partial fulfillment of the
requirements for the degree of Doctor of Philosophy in the
College of Arts and Sciences
at the University of Kentucky

By
Eduardo Santillan-Jimenez

Lexington, Kentucky

Co-Directors: Dr. Mark Crocker, Professor of Chemistry
and Dr. David Atwood, Professor of Chemistry

Lexington, Kentucky

2008

Copyright © Eduardo Santillan-Jimenez 2008

A MIS PADRES.

ACKNOWLEDGEMENTS

First and foremost I would like to thank Dr. Mark Crocker, whom I ineffably appreciate having had as advisor and having now as mentor.

I would also like to express my gratitude to Dr. David Atwood, to whom I owe having joined the University of Kentucky in the first place.

I also recognize and credit the other members of my advisory committee: Dr. Mark Meier, Dr. Stephen Rankin and Dr. Rodney Andrews, both for their time and their helpful insight.

Thanks to Dr. Agustín Bueno-López, Dr. Concepción Salinas-Martínez de Lecea and Dr. María José Illán-Gómez for their kind invitation to the Department of Inorganic Chemistry of the University of Alicante and to Dr. Karen Wilson for her help with the XPS analyses performed at the University of York.

Many thanks to the faculty and staff at the Chemistry Department, the Center for Applied Energy Research, the Electron Microscopy Center and the Environmental Research Training Laboratory of the University of Kentucky, as well as to the staff at the Department of Inorganic Chemistry of the University of Alicante for their approachability and their helpfulness. My special thanks to Dennis Sparks and Sonia Parres, without whom (quite literally) most of my work would have been impossible.

My appreciation to all the friends and colleagues I have met in the United States and in Spain during the last four years who, I am fortunate enough to say, are simply too many to mention and thank individually.

Last, but certainly not least, my thoughts go to my family (including my extended family and friends) in Mexico, who are still (and will always be) near me in spite of being geographically distanced.

TABLE OF CONTENTS

Acknowledgements.....	iii
List of Tables	viii
List of Figures	ix
Chapter 1. General Introduction	1
1.1. NO _x as a threat to health and the environment.....	2
1.2. Sources of NO _x	4
1.3. Removal of NO _x	6
1.4. Lean deNO _x <i>via</i> HC-SCR	9
1.5. A novel technique for NO _x reduction in an oxidative environment	10
1.6. Carbon nanotube-supported PGMs as low temperature HC-SCR catalysts ...	12
1.7. Scope of the dissertation	13
Chapter 2. Selective Catalytic Reduction of Nitrogen Oxides with Hydrocarbons.....	15
2.1. Introduction.....	15
2.2. HC-SCR fundamentals.....	16
2.3. HC-SCR catalysts used throughout the years	17
2.3.1. Zeolitic catalysts	17
2.3.2. Supported platinum group metal catalysts	18
2.3.3. Supported base metal oxide catalysts	19
2.4. HC-SCR on supported PGM catalysts.....	20
2.4.1. Monometallic PGM catalysts.....	20
2.4.2. Multimetallic PGM catalysts	22
Chapter 3. Multiwalled Carbon Nanotubes as Catalyst Supports.....	25
3.1. Introduction.....	25
3.2. Experimental methods	28
3.2.1. CVD synthesis of MWCNTs	28
3.2.2. Funtionalization of MWCNTs with a mixture of 1:1 H ₂ SO ₄ -HNO ₃	28
3.2.3. Elemental analyses.....	29
3.2.4. Surface analyses.....	29
3.2.5. Transmission Electron Microscopy analyses.....	29
3.2.6. Attenuated Total Reflectance Infrared analyses	29
3.2.7. X-ray Photoelectron Spectroscopy analyses.....	30
3.2.8. Thermogravimetric analyses	30
3.3. Preparation of support materials	30
3.4. Characterization of support materials	33
Chapter 4. HC-SCR Catalyst Preparation and Characterization.....	46
4.1. Introduction.....	46
4.2. Experimental methods	47
4.2.1. PGM deposition <i>via</i> the polyol method	47
4.2.2. PGM deposition <i>via</i> wet impregnation	47
4.2.3. PGM deposition <i>via</i> incipient wetness impregnation	47
4.2.4. Determination of precious metal loadings	47
4.2.5. Precious metal particle size analyses	48

4.2.6. Scanning Transmission Electron Microscopy analyses.....	48
4.3. Catalysts preparation.....	49
4.4. Catalyst characterization.....	52
Chapter 5. Testing and Optimization of Powder-type MWCNTs-based HC-SCR Catalysts	
.....	63
5.1. Introduction.....	63
5.2. Experimental methods.....	65
5.2.1. Powder-type catalysts testing.....	65
5.2.2. Kinetic studies.....	66
5.3. Preliminary powder-type catalyst testing in a microflow reactor.....	66
5.3.1. Microflow reactor construction.....	66
5.3.2. Initial powder-type catalyst testing.....	67
5.4. Catalyst optimization.....	70
5.4.1. Effect of the catalyst support.....	71
5.4.2. Effect of the catalysts preparation method.....	73
5.4.3. Effect of the reductant concentration.....	80
5.4.4. Effect of promotion with Rh and/or Ir.....	81
5.4.5. Sodium promotion.....	90
5.4.6. Examination of alternative metals and metal promoters.....	92
5.5. Kinetic studies.....	93
Chapter 6. Probing of Structure-activity Relationships in HC-SCR Catalysts.....	95
6.1. Introduction.....	95
6.2. Experimental methods.....	98
6.2.1. Elemental analysis under the Transmission Electron Microscope.....	98
6.2.2. Temperature Programmed Desorption experiments.....	98
6.2.3. X-ray Photoelectron Spectroscopy analyses.....	98
6.2.4. X-ray Absorption Fine Structure measurements.....	98
6.2.5. Diffuse Reflectance Infrared Fourier Transform Spectroscopy	
analyses.....	99
6.3. TEM-EDS and STEM-EDS studies.....	100
6.4. TPD studies.....	107
6.4.1. NH ₃ -TPD.....	107
6.4.2. C ₃ H ₆ -TPD.....	108
6.5. XPS studies.....	112
6.6. X-ray Absorption Fine Structure (XAFS) studies.....	119
6.7. Elemental mapping.....	120
6.8. DRIFTS studies.....	127
Chapter 7. Mechanistic Studies on HC-SCR Catalysts.....	128
7.1. Introduction.....	128
7.1.1. Mechanisms involving NO decomposition followed by HC-assisted	
surface reduction.....	128
7.1.2. Mechanisms involving the formation of C-N bonds.....	131
7.1.2.1. Mechanisms involving cyanide or isocyanate species as an	
intermediate.....	132
7.1.2.2. Mechanisms involving organo-nitro or related species as	
an intermediate.....	136

7.2. Experimental methods	138
7.2.1. Transient experiments	138
7.3. Transient experiments	140
7.3.1. Transient experiments below T_{\max} (260 °C)	140
7.3.1.1. NO/C ₃ H ₆ /O ₂ → Ar/C ₃ H ₆ /O ₂ switch	140
7.3.1.2. Ar/C ₃ H ₆ /O ₂ → NO/C ₃ H ₆ /O ₂ switch	142
7.3.1.3. NO/C ₃ H ₆ /O ₂ → NO/Ar/O ₂ switch	143
7.3.1.4. NO/Ar/O ₂ → NO/C ₃ H ₆ /O ₂ switch	145
7.3.1.5. NO/C ₃ H ₆ /O ₂ → NO/C ₃ H ₆ /Ar switch	146
7.3.1.6. NO/C ₃ H ₆ /Ar → NO/C ₃ H ₆ /O ₂ switch	147
7.3.2. Transient experiments above T_{\max} (300 °C)	149
7.3.2.1. NO/C ₃ H ₆ /O ₂ → Ar/C ₃ H ₆ /O ₂ switch	149
7.3.2.2. Ar/C ₃ H ₆ /O ₂ → NO/C ₃ H ₆ /O ₂ switch	150
7.3.2.3. NO/C ₃ H ₆ /O ₂ → NO/Ar/O ₂ switch	151
7.3.2.4. NO/Ar/O ₂ → NO/C ₃ H ₆ /O ₂ switch	152
7.3.2.5. NO/C ₃ H ₆ /O ₂ → NO/C ₃ H ₆ /Ar switch	153
7.3.2.6. NO/C ₃ H ₆ /Ar → NO/C ₃ H ₆ /O ₂ switch	154
7.4. The state of the catalyst surface	155
7.4.1. The state of the Pt/fMWCNTs catalyst below T_{\max}	156
7.4.2. The state of the Pt/fMWCNTs catalyst above T_{\max}	157
7.4.3. The state of the Pt/fMWCNTs catalyst at T_{\max}	157
7.5. Mechanistic conclusions	157
Chapter 8. Preparation, Characterization and Testing of Monolithic HC-SCR MWCNTs- based Catalysts	160
8.1. Introduction	160
8.2. Experimental methods	162
8.2.1. Growth of MWCNTs on a metal monolith	162
8.2.2. Functionalization of metal monolith-grown MWCNTs with 0.5 % NO ₂ in N ₂	162
8.2.3. PGM deposition on NO ₂ -functionalized monolith-grown MWCNTs via the polyol method	162
8.2.4. Scanning Transmission Electron Microscopy analysis	163
8.2.5. Determination of the precious metal content of PGM/NO ₂ - fMWCNTs/metal monolith catalyst	163
8.2.6. Testing of monolithic catalysts in a diesel engine	163
8.3. Preparation and characterization of monolithic catalysts	165
8.3.1. Growth of MWCNTs on a metal monolith	165
8.3.2. Precious metal deposition on monolith-grown MWCNTs	166
8.3.3. Activation of monolith-grown MWCNTs	168
8.4. Engine tests	175
8.4.1. Pt/NO ₂ -fMWCNTs/metal monolith catalyst	175
8.4.2. 3:1 Pt-Rh/NO ₂ -fMWCNTs/metal monolith catalyst	179
Chapter 9. Concluding Remarks	185
Appendix – List of Abbreviations	187
References	189
Vita	201

LIST OF TABLES

Table 3.1. Elemental analysis (by combustion) of pristine and acid-treated MWCNTs ...	34
Table 3.2. EDS analysis of pristine and acid-treated MWCNTs	34
Table 3.3. Surface properties of pristine and acid-treated MWCNTs	34
Table 3.4. A comparison of different acid activation methods with regard to the oxygen content of the resulting materials	39
Table 3.5. Elemental surface analysis (by XPS) of pristine and acid-treated MWCNTs.	40
Table 3.6. XPS quantification of oxygen present in different chemical states (% of total oxygen analyzed) calculated from O 1s peak fitting	41
Table 3.7. Elemental analysis (by combustion) of the activated carbon fiber monolith ...	42
Table 3.8. Physical properties of the carbon fiber monolith.....	44
Table 3.9. Differential thermogravimetric maxima for selected samples (measured under two different gas mixtures)	43
Table 4.1. Precious metal loadings of the catalysts prepared via the polyol method (using conventional heating) determined by ICP-AES.....	52
Table 4.2. Elemental analysis data (in wt.%) for two catalysts prepared via the polyol analyzed by different techniques	53
Table 4.3. Hydrogen chemisorption results showing the dispersion and average diameter of Pt particles on different substrates (Pt loading = 2 wt.%)	54
Table 5.1. Elemental analysis (by combustion) of fMWCNTs and bfMWCNTs	77
Table 5.2. NO conversion data for selected Pt and Pt-Rh catalysts.....	84
Table 5.3. Kinetic data for 2 wt.% Pt/fMWCNTs and 1.5 wt.% Pt – 0.5 wt.% Rh/fMWCNTs	93
Table 6.1. Metal dispersion and average particle size of model Pt/Al ₂ O ₃ reference catalysts.....	113
Table 6.2. XANES quantification of Pt present in different oxidation states (% of total Pt analyzed) calculated using a linear combination of reference spectra for Pt ⁰ (Pt foil) and Pt(II) (Pt(acac) ₂) to fit the sample spectra over the range 11.535 – 11.615 keV	119
Table 6.3. Atomic concentrations (%) determined <i>via</i> XPS.....	125
Table 6.4. XPS quantification of Pt present in different oxidation states (% of total Pt analyzed) calculated from Pt 4f peak fitting	125
Table 8.1. Surface properties of pristine MWCNTs, acid treated MWCNTs and NO ₂ -treated MWCNTs.....	171
Table 8.2. Elemental surface analysis (by XPS) of pristine, NO ₂ -treated and acid-treated MWCNTs.....	172
Table 8.3. XPS quantification of oxygen present in different chemical states (% of total O analyzed) calculated from O 1s peak fitting	173

LIST OF FIGURES

Figure 1.1. The cycling of nitrogen in the environment	3
Figure 1.2. NO _x emissions in the United States by source sector based on the most recent inventory (2002).....	5
Figure 1.3. Regional contribution (%) to global NO _x emissions from combustion.....	6
Figure 1.4. Three way catalyst (TWC) performance determined by engine air to fuel ratio	7
Figure 1.5. The FTP-75 cycle	8
Figure 1.6. Series catalysts with dual injection configuration for application of dual HC-SCR catalysts	11
Figure 1.7. Parallel catalysts with exhaust gas switching configuration for application of dual HC-SCR catalysts	11
Figure 3.1. Schematics of the three different kinds of SWNTs: (a) armchair; (b) zigzag; and (c) chiral	25
Figure 3.2. High-resolution transmission electron micrograph of a MWCNT with ~20 concentric walls	26
Figure 3.3. Schematic of carbon nanotube functionalization with acid.....	32
Figure 3.4. Schematic of Pt deposition on acid activated MWCNTs	32
Figure 3.5. TEM image showing the disruption of the MWCNT graphene structure as a result of acid treatment (1:1 H ₂ SO ₄ -HNO ₃ reflux for 4 h).....	36
Figure 3.6. Background corrected ATRIR spectra of 1:1 H ₂ SO ₄ -HNO ₃ treated MWCNTs (top: 3 h sonication at room temperature; middle: 4 h reflux; bottom: 3 h sonication at 60 °C) showing different functionalities introduced onto the MWCNTs.....	37
Figure 3.7. O 1s region in the XPS spectra of pristine MWCNTs and fMWCNTs produced by a 4 h reflux in a 1:1 mixture of sulfuric and nitric acids.....	40
Figure 3.8. Combined thermogravimetric plot for selected samples (measured under 10 % O ₂ balance N ₂ (ramp= 5 °C/min)	49
Figure 4.1. Particle size distribution histograms of 2 wt.% Pt/MWCNTs-I (left) and 2 wt.% Pt/fMWCNTs-I (right) (200 particles measured per histogram).....	55
Figure 4.2. TEM micrographs of 2 wt.% Pt/MWCNTs-I (above) and of 2 wt.% Pt/fMWCNTs-I (below) under different magnifications	56
Figure 4.3. STEM micrographs under different magnifications of approximately the same region of 2 wt.% Pt/fMWCNTs-I	57
Figure 4.4. STEM-Z image showing Pt particles (in white) deposited on Darco KB-B (in black).....	58
Figure 4.5. Different magnification TEM images of Pt/Al ₂ O ₃ , EDS spectrum of the region shown in the low magnification micrograph (top) and a close-up of the low intensity peaks in the spectrum (bottom).....	61
Figure 5.1. Microflow reactor schematic.....	67
Figure 5.2. Combined plot comparing the performance of 2 wt. % Pt/fMWCNTs-I with that of 2 wt.% Pt/activated carbon fibers-I with and 2 wt.% Pt/Al ₂ O ₃ -I reference catalysts in NO reduction with propene.....	69

Figure 5.3. Combined plot comparing the performance of Pt/MWCNTs-I with that of Pt/fMWCNTs-I in NO reduction with propene	72
Figure 5.4. Combined plot comparing the performance of 2 wt.% Pt/fMWCNTs-I, 2 wt.% Pt/fMWCNTs-P and 2 wt.% Pt/MWCNTs-I in NO reduction with propene	73
Figure 5.5. Particle size distribution histograms of 2 wt.% Pt/fMWCNTs-I, 2 wt.% Pt/fMWCNTs-P and 2 wt.% Pt/MWCNTs-I	74
Figure 5.6. TEM micrographs of fMWCNTs (left) and bfMWCNTs (right) with oxidation debris highlighted by the red rectangles	76
Figure 5.7. Combined TGA plot for fMWCNTs and bfMWCNTs under an atmosphere of 10 % O ₂ (balance N ₂). Ramp = 5 °C/min.....	77
Figure 5.8. Particle size distribution histograms for 2 wt.% Pt/fMWCNTs-I (left) and 2 wt.% Pt/bfMWCNTs-I (right).....	78
Figure 5.9. Combined plot comparing the performance of 2 wt.% Pt/fMWCNTs with that of 2 wt.% Pt/bfMWCNTs in NO reduction with propene	79
Figure 5.10. Combined plot comparing the performance of 2 wt.% Pt/fMWCNTs-P in NO reduction with propene under different propene:NO ratios. Feed composition: 500 ppm NO, 500 or 1500 ppm C ₃ H ₆ , 10 % O ₂ and 10 % H ₂ O, balance nitrogen	80
Figure 5.11. Combined plot comparing the performance of 2 wt.% Pt/fMWCNTs-I, 1 wt.% Pt – 1 wt.% Rh/fMWCNTs-I and 1 wt.% Pt – 1 wt.% Ir/fMWCNTs-I in NO reduction with propene	81
Figure 5.12. Combined plot comparing the performance of Pt/fMWCNTs-I to that of Pt-Rh/fMWCNTs-I with different Pt:Rh ratios in NO reduction with propene	83
Figure 5.13. Particle size distribution histograms for 1 wt.% Pt – 1 wt.% Rh/fMWCNTs-I (left), 1.5 wt.% Pt – 0.5 wt.% Rh/fMWCNTs-I (center) and 1.8 wt.% Pt – 0.2 wt.% Rh/fMWCNTs-I (right)	85
Figure 5.14. Particle size distribution histograms for fresh 2 wt.% Pt/fMWCNTs-I (top left), 2 wt.% Pt/fMWCNTs-I after exposure for ~12 h to reaction conditions (top right), fresh 1.5 wt.% Pt – 0.5 wt.% Rh/fMWCNTs (bottom left) and 1.5 wt.% Pt – 0.5 wt.% Rh/fMWCNTs after exposure for ~12 h to reaction conditions (bottom right).....	87
Figure 5.15. Combined plot showing the performance of three 1.5 wt.% Pt – 0.5 wt.% Rh/fMWCNTs catalysts prepared by different methods in NO reduction with propene.....	89
Figure 5.16. Plot showing the performance of 2 wt.% Pt – 10 wt.% Na/fMWCNTs-I, 2 wt.% Pt – 1 wt.% Na/fMWCNTs-I and 2 wt.% Pt – 5 wt.% Na/fMWCNTs-I in NO reduction with propene.....	91
Figure 6.1. TEM micrograph of Pt-Ir/fMWCNTs-I (upper left), STEM (under contrast mode) micrograph of approximately the same region of the sample (upper right) and EDS spectrum showing peaks corresponding to both Pt and Ir (bottom).....	101
Figure 6.2. STEM micrograph of 2 wt.% Pt/fMWCNTs-I and EDS spectrum of the region highlighted in the micrograph.....	102
Figure 6.3. STEM micrograph of 1 wt.% Pt - 1 wt.% Rh/fMWCNTs-I and EDS spectrum of the highlighted region.....	103
Figure 6.4. TEM micrograph of a region containing a MWCNTs aggregate (left) within a 2 wt.% Pt – 10 wt.% Na/fMWCNTs-I catalyst, a close-up of the highlighted area	

	(right), EDS spectrum of the highlighted area (top) and a close-up of the low intensity peaks of the spectrum (bottom).....	105
Figure 6.5.	TEM micrograph of a region containing well dispersed MWCNTs within a 2 wt.% Pt – 10 wt.% Na/fMWCNTs-I catalyst and EDS spectrum of the highlighted area.....	106
Figure 6.6.	NH ₃ -MS-TPD profiles of pristine MWCNTs (left) and fMWCNTs (right) .	108
Figure 6.7.	C ₃ H ₆ -MS-TPD profiles of pristine MWCNTs (top left), fMWCNTs (top right), 2 wt.% Pt/fMWCNTs (bottom left) and 1.5 wt.% Pt – 0.5 wt.% Rh/fMWCNTs (bottom right).....	110
Figure 6.8.	Particle size distribution histograms for 10 wt.% Pt/Al ₂ O ₃ (top left), 10 wt.% Pt/MWCNTs (top right), 10 wt.% Pt/fMWCNTs (bottom left) and 7.5 wt.% Pt – 2.5 wt.% Rh/fMWCNTs (bottom right) (200 particles measured per histogram).....	114
Figure 6.9.	Expanded view of the Pt 4d region in the XPS spectrum of the 10 wt.% Pt/Al ₂ O ₃ reference catalyst. The ranges shown in the spectrum correspond to those of the Pt 4d _{5/2} peak (right peak in the spectrum) as reported in the X-ray Photoelectron Spectroscopy Database of the National Institute of Standards and Technology (NIST)	115
Figure 6.10.	Combined plot showing an expanded view of the Pt 4f region in the XPS spectra of 10 wt.% Pt/MWCNTs (top), 10 wt.% Pt/fMWCNTs (middle) and 7.5 wt.% Pt – 2.5 wt.% Rh/fMWCNTs (bottom) catalysts. The ranges shown in the spectrum correspond to those of the Pt 4f _{7/2} peak (right peak in the spectrum) as reported in the X-ray Photoelectron Spectroscopy Database of the National Institute of Standards and Technology (NIST)	116
Figure 6.11.	Expanded view of the Pt 4f and the Al 2p region in the XPS spectrum of 10 wt.% Pt/Al ₂ O ₃ prepared by impregnation followed by H ₂ reduction	118
Figure 6.12.	STEM micrograph (top row, left) of a 1.5 wt.% Pt – 0.5 wt.% Rh/fMWCNTs catalyst; elemental maps (bottom row) for carbon (red), platinum (blue) and rhodium (green); and a composite image of all three elemental maps (top row, right).....	121
Figure 6.13.	Carbon, platinum and sodium maps of three 2 wt.% Pt – 10 wt.% Na/fMWCNTs catalysts prepared by different preparation methods (the mapped region corresponds to the highlighted rectangles in the STEM micrographs).....	123
Figure 6.14.	Pt 4f region in the XPS spectrum of 2 wt.% - 10 wt.% Na/fMWCNTs.....	126
Figure 7.1.	Schematic HC-SCR redox mechanism over a Pt surface	129
Figure 7.2.	Mechanistic scheme for the HC-SCR of NO _x as proposed by Bamwenda ..	133
Figure 7.3.	Mechanistic scheme for the HC-SCR of NO _x on Pt/Al ₂ O ₃ and Pt/SiO ₂ catalysts as proposed by Captain and Amiridis	134
Figure 7.4.	Mechanism of N ₂ O production <i>via</i> 2-nitropropane hydrolysis as proposed by Nef	137
Figure 7.5.	NO/C ₃ H ₆ /O ₂ → Ar/C ₃ H ₆ /O ₂ switch performed at 260 °C	140
Figure 7.6.	Ar/C ₃ H ₆ /O ₂ → NO/C ₃ H ₆ /O ₂ switch performed at 260 °C	142
Figure 7.7.	NO/C ₃ H ₆ /O ₂ → NO/Ar/O ₂ switch performed at 260 °C.....	143
Figure 7.8.	NO/Ar/O ₂ → NO/C ₃ H ₆ /O ₂ switch performed at 260 °C.....	145
Figure 7.9.	NO/C ₃ H ₆ /O ₂ → NO/C ₃ H ₆ /Ar switch performed at 260 °C.....	146
Figure 7.10.	NO/C ₃ H ₆ /Ar → NO/C ₃ H ₆ /O ₂ switch performed at 260 °C.....	147

Figure 7.11. NO/C ₃ H ₆ /O ₂ → Ar/C ₃ H ₆ /O ₂ switch performed at 300 °C	149
Figure 7.12. Ar/C ₃ H ₆ /O ₂ → NO/C ₃ H ₆ /O ₂ switch performed at 300 °C	150
Figure 7.13. NO/C ₃ H ₆ /O ₂ → NO/Ar/O ₂ switch performed at 300 °C.....	151
Figure 7.14. NO/Ar/O ₂ → NO/C ₃ H ₆ /O ₂ switch performed at 300 °C.....	152
Figure 7.15. NO/C ₃ H ₆ /O ₂ → NO/C ₃ H ₆ /Ar switch performed at 300 °C.....	153
Figure 7.16. NO/C ₃ H ₆ /Ar → NO/C ₃ H ₆ /O ₂ switch performed at 300 °C.....	154
Figure 8.1. Photograph of a metal monolith coated with MWCNTs and SEM image of the MWCNTs showing their alignment.....	165
Figure 8.2. TEM image of a Pt/MWCNTs/metal monolith catalyst and EDS spectrum of the area highlighted in red. An iron particle (the catalyst used in the production of the MWCNTs) is highlighted in green.....	167
Figure 8.3. TEM image of a Pt/MWCNTs/metal monolith catalyst showing both Pt metal particles of 2-5 nm in diameter (red) and iron catalyst particles remaining from the MWCNT synthesis (green).....	168
Figure 8.4. Combined TGA plot of MWCNTs thermally treated under a flow of 0.5 % NO ₂ balance N ₂ (all samples were initially ramped to the indicated temperature at a rate of 5 °C/min).....	170
Figure 8.5. O 1s region in the XPS spectrum of NO ₂ -fMWCNTs	172
Figure 8.6. TEM micrographs of Pt/NO ₂ -fMWCNTs/metal monolith (an iron catalyst particle remaining from the MWCNT synthesis is highlighted in green)	174
Figure 8.7. TEM micrographs of 3:1 Pt-Rh/NO ₂ -fMWCNTs/metal monolith (an iron catalyst particle remaining from the MWCNT synthesis is highlighted in green)	175
Figure 8.8. Results of temperature sweep for Pt/NO ₂ -fMWCNTs/metal monolith catalyst. GHSV = 30,000 h ⁻¹ , C:NO _x = 8:1	176
Figure 8.9. Results of temperature sweep for Pt/NO ₂ -fMWCNTs/metal monolith catalyst. GHSV = 50,000 h ⁻¹ , C:NO _x = 8:1	177
Figure 8.10. Low magnification TEM micrograph of post-mortem Pt/NO ₂ -fMWCNTs/metal monolith (left) and a close-up of the highlighted area (right)	178
Figure 8.11. Results of temperature sweep for 3:1 Pt-Rh/NO ₂ -fMWCNTs/metal monolith catalyst. GHSV = 30,000 h ⁻¹ , C:NO _x = 8:1	180
Figure 8.12. Results of temperature sweep for 3:1 Pt-Rh/NO ₂ -fMWCNTs/metal monolith catalyst. GHSV = 50,000 h ⁻¹ , C:NO _x = 8:1	180
Figure 8.13. Results of C:NO _x sweep for 3:1 Pt-Rh/NO ₂ -fMWCNTs/metal monolith catalyst. GHSV = 50,000 h ⁻¹ , T = 270-290 °C.....	182
Figure 8.14. N ₂ O make during C:NO _x sweep for 3:1 Pt-Rh/NO ₂ -fMWCNTs/metal monolith catalyst. GHSV = 50,000 h ⁻¹ , T = 270-290 °C	182

Chapter 1. General Introduction.

Environmental catalysis has been defined as “a collection of chemical processes that use catalysts to control the emission of environmentally unacceptable compounds” [1]. This field, which was virtually nonexistent before 1976, has grown into a multi-billion dollar worldwide business during the past three decades [2]. In the automotive industry, heterogeneous catalysts are used to accomplish the conversion of pollutants into more benign substances at high rates and reasonable temperatures, therefore achieving cost-effective pollution control.

It is a well-known fact that nitrogen oxides (NO_x) are atmospheric pollutants that pose a serious threat to both the environment and human health. The three-way catalyst (TWC), which gets its name from the fact that it addresses three different pollutants (NO_x , CO and hydrocarbons) simultaneously, is quite effective at reducing NO_x emissions from engines working under stoichiometric air-to-fuel ratios (i.e., most gasoline engines). However, its performance is unsatisfactory under excess air conditions like those under which diesel engines operate (*vide infra*). This is because in the TWC, at stoichiometry, CO and hydrocarbons (HCs) can act as reducing agents for NO_x ; whereas under oxidizing conditions, the conversion of both CO and HCs into CO_2 is favored.

The use of hydrocarbons as reductants in the Selective Catalytic Reduction (HC-SCR) of NO_x has been proposed as a possible solution for mobile NO_x emission control under such lean conditions. Given that the operating temperatures of light duty diesel (LDD) engines (LDD engines are those used in passenger vehicles of up to about 3.5 tonnes or 8,500 pounds in weight in Europe and in American States other than California, respectively [3]) typically range from ~ 150 °C to ~ 500 °C, it is very unlikely that a single catalyst can be developed showing acceptable activity throughout this entire temperature span. Therefore, the use of a system in which two catalysts would be placed in parallel (with gas switching to ensure the use of the appropriate catalyst depending on the exhaust gas temperature) is proposed in this dissertation. One of these catalysts would operate in the ~ 150 to 300 °C temperature range, while the other would be used for exhaust gas

temperatures ranging from ~300 to 500 °C. Whereas several catalysts active in this high temperature span are already available, a catalyst active across the low temperature range proposed above is yet to be found. Supported Platinum Group Metals (PGMs) show the best performance at low temperatures. However, these catalysts possess two main drawbacks that have to be addressed, namely, a narrow temperature window of operation and a high selectivity towards N₂O. Thus, the research described in this dissertation had two main goals: 1) to develop a catalyst with improved low temperature performance; and 2) to derive fundamental insights that will assist in furthering the development of HC-SCR catalysts.

In the present chapter, NO_x is defined, some of the environmental and health problems it causes are mentioned, and its sources are classified and compared vis-à-vis their relative contribution to total NO_x emissions. Further, NO_x emission regulations and some control technologies are addressed. Finally, the novel dual catalyst technique for NO_x reduction in an oxidative environment described above is discussed in more detail.

1.1. NO_x as a threat to health and the environment.

The term NO_x makes reference to two oxides of nitrogen: NO (nitric oxide) and NO₂ (nitrogen dioxide). N₂O (nitrous oxide) does not form part of what one would term NO_x, but it is important to keep this compound in mind given that it is a stratospheric source of NO and a very powerful greenhouse gas (its global warming potential (GWP) is 300 times that of CO₂ over a hundred year time span) [4-7]. Figure 1.1 shows how the formation and emission of nitrogen oxides to the atmosphere and their subsequent reactions therein are among the main features within the cycling of nitrogen in the environment.

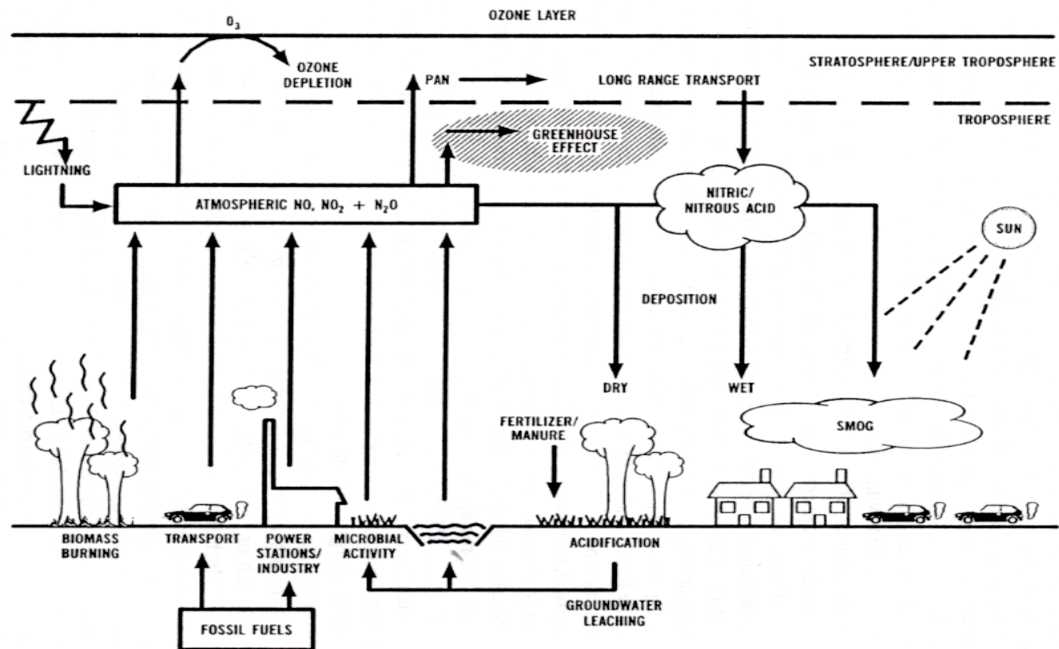


Figure 1.1. The cycling of nitrogen in the environment. PAN= peroxyacyl nitrates (R-COOO-NO₂). Nitrogen Oxides Control Technology Fact Book by Leslie L. Sloss, 1992, Noyes Data Corp./William Andrew Inc. Reprinted with permission.

NO_x has been proven to contribute to a variety of environmental and health-related problems, some of which are also illustrated in Figure 1.1. When emitted to the troposphere, NO_x is involved in a series of photochemical reactions that lead to ozone formation. In turn, tropospheric ozone is known to contribute to both global warming and smog formation [8]. On the other hand, the NO that reaches the stratosphere, together with the NO that is produced in that region of the atmosphere by the *in situ* decomposition of N₂O, is the cause of about half the stratospheric ozone depletion [9]. NO_x is also oxidized in the atmosphere to higher oxides that include HNO₂, HO₂NO₂ and HNO₃ [10], which are also involved in the process of smog formation and, because of their acidic properties, can be blamed for ~30 % of the total acidification of rain (the other ~70 % being caused by SO_x) [11]. Obviously, ground level NO_x can be inhaled by humans, thus causing a variety of problems in the respiratory system, such as bronchitis and pneumonia. Further, NO_x has been proven to cause alterations to the immune system that can lead to a heightened susceptibility to viral infections [12]. Finally, one must

consider the carcinogenicity that both NO and some products formed during atmospheric reactions that involve NO_x have been found to possess [13,14].

1.2. Sources of NO_x.

NO_x has both natural and anthropogenic sources. In nature, it is produced by lightning, volcanic activity, the microbial decomposition of proteins in soils and forest fires. On the other hand, human activity produces these compounds in all combustion processes where the temperatures are high enough for nitrogen in the air or in the fuel to be oxidized. In fact, as can be seen in Figure 1.2., processes involving the combustion of fossil fuels represent the main source of NO_x emissions in the United States (Figure 1.3 illustrates the proportion in which different regions in the world have contributed and are projected to contribute to global combustion-generated NO_x emissions). This is not surprising, since the vast majority of the energy requirements of mankind are satisfied by processes that involve the combustion of fossil fuels, something that is not likely to change in the near future.

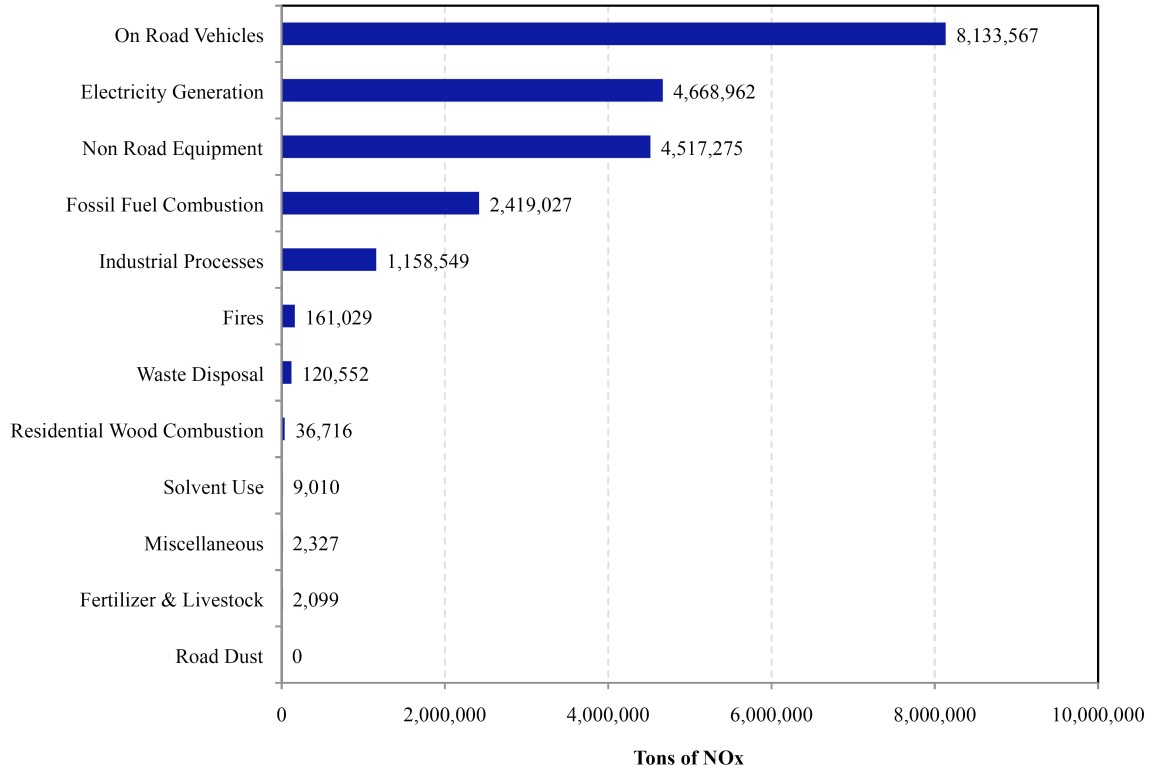


Figure 1.2. NO_x emissions in the United States by source sector based on the most recent inventory (2002) [7].

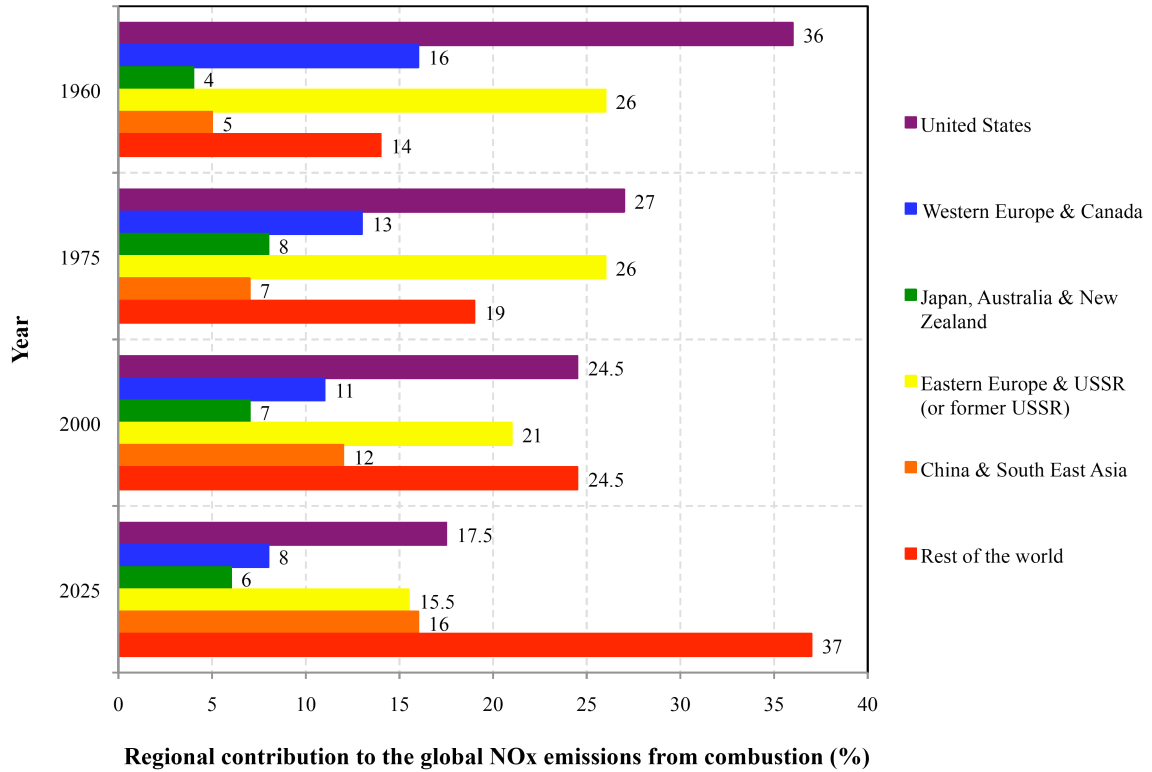


Figure 1.3. Regional contribution (%) to global NO_x emissions from combustion [15].

Taking this into account, it is unrealistic to deal with the problem of NO_x pollution by eliminating the anthropogenic sources of NO_x altogether and therefore, the post-emission conversion of these noxious pollutants into innocuous gases appears to be the best solution to this problem.

1.3. Removal of NO_x.

Anthropogenic sources of NO_x can be categorized into stationary and mobile. In turn, mobile sources can be further classified depending on the air-to-fuel ratio under which they operate. Thus, mobile NO_x sources can be 1) stoichiometric; 2) rich (excess fuel); or 3) lean (excess oxygen). As mentioned above, for rich or stoichiometric conditions, the three-way catalyst is quite efficient at reducing NO_x, along with hydrocarbons and carbon monoxide emissions. However, its deNO_x performance is disappointing under lean

conditions such as the ones under which diesel engines operate (the air/fuel ratio in diesel engines is rarely less than 22 [2] and can be as high as 50 [3]), as can be seen in Figure 1.4.

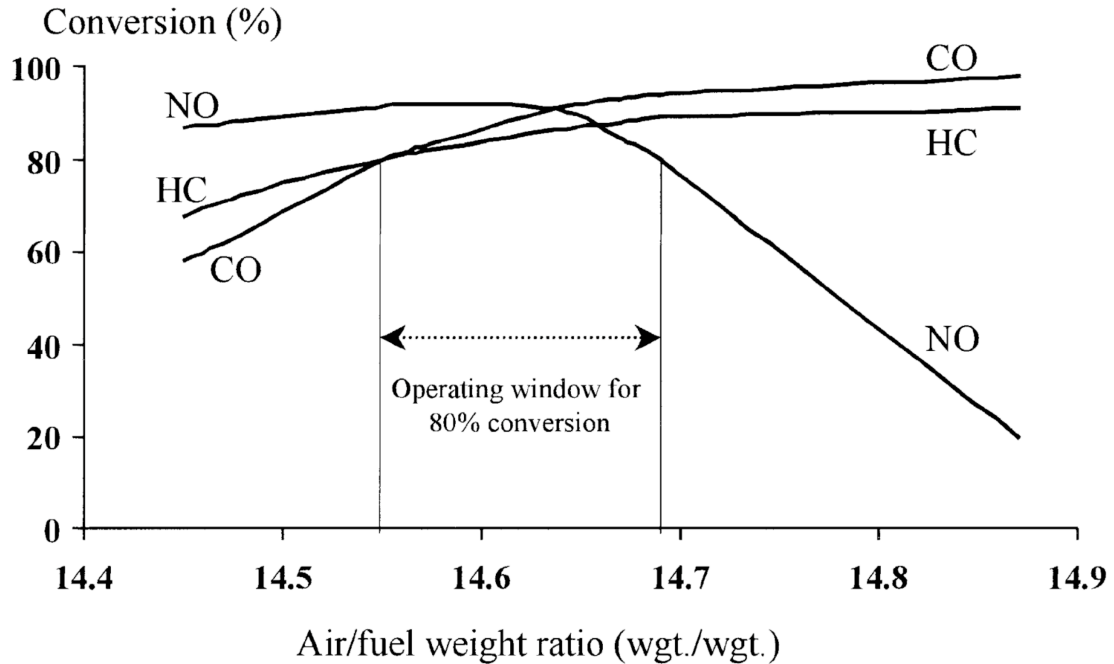


Figure 1.4. Three-way catalyst (TWC) performance determined by engine air to fuel ratio. Reprinted from Applied Catalysis A: General, Vol. 221, R.H. Heck, R.J. Farrauto, Automobile exhaust catalysts, Pages No. 443-457, Copyright (2001), with permission from Elsevier.

This is unfortunate, since diesel engines show fuel efficiencies 20-40 % higher than those of gasoline-fuelled engines. This increased fuel economy, combined with the recent interest in reducing carbon emissions to curb global warming, explains the growing number of LDD engine vehicles, which are also more durable than gasoline engines and deliver greater torque. However, diesel fuelled vehicles contribute ~63 % and ~27 % of particulate matter (PM) and NO_x emissions, respectively [16]. The use of diesel fuels with sulfur levels below 0.05 % has enabled the diesel oxidation catalyst (DOC) to achieve reductions of ~20 % of PM [17], but the relatively high NO_x emissions are yet to

be addressed. Therefore, the oxygen rich streams produced by diesel-fuelled engines represent major sources of NO_x that must be treated in order to comply with ever more stringent emission standards. Parenthetically, the current American set of standards for light-duty vehicles defined in the Clean Air Act Amendments (CAAA) of 1990 is known as the Tier 2 standards and was adopted on December 21, 1999, with a phase-in implementation schedule from 2004 to 2009 [18]. When fully implemented in 2009, the average NO_x emissions of the entire light-duty vehicle fleet sold by each manufacturer has to meet the average NO_x standard of 0.07 g/mi when tested according to the Federal Test Procedure-75 (FTP-75) [19]. The FTP-75 is used for emission certification of LDD vehicles in the United States and its cycle consists of three segments (a cold start, a transient phase and a hot start), as shown in Figure 1.5.

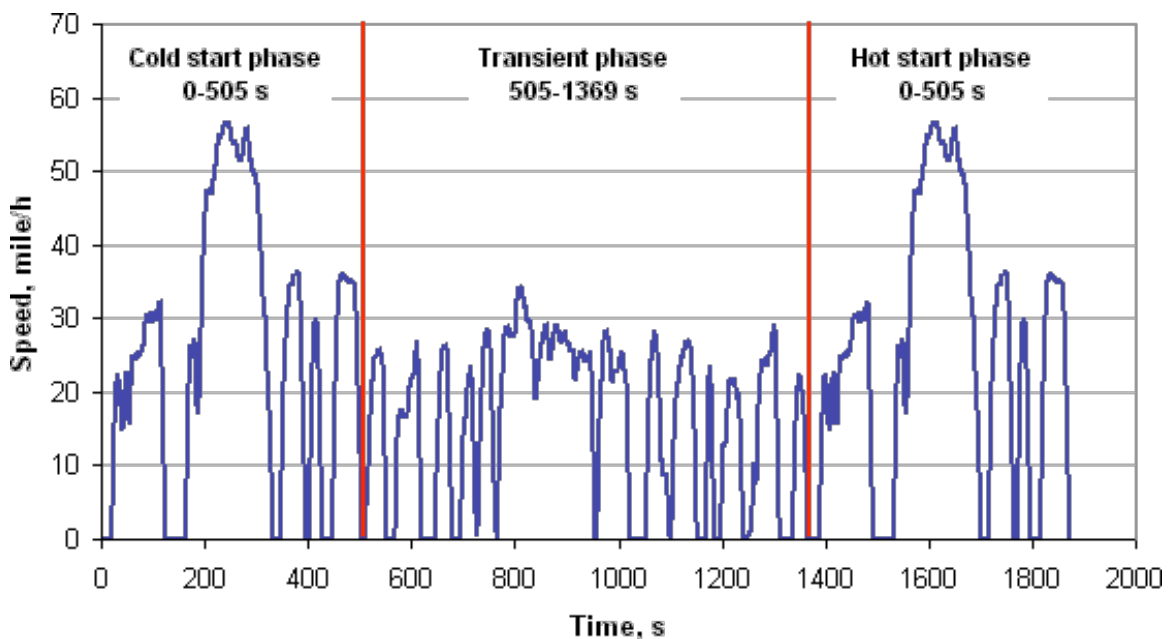


Figure 1.5. The FTP-75 cycle [20]. Source: DieselNet.com. Figure reprinted with permission.

Other basic parameters of the cycle include a distance travelled of 11.04 miles (17.77 km), a total duration of 1,874 seconds and an average speed of 21.2 mph (34.1 km/h). The emissions from each phase must be collected in a separate teflon bag, analyzed and

expressed in g/mile (g/km). The weighting factors are 0.43, 1.0 and 0.57 for the cold start, the transient phase and the hot start phase, respectively.

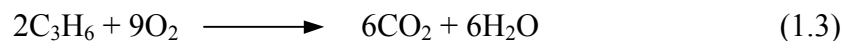
The Selective Catalytic Reduction of NO_x using ammonia as the reductant (NH₃-SCR) is known to be a very effective approach for the abatement of NO_x emissions from stationary sources. Indeed, NH₃-SCR has been so successful at removing NO_x from these sources (even under excess oxygen conditions) that several efforts have been made to apply this technology to mobile sources. However, several issues, namely the transportation of ammonia through residential areas, equipment corrosion, lack of refueling infrastructure, need of on board diagnostics to control injection and the risk of unreacted ammonia being emitted to the environment, have made this impractical. Since urea can be hydrolyzed into ammonia, its use as an alternative carrier is being explored. However, even though this would solve many of the aforementioned problems it would leave some others unsolved, most notably the risk of ammonia slippage. Thus, the removal of NO_x produced by mobile sources has proven to be a technological challenge. The Selective Catalytic Reduction of NO_x using hydrocarbons as reductants offers itself as a potential deNO_x alternative.

1.4. Lean deNO_x via HC-SCR.

HC-SCR uses a catalyst to facilitate the reaction between NO_x and a hydrocarbon reductant in the presence of excess oxygen. Using propene as a model hydrocarbon, the ideal HC-SCR reaction would have the form:



However, other undesired reactions can also take place:



Reaction (1.2) is undesirable given that it represents an incomplete redox reaction which produces two noxious gases: CO and N₂O. Reaction (1.3) is undesired given that it consumes the hydrocarbon reductant by a reaction with oxygen, which is present in the exhaust in large excess.

HC-SCR was independently reported for the first time in 1990 by Iwamoto [21,22] and Held [23]. These two authors observed that Cu-ZSM-5 was capable of reducing NO_x with hydrocarbons when excess oxygen was present. Unfortunately, although this and other zeolitic catalysts show a high initial deNO_x activity, they have a variety of drawbacks, namely a narrow deNO_x temperature window, low hydrothermal stability, low resistance to sulfur poisoning and an undesirable selectivity towards CO. With the aim of finding a material that shows high deNO_x activity across a wide temperature window, along with a good selectivity towards N₂ and CO₂, and acceptable durability, literally thousands of materials have been investigated for HC-SCR activity [24]. Unfortunately, no such material has been found to date.

The following chapter in this thesis aims at presenting the state of the art of HC-SCR by reviewing the relevant scientific literature that has been published about the subject. Special emphasis is made on the pros and cons of catalysts that have been found to be promising throughout the years.

1.5. A novel technique for NO_x reduction in an oxidative environment.

The main and recurrent problem observed in materials active towards the HC-SCR reaction is the narrow deNO_x temperature window in which they show acceptable NO_x conversion. This problem arises because, at high temperatures, the total combustion of the hydrocarbon, represented by reaction (1.3), is favored and this renders those formulations capable of activating the hydrocarbon at low temperatures unsuitable. Taking this into account, along with the fact that typical LDD engines show exhaust temperatures ranging from 150 to 500 °C, it is unlikely that a single catalyst can be developed that shows acceptable deNO_x activity across this entire temperature range.

The use of two catalysts, one active in the low temperature (LT) range (150-300 °C) and another in the high temperature (HT) range (300-500 °C), is a potential solution to this problem. These two catalysts could be placed in series and a dual injection system could be used to direct the fuel upstream either of the LT or the HT catalyst. However, this configuration, which is shown schematically in Figure 1.6, has been investigated in the past with disappointing results [25].

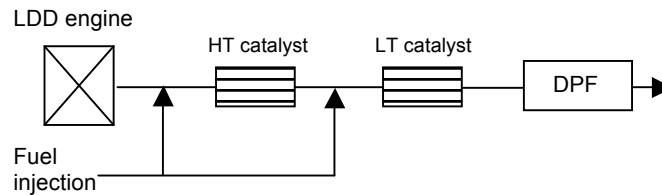


Figure 1.6. Series catalysts with dual injection configuration for application of dual HC-SCR catalysts. DPF= diesel particulate filter.

Alternatively, the two catalysts could be placed in parallel in a setup similar to that shown in Figure 1.7, in which a gas-switching valve would ensure the use of the appropriate catalysts based on the exhaust gas temperature.

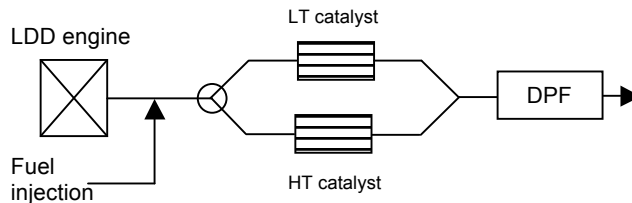


Figure 1.7. Parallel catalysts with exhaust gas switching configuration for application of dual HC-SCR catalysts. DPF= diesel particulate filter.

Several reasons can be invoked in order to support the proposition that this last configuration should exhibit improved performance: 1) if the HT catalyst preceded the LT formulation, the former would act like a heat sink, delaying the light-off of the latter; 2) placing the two formulations in series would prevent the use of hydrocarbons present

in the exhaust by both catalysts (given that they would be adsorbed at low temperatures by the HT formulation); 3) a single fuel injector is required when the catalysts are placed in parallel; 4) a dual injector system would lead to a poorer mixing of the fuel with the exhaust gas and therefore to an uneven fuel distribution over the catalysts; and 5) placing the catalysts in parallel and setting a maximum temperature for the LT formulation would minimize the thermal aging and increase the durability of the latter.

It could be argued that the use of a gas-switching valve represents a potential drawback of the proposed system. However, such a device is already being used in the Mercedes-Benz CLK 200 CGI [26]. Further, the design of a switching valve with no moving parts has also been described recently [27].

Obviously, the effectiveness of this dual catalyst system would be limited by the performance of the LT and HT formulations used. Unfortunately, although high temperature formulations showing satisfactory activity, selectivity and durability, such as $\text{In}_2\text{O}_3/\text{Al}_2\text{O}_3$ or $\text{Ag}/\text{Al}_2\text{O}_3$, are already available [28], this is not the case for low temperature formulations.

1.6. Carbon nanotube supported PGMs as low temperature HC-SCR catalysts.

Supported PGMs are the best low temperature HC-SCR catalysts developed so far (maximum activities of >90 % achieved at temperatures as low as 200 °C have been reported for catalysts with a 1 wt.% metal loading and a weight hourly space velocity (WHSV) of $12,000 \text{ mL} \cdot \text{h}^{-1} \cdot \text{g}^{-1}$) [29]). However, as mentioned above, these catalysts possess two main drawbacks: 1) a narrow temperature window of activity; and 2) a high selectivity towards N_2O . A third drawback shown by PGMs supported on activated carbon (one of the catalysts that shows the best low temperature deNO_x performance) is the propensity of the support to undergo combustion. Given that multiwalled carbon nanotubes (MWCNTs) have a higher resistance to oxidation compared to other forms of carbon [30], their use as catalytic support should help in addressing this last problem. Further, compared to oxidic supports, MWCNTs may also offer the advantage of keeping the supported PGMs in a more reduced state, which in turn may increase activity.

With respect to the metallic phase, Pt is the most active PGM for low temperature HC-SCR, although Rh and Ir have also been found to be catalytically active. Therefore, the alloying of PGMs is also of interest, given that the use of PGM alloys as an active phase may further improve the performance of MWCNTs-based catalysts.

1.7. Scope of the dissertation.

As stated above, the goal of the research described in this thesis is twofold: 1) to develop an improved low temperature HC-SCR catalyst; and 2) to derive fundamental insights that will assist in the future development of HC-SCR catalysts.

The following chapter of this dissertation provides a literature review of HC-SCR lean deNO_x strategies in which special attention is given to the catalysts developed to date, their advantages and their disadvantages.

The third chapter focuses on multiwalled carbon nanotubes, the material chosen as the catalyst support for these studies. In this chapter, the physical and chemical properties of MWCNTs are considered, in particular those that are relevant to catalysis. An overview of the method by which this material is synthesized is also given. Emphasis is placed on the surface modification of MWCNTs, a step that has been reported to assist the deposition of highly dispersed metal particles onto the surface of this support.

In the fourth chapter, the preparation of PGM/MWCNTs catalysts is discussed. Several methods by which the deposition of PGMs on MWCNTs was attempted are described, as is the characterization of the resulting materials. The preparation and characterization of reference catalysts is also addressed.

The fifth chapter covers the testing of the prepared powder catalysts for activity in the HC-SCR reaction. A comparison of their activity-selectivity curves is included, along with the kinetic parameters determined for the formulations found to be most promising in catalyzing the reduction of NO_x with propene.

In chapter six, experiments performed in order to probe the relationship between catalyst structure and catalytic performance are described. Special emphasis is placed on the insights provided by the use of spectroscopic techniques.

The seventh chapter includes both a literature review of the mechanistic studies performed in the past on precious metal HC-SCR catalysts and the results of transient studies performed to probe the reaction mechanism on MWCNTs-based formulations.

The eighth chapter of this thesis covers the preparation and characterization of PGMs/MWCNTs monolithic catalysts, along with their testing on a LDD engine.

A synopsis and an assessment of all the results reported in this thesis are given in the ninth chapter. Additionally, future lines of research are suggested in this final section.

Finally, the most common abbreviations used throughout this dissertation are included in the Appendix titled List of Abbreviations.

Chapter 2. Selective Catalytic Reduction of Nitrogen Oxides with Hydrocarbons.

2.1. Introduction.

Diesel engines are known to be reliable, durable, easy to maintain, inexpensive to operate and fuel-efficient [31]. This last attribute has heightened the relevance of diesel engines in recent times, given that increased fuel efficiency, which translates into lower carbon emissions, might help to curb global warming.

The high fuel efficiency of diesel engines originates from their principle of operation, which is that fuel is injected into a chamber containing highly pressurized air where the temperature is high enough for combustion to take place. This compression-ignited process used in diesel engines differs from the spark-ignited process of gasoline-fuelled engines in two main points: 1) a vast excess of oxygen needs to be present in the combustion mixture (in order to shift the reaction equilibrium to the right in the absence of a spark); and 2) the combustion is considerably cooler. The latter point explains why less NO_x (and more particulate matter) is produced by diesel engines, while the former explains why NO_x emissions from diesel engines are more difficult to treat.

A variety of strategies have been used to address the problem of treating NO_x emissions from lean exhaust gases, most of which involve the use of a heterogeneous catalyst capable of reducing NO_x in an oxidizing atmosphere [32]. Mainly because of its ease of installation and operation, the selective catalytic reduction of NO_x using hydrocarbons as reductants (HC-SCR) has been found to be one of the most propitious lean de NO_x technologies.

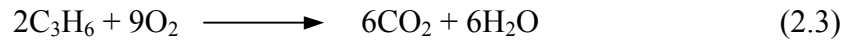
In this chapter, the HC-SCR formulations that have been found to be most promising throughout the years are reviewed, along with their respective advantages and disadvantages.

2.2. HC-SCR fundamentals.

Recapitulating what has already been stated in the introductory chapter of this dissertation, HC-SCR involves the use of a catalyst to facilitate the reaction between NO_x and a hydrocarbon reductant in an oxidizing environment. The ideal HC-SCR reaction, when propene is used as the hydrocarbon reductant, would have the form:



However, other undesired reactions can also occur:



What makes reaction (2) undesirable is that it represents an incomplete redox reaction in which two noxious gases (CO and N_2O) are produced. Reaction (1.3) is undesired because it consumes the hydrocarbon reductant by a reaction with oxygen, which is present in the exhaust in large excess. Indeed, in diesel exhausts, the oxygen concentration (5-10 %) is well above the ppm levels in which both NO_x and HCs are present. Therefore, the use of a catalyst is indispensable to favor the reaction of NO_x with HCs, which would otherwise react with O_2 [16]. The fact that a particular formulation favors reactions (2.1) and (2.2) over reaction (2.3), is what makes the reduction carried by the catalyst “selective”. The terms “selective” and “non-selective” were introduced at an early stage of the development of Cu-ZSM-5 lean de NO_x catalysts by Iwamoto and Hamada [14]. These authors termed “non-selective” catalysts those which in the presence of oxygen were unable to reduce NO_x and could only oxidize the hydrocarbon [33]. By inference, a “selective” catalyst is one which in the presence of oxygen favors the reaction between the hydrocarbon and NO_x over its combustion by oxygen.

2.3. HC-SCR catalysts used throughout the years.

In the previous chapter it was stated that HC-SCR was independently reported for the first time in 1990 by Iwamoto and Held. However, as early as 1979 Ritscher and Sandner had reported the simultaneous occurrence of NO_x reduction and CO and HC oxidation in excess air on Cu/high-silica zeolites [12,34]. Further, Held and Koenig proposed in a 1987 patent that the reduction of NO_x in an oxidative environment is carried by CO formed by the partial oxidation of hydrocarbons present in the exhaust [35]. Thus, although the proposed intermediacy of CO was eventually abandoned, these patents can be considered the first reports of a catalyst active in the HC-SCR reaction in the scientific literature. Indeed, all of the aforementioned authors observed that metal-containing zeolites and supported Cu catalysts were capable of reducing NO_x with hydrocarbons when excess oxygen was present.

2.3.1. Zeolitic catalysts.

Through research inspired by these reports, Hamada *et al.* discovered that the protonated form of several zeolites was active in the NO reduction with C₃H₈ at 300 °C in the presence of 10 % O₂ [36]. Notably, the use of C₃H₆ in place of C₃H₈ was found to lower the reaction temperature to 200 °C and to yield CO₂ as the exclusive oxidation product. In subsequent publications, these workers reported that alumina was also active in NO reduction at 400 °C (with 100 % conversion to CO₂ at 600 °C) [37] and that sulfated TiO₂, ZrO₂ and Fe₂O₃ solid superacids afforded 50 % conversion of NO to N₂ when C₃H₈ was used as the reductant [38].

After reporting in 1991 that Cu-ZSM-5 (a copper-exchanged aluminosilicate pentasil zeolite) was capable of catalyzing NO reduction by C₂H₄, C₃H₆, C₃H₈ and C₄H₈ in the presence of oxygen with only minor SO₂ effect on catalyst performance, Iwamoto and co-workers proceeded to report the improved reduction of NO by C₂H₄ under oxidizing conditions at 200 °C on a Fe-mordenite catalyst [39]. The use of these zeolite-supported catalysts for NO_x abatement from a diesel engine exhaust was also reported [37].

These discoveries led to a period of intense research on the development of HC-SCR catalysts and by 1994 over 200 patents had been published in this area [40]. In the case of zeolite-supported HC-SCR catalysts, workers soon discovered that although short-term NO_x conversions up to 95 % could be obtained, the relatively poor durability of the zeolitic supports represented a major drawback. Indeed, several factors conspire to limit the use of these materials in practical applications: 1) an undesirable selectivity towards CO [41]; 2) an unacceptably low hydrothermal stability [33]; and 3) low activity in the presence of H_2O and SO_2 [42]. Some authors have found zeolitic catalysts to display acceptable resistance to sulfur-poisoning under dry conditions [43], while other workers have suggested the existence of synergistic effects between SO_2 and water which cause the deactivation of Cu-ZSM-5 catalysts through the formation of CuSO_3 and CuSO_4 [44]. The latter seems to be consistent with the fact that metal cations tend to migrate out of the pores of the zeolites upon hydrothermal aging, becoming more vulnerable to sulfur-poisoning.

2.3.2. Supported platinum group metal catalysts.

These limitations of zeolite-based materials prompted the search for alternatives and, as early as 1993, supported platinum groups metals (PGMs) were shown to be promising HC-SCR catalysts. Indeed, Obuchi *et al.* found that under real diesel exhaust conditions, PGMs supported on γ -alumina not only showed a higher activity at a lower temperature than Cu-ZSM-5, but also showed improved durability [44]. Unfortunately, since the early stages of their study as HC-SCR catalysts, supported PGMs have been known to have a challenging drawback, namely, their limited selectivity to N_2 as opposed to N_2O . Throughout the years, a variety of approaches to improve the N_2 -selectivity of these catalysts have been attempted [45,46], however, reductions in the N_2O make have only been modest and N_2 -selectivity remains a shortcoming of supported PGM HC-SCR catalysts to this day. As mentioned in the previous chapter, another widely documented limitation of these catalysts is their narrow temperature window of operation [47-51], which typically ranges from 200 to 250 °C [29]. Above 250 °C, the catalysts tend to favor the combustion of the hydrocarbon (reaction (2.3)) over its reaction with NO_x (reactions (2.1) and (2.2)). Vis-à-vis the temperature window of operation of supported these

catalysts, the full width at half maximum (FWHM) has been shown to be ~ 50 °C by Burch and Millington, who also determined alumina-supported base metal oxides to show much wider activity windows (FWHM ≈ 200 °C) and comparable deNO_x activities to those of supported PGM formulations, although at higher temperatures [52].

2.3.3. Supported base metal oxide catalysts.

Alumina-supported base metal oxides can be considered the third main class of catalysts which are active for HC-SCR. The use of these materials as HC-SCR catalysts offer several advantages, namely, a remarkable stability at elevated temperatures, an efficient use of the hydrocarbon as reductant and a high N₂-selectivity. However, the water and sulfur-tolerance of supported base metal oxides appears to be less than ideal, although this depends on the nature of the catalyst, the water and SO₂ concentration and even on the reductant used [53]. Nevertheless, the main disadvantage shown by this type of catalyst is that NO_x reduction activity is confined to high temperatures, typically in excess of 350 °C. Thus, supported base metal oxides are unsuitable for LDD applications due to their lack of low temperature deNO_x activity. Nevertheless, these materials could prove useful if used in combination with other formulations active in the low-temperature regime, as stated in the previous chapter. With this in mind, the most promising catalyst of this type appears to be In₂O₃/Al₂O₃. Indeed, Hamada *et al.* have systematically tested a number of metal oxides supported on alumina for activity in NO_x reduction with propene and found In₂O₃ to show the best overall performance [28].

Silver supported on alumina has also attracted considerable interest given its high activity and selectivity in the HC-SCR reaction [53]. Meunier *et al.* have shown bare alumina to be active for C₃H₆-SCR and very N₂-selective, but only at very high temperatures (well above 500 °C). These authors have also found 1.2 % Ag/Al₂O₃ to show a similar performance, albeit shifted to lower temperatures (~ 500 °C). In turn, 10 % Ag/Al₂O₃ is also active at even lower temperatures (~ 350 °C), yet highly selective for N₂O production [54]. Interestingly, these and other workers have assigned these activity patterns to the presence of different catalytically phases, large metallic silver particles and small silver oxide clusters being responsible for the behavior of the high and the low loaded

materials, respectively [55-57]. However, although these results appear promising, several factors hamper the utilization of these catalysts in automotive applications, such as concerns about the long term susceptibility of Ag/Al₂O₃ to poisoning by SO₂ and the lack of low temperature (<300 °C) HC-SCR activity shown by this material [28].

2.4. HC-SCR on supported PGM catalysts.

2.4.1. Monometallic PGM catalysts.

Thus, of the three main classes of HC-SCR catalysts, *viz.*, zeolitic materials, supported base metal oxides and supported PGM, the latter remain the most promising HC-SCR formulations (in spite of their aforementioned limitations) due to their well-documented high activity at low temperatures [47,52,58-63], their hydrothermal stability [33,50,64] and their resistance to sulfur-poisoning [44,65]. Hence, intense effort have been focused on the identification of the support and the metal (or combination of metals) with the best low-temperature HC-SCR performance, in an attempt to develop a carrier-PGM composite showing maximum NO_x conversion and N₂-selectivity. Although oxidic supports (mainly zeolites, alumina and silica) have been customarily used as carriers in supported PGM-catalysts, activated carbon (AC) has been the subject of several recent studies [29,66-68]. Through these studies, Salinas-Martínez de Lecea, Illán-Gómez, García-Cortés *et al.* have found Pt/AC catalysts to be superior (more active and more N₂-selective) to Pt/Al₂O₃ in the NO_x reduction with C₃H₆, which has been attributed by these workers to the higher degree of acidity of the support. However, these authors also encountered a problem with the use of AC as support, namely its tendency to be oxidized by NO₂, the onset of which typically occurs at approximately 250 °C.

With respect to the active phase, all of the PGMs (Ru, Rh, Pd, Os, Ir and Pt) have been investigated for activity in the HC-SCR reaction. 1 % Ru/Al₂O₃ has been reported to show a maximum NO_x conversion at 300 °C when tested under model reactants. However, when activity tests were performed on a 0.15 % Ru/Al₂O₃ catalyst using real exhaust gas, the conversion observed was negligible [44]. It appears that Ru is susceptible to SO₂-deactivation, although the phenomenon might have been exacerbated by the low metal loading used in the tests involving real exhaust gas. Pd HC-SCR

catalysts have been shown to have an interesting behavior: although they exhibit rather low NO_x conversion and N₂-selectivity (1 % Pd/Al₂O₃ has been reported to show a maximum NO_x conversion of 25 % at 250 °C and a selectivity towards N₂O of *ca.* 50 % [52]), their temperature window of operation is remarkably broad, ranging from ~200 to ~300 °C [69]. With respect to Ir, maximum NO_x conversions of 10-20 % at 350-400 °C have been reported for a 1 % Ir/Al₂O₃ catalyst [44,52]. More recently, 1 % Ir/SiO₂ catalysts have been proven able to achieve higher NO_x conversions (>50 %) with remarkable N₂-selectivity (>90 %). However, the latter only occurs in temperatures in excess of 600 °C [70]. Ir catalysts have been used by Mitsubishi for lean burn vehicles sold in Europe [71], however, this is no longer the case. This is in part due to concerns surrounding the volatility of IrO₃ at high temperatures, which can result in loss of Ir from the catalyst.

Most of the research on supported PGMs HC-SCR catalysts involve the use of Pt or Rh as the catalytically active phase. Indeed, the work done involving these two metals is so extensive (particularly for Pt [47,58-60,72-82]), that it is difficult to assess the catalytic performance of supported Pt or Rh catalysts due to the great variation within the supports, metal loadings, reductants and experimental conditions used in different studies. With respect to supported Pt catalysts, NO_x conversions as high as 90 % at temperatures as low as 200 °C have been reported for both 1 % Pt/zeolites and 1 % Pt/AC [29]. However, more modest activities are typically reported for alumina-supported Pt (one of the most intensively studied HC-SCR catalysts), 1-3 % Pt/Al₂O₃ materials showing maximum NO_x conversions between 50 and 60 % at temperatures ranging from 250 to 270 °C [44,52,83]. Further, tests performed using real exhaust gas have proven 0.5 % Pt/Al₂O₃ to afford a maximum NO_x conversion of 40 % at 290 °C [44]. Reports on the selectivity of supported Pt HC-SCR catalysts also show a degree of variability, however, N₂O-selectivity values are typically around 50 % at the temperature of maximum NO_x conversion [44,47,52,83]. On the other hand, 1-3 % Rh/Al₂O₃ catalysts have been reported to display maximum NO_x conversions between 35 and 50 % at temperatures ranging from 300 to 350 °C [44,52,83]. Interestingly, results of activity tests performed using real exhaust gas showed 0.5 % Rh/Al₂O₃ to achieve a maximum NO_x conversion of

12 % at 350 °C [44]. This drop in activity when real exhaust gas is used has also been observed in an identical experiment involving Pt/Al₂O₃ (*vide supra*), although the magnitude of the activity loss was considerably smaller. With regards to the selectivity shown by supported Rh HC-SCR catalysts, it has been reported that up to 90 % of the NO converted by Rh/Al₂O₃ is turned into N₂ [44]. Indeed, there seems to be a consensus in the scientific literature pointing to the fact that although supported Rh catalysts require higher temperatures to achieve lower NO_x conversion maxima when compared to similar Pt catalysts, formulations with Rh as the active phase display wider activity windows of operation and show better N₂-selectivity across the whole temperature range [14,50,83-85]. Finally, the use of Os as HC-SCR catalyst has only been attempted in combination with Cu. Although a 13X zeolite-supported 10 % Cu – 1 % Os material exhibited NO conversion to N₂ of 54-68 % at 350-500 °C, the catalyst was shown to become severely and irreversibly deactivated when exposed to water or SO₂ [86].

2.4.2. Multimetallic PGM catalysts.

Although the above Cu-Os catalyst is not the only example of PGMs being used in alloys to catalyze the HC-SCR reaction, to date there has been relatively little research directed at identifying PGM alloys able to reduce NO_x with hydrocarbons under net oxidizing conditions. This is unfortunate, given the fact that the alloying of different PGMs (Pt and Rh, for example) could potentially lead to the development of an active phase able to achieve high deNO_x activity at low temperatures (as Pt is capable of delivering) as well as a wide temperature window of operation and high N₂-selectivity (as those displayed by Rh). Indeed, this was the rationale that led Obuchi *et al.* to investigate the performance of supported Pt-Rh alloys in the HC-SCR reaction [44]. A series of Pt:Rh ratios were examined by these workers, who found a 0.75 % Pt – 0.25 % Rh/ γ -Al₂O₃ catalyst to show the highest NO conversion (around 60 % at 250 °C, compared to 50 % for Pt and Rh monometallic catalysts at 250 and 300 °C, respectively). This alumina-supported 3:1 Pt-Rh alloy displayed a selectivity towards N₂ of ~45 % (in contrast to the 33 and 90 % N₂-selectivities shown by the Pt and Rh monometallic catalysts, respectively). These authors concluded that the catalytic properties of the 3:1 Pt-Rh/ γ -Al₂O₃ formulation were similar to those of monometallic Pt catalysts, but according to their results there was a slight

improvement on both conversion and selectivity (which was attributed to the ability of the alloy catalyst to maximize the amount of partially oxidized hydrocarbon intermediates). This behavior was also confirmed when the results of activity tests performed using real diesel exhaust gas and a 0.2 % Pt – 0.05 % Rh honeycomb catalyst, were compared to those obtained using a 0.2 % Pt honeycomb catalyst. Other examples of the use of supported PGM alloys as HC-SCR catalysts include the finding by some workers that in the fresh state zeolite- and alumina-supported Pt-Rh alloys show enhanced activity over monometallic Pt catalysts [87]. However, upon hydrothermal aging at 600 °C, the performance of the Pt-Rh catalyst declines significantly, whereas Pt/Al₂O₃ shows only a small decline at this temperature [88]. A related trimetallic system comprises Pt-Rh-Ir supported on ZSM-5, which was developed for *Mazda 323* lean burn vehicles sold in the Japanese market [89]. Testing of various PGM combinations gave the order Pt-Rh-Ir > Pt-Ir > Pt > Ir for NO_x reduction activity at 300 °C (using propene as the reductant). N₂O make over the Pt-Rh-Ir catalyst was reported to be negligible and although some deactivation was observed upon aging the catalyst at 700 °C, durability was said to be adequate for the application. Unfortunately data pertaining to the state of the metals in the catalyst were not provided, so it is not clear if Pt-Rh-Ir alloy particles are indeed the active sites (as opposed to mono or bimetallic particles). Additionally, some ASEC patents [90,91] have claimed the use of Pt-Rh and Pt-Rh-Co alloys for HC-SCR. Although the alloy catalysts were shown to be superior to reference Pt/Al₂O₃ catalysts, the method of catalyst preparation (as used for both the alloy and Pt reference catalysts), involving treatment at 1100-1200 °C in 10 % steam/N₂ to promote alloy formation, can be expected to exert a detrimental effect on both the surface area of the support and the metal dispersion.

In conclusion, virtually all categories of catalysts including ion-exchanged zeolites, metal and supported metal catalysts, monocrystals and mixed phases, both acidic and basic oxides and mixed oxides, heteropolyacids, alloys and amorphous alloys, membranes and monolithic catalysts, etc., have been probed for activity in the HC-SCR reaction [14]. However, of all the catalysts investigated, only a few have been found to show promising performance. Of these, supported PGMs appear to have the greatest potential for

commercial application, due to their high activity at low temperatures, their hydrothermal stability and their resistance to sulfur-poisoning. Among the latter, the use of a 3:1 Pt-Rh alloy catalyst could be particularly advantageous if sufficiently protected from hydrothermal aging. Furthermore, the use of a carbon-based support, rather than an oxide, may be beneficial by helping to maintain the Pt-Rh alloy in a more reduced state, given that over-oxidation of Rh is well-known in three-way catalysis as a cause of (reversible) deactivation (Rh^{III} being significantly less active in NO_x reduction than $\text{Rh}^{\text{I}}/\text{Rh}^0$).

Chapter 3. Multiwalled Carbon Nanotubes as Catalyst Supports.

3.1. Introduction.

Since their “rediscovery” by Ijima in 1991 [92,93], carbon nanotubes (CNTs) have attracted considerable interest from the scientific community. A single-walled carbon nanotube (SWCNT) can be described as a hollow tube whose wall is formed by a graphene sheet and ends are capped by one half of a Buckminsterfullerene (C_{60}).

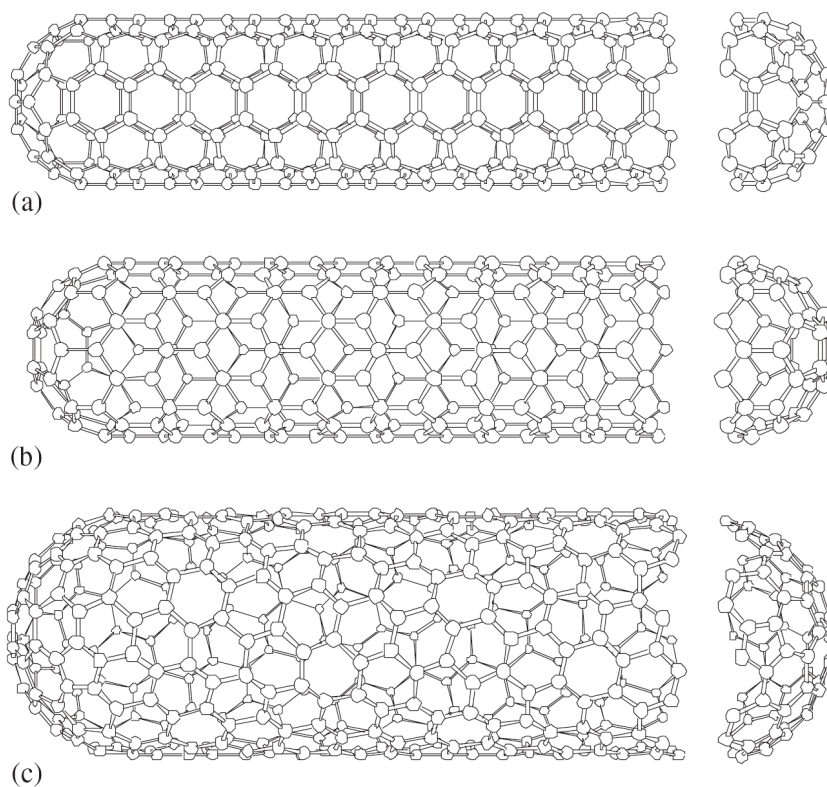


Figure 3.1. Schematics of the three different kinds of SWCNTs: (a) armchair; (b) zigzag; and (c) chiral. Reprinted from Physics Reports, Vol. 431, E.B. Barros, A. Jorio, G.G. Samsonidze, R.B. Capaz, A.G. Souza Filho, J. Mendes Filho, G. Dresselhaus, M.S. Dresselhaus, Review on the symmetry-related properties of carbon nanotubes, Pages No. 261-302, Copyright (2006), with permission from Elsevier.

It is possible for larger diameter carbon nanotubes to surround smaller nested ones, the result being a multi-walled carbon nanotube (MWCNT). MWCNTs can have as many as 20-30 concentric walls or as few as two, as is the case with double-walled carbon nanotubes (DWCNTs).

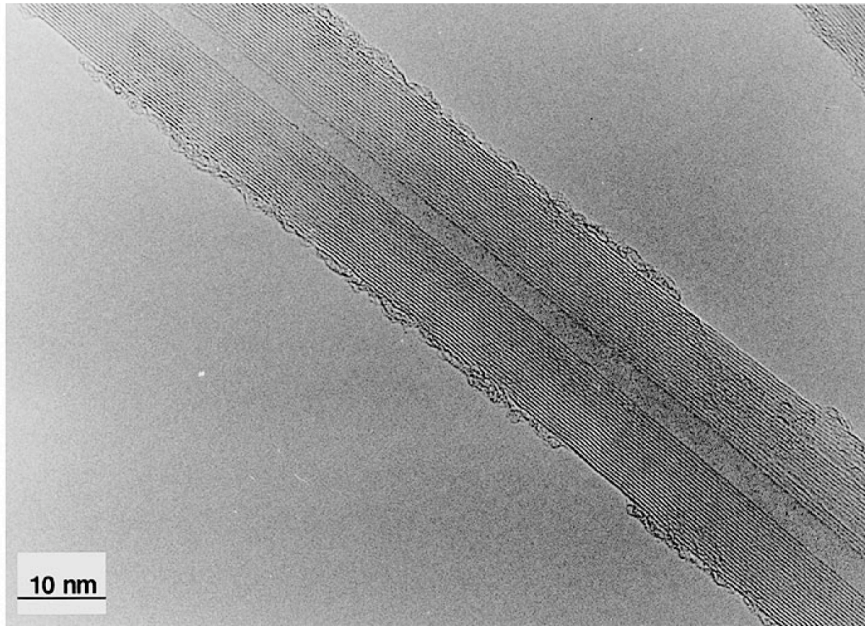


Figure 3.2. High-resolution transmission electron micrograph of a MWCNT with ~20 concentric walls [94].

The diameter of MWCNTs varies from a couple to tens of nanometers (10^{-9} m) and their length from micrometers (10^{-6} m) to millimeters (10^{-3} m), which gives them very high aspect ratios and a one-dimensional nature.

This nanostructure inherent to MWCNTs gives rise to a host of mechanical, electronic, magnetic and optical properties that have inspired the use of these materials in a wide range of fields. Of relevance is the fact that CNTs can be counted amongst the strongest materials in nature, as exemplified by their Young's modulus of *ca.* 1 TPa and their tensile strength in the tens of GPa [95-97]. These and other mechanical properties shown by MWCNTs have led to their use as mechanical probes [98] and as a reinforcing agent in composite materials [99]. Also of interest is that CNTs can act either as a

semiconductor or as a metal, the metallic form being able to carry extraordinarily high electron densities (10 GA/cm^2) [100]. In energy-related areas, their electronic properties have prompted research which aims at incorporating MWCNTs in fuel cells, supercapacitors and lithium batteries [101-104], while their porosity and adsorption properties have rendered them potential hydrogen storage materials [102]. Further, the anisotropy of MWCNTs makes them strongly diamagnetic materials [105,106], whose application in the field of spintronics has been investigated [107]. Moreover, suspension-polymer composites of MWCNTs have been found to show strong nonlinear optical properties [108-112], which makes these composites interesting as materials capable of protecting optical sensors from laser beam radiation [110].

Indeed, the applications that have been investigated for this allotropic form of carbon are as numerous as they are varied. In the field of catalysis, one of the most interesting employments of CNTs has been their use as catalyst supports. This is unsurprising, since the use of other carbonaceous materials (especially activated carbons) to stabilize a catalytically active phase is quite commonplace. The ubiquity of activated carbons (ACs) in catalysis can be attributed to the important advantages that these materials enjoy over oxidic supports, such as their ability to stabilize metal particles in a more reduced state and their resistance to both sulfur poisoning and hydrothermal deactivation. However, while CNTs share with ACs most of the properties that make the latter interesting as catalyst supports (high surface area, stability under reducing conditions, the ability to support highly dispersed metals, and a modifiable surface chemistry that can be tailored for a variety of applications), CNTs also offer some distinct advantages over ACs. These include rendering the dispersed metal particles more accessible (as opposed to ACs, CNTs do not confine deposited particles in a pore system), the ability to be grown on substrates of varied shape and composition, and a higher resistance to oxidation. The latter advantage is particularly important for the application of the material as support in HC-SCR catalysts, since the occurrence of this reaction entails highly oxidizing conditions. In effect, CNTs-based formulations have not only proved suitable for catalyzing representative reactions relevant to the fine chemicals industry [113] and to fuel cell technology [114], but they have also proved they can outperform AC-supported

catalysts in doing so. Examples of these reactions include the selective partial hydrogenation of 3-methyl-2-butenal (prenal) to 3-methyl-2-butenol (prenol) [113], the liquid-phase hydrogenation of cinnamaldehyde [115], CO hydrogenation to methane and hydrogenation of p-nitrotoluene to p-toluidine [116], oxygen reduction [117,118], and the dissociative adsorption of H₂ followed by electron transfer and proton formation [119]. The fact that superior performances than those displayed by AC-based catalysts can be obtained through the use of the corresponding CNTs-supported materials is particularly relevant to the preparation of an improved low-temperature HC-SCR formulation, because some of the best catalysts found to date utilize AC as a support material [29,66,120].

3.2. Experimental Methods.

3.2.1. CVD synthesis of MWCNTs.

A solution of ferrocene in xylenes with a 0.75 Fe:C atomic ratio was prepared, preheated to 175 °C, and continuously fed by a syringe pump into a two-stage horizontal quartz tube reactor (34 mm inner diameter) kept at 800 °C and at 1 in of H₂O pressure above 1 atmosphere. The volatilized liquid was then swept through the reactor using a flow of 10 % H₂ in Ar. After 2 h, both preheater and furnace are allowed to cool to room temperature under a flow of Ar. The resulting MWCNTs are then scraped of the walls of the reactor tube and of the surface of quartz substrates placed within the reactor prior to the run.

3.2.2. Functionalization of MWCNTs with a mixture of 1:1 H₂SO₄-HNO₃.

15 g of MWCNTs were suspended in a mixture of 750 mL of H₂SO₄ and 750 mL of HNO₃ *via* bath sonication for 30 min. The resulting suspension was refluxed for 4 h, allowed to cool, mixed with an equal volume of deionized water and allowed to settle. The supernatant was then decanted and replaced by an equal volume of deionized water. The resulting suspension was filtered and the cake was washed with deionized water and allowed to dry in a vacuum oven. The dry product was then pulverized, re-suspended in deionized water *via* bath sonication for 30 min and washed by a cycle of centrifuging, decanting and suspending in deionized water until the washings attained a neutral pH, at which point the supernatant was decanted and the solid dried in a vacuum oven.

3.2.3. Elemental analyses.

Elemental analyses were performed either by combustion (Leco CHN-200 for carbon, hydrogen and nitrogen and ELTRA CS-500 for carbon and sulfur) or *via* Energy Dispersive X-ray Spectroscopy (EDS) analyses performed converging the beam of the transmission electron microscope (*vide infra*).

3.2.4. Surface analyses.

Porosity analyses *via* N₂ physisorption were conducted at the boiling temperature of nitrogen (77 K) using a Micromeritics Tristar 3000 analyzer. Prior to nitrogen adsorption the samples were degassed at 160 °C for 15 h. Surface area was subsequently calculated using the Brunauer-Emmett-Teller (BET) equation.

3.2.5. Transmission Electron Microscopy (TEM) analyses.

To prepare samples for TEM, a small amount of the material was first dispersed in the appropriate solvent (acetone and *o*-xylene for alumina-supported and MWCNTs-based catalysts, respectively) *via* bath sonication for 5 min. A drop of the resulting dispersion was then placed on a 200 mesh lacey carbon-copper grid and the solvent was allowed to evaporate in a vacuum oven. TEM observations were performed using a JEOL 2010F field emission analytical transmission electron microscope operated at an accelerating voltage of 200kV, coupled to a Gatan Imaging Filter. The electron beam had a point-to-point resolution of 0.2 nm.

3.2.6. Attenuated Total Reflectance Infrared (ATRIR) analyses.

A Nicolet Nexus 870 FTIR system with an ATR accessory including a diamond crystal was employed to analyze the acid-functionalized MWCNTs. To identify the peaks corresponding to the introduced functionalities, the spectrum of untreated MWCNTs was acquired and subtracted from the spectra of acid-treated MWCNTs.

3.2.7. X-ray photoelectron spectroscopy (XPS) analyses.

XPS measurements were performed on a Kratos AXIS HSi instrument equipped with a charge neutralizer and monochromated Al K α X-ray source. Spectra were recorded at normal emission using an analyzer pass energy of 40 eV and an X-ray power of 144 W and were energy referenced CH_x at 285 eV. Peak analysis was performed using CasaXPS Version 2.1.9 software with all spectra Shirley-background subtracted prior to fitting. Components for the O 1s and C 1s regions were fitted with a Gaussian-Lorentzian mix or an asymmetric Doniach-Sunjic lineshape respectively. The elemental composition was calculated from the respective atomic sensitivity factors for C (0.278), O (0.780), S (0.668) and N (0.477).

3.2.8. Thermogravimetric analyses.

Thermogravimetric measurements were made using a TA Instruments Q500 analyzer. In all cases the total gas flow was 50 mL/min and the temperature was ramped from room temperature to 800 °C at a rate of 5 °C/min.

3.3. Preparation of support materials.

As a first step, a batch of MWCNTs was prepared using a chemical vapor deposition (CVD) method developed by Andrews *et al.* at the University of Kentucky Center for Applied Energy Research (UK CAER) [121]. This method involves the use of ferrocene as the metal catalyst precursor and xylenes as the organic feedstock. In a typical synthesis, the reactants are flowed through a horizontal reactor kept at ~800 °C by a carrier gas (10 % H₂ in Ar). At this temperature, the ferrocene decomposes and iron nanoparticles start depositing on any surface available inside the reactor (quartz substrates are routinely used). These iron nanoparticles catalyze the growth of CNTs, the final product being thick mats of MWCNTs of uniform length aligned perpendicular to the substrates. These mats can be scraped off the substrate to yield MWCNTs in a powder form. The conversion of carbon in the feed materials into MWCNTs is ~70 %, while the purity of the resulting MWCNTs is >95 % (purity being defined as the amount of carbon in multi-walled carbon nanotube form and amorphous carbon being the most prevalent impurity). MWCNTs prepared by this method show dominant tube diameters in the range

30-50 nm, typical tube lengths of 65 μm and an iron content of 5 wt.% (iron catalyst particles remain encapsulated in the MWCNTs).

For catalytic applications, MWCNTs are usually first treated with a strong mineral acid or mixture of acids to introduce oxygen-containing functional groups onto their surface. Although not essential, this treatment is generally beneficial for the dispersion of the supported phase since these functionalities can act as nucleation sites when depositing metals or metal oxides. This acid activation of CNTs has been postulated to occur in two steps: a defect-generating step and a defect-consuming step [122]. In the former, electrophilic addition begins to occur at the most reactive sites of the CNTs ($-\text{CH}_2$, $-\text{CH}$, heptatomic rings and the boundaries between hexatomic rings), effectively introducing oxygen-containing functional groups such as $-\text{OH}$ and $-\text{C}=\text{O}$ to the surface of the tube; in the latter step, the graphene structure surrounding these functionalities is eroded *via* further oxidation, effectively etching the surface of the tube. Fortunately, the defect generating-step is considerably faster than the defect-consuming step (the generation of $-\text{C}-\text{OH}$ functionalities and their transformation into $-\text{C}=\text{O}$ is much more expeditious than the subsequent disruption of the graphite-like structure around the resulting $-\text{C}=\text{O}$ groups), so the overall graphitic structure of the CNTs remains. Reflux in $\text{H}_2\text{SO}_4\text{-HNO}_3$ has been found to be quite effective at disrupting the graphite structure because the mixture produces electrophilic NO_2^+ groups which can efficaciously attack $-\text{C}=\text{C}-$ moieties (as do OH^+ electrophiles produced in $\text{H}_2\text{SO}_4\text{-H}_2\text{O}_2$ mixtures) [122]. The nanotubes resulting from this chemical treatment have been found to be uncapped and to show a high concentration of carboxylic groups at the open ends [123]. In general, the tips and the outer walls of MWCNTs submitted to chemical oxidation with mineral acids are known to be covered by a variety of oxygen-containing functional groups [124-128]. This is particularly convenient when the final use of these materials is to support a highly dispersed metallic phase, since metal ions can be anchored by these functionalities prior to their reduction, thus aiding in the production of small metal nanoparticles.

Figure 3.3 schematically shows how these functionalities are introduced to both the outer-wall and the tip of a MWCNT, and Figure 3.4 illustrates how these functionalized multi-walled nanotubes (fMWCNTs) can nucleate precious metal particles.

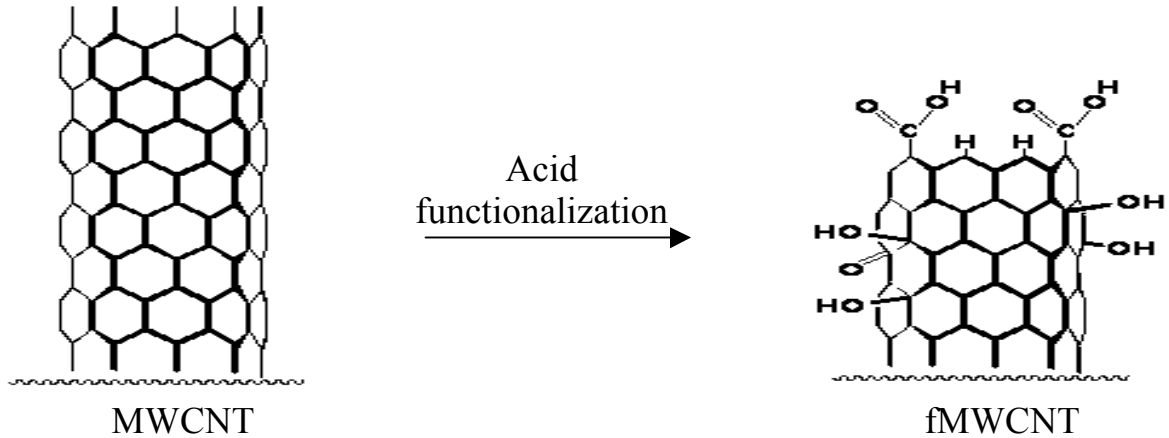


Figure 3.3. Schematic of carbon nanotube functionalization with acid.

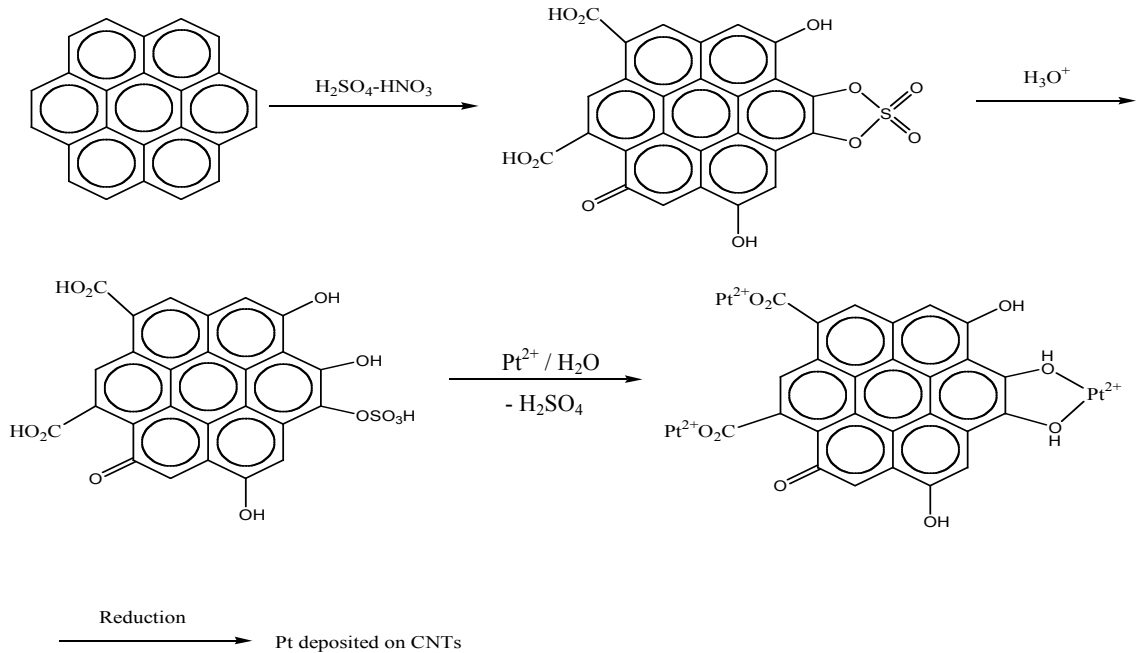


Figure 3.4. Schematic of Pt deposition on acid activated MWCNTs [129].

To prepare a suitable support, several literature-based procedures were studied for the acid activation of the as-synthesized MWCNTs. Procedures utilized comprised (i) treatment with refluxing HNO_3 [130], (ii) refluxing with 1:1 $\text{H}_2\text{SO}_4\text{-HNO}_3$ [129], (iii) treatment with 1:1 $\text{H}_2\text{SO}_4\text{-HNO}_3$ under ultrasound irradiation [131], and (iv) refluxing with 3:1 $\text{H}_2\text{SO}_4\text{-HNO}_3$ [132]. In the case of methods (i)-(iii) the resulting fMWCNTs were readily isolated by filtration, whereas the material prepared according to method (iv) could not easily be isolated by filtration or centrifugation. We speculate that the surface oxidation of the MWCNTs is so effective in this case that the MWCNT bundles are broken up into very small units (possibly individual nanotubes), a process which is presumably driven by the high degree of solvation of the oxidized nanotubes. Given typical MWCNT dimensions (30-50 nm in diameter x 65 μm in length), this renders their isolation problematic; although use of a 20 nm filter does permit their isolation by filtration, the process is extremely time-consuming. For this reason, this activation method was not pursued in subsequent work.

3.4. Characterization of support materials.

Characterization of the fMWCNTs resulting from procedures (i)-(iii) was accomplished using nitrogen physisorption (for determination of the surface area), titration with NaOH (to quantify the concentration of acid groups present), elemental analysis (*via* combustion), and Transmission Electron Microscopy - Energy Dispersive X-ray Spectroscopy (TEM-EDS). Results of the elemental analysis are summarized in Table 3.1, EDS analysis is given in Table 3.2, and N_2 physisorption data and titration results are collected in Table 3.3.

Table 3.1. Elemental analysis (by combustion) of pristine and acid-treated MWCNTs.

Sample / treatment	%C	%H	%N	%S	%O ⁽¹⁾	% Ash
As synthesized nanotubes	93.12	<0.01	0.19	-	<0.01	7.69
HNO ₃ -treated (4 h reflux)	97.01	0.01	0.25	-	0.58	2.15
1:1 H ₂ SO ₄ -HNO ₃ -treated (2 h bath sonication)	93.32	0.15	0.32	0.15	1.64	4.42
1:1 H ₂ SO ₄ -HNO ₃ -treated (4 h reflux)	88.4	0.42	0.27	0.12	7.15	3.64

⁽¹⁾ Determined by difference, i.e., wt.% O = 100 – wt.%[C + H + N + S + ash].

Table 3.2. EDS analysis of pristine and acid-treated MWCNTs. ⁽¹⁾

Sample / treatment	%C	%S	%O	%Si ⁽²⁾
As synthesized nanotubes	>99.5	-	n.d. ⁽³⁾	n.d.
HNO ₃ -treated (4 h reflux)	>98.6	-	n.d.	0.9
1:1 H ₂ SO ₄ -HNO ₃ -treated (2 h bath sonication)	95.3	2.4	1.6	0.8
1:1 H ₂ SO ₄ -HNO ₃ -treated (4 h reflux)	88.4	0.12	7.15	n.d.

⁽¹⁾ Element concentrations in wt.%; figures given represent the average of at least three measurements performed on different sample areas.

⁽²⁾ Impurity associated with the presence of silicone grease.

⁽³⁾ Not detected.

Table 3.3. Surface properties of pristine and acid-treated MWCNTs.

Sample / treatment	Surface area (m ² /g)	Pore volume (cm ³ /g)	NaOH titration: acid eq. neutralized (meq/g)
As synthesized nanotubes	42.1	0.182	0.02
HNO ₃ -treated (4 h reflux)	51.2	0.160	0.40
1:1 H ₂ SO ₄ -HNO ₃ -treated (2 h bath sonication)	46.5	0.182	0.59
1:1 H ₂ SO ₄ -HNO ₃ -treated (4 h reflux)	59.2	0.272	0.77

Taken as a whole, these data present a consistent picture. The presence of oxygen in the activated nanotubes is indicative of surface oxygen-containing groups, while the detection of increased concentrations of nitrogen suggests the presence of nitro (-NO₂) groups (presumably resulting from electrophilic substitution reactions of NO₂⁺) [133,134].

Similarly, the use of H_2SO_4 during the activation procedure results in the incorporation of sulfur in the product MWCNTs, presumably present as sulfonic acid groups ($-\text{SO}_3\text{H}$) [135].

The results of aqueous titrations provided further evidence for the introduction of acidic groups onto the nanotubes. Given that NaOH was used as the titrant, the measured acid concentrations in each case correspond to the total number of carboxylic, phenolic and lactonic groups present (since each of these functionalities is titrated by NaOH [136]). Based on the measured acid site concentrations, the severity of the treatment follows the order 1:1 $\text{H}_2\text{SO}_4\text{-HNO}_3/\text{reflux}$ > 1:1 $\text{H}_2\text{SO}_4\text{-HNO}_3/\text{ultrasound}$ > $\text{HNO}_3/\text{reflux}$. This ordering is broadly supported by the results of elemental analyses as reflected in the measured oxygen concentrations (determined by TEM-EDS and combustion analyses). Acid treatment also results in a reduction in the ash content of the samples, indicative of acid-leaching of the residual iron particles present in the MWCNTs (the MWCNTs having been grown via an iron-catalyzed process [121] and the ash left by the combustion analysis being iron oxide formed from these residual iron particles).

N_2 physisorption measurements show an increase in the surface area of the MWCNTs after activation, consistent with tube opening via acid attack at the semi-fullerene capped ends [129] and with the etching of the MWCNTs outer surface. The latter phenomenon was confirmed by TEM. Figure 3.5 shows the etched outer wall of a MWCNT subjected to treatment with refluxing 1:1 $\text{H}_2\text{SO}_4\text{-HNO}_3$.

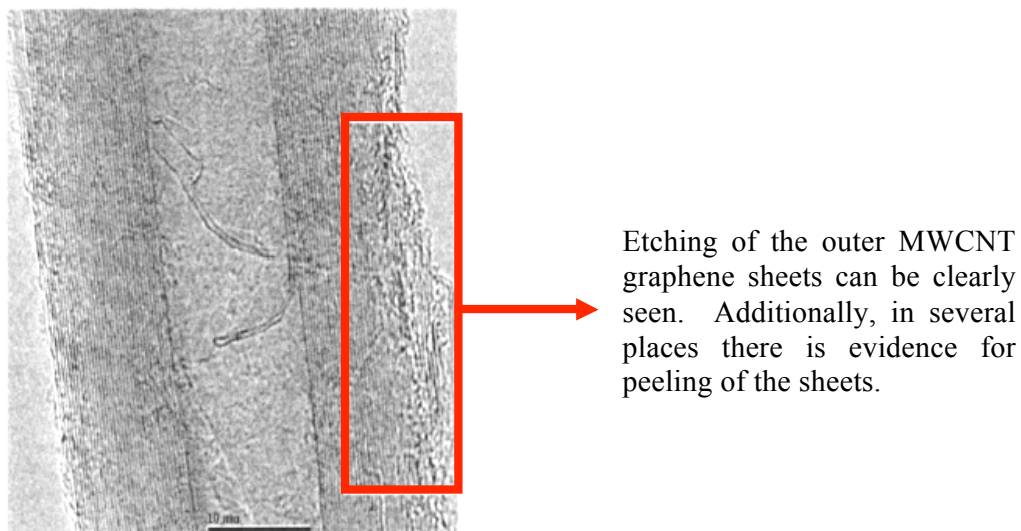


Figure 3.5. TEM image showing the disruption of the MWCNT graphene structure as a result of acid treatment (1:1 H₂SO₄-HNO₃ reflux for 4 h).

Infrared spectroscopic studies were performed in order to determine which functionalities had been introduced onto the MWCNTs. Figure 3.6 shows the Attenuated Total Reflectance Infrared (ATRIR) spectra of MWCNTs activated by the different acid treatments.

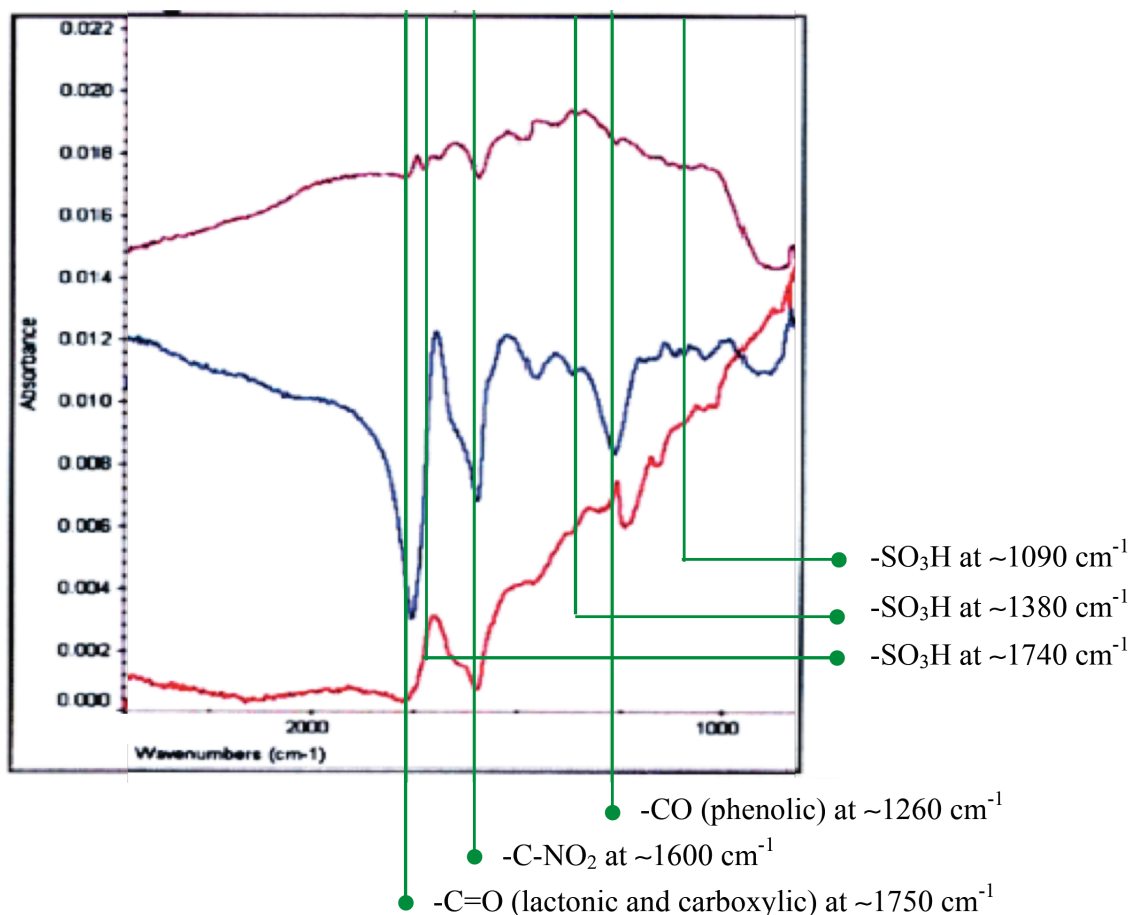


Figure 3.6. Background corrected ATRIR spectra of 1:1 H₂SO₄-HNO₃ treated MWCNTs (top: 3 h bath sonication at room temperature; middle: 4 h reflux; bottom: 3 h bath sonication at 60 °C) showing different functionalities introduced onto the MWCNTs.

Four main peaks in the spectra can be correlated to oxygen containing functionalities introduced by the activation: a peak around 3740 cm⁻¹ (not shown) may be caused by the O-H stretch in a carboxylic acid functionality (although the possibility of this stretch being caused by physisorbed water cannot be discounted); the peak around 1750 cm⁻¹ can be assigned to the C=O stretch in lactonic or carboxylic groups; the peak around 1600 cm⁻¹ can be assigned to nitro groups [133]; and the peak around 1260 cm⁻¹ is most readily assigned to the C-O stretch in carboxylic or phenolic groups. Peng *et al.* have reported

bands attributed to the stretching modes of $\text{-SO}_3\text{H}$ groups at 1743, 1384 and 1090 cm^{-1} in sulfonated MWCNTs analyzed *via* FTIR [135]. In the spectra shown in Figure 3.6 these bands seem to be present, even though they are not very intense. However, the latter is in agreement with both the intensity of the bands observed by Peng and coworkers and the results of elemental analyses (which indicated fMWCNTs to have fairly low amounts of sulfur). It is also interesting to note that more intense peaks are observed in the sample that underwent a more aggressive activation, indicating that higher concentrations of functionalities are introduced by harsher acid treatments.

With respect to the infrared data, the comparison between the ATRIR spectra shown in Figure 3.6 and Fourier Transform Infrared (FTIR) spectra previously reported in the literature for acid treated MWCNTs is quite straightforward, since the spectra tend to share the features corresponding to oxygen containing functionalities such as carboxylic, phenolic and lactonic groups [137,138] in the $1000\text{-}2000\text{ cm}^{-1}$ region. Unfortunately, a comparison between the characterization data obtained through other techniques with those reported in the literature is rendered difficult by a variety of factors. First, the different morphologies of the MWCNTs used as the starting material may impact the properties of the corresponding functionalized materials. Further, given the number of variables that can be changed within an activation method (acid mixture employed, the use of sonication vs. reflux, sonication or reflux time, reflux temperature, etc.) there are countless possible experimental permutations. Indeed, great variability is observed within the fMWCNTs characterization data reported in the scientific literature. Given that MWCNT acid functionalization is rarely an end in itself, most workers seem to have taken an utilitarian approach in which a particular activation is deemed acceptable if the resulting material can be successfully employed in a subsequent step (metal deposition, composite formation, further functionalization, etc.). Based on this approach and on the ease of recovery of the products of the different acid treatments attempted, the 1:1 $\text{H}_2\text{SO}_4\text{-HNO}_3$ /reflux activation method can be deemed satisfactory. Nevertheless, Table 3.4 offers a comparison of the C:O ratio between fMWCNTs obtained through this method with the products of similar acid activations reported in the literature.

Table 3.4. A comparison of different acid activation methods with regard to the oxygen content of the resulting materials.

Starting material	Activation method	C:O atomic ratio	Characterization technique	Reference
MWCNTs (diam=30-50 nm)	4 h reflux in 1:1 H ₂ SO ₄ -HNO ₃	16.5	Elemental analysis by combustion/EDS	This work
Thin MWCNTs (diam=3-10 nm)	4 h reflux in 3:1 H ₂ SO ₄ -HNO ₃	9.0	X-ray Photoelectron Spectroscopy	[139]
MWCNTs (diam=10-30 nm)	36 h reflux in HNO ₃	3.8	X-ray Photoelectron Spectroscopy	[138]

Quite surprisingly, an activation method involving the reflux of MWCNTs in HNO₃ (a milder oxidizer than the H₂SO₄-HNO₃ mixtures) is reported to yield a product with the highest oxygen content. Several factors can be invoked in order to explain this: 1) the smaller diameter of the MWCNTs vis-à-vis the material used in our work, which would logically lead to lower C:O ratios (higher oxygen content) in the resulting product due to the lower amount of inner walls contributing to the carbon content of the sample; 2) a considerably longer reflux time, which might compensate for the use of a milder oxidizing agent; and 3) the use of XPS (which probes the materials at depths within ~2 nm) as a characterization technique, which might cause the amount of surface oxygen-containing groups in thick-walled MWCNTs to be overestimated. Indeed, it seems that XPS exaggerates these values in large-diameter MWCNTs, since its use in the analysis of thin MWCNTs treated with a more aggressive oxidizing agent (a 3:1 H₂SO₄-HNO₃ mixture) reveals a lower oxygen content in the latter material, which would be otherwise counterintuitive. All these considerations make the oxygen content of our fMWCNTs to appear very reasonable, both because a 1:1 H₂SO₄-HNO₃ mixture is bound to be a milder oxidizer than a 3:1 mixture and because the MWCNTs used as starting material in this work have a larger diameter.

XPS analyses, performed on both pristine MWCNTs and on fMWCNTs produced by a 4 h reflux in a 1:1 mixture of sulfuric and nitric acids, provided information on the surface

elemental composition of the samples and on the nature of the functional groups introduced by the acid treatment. Figure 3.7 shows the O 1s region within the XPS spectra of these two samples and Table 3.5 shows their atomic surface composition, while Table 3.6 shows the amount of oxygen present in different chemical states (binding energy assignments were based on both the X-ray Photoelectron Spectroscopy Database of the National Institute of Standards and Technology (NIST) [140] and previous literature reports [141,142]).

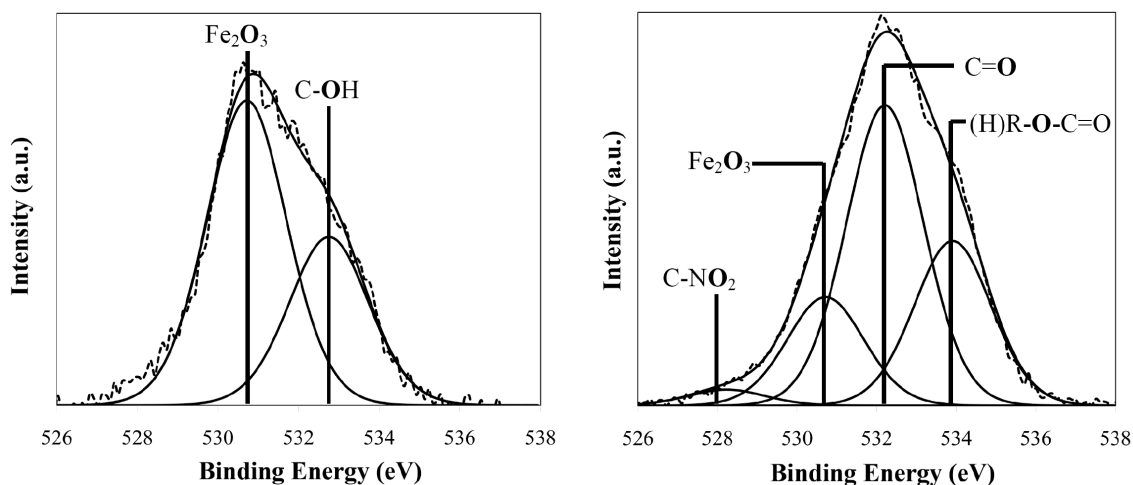


Figure 3.7. O 1s region in the XPS spectra of pristine MWCNTs (left) and fMWCNTs produced by a 4 h reflux in a 1:1 mixture of sulfuric and nitric acids (right).

Table. 3.5. Elemental surface analysis (by XPS) of pristine and acid-treated MWCNTs.

Sample / treatment	at.% C from C 1s	at.% N from N 1s	at.% S from S 2p	at.% O from O 1s
As synthesized nanotubes	95.2	0.3	-	4.5
1:1 H ₂ SO ₄ -HNO ₃ -treated (4 h reflux)	84.6	0.7	0.1	14.6

Table 3.6. XPS quantification of oxygen present in different chemical states (% of total oxygen analyzed) calculated from O 1s peak fitting.

Sample / treatment	Fe ₂ O ₃	-NO ₂	C-OH	C- <u>OO</u> R(H)	C- <u>OO</u> -R(H)
As synthesized nanotubes	64.5	-	35.5	-	-
1:1 H ₂ SO ₄ -HNO ₃ -treated (4 h reflux)	18.4	2.8	-	50.9	27.9

The XPS elemental analysis of the surface is in agreement with the results of the elemental analysis of the bulk material by combustion and EDS shown in Tables 3.1 and 3.2. In all cases, the O, N, and S content is increased by the acid treatment, which also causes a concomitant decrease in the C content. As mentioned above, this is consistent with the introduction of O, N, and S containing functional groups to the carbon nanotube surface.

Interesting insights can also be withdrawn from the different chemical states in which oxygen is present in these samples as determined by XPS analysis. The results included in Table 3.6, however, should be approached with caution because of two main reasons: 1) the overlap between peaks arising from different oxygen-containing species, which may impact the quantification of oxygen present in different chemical states; and 2) the fact that the quantification is reported as the percentage of oxygen in a given chemical state with respect to the total surface oxygen present, which increases from 4.5 at.% to 14.6 at.% *via* the acid treatment as shown in Table 3.5. With this in mind, the decrease in the amount of oxygen present as Fe₂O₃ (from the iron particle catalysts remaining from MWCNTs synthesis) can be attributed to both a fraction of the metal oxide being leached during the acid reflux and to the considerable amount of oxygen containing functionalities introduced to the material, which also reduce the contribution of oxygen in Fe₂O₃ towards the total. Indeed, a notably large amount of lactonic (COOR) and carboxylic (COOH) functional groups are introduced to the nanotube surface, judging from the increase on the surface oxygen content of the sample and from the O 1s signals attributable to these functionalities. Parenthetically, the decrease in the amount of oxygen present as part of phenols suggests that the introduction of –COOR and –COOH functionalities occurs at the expense of –OH groups. Arguably, –OH groups are very likely close to defects sites in pristine MWCNTs and thus, the reactions leading to the

incorporation of lactonic and carboxylic functionalities to the nanotube surface (which should preferentially take place in these regions) may lead to –OH elimination. An additional peak (with a maximum at ~528 eV) in the O 1s signal of fMWCNTs has been attributed to organo-nitro species, albeit no literature reference could be found to confirm this assignment. Further analysis of the O 1s region also suggests that sulfonic groups are introduced to the nanotube surface by the acid treatment, however, the quantification of the oxygen in –SO₃H groups is rendered difficult by the other, more intense peaks in the region. Finally, the presence of –NO₂ and –SO₃H functionalities on the fMWCNTs surface has been qualitatively confirmed through the analysis of the N 1S and the S 2p regions within this sample.

A commercially available activated carbon fiber monolith (made in house using P-200 activated Anshan fiber, with phenolic resin as the binder), which was subsequently employed in this work as the support in a reference catalyst, was also characterized using elemental analysis and N₂ physisorption. Tables 3.7 and 3.8 summarize the results of these measurements.

Table 3.7. Elemental analysis (by combustion) of the activated carbon fiber monolith.

Material	%C	%H	%N	%S	%O	%Ash
Carbon fiber monolith	94.99	0.61	0.8	1.21	0.68	1.71

Table 3.8. Physical properties of the carbon fiber monolith.

Material	Surface area (m²/g)	Pore volume (cm³/g)	Mean pore radius (nm)
Carbon fiber monolith	728	0.342	0.94

The high surface area and the large pore volume shown by the activated carbon fiber monolith render it well suited for use as a catalyst support.

Given that one of the main reasons to use MWCNTs, as opposed to AC, as an HC-SCR catalyst support lies in the higher resistance to oxidation shown by the former materials, the combustion profiles of these materials under different atmospheres was investigated *via* thermogravimetric analysis (TGA). Two atmospheres were chosen in an attempt to simulate HC-SCR conditions: 1) 10 % O₂; and 2) 500 ppm NO + 9.5 % O₂, the balance being N₂. The heating ramp was 5° C/min in both cases. The results of these experiments are summarized in Table 3.9 and Figure 3.8.

Table 3.9. Differential thermogravimetric maxima for selected samples (measured under two different gas mixtures).

Sample	dTG max. under 10 % O ₂ /balance N ₂ (°C)	dTG max. under 500 ppm NO + 9.5 % O ₂ /balance N ₂ (°C)
Darco KB-B (AC)	500	520
Pristine MWCNTs	560	570
Acid Treated MWCNTs	565	580
Carbon fiber monolith	600	Not measured
2 wt.% Pt/Darco KB-B (AC)	365	380
2 wt.% Pt/pristine MWCNTs	550	550
2 wt.% Pt/Acid Treated MWCNTs	400	400
2 wt.% Pt/Carbon fiber monolith	560	Not measured

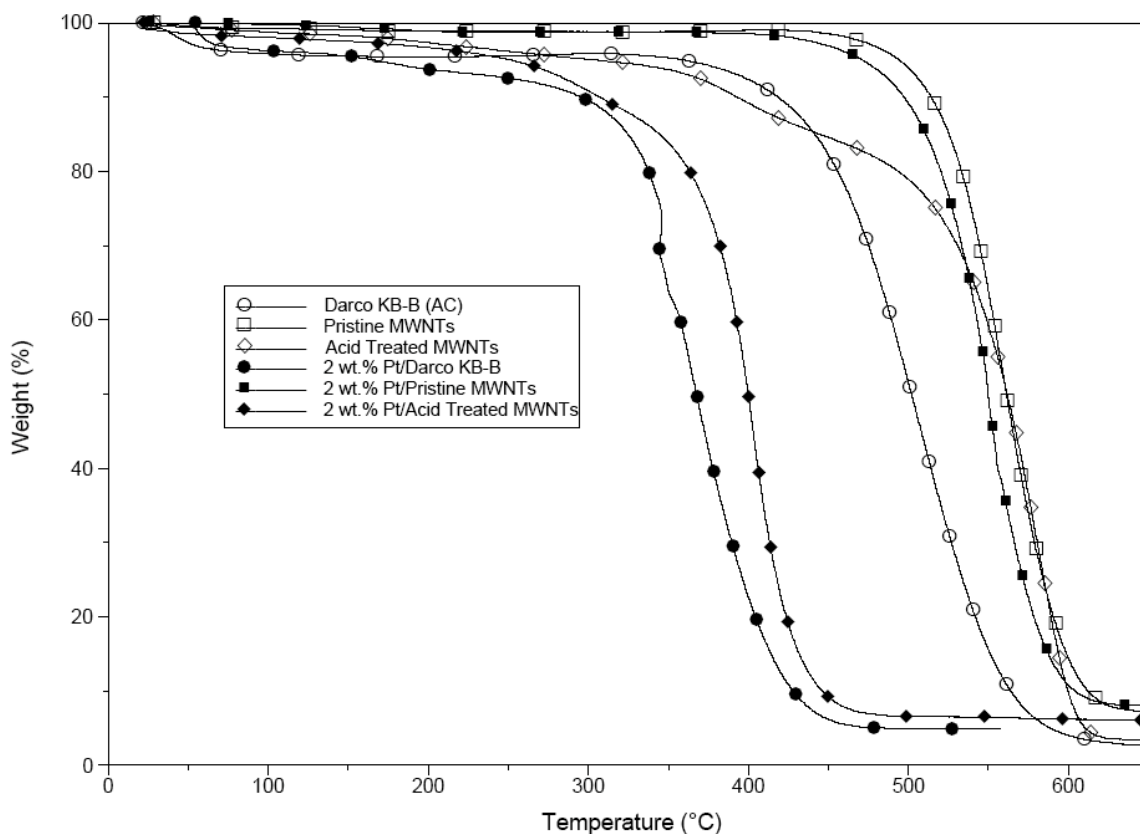


Figure 3.8. Combined thermogravimetric plot for selected samples measured under 10 % O₂ balance N₂ (ramp= 5 °C/min).

These values clearly show MWCNTs to be more resistant to oxidation than Darco KB-B (Darco KB-B is a commercial, amorphous, AC), even in the presence of Pt (it should be noted that the preparation of the Pt-loaded materials is described in the following chapter). This is not unexpected, given that as for the chemical oxidation with acids, the gas phase oxidation of these materials should be facilitated by the presence of surface defects in which ACs are considerably richer than MWCNTs. With this in mind, the similar dTG values shown by MWCNTs and fMWCNTs seem to be counterintuitive (one would expect structural defects to be more prevalent in fMWCNTs). However, a closer look at the TGA profile of fMWCNTs reveals that while the material shows its dTG maximum at 565 °C, it also experiences a significant weight loss at lower temperatures, which is attributed to the combustion of the fraction of the material rendered defective by

the acid treatment, as well as to the thermal expulsion of $-\text{COOH}$ and $-\text{OH}$ groups as CO_2 and H_2O . Thereafter, the TG curve of the fMWCNTs follows that of the pristine MWCNTs, suggesting that the MWCNT structure is essentially intact after the elimination of the surface functional groups is complete. The trend shown by the dTG maxima of the Pt-containing materials is of particular interest, given that this metal, which would be present in HC-SCR catalysts, is known to catalyze the combustion of carbonaceous materials. That the latter indeed occurs is apparent from the lower temperature at which the materials show their dTG maxima when Pt is present. As expected, the magnitude of this shift to lower temperatures is more acute for the supports showing the highest amount of defect sites. Nevertheless, it seems to be the case that MWCNTs materials show a higher resistance to oxidation than AC regardless of the atmosphere and the presence of Pt.

In conclusion, based on their surface properties and on their high resistance to oxidation, MWCNTs functionalized *via* a 4 h reflux in a 1:1 $\text{H}_2\text{SO}_4\text{-HNO}_3$ mixture are a suitable support for HC-SCR catalysts. Nevertheless, the use of pristine MWCNTs was also investigated for comparison purposes.

Chapter 4. HC-SCR Catalyst Preparation and Characterization.

4.1. Introduction.

In heterogeneous catalysis, the number of reactant molecules converted to products in a given time is directly proportional to the number of catalytically active sites. Thus, there is a vested interest in maximizing the latter as a means to maximize the former. This is usually achieved through the dispersion of the active phase onto the surface of a material that is commonly referred to as the catalyst support.

The most common formulations used as environmental heterogeneous catalysts are metals or metal oxides supported by high surface area carriers. The latter are commonly oxides such as Al_2O_3 , SiO_2 , TiO_2 or zeolites, although carbon materials have become quite commonplace in recent years.

Obviously, the structure (and thus the properties) of a particular catalyst is highly dependent on the way in which it is prepared. Indeed, the subtleties of a given preparation method tend to have such an impact on the performance of the resulting formulations, that the manufacturing procedures of industrial catalysts are kept as valuable trade secrets. Nevertheless, most environmental heterogeneous catalysts are prepared through variations of very general methods, the most representative of these being impregnation, *in situ* chemical reduction, electrostatic adsorption and ion exchange. In our work, several of these methods were employed to prepare both MWCNTs-based and reference HC-SCR catalysts, however, all syntheses investigated share three common steps: 1) a metal precursor is provided to the system in an ionic state; 2) chemical changes are effected to change the metal ions to metal atoms which agglomerate to form nanoparticles; and 3) particle growth is restricted to different degrees depending on the confining substrate present, the result being supported and size-controlled metallic nanoparticles.

4.2. Experimental methods.

4.2.1. PGM deposition via the polyol method.

1 g of catalyst support was suspended in 100 mL of ethylene glycol *via* bath sonication for 30 min. The appropriate amount of metal precursor(s) ($\text{H}_2\text{PtCl}_6 \cdot 6\text{H}_2\text{O}$ or $\text{H}_2\text{PtCl}_6 \cdot 6\text{H}_2\text{O}$ and RhNO_3 in aqueous solution) was added dropwise to the resulting suspension while stirring. A saturated solution of KOH in ethylene glycol was then added dropwise to the mixture until it attained a pH of >13 . The resulting mixture was refluxed for 3 h, allowed to cool and filtered. The cake was washed (first with a dilute aqueous solution of NH_4OH , then with deionized water) and dried in a vacuum oven.

4.2.2. PGM deposition via wet impregnation.

1 g of catalyst support was mixed with 100 mL of solvent (ethanol for MWCNTs and deionized water for fMWCNTs) and the appropriate amount of metal precursor(s) ($[(\text{NH}_3)_4\text{Pt}](\text{NO}_3)_2$ or $[(\text{NH}_3)_4\text{Pt}](\text{NO}_3)_2$ and RhNO_3). The mixture was sonicated for 30 min and the solvent was then removed from the resulting suspension using a rotary evaporator. The resulting material was dried in a vacuum oven and then reduced under a flow of H_2 (350 °C, 3 h).

4.2.3. PGM deposition via incipient wetness impregnation.

5 g of catalyst support was mixed with an amount of $[(\text{NH}_3)_4\text{Pt}](\text{NO}_3)_2$ aqueous solution equal to the total pore volume of the support containing the adequate quantity of metal precursor. The resulting mixture was stirred for 30 min and the solvent was then removed using a rotary evaporator. The resulting material was dried in a vacuum oven and then calcined under air (400 °C, 2.5 h) or reduced under a flow of H_2 (350 °C, 3 h).

4.2.4. Determination of precious metal loadings.

Inductively Coupled Plasma – Atomic Emission Spectroscopy (ICP-AES) analyses were performed using a Varian Vista-PRO instrument. Prior to analysis, the MWCNTs-based samples were ashed in a muffle furnace at 700 °C and the resulting ashes were dissolved in *aqua regia*. Proton Induced X-ray Emission (PIXE) measurements were performed at Elemental Analysis, Inc. (Lexington, KY), using a General Ionex Corp. Tandetron Model

4110A proton accelerator coupled with a custom X-ray Emission apparatus. Prior to PIXE analysis, solid samples were homogenized in an agate or cryogenic mixer mill and a pellet was pressed using ~300 mg of material. Inductively Coupled Plasma – Mass Spectrometry (ICP-MS) analyses were also performed at Elemental Analysis, Inc., using a Perkin Elmer 6100 apparatus. Prior to analysis, the samples were submitted to a microwave-assisted digestion in a mixture of *aqua regia*, HF and H₂O₂. For alumina-supported reference catalysts, the precious metal loading was determined by means of X-ray Fluorescence (XRF).

4.2.5. Precious metal particle size analyses.

H₂-chemisorption measurements were performed in a Zeton Altamira AMI-200 instrument by first ramping at 1 °C/min to a reduction temperature of 400 °C and holding at this temperature for 1 h under a flow of 10 % H₂ in He. The sample was then cooled to 100 °C under a flow of Ar. To count the active metal sites, the temperature was then ramped to 400 °C under a flow of Ar, the desorbed hydrogen being monitored with a thermal conductivity detector (TCD). The temperature was held at 400 °C until the TCD signal returned to the baseline condition. The Pt dispersion was calculated on the assumption of a 1:1 H:Pt stoichiometric ratio and a spherical particle morphology. To obtain particle size distribution histograms, 200 precious metal particles were measured in high magnification TEM micrographs using image analysis software (Gatan Digital Micrograph®). TEM sample preparation, as well as TEM instrumentation and operational parameters, have already been described in Chapter 3.

4.2.6. Scanning Transmission Electron Microscopy (STEM) analyses.

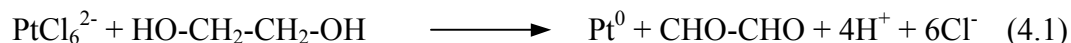
STEM observations were performed using a JEOL 2010F field emission analytical transmission electron microscope operated at an accelerating voltage of 200kV, coupled to a STEM unit with a high-angle annular dark field (HAADF) detector and a Gatan Imaging Filter. Sample preparation for STEM is identical to that for TEM.

The experimental methods used for TGA and EDS analyses have already been described in Chapter 3.

4.3. Catalyst preparation.

The preparation of a first set of MWCNT-supported catalysts was performed using a standard literature method involving the chemical reduction of Pt salts in ethylene glycol [143], which shall be henceforth referred to as the polyol method and indicated with a letter “P” after the name of catalysts prepared by that route.

In a typical preparation, aqueous solutions of H_2PtCl_6 (chloroplatinic acid or CPA) and a strong base (typically KOH) are mixed with ethylene glycol and the support is dispersed in the resulting mixture through sonication. Heating this dispersion reduces the Pt in solution to Pt metal, which deposits onto the support. During the synthesis, the polyol plays the role of both reductant and protecting agent. The detection of glyoxal (*via* gas chromatography coupled to mass spectrometry) in the vapors evolved during the course of the reaction [144], has led some workers to propose a one-step redox reaction mechanism:



Other authors have proposed the reductant to be CH_3CHO generated *in situ* by the thermal decomposition of ethylene glycol [145]. The colloidal nanoparticles resulting from the reduction of the metal are stabilized and protected by glycol molecules, which through steric hindrance impede their agglomeration [146] allowing fairly small metal particles to deposit onto the support.

In initial scouting experiments, two sources of heat were used: conventional heating (i.e., refluxing) and microwave irradiation [147]. The use of microwave heating offered two main advantages: 1) it achieves excellent Pt dispersions (which has been ascribed to the quick nucleation and the complete separation of the nucleation and particle-growth steps [148-150]), and 2) it reduces the reaction time from several hours to just a few minutes. However, this method was also found to have an important drawback: it yields rather

inconsistent precious metal loadings, arguably because such a short reaction time does not compensate for the effect that small changes in the preparation's variables (reactant concentrations, stirring, etc.) have on the reaction kinetics. On the other hand, the use of conventional heating proved to yield more consistent products loading-wise. Taking this important factor into account, it was decided that even though the preparation involving conventional heating is considerably more time consuming than the microwave-assisted one, the more consistent loadings achieved with conventional heating renders it the more suitable method. Nevertheless, the microwave-assisted preparations were useful to study the effect of the basification of the reaction mixture on the product, since the microwave-assisted process was also attempted without the addition of the base (following a literature report that high Pt dispersions could be obtained in the absence of base [118]).

The results of these various experiments are reported below. In the initial studies, Pt/MWCNTs catalysts were prepared in the micro-scale using both heat sources. Subsequently, the preparations were scaled up using the conventional heating route, and alloy catalysts were prepared using the same method. The catalysts synthesized included Pt, Pt-Rh, Pt-Ir and Pt-Rh-Ir on MWCNTs and Pt supported on fMWCNTs. At this stage, all the catalysts were prepared with a target metal loading of 1 wt.%.

The preparation of a second set of MWCNTs-based catalysts was performed using wet impregnation followed by reduction with H_2 [151], a method which shall henceforth be called the impregnation method and indicated with a letter "I" after the catalyst name. This synthetic technique involves the mixing of the support with a solution of the metal precursor(s), the elimination of the solvent, and the subsequent reduction or decomposition of the precursor to a metallic state.

Impregnation is the most common procedure used to disperse a catalytically active phase on a support. There are two different types of impregnation: incipient wetness impregnation and wet or excess solution impregnation. In the former, the quantity of the precursor solution used corresponds to the total pore volume of the support, while in the latter the carrier is immersed in an excess of precursor solution. Since electrostatic forces

govern the distribution of the precursor over the surface of the support, a precursor that facilitates adsorption or even ion exchange should be utilized. Thus, $[(\text{NH}_3)_4\text{Pt}](\text{NO}_3)_2$ was employed in an attempt to promote the adsorption of the Pt-containing cation onto the surface of the MWCNTs or its ion exchange with the protons of Brønsted acidic groups present. Further, the solvent used in the preparation was chosen so as to take into account the nature of the support and optimize its wetting (ethanol was used with MWCNTs, while water was used with fMWCNTs).

In this work, the excess solution impregnation method was preferred for the preparation of MWCNTs-based HC-SCR catalysts due to the fact that, according to Inductively Coupled Plasma – Atomic Emission Spectroscopy (ICP-AES) analyses, the polyol method failed to deposit Rh and Ir on the MWCNT support. Although it was eventually established that the source of this problem was of an analytical rather than a preparative nature (*vide infra*), it was decided to use the impregnation method to prepare MWCNTs-based catalysts from that point on. This decision was taken due to three main factors: 1) the straightforwardness and the essentially quantitative yields of the impregnation method, 2) the promising performance of the resulting catalysts in NO reduction with propene, and 3) the lower cost of the chemicals (other than the precious metal precursors) involved.

Finally, reference catalysts, comprising Pt/Darco KB-B (an AC) and Pt/ Al_2O_3 , were prepared using the polyol and the incipient wetness impregnation methods, respectively. However, when trying to test the Pt/Darco KB-B sample for NO reduction activity, a pressure drop was encountered over the catalyst bed which was sufficient to prevent the flow of reactants. This problem could not be solved by diluting the catalyst with glass beads and, therefore, the use of an activated carbon fiber monolith was examined as a potential solution. To this end, the monolith was characterized (see Chapter 2) and deemed well suited for use as a catalyst support. Pt was then deposited onto this material *via* the incipient wetness impregnation method followed by H_2 reduction.

4.4. Catalyst characterization.

ICP-AES was used for the determination of the metal loadings of the first set of catalysts prepared *via* the polyol method. In principle, metal loadings can be determined by either analyzing the filtrate from the preparation for residual metal in solution (and then calculating the loading on the catalyst by difference), or by directly analyzing the solid product after digestion in an appropriate medium (e.g., ashing the catalysts in a muffle furnace at 700 °C for one hour and then dissolving the resulting ashes in *aqua regia*). In initial experiments, the use of both methods was investigated; and while the two methods gave similar results in many cases, discrepancies were also observed. For this reason, the results from the digestion method were analyzed statistically to determine the method's percent recovery and precision. These factors were found to be satisfactory, such that the direct method was used for the determination of metal loadings. Table 4.1 shows the metal loadings determined for the first batch of catalysts (which were prepared aiming for a 1 wt.% total metal loading).

Table 4.1. Precious metal loadings of the catalysts prepared via the polyol method (using conventional heating) determined by ICP-AES.

Sample	Pt (wt.%)	Rh (wt.%)	Ir (wt.%)	K* (wt.%)
Pt/MWCNTs	0.953	N/A	N/A	Below detection
Pt-Rh/MWCNTs	0.358	0.230	N/A	Below detection
Pt-Ir/MWCNTs	0.281	N/A	0.178	Below detection
Pt-Rh-Ir/MWCNTs	0.177	0.112	0.119	Below detection
Pt/fMWCNTs	1.185	N/A	N/A	0.381

*Potassium was measured due to its known activity as a carbon combustion catalyst and its use in the polyol method.

For the Pt/MWCNTs catalysts, the Pt loadings were found to be within ± 0.2 wt.% of the target loading of 1 wt.%. However, for the Rh- and Ir-containing catalysts, metal loadings were found to be roughly half of the target loadings. At the time, the reason for this was unclear, given that it was thought that the source of the problem was preparative (as opposed to analytical) and that during the preparation Ir^{3+} should be easier to reduce than

PtCl₆²⁻ (while the electrode potential of Rh³⁺ is similar to that of PtCl₆²⁻). Therefore, an alternative route was examined for the preparation of the MWCNTs-based catalysts, based on wet impregnation, followed by reduction under hydrogen [151]. In parallel, in order to investigate whether the origin of this discrepancy was of analytical or preparative nature, it was decided to increase the metal loading, to reanalyze the samples through ICP-AES and to submit representative samples to an outside laboratory for analysis *via* an alternative technique, namely PIXE. Additionally, one of these samples was also subjected to ICP-MS for comparison purposes. The results of these analyses (presented in Table 4.2), show the ICP measurements to be inconsistent, while PIXE places the precious metal loadings quite close to those targeted (2 wt.% total metal loading).

Table 4.2. Elemental analysis data (in wt.%) for two catalysts prepared via the polyol analyzed by different techniques.

Catalyst	ICP-AES			ICP-MS			PIXE		
	Pt	Rh	Ir	Pt	Rh	Ir	Pt	Rh	Ir
Pt-Rh/MWCNTs	1.05	0.43	NA	0.94	1.42	NA	1.08	0.92	NA
Pt-Rh-Ir/MWCNTs	0.51	0.16	0.15	NA	NA	NA	0.78	0.80	0.74

Since both ICP techniques involve preparative steps before the actual analysis and PIXE does not, these preparative steps are believed to be the source of the observed discrepancies. Indeed, two phenomena occurring during the digestion of the catalysts might be invoked: 1) the formation of volatile oxides of Rh and Ir during the ashing of the sample, and 2) the dissolution of Pt by *aqua regia* being favored over that of Rh and Ir. Based on the foregoing, the elemental analysis of prepared catalysts was routinely performed in the remainder of this work using PIXE (Elemental Analysis Corp., Lexington, KY). Given that the degree in which the results of the PIXE analyses (measured loadings) differ from the targeted metal loadings (nominal loadings) is within the analytical error (~10 %), the loadings reported in this document are nominal loadings unless otherwise indicated.

In the case of the Pt/Al₂O₃ reference catalyst, the Pt loading was determined by means of XRF and found to be 2.1 wt.%.

Another analytical problem was encountered when trying to determine precious metal dispersions. Hydrogen chemisorption is the most commonly used method for establishing mean metal particle sizes in heterogeneous catalysts. However, due to the very low density of the MWCNT support materials employed, only a small amount of material could be placed in the sample vessel. This lowered the measurement accuracy, thus making H₂ chemisorption measurements alone insufficient to determine precious metal dispersion in MWCNTs-based catalysts. Therefore, TEM observations were coupled to H₂ chemisorption measurements as a means to achieve this goal. TEM has one important advantage over H₂ chemisorption: whereas the latter method is only useful for determining the average metal particle size, TEM is able to provide both the average metal particle size and the metal particle size distribution of a given catalyst. On the other hand, H₂ chemisorption also has an important advantage over TEM: the former is a bulk technique, whereas the latter is a spot technique only able to analyze a minuscule portion of the sample. Hence, the use of these two techniques in combination not only yields more information but also more reliable data. H₂ chemisorption results for Pt dispersion and average Pt particle size of various catalysts are shown in Table 4.3.

Table 4.3. Hydrogen chemisorption results showing the dispersion and average diameter of Pt particles on different substrates (Pt loading = 2 wt.%).

Substrate	H-ZSM-5	Darco KB-B	MWCNTs	fMWCNTs*	Al₂O₃
Dispersion (%)	67.2	66.0	11.1	83.4	56.9
Average particle diameter (nm)	1.8	2.0	10.4	1.4	2.1

* Acid treatment performed with a 1:1 mixture of H₂SO₄ and HNO₃ / 4 hour reflux.

For the reference catalysts, chemisorption experiments show good results, i.e., high dispersions, corresponding to small particles (<2.5 nm). They also show that better dispersions can be achieved using 1:1 H₂SO₄/HNO₃ treated MWCNTs as the support than with the use of pristine nanotubes. This was confirmed by the particle size distribution histograms shown in Figure 4.1, which were obtained by measuring 200 particles on high-magnification TEM micrographs.

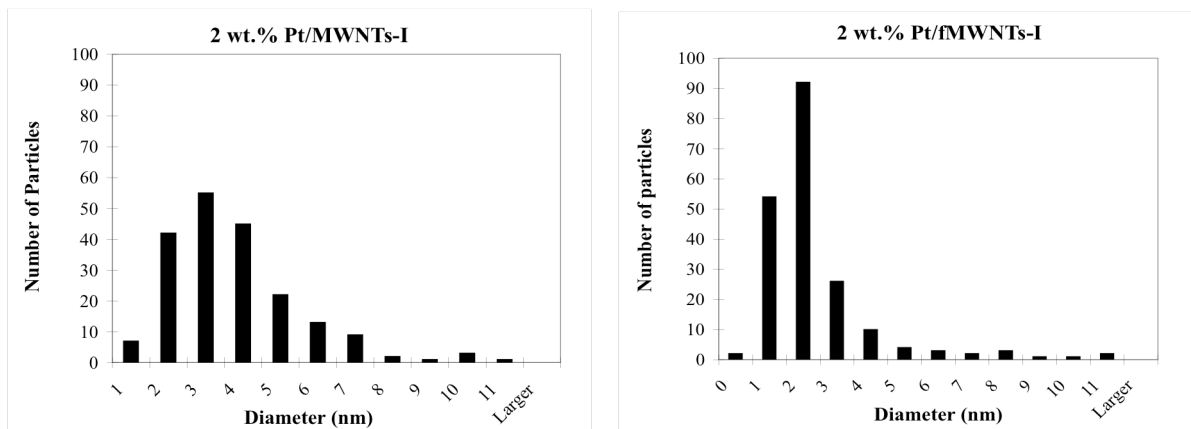


Figure 4.1. Particle size distribution histograms of 2 wt.% Pt/MWCNTs-I (left) and 2 wt.% Pt/fMWCNTs-I (right) (200 particles measured per histogram).

The difference in the Pt dispersion achieved on MWCNTs and fMWCNTs is less pronounced according to TEM observations than based on H₂ chemisorption. This is more readily assigned to the already mentioned fact that TEM is not a bulk technique. However, the use of the same assumptions (H:Pt stoichiometric ratio and particle morphology) while interpreting the results of H₂ chemisorption analyses of materials with dissimilar dispersions can also explain the apparent discrepancy. Nevertheless, both techniques agree on the fact that improved dispersions are obtained when fMWCNTs are utilized as the catalyst support.

Figure 4.2 shows two TEM micrographs of a 2 wt.% Pt/MWCNTs-I catalyst and two TEM micrographs of a 2 wt.% Pt/fMWCNTs-I formulation, while Figure 4.3 shows four

contrast Scanning Transmission Electron (STEM-Z) micrographs of approximately the same region of the latter catalyst taken at different magnifications.

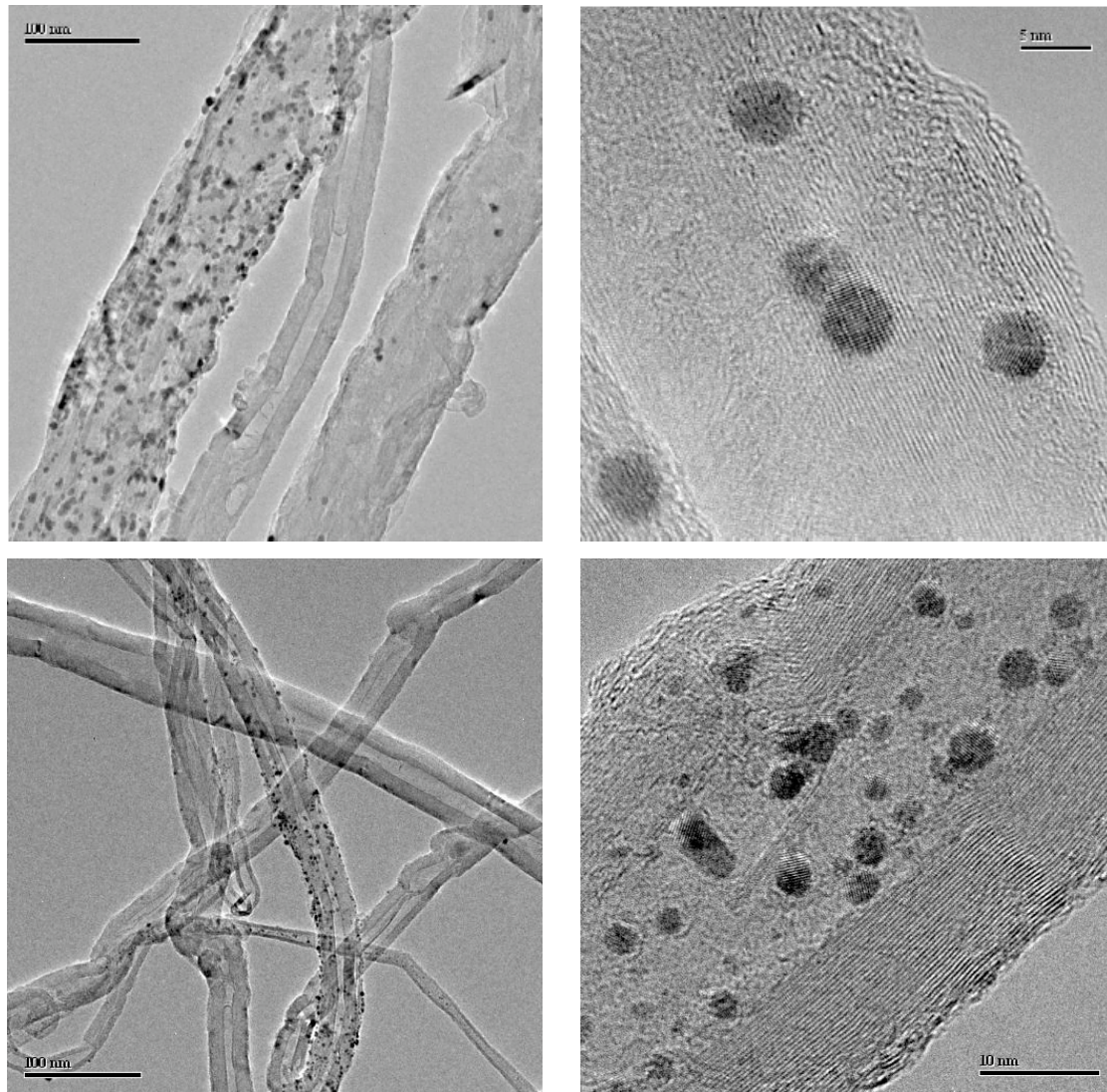


Figure 4.2. TEM micrographs of 2 wt.% Pt/MWCNTs-I (above) and of 2 wt.% Pt/fMWCNTs-I (below) under different magnifications.

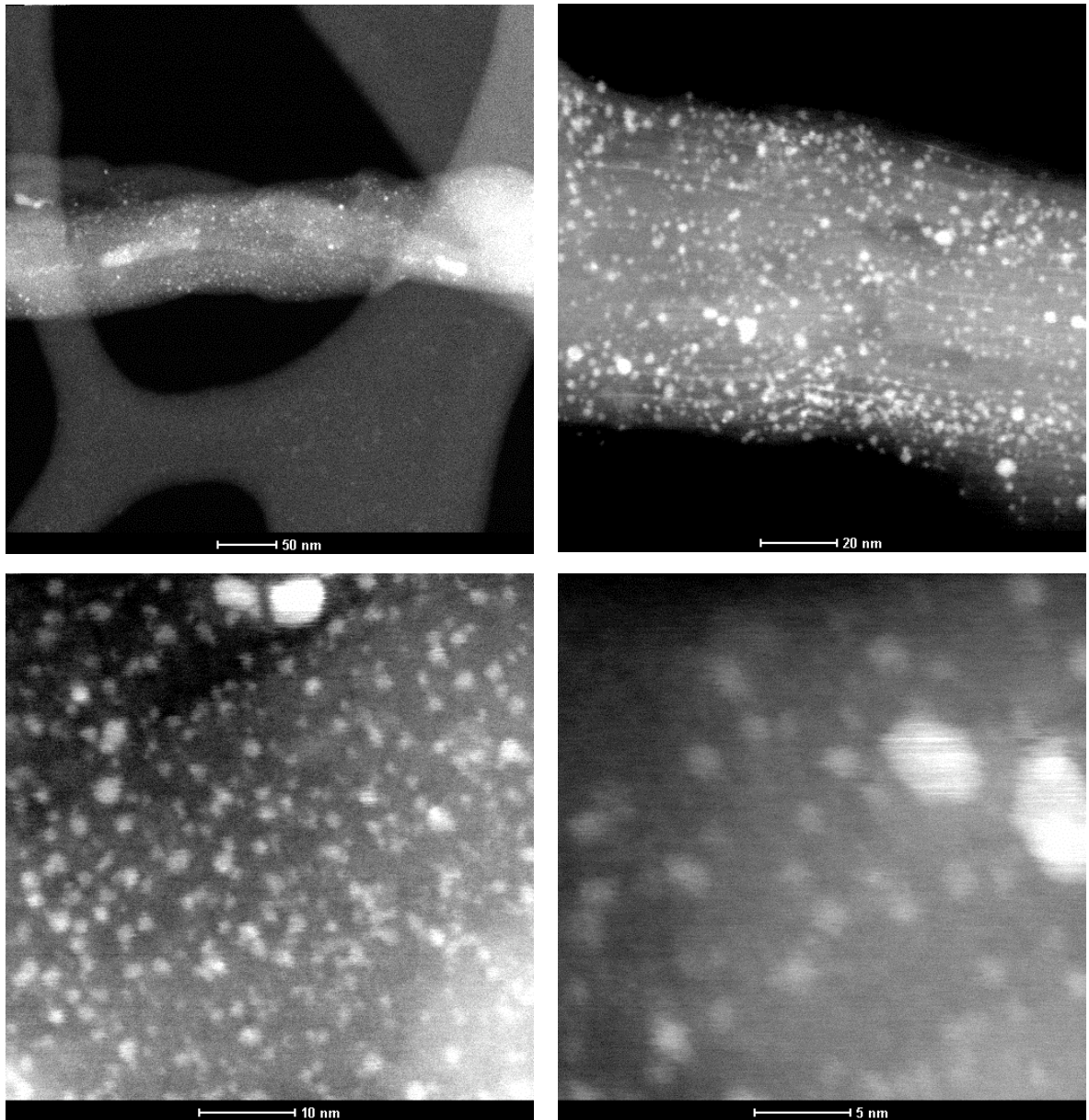


Figure 4.3. STEM micrographs under different magnifications of approximately the same region of 2 wt.% Pt/fMWCNTs-I.

The results of both TEM and STEM-Z studies validate the use of MWCNTs and fMWCNTs as supports and impregnation as the preparation method as means to obtain HC-SCR catalysts in which the metal phase is highly dispersed, while they also prove electron microscopy to be a powerful technique for the characterization of MWCNTs-

based materials. From TEM observations, it appears that small crystalline particles are deposited onto (and potentially into) MWCNTs supports, nanotube defects (tips, bends and grooves) presumably being the preferential deposition sites.

In the case of the Pt/Darco KB-B reference sample, STEM-Z observations also showed good agreement with the results of H₂ chemisorption, an average particle size of 2 nm being indicated by chemisorption versus particles of between 1 and 3 nm that can be seen in STEM-Z micrographs (see Figure 4.4).

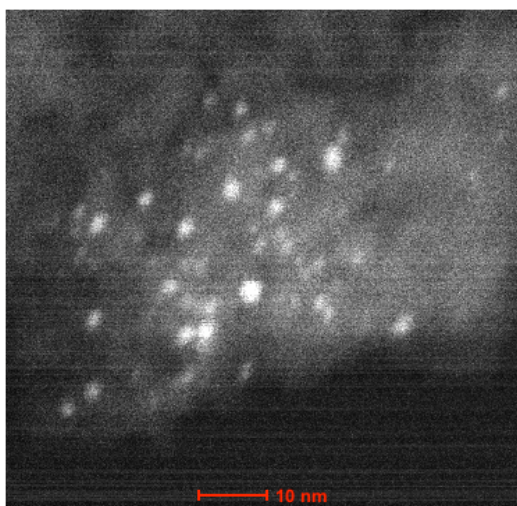


Figure 4.4. STEM-Z image showing Pt particles (in white) deposited on Darco KB-B (in black).

The products of the microwave-assisted process without basification were also observed by TEM (not shown); the observed Pt dispersion was very poor. Indeed, it can be argued that if the reduction reaction occurs through the one-step mechanism represented by equation (4.1), a lack of OH⁻ able to neutralize the produced H⁺ would result in a slow nucleation and in the coupling of the nucleation and particle-growth steps, which would in turn worsen the metal dispersion of the resulting catalysts. Therefore, in all subsequent polyol preparations the basification step was employed.

As has been already mentioned in Chapter 3, thermogravimetric analyses were performed in order to determine the thermal stability of the catalyst supports in PGMs-containing catalysts under typical HC-SCR (oxidizing) conditions. Three main trends were observed (see Table 3.7 and Figure 3.7): 1) the Darco KB-B activated carbon support combusts at lower temperatures than the MWCNTs; specifically, the differential thermogravimetric (dTG) maximum for Darco KB-B occurs at a temperature 50 °C lower than that of the MWCNTs, regardless of whether NO is present in the gas mixture or not; 2) the activated MWCNTs experience a weight loss due to the combustion of some surface functionalities in the temperature range ~350-500 °C, although the combustion of the nanotubes themselves occurs at temperatures comparable to the untreated MWCNTs; and 3) deposition of Pt and Pt alloys on the various carbon supports results in a lowering of the combustion temperature in all cases, this effect being significant for the AC and fMWCNTs, whose dTG maximum is lowered by as much as 180 °C (relative to the bare supports). Clearly, the supported Pt phase plays a major role in catalyzing the oxidation of these defect-rich supports. In the case of the untreated MWCNTs, the dTG maximum was lowered by only 20 °C in the worst case, reflecting the lack of defects in the outer graphene sheets of the pristine MWCNTs, and, consequently, their greater stability towards oxidation. Further, given that the carbon fiber monolith showed the highest resistance to oxidation among the selected materials, its use as a carbonaceous reference support is validated. Notably, the deposition of Pt onto this support lowered its dTG maximum to a value comparable to that of Pt/MWCNTs. On this basis, untreated MWCNTs appeared to be the support of choice, providing that an acceptable metal dispersion on this carrier could be obtained and a satisfactory HC-SCR performance was displayed by the resulting catalyst.

The Pt/activated carbon fiber monolith reference catalyst was also characterized *via* PIXE, H₂ chemisorption and TEM before being tested for deNO_x activity. Both Pt loading (a nominal 2 wt.% was confirmed by PIXE measurements) and Pt dispersion (an average Pt particle size of ~1.1 nm was measured by H₂ chemisorption) were found to be satisfactory. Unfortunately, TEM was not able to yield good micrographs since the sample preparation method proved to be rather destructive for this particular catalyst.

The characterization of the 2 wt.% Pt/Al₂O₃ reference catalyst was expanded to include H₂ chemisorption and TEM measurements. An average Pt particle size of ~2 nm was measured by means of the former technique and visually confirmed through the latter. Further, the chemical analysis of the material was performed *via* TEM-EDS. Figure 4.5 shows the appearance of the sample under the microscope (using two different magnifications), and the EDS spectrum of the region shown in the low magnification micrograph. Peaks corresponding to Al, O, and Pt can be observed, which confirms the presence of Al₂O₃-supported Pt.

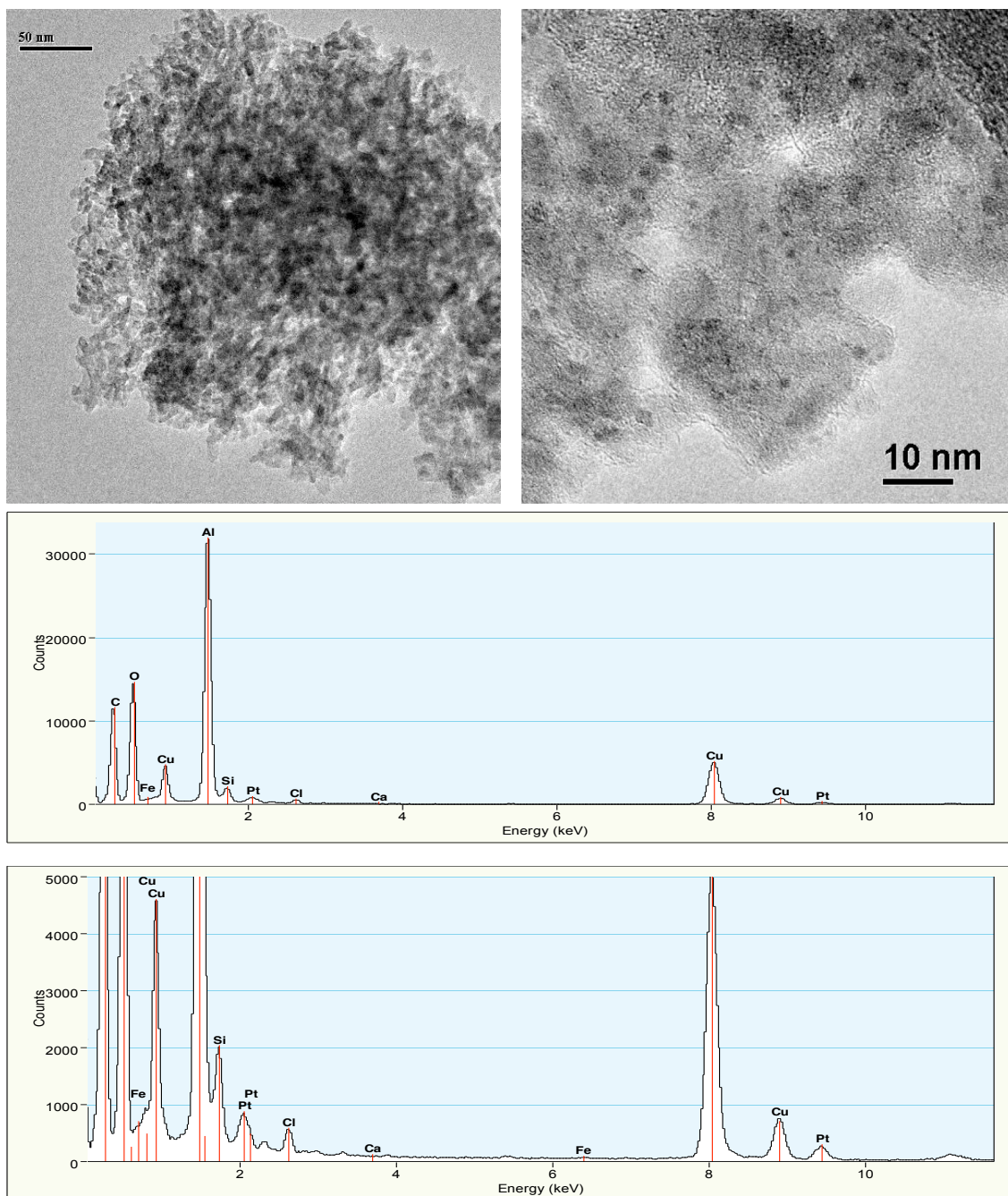


Figure 4.5. Different magnification TEM images of Pt/Al₂O₃, EDS spectrum of the region shown in the low magnification micrograph (top) and a close-up of the low intensity peaks in the spectrum (bottom). Cu and C peaks are due to the TEM grid.

In conclusion, PGMs nanoparticles can be deposited onto both pristine and acid-functionalized MWCNTs through *in situ* chemical reduction and *via* impregnation. The latter approach was not only found to be more economical and less involved than the former method, but also to more reliably afford the targeted metal loadings. With respect to the support, the use of fMWCNTs led to HC-SCR catalysts with improved metal dispersion as compared to unfunctionalized MWCNTs, while MWCNTs-based catalysts showed a superior resistance to oxidation compared to fMWCNTs-based formulations. However, the testing of the resulting catalysts for activity in the HC-SCR reaction (which is covered in Chapter 5) remained indispensable for the determination of the best combination of catalyst support and catalyst preparation method.

Chapter 5. Testing and Optimization of Powder-type MWCNT-based HC-SCR Catalysts.

5.1. Introduction.

Catalytic air pollution control calls for active and selective formulations able to turn, under realistic conditions, noxious exhaust components into innocuous compounds. Thus, an ideal automotive HC-SCR catalyst would convert to N₂ the entirety of the NO_x emitted by diesel-powered vehicles across the entire temperature span of the exhaust. An attempt to develop a material capable of attaining such an ambitious goal requires a two-fold, systematic approach. As a first step, a multitude of formulations must be screened for activity in the HC-SCR reaction to identify materials showing acceptable conversions in the required temperature range. Secondly, a catalyst optimization process is enacted, using as a starting point the most promising formulations found in the previous stage.

In our work, the first phase of this approach was accomplished through a literature survey (summarized in Chapter 2), which placed catalysts containing PGMs as the active phase among the materials showing the highest low temperature activity in the HC-SCR reaction, while also possessing acceptable durability. Therefore, supported PGMs were chosen as the starting point in the catalyst optimization process. The strategy utilized in the latter stage involved a systematic study of the effect of a variety of parameters on the HC-SCR performance shown by the catalyst. When at all possible, only one variable was altered at the time in an attempt to investigate its discrete influence on catalyst performance. However, the interdependency of some variables (e.g. catalyst support and precious metal dispersion) had to be taken into account when conclusions were drawn.

Since this optimization process involved the screening of a considerable number of formulations, the use of a reliable catalyst testing methodology was paramount [152]. Consequently, the development of a dependable catalyst screening technique was deemed crucial. This proved to be a challenging task, especially because of its multileveled nature. These levels included the selection, construction and validation of the appropriate reactor; the selection, installation and calibration of the necessary analytical

instrumentation; and the establishment of adequate data acquisition and data processing practices. Indeed, only after these steps had been taken could the resulting data be deemed valid and their interpretation attempted.

By definition, a catalyst is a material able to increase the rate of a chemical reaction (the number of molecules converted by unit of time) without itself undergoing any permanent chemical change. Catalysts are able to achieve this through the reduction of a reaction's activation energy (an energy barrier that reactants must pass in order to be converted into products), since the rate of reaction is inversely proportional to the exponential of the activation energy, as shown in equations (5.1) and (5.2):

$$d[C]/dt = k[A]^x[B]^y \quad (5.1)$$

$$k = Ae^{-E_a/RT} \quad (5.2)$$

In expression (5.1), known as the rate equation, [A], [B] and [C] represent the concentrations of the reactants and the product in the generic reaction $A + B \rightarrow C$, while the superscripts x and y denote the reaction order in [A] and [B], respectively. The k in both equations is known as the rate constant and, as the form of the Arrhenius equation represented by expression (5.2) shows, it is: (i) related to the pre-exponential function A ; (ii) directly proportional to the exponential of both temperature (T) and the universal gas constant (R); and (iii) inversely proportional to the exponential of the activation energy (E_a), as stated above.

In effect, a catalyst allows the reaction to occur at lower temperatures *via* lowering the activation energy of a chemical reaction. Thus, the determination of the kinetic parameters of MWCNTs-based deNO_x catalysts was tackled as a means to quantitatively assess the effectiveness of these formulations and obtain potentially valuable mechanistic information.

5.2. Experimental methods.

5.2.1. Powder-type catalyst testing.

Experiments were performed in a vertical stainless steel tube reactor (1 cm inner diameter). The catalyst (1 g) was packed into a ~2.5 cm bed between plugs of glass wool. The gas mixture was flowed downwards through the catalyst bed and consisted of 500 ppm NO, 10 % O₂, 10 % H₂O and 500 ppm of propene as the reductant balanced with N₂. The gas flows were regulated with mass flow controllers and the total flow rate was kept at 1667 cm³/min (STP), corresponding to a space velocity of ca. 50,000 h⁻¹ (W/F = 0.01 g · h · dm⁻³). Data points were taken at steady state in non-sequential intervals of 10 °C to account for possible hysteresis in the range 180-300 °C, the temperature being monitored by a thermocouple placed in the catalyst bed. The outlet gases were continuously analyzed using a chemiluminescence NO-NO₂ analyzer (ECO PHYSICS® CLD 700 EL ht) and discontinuously analyzed for N₂O with a high-level gas filter correlation analyzer (Thermo Electron Corp. model 46C). NO conversion and N₂O selectivity were calculated according to expressions (5.3) and (5.4):

$$\text{NO conv. (\%)} = \frac{([\text{NO}_x]_i - [\text{NO}_x]_o) \times 100}{[\text{NO}_x]_i} \quad (5.3)$$

$$\text{N}_2\text{O selec. (\%)} = \frac{([\text{N}_2\text{O}]_o \times 2) \times 100}{([\text{NO}_x]_i - [\text{NO}_x]_o)} \quad (5.4)$$

where $[\text{NO}_x]_i$ and $[\text{NO}_x]_o$ are inlet and outlet NO_x (NO+NO₂) concentrations, respectively, and $[\text{N}_2\text{O}]_o$ represents the outlet N₂O concentration. It is important to note that equation (5.3) implies that “NO conversion” refers to the conversion of NO to reduction products; i.e., both to N₂ and N₂O. This definition of NO conversion will be used henceforth.

The accuracy and the repeatability of these measurements were determined by the random re-measurement of individual temperature data points during the screening of a given formulation, as well as through the duplicate testing of the same catalyst. Notably, in some instances the time lapse between the latter tests amounted to months or even years. Reassuringly, both individual data points and full plots were found to show a remarkable repeatability (well within the analytical error of the gas analyzers employed).

5.2.2. Kinetic studies.

Apparent activation energies were calculated from a series of twelve Arrhenius plots obtained by permutation of the following reactant concentrations: [NO]= 250, 500, 800 and 1200 ppm; [C₃H₆]= 500, 1000 and 1500 ppm. The data points used to calculate the slope corresponded to temperatures below that at which the maximum NO conversion was observed (and at which the reactor can be considered as operating in a differential manner). Reaction orders in NO were calculated from the slope of log-log plots of NO reduction rates vs. initial NO concentrations, using the following reactant concentrations: [NO]= 100, 250, 500, 800 and 1200 ppm; [C₃H₆]= 1000 ppm. Reaction orders in propene were calculated from the slope of log-log plots of NO reduction rates vs. initial C₃H₆ concentrations, using the following reactant concentrations: [C₃H₆]= 250, 500, 1000, 1500 and 2000 ppm; [NO]= 500 ppm.

Experimental methods for TEM, TEM-EDS, TGA and elemental analysis by combustion have already been presented in the two previous chapters.

5.3. Preliminary powder-type catalyst testing in a microflow reactor.

5.3.1. Microflow reactor construction.

For the purpose of catalyst screening, a dedicated reactor was constructed. On-line analyzers were installed (for measurement of NO, NO₂ and N₂O) and mass flow controllers and analyzers calibrated. Figure 5.1 shows a schematic of the microflow reactor used for powder-type catalyst testing throughout this work.

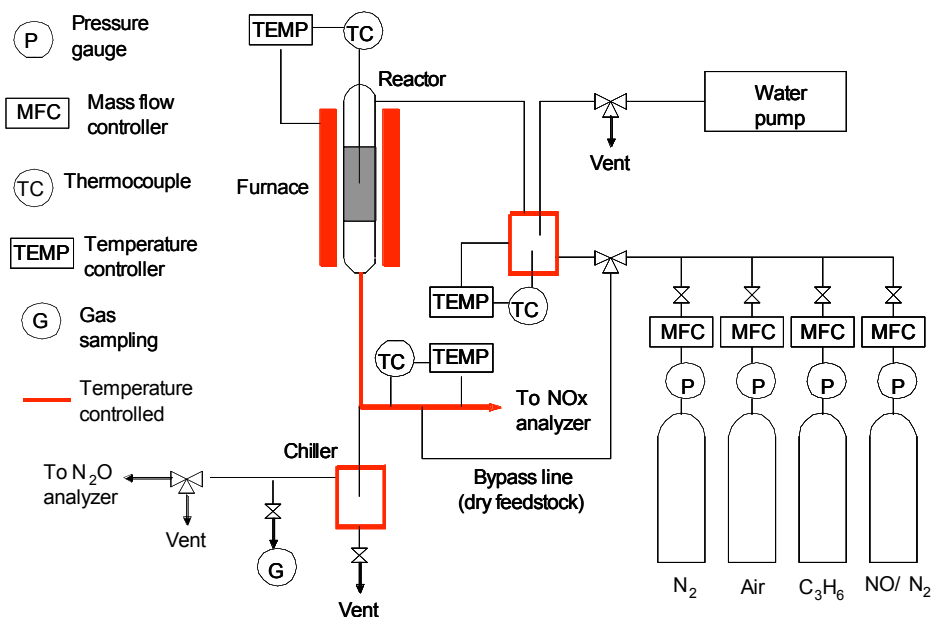


Figure 5.1. Microflow reactor schematic.

5.3.2. Initial powder-type catalyst testing.

A 2 wt.% Pt/Al₂O₃ reference catalyst was the first to be screened for NO reduction, using propene as the reductant. The purpose of this was two-fold: first, since the behavior of this catalyst is well known, it was used to validate the performance of the microflow reactor; second, the performance of this catalyst provided a reference against which the performance of other catalysts could be compared. This reference catalyst showed a maximum NO conversion of 45 % achieved at 230 °C, the selectivity towards N₂O being *ca.* 68 % at this temperature. Reassuringly, these results are comparable to those reported by other workers for Pt/Al₂O₃ catalysts [66,83,153-155], albeit small differences are observed due to the differences in experimental conditions used (e.g., C₃H₆ and NO concentrations, precious metal loading and gas flow). Therefore, the microflow reactor system built and the testing methodology developed were deemed able to yield reliable data.

Previous reports [29,66] have suggested that Pt/AC catalysts are more active for NO reduction than Pt supported on metal oxides. Thus, further preliminary tests aimed to determine whether MWCNTs-based formulations are similarly active in the HC-SCR reaction. In our work, a Pt/activated carbon fibers monolith was preferred over a Pt/Darco KB-B formulation for reasons already disclosed in the previous chapter, while functionalized MWCNTs were initially chosen as the carrier in CNTs-based catalysts. The latter choice was prompted by a report in which both the metal dispersion and the activity towards the catalytic decomposition of propylene shown by CNTs-based formulations improved when the support was subjected to an acid treatment prior to metal deposition [156].

Figure 5.2 shows the behavior of the 2 wt.% Pt/fMWCNTs catalyst in NO reduction with propene and compares it to that of the 2 wt.% Pt/Al₂O₃ and 2 wt.% Pt/activated carbon fibers reference catalysts.

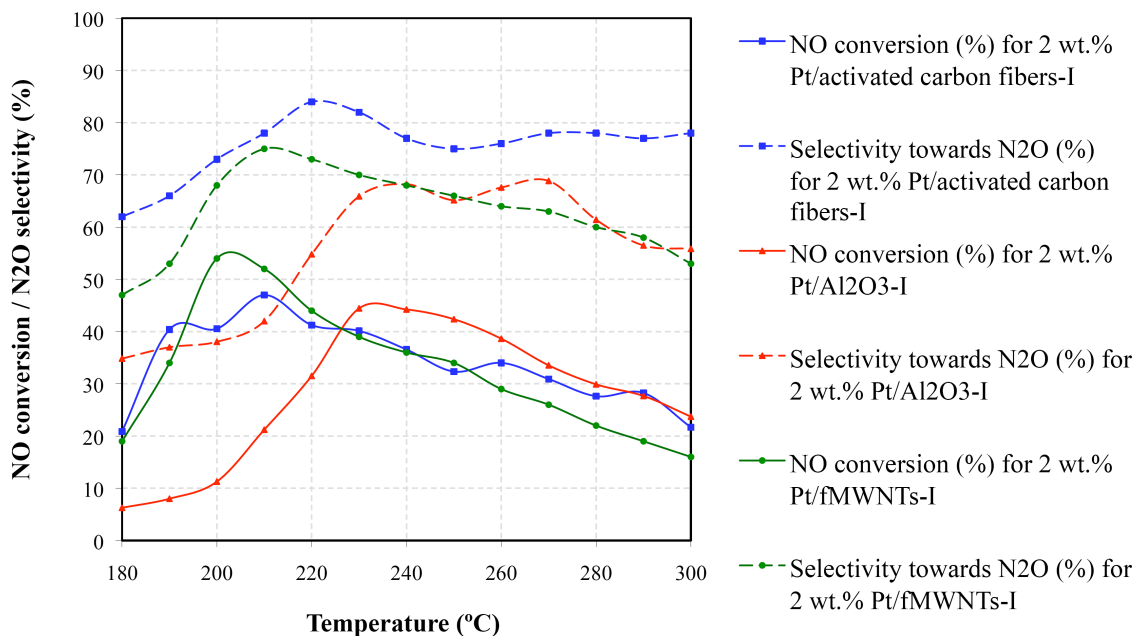


Figure 5.2. Combined plot comparing the performance of 2 wt.% Pt/fMWCNTs-I with that of 2 wt.% Pt/activated carbon fibers-I with and 2 wt.% Pt/Al₂O₃-I reference catalysts in NO reduction with propene.

From the figure, it can be seen that both reference catalysts show a similar maximum NO conversion of *ca.* 45 %. However, there are three main differences in the performance of Pt/activated carbon fibers with respect to that of Pt/Al₂O₃: 1) a lower temperature of maximum NO conversion (~25 °C lower), 2) a wider deNO_x temperature window, and 3) a slightly higher selectivity towards N₂O. The figure also shows Pt/fMWCNTs to achieve a higher maximum NO conversion than both reference catalysts and to do so at a considerably lower temperature (~25 °C lower) than Pt/Al₂O₃. Further, the selectivity towards N₂O shown by the fMWCNTs-based formulation is slightly better than that of Pt/activated carbon fibers and comparable to that of Pt/Al₂O₃. Given that both reference catalysts and the fMWCNTs-based catalyst show similar loadings and dispersions (as determined by PIXE analyses and TEM observations, respectively), these differences in activity can be attributed to a catalyst support effect. This observation is particularly interesting, given that the influence of the support on lean NO_x HC-SCR finds both supporters [52,74,157,158] and detractors [159-161] in the scientific literature.

Nevertheless, an important body of work supports the idea that catalytic behavior depends, at least to some extent, on the nature of the support, since a degree of support acidity has been found to improve deNO_x activity and/or N₂-selectivity [29,31,74,162-167]. In other words, the higher activity of the carbon-based catalysts in comparison with Pt/Al₂O₃ may be a consequence of the higher Brønsted acidity of these supports. An additional possibility is that the oxidation state of platinum plays a role in determining catalyst activity and selectivity, Pt supported on carbonaceous supports likely being in a more reduced state than Pt supported on an oxidic carrier such as alumina. Given that dissociative adsorption of NO on Pt is thought to be one of the main pathways for NO reduction in the presence of propene [52,158], and that a metallic surface, largely free of adsorbed oxygen, should be able to adsorb and dissociate NO more effectively than an oxidic Pt surface, Pt supported on carbon can be expected to be more active in NO reduction than Pt/Al₂O₃. In order to probe this hypothesis, X-ray Photoelectron Spectroscopy (XPS) studies aimed at investigating the oxidation state in these two types of catalyst were performed. These and other *in situ* spectroscopic studies (whose results are presented in the following chapter) were carried out in parallel to the optimization of the MWCNTs-based catalysts (covered in section 5.4 below). However, in this dissertation the results of these studies are presented sequentially to enhance the readability of the document.

5.4. Catalyst optimization.

Experiments were performed in order to determine which support material (pristine nanotubes or functionalized nanotubes), catalyst preparation method, and metal or combination of metals yields catalysts with the best performance, i.e., high deNO_x activity over a wide temperature window accompanied by high selectivity towards N₂. As mentioned above, the experimental approach to this optimization consisted of systematically changing these variables while studying the effect of these changes on the performance shown by the catalysts.

5.4.1. Effect of the catalyst support.

As mentioned in the previous chapter, nanotube-based HC-SCR catalysts were obtained by depositing PGMs on both pristine and functionalized MWCNTs. Probing the effect of these supports on catalyst performance was deemed worthwhile since each carrier offered potential advantages as well as probable drawbacks. On the one hand, the use of fMWCNTs as the carrier should yield materials with higher metal dispersions and increased support acidity. However, at very high dispersions the Pt can be expected to exist in a partially oxidized state (i.e., as PtO), which could in turn be detrimental to catalyst activity. On the other hand, the use of untreated MWCNTs as a carrier could be expected to lead to poor Pt dispersions, a lack of surface Brønsted acidity and thus poor catalytic activity, although it represents a less involved preparation which could potentially yield catalysts in which PGMs are present in a more reduced state.

First, 2 wt.% Pt/MWCNTs and 2 wt.% Pt/fMWCNTs catalysts were prepared *via* wet impregnation followed by reduction with H₂ at 350 °C [151]. PIXE analysis confirmed the nominal Pt loadings of both catalysts. Subsequently, the samples were tested for activity in NO reduction with propene in a microflow reactor. Figure 5.3 compares the performance of these two catalysts.

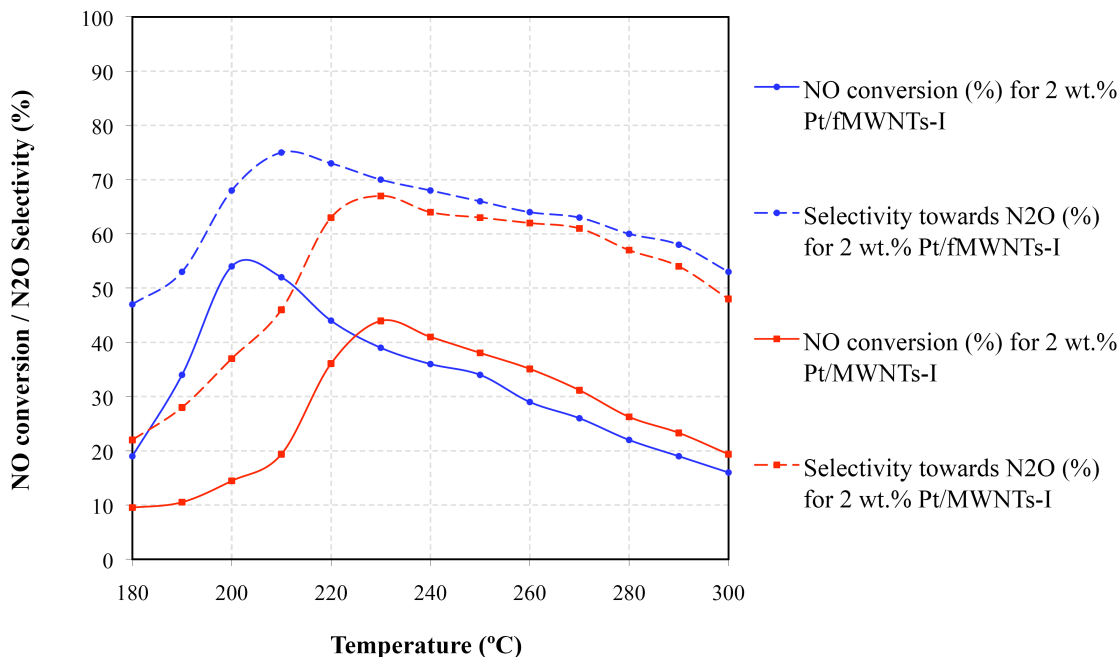


Figure 5.3. Combined plot comparing the performance of Pt/MWCNTs-I with that of Pt/fMWCNTs-I in NO reduction with propene.

Evidently, the support does not have an appreciable impact on the selectivity towards N_2 shown by the catalysts. However, the use of fMWCNTs as a catalyst support does have three effects: 1) it shifts the maximum NO conversion towards lower temperatures (*ca.* 30 °C) relative to the Pt/MWCNTs catalyst; 2) it produces an increase in the maximum NO conversion achieved ($\sim 10\%$); and 3) it slightly widens the deNO_x temperature window. It is interesting to note that for bimetallic catalysts (not shown), the temperature shift shown by the maximum NO conversion is even more accentuated (*ca.* 50 °C). Both the metal loading and the metal dispersion of the catalysts compared in Figure 5.3 were determined to be fairly similar. Thus, the improved performance of the fMWCNTs-based catalyst can be tentatively attributed to the higher Brønsted acidity of the support (*vide supra*). This explanation is consistent with the higher degree in which the performance of bimetallic catalysts was enhanced. Indeed, Figueras *et al.* have shown that the activity of Rh in the HC-SCR reaction is highly dependent on support acidity [168].

5.4.2. Effect of the catalyst preparation method.

Having established the favorable properties of fMWCNTs as a catalyst support, Pt was deposited onto fMWCNTs *via* the polyol method [169], in order to study the effect of the preparation method on catalyst performance. The nominal 2 wt.% Pt loading of the resulting catalyst was confirmed by PIXE analysis. Figure 5.4 compares the performance of the 2 wt.% Pt/fMWCNTs catalysts prepared by the two different methods. The only difference seems to lie in the temperature of the maximum NO conversion, which is *ca.* 20 °C lower for the catalyst prepared by impregnation. Shifts of similar magnitude can also be observed for the bi-metallic catalysts (not shown). To illustrate the following discussion, Figure 5.4 also includes the performance of a Pt/MWCNTs-I catalyst.

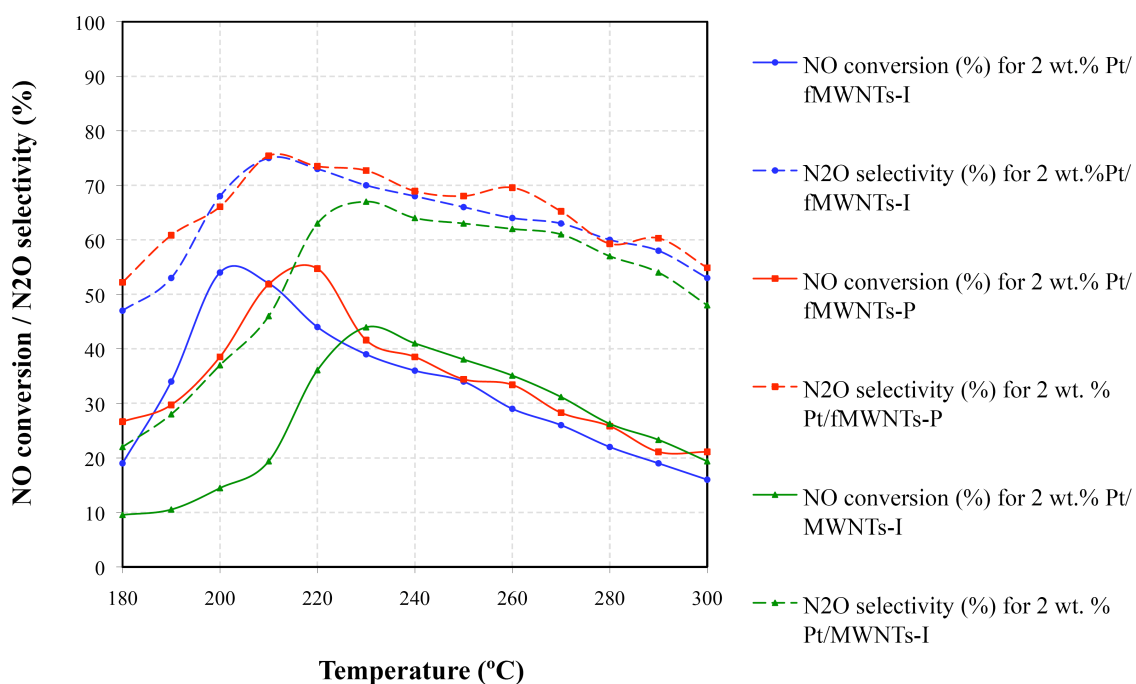


Figure 5.4. Combined plot comparing the performance of 2 wt.% Pt/fMWCNTs-I, 2 wt.% Pt/fMWCNTs-P and 2 wt.% Pt/MWCNTs-I in NO reduction with propene.

Additional measurements were performed in an attempt to understand why the use of fMWCNTs as the catalyst support and impregnation as the catalyst preparation method yields catalysts with improved NO_x reduction performance. As a first step, the metal dispersions of catalysts obtained using different carriers and preparation methods were studied in more detail. To this end, the particle size distributions of representative catalysts were determined by measuring the diameter of 200 particles from micrographs obtained with a Transmission Electron Microscope. Figure 5.5 shows the particle size distribution histograms of the catalysts.

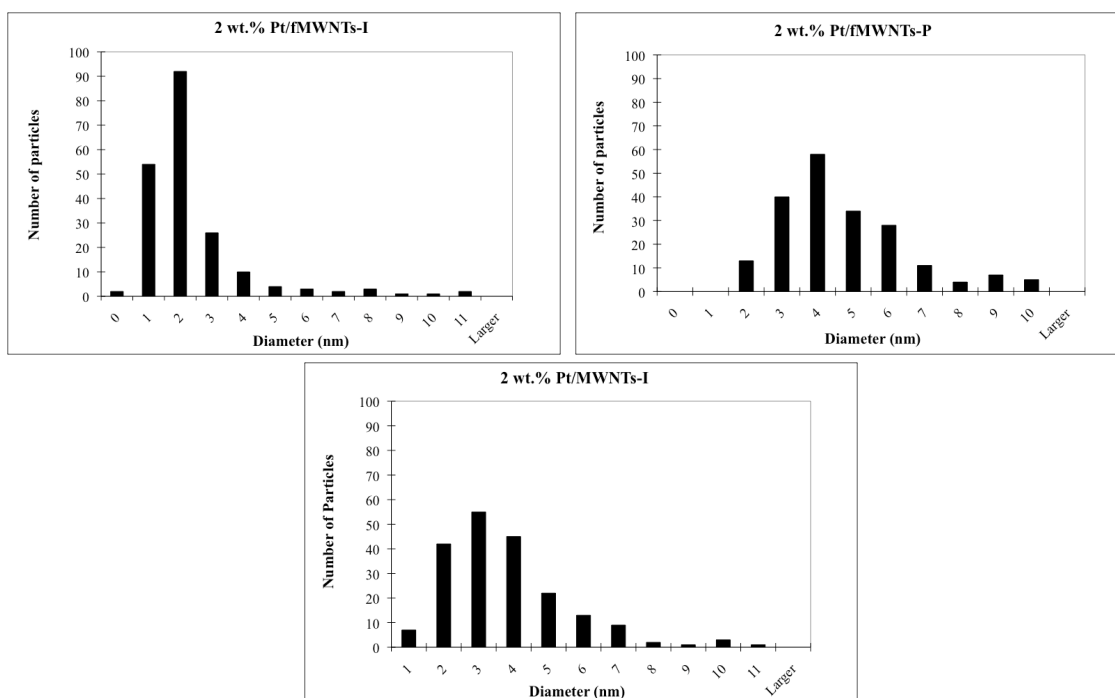


Figure 5.5. Particle size distribution histograms of 2 wt.% Pt/fMWCNTs-I, 2 wt.% Pt/fMWCNTs-P and 2 wt.% Pt/MWCNTs-I.

From Figure 5.5 it can be concluded that the use of fMWCNTs as the support and impregnation as the preparation method yields catalysts with higher metal dispersions than those obtained using pristine MWCNTs or the polyol method. Further, although Pt/MWCNTs-I and Pt/fMWCNTs-P show similar Pt dispersions, their catalytic performances are noticeably dissimilar. This last point is particularly interesting, since

there is an on-going debate regarding the effect of Pt dispersion on the performance of Pt catalysts. While some authors find no correlation between Pt dispersion and NO_x reduction performance [29,66,75,170], other authors propose that Pt dispersion has a noticeable influence on deNO_x activity and/or N₂-selectivity [47,52,72,170,171]. Further, it seems that the extent of such influence depends on both the nature of the support and the reaction under study (propene oxidation, NO oxidation, NO dissociation or NO reduction) [171-175]. Unfortunately, our work does not allow an unambiguous conclusion to be drawn in this regard, given the added variable of support acidity. Indeed, even when the same carrier is used as starting material, it is possible for different preparation methods to yield catalysts with dissimilar support acidities. Thus, in order to probe the extent of the influence of the support in the catalytic performance of MWCNT-supported formulations, STEM-EDS, XPS and acidity studies were performed (see Chapter 6).

Finally, inspired by a recent report in the literature dealing with the removal of oxidation debris from acid-treated MWCNTs [176], we decided to investigate the effect of a base washing step on the functionalized multi-walled nanotubes (fMWCNTs). Acid treatment of MWCNTs (4 h reflux in a 1:1 H₂SO₄-HNO₃ mixture) was performed in order to produce fMWCNTs, which were then suspended in 0.01 M NaOH *via* bath sonication for 30 min. This suspension was then centrifuged and the supernatant was decanted. The solid was next re-suspended in de-ionized water, centrifuged and decanted. A wash with 0.01 M HCl, followed by a final wash with de-ionized water, was performed before allowing the product (denoted hereafter bfMWCNTs) to dry in a vacuum oven. Both the fMWCNTs used as starting material and the bfMWCNTs product were characterized by means of TEM and TGA. Figure 5.6 shows representative micrographs of these two materials.

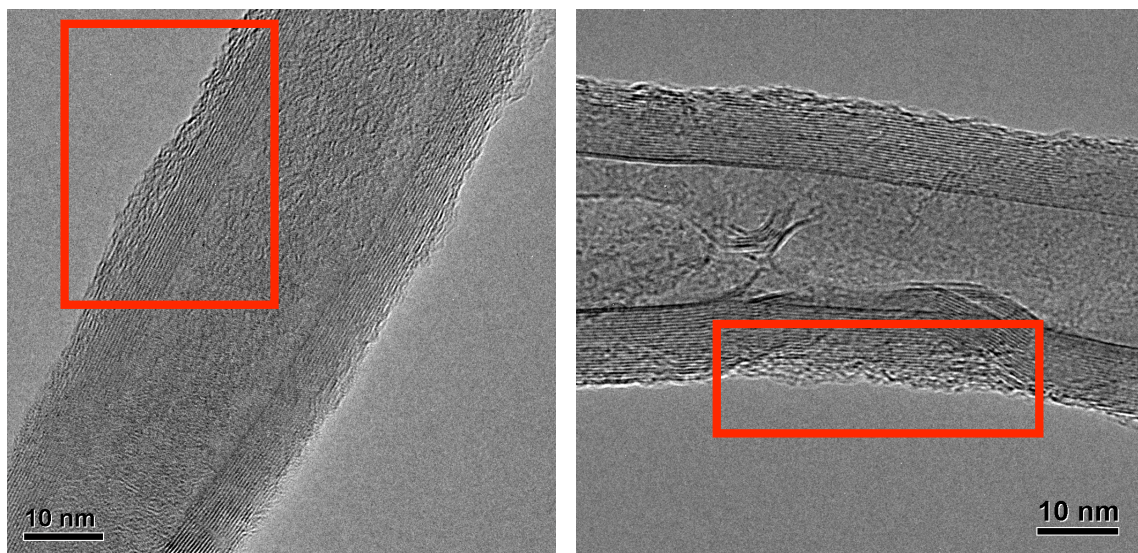


Figure 5.6. TEM micrographs of fMWCNTs (left) and bfMWCNTs (right) with oxidation debris highlighted by the red rectangles.

TEM observations suggest that the amount of residual oxidation debris is lessened by the base washing step. However, as the highlighted region of the micrograph of a bfMWCNT shows, the produced material is not debris-free. Given that TEM is not a bulk technique, TGA experiments were performed in which both fMWCNTs and bfMWCNTs were combusted under an atmosphere of 10 % O₂ (balance N₂) using a temperature ramp of 5 °C/min. The resulting plots are shown in Figure 5.7.

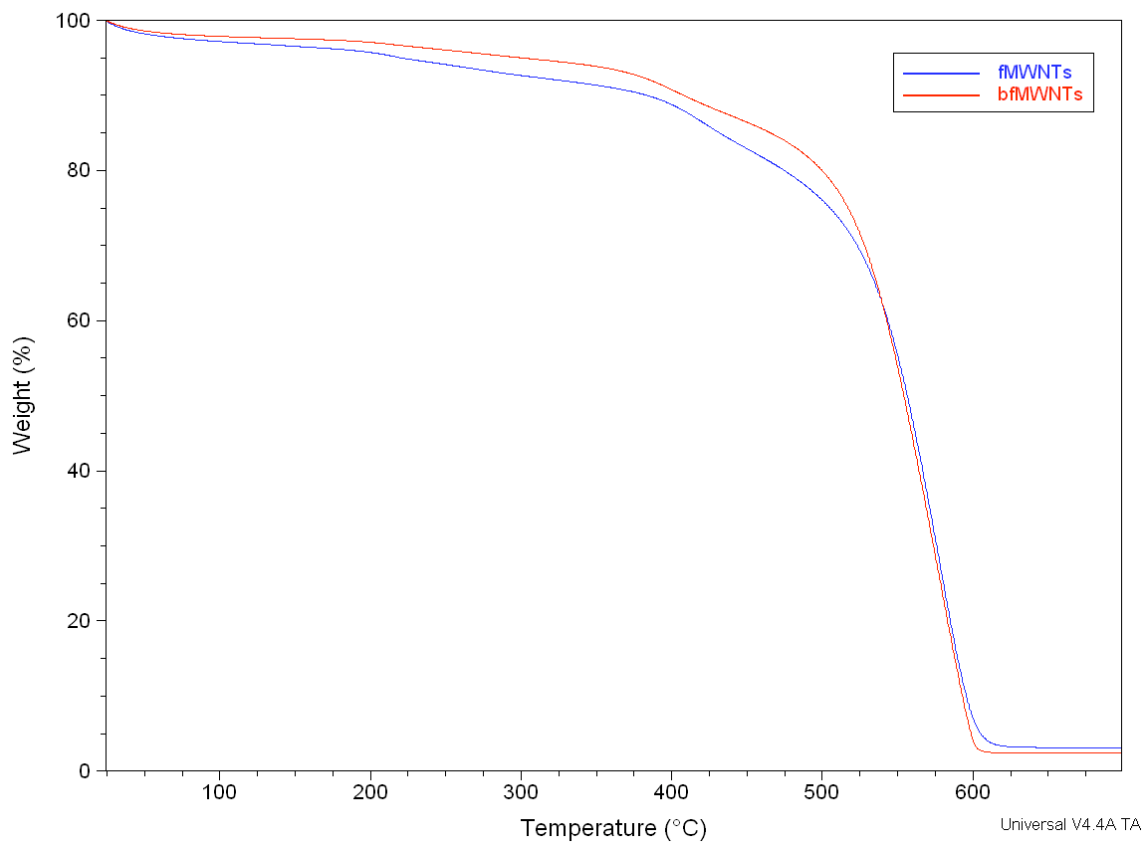


Figure 5.7. Combined TGA plot for fMWCNTs and bfMWCNTs under an atmosphere of 10 % O₂ (balance N₂). Ramp = 5 °C/min.

From the figure, it is apparent that some of the oxidation debris, which is combusted at relatively low temperatures compared to the actual MWCNTs, is successfully removed by the base wash. Elemental analysis of fMWCNTs and bfMWCNTs, shown in Table 5.1, appears consistent with this conclusion.

Table 5.1. Elemental analysis (by combustion) of fMWCNTs and bfMWCNTs.

Material	Ash (%)	Moisture (%)	Carbon (%)	Hydrogen (%)	Nitrogen (%)	Oxygen (%)
fMWCNTs	1.13	3.09	85.66	0.62	0.22	12.37
bfMWCNTs	2.41	1.68	87.97	0.51	0.28	8.83

As can be seen from the table, there is a significantly lower oxygen and water content in the base-washed material, which further points to the successful removal of some of the highly functionalized hydrophilic matter from the surface of the fMWCNTs.

Further, in order to determine the effect on precious metal deposition of removing oxidation debris, both a 2 wt.% Pt/fMWCNTs-I catalyst and a 2 wt.% Pt/bfMWCNTs-I catalyst were prepared and characterized. As can be seen in Figure 5.8, which compares the particle size distribution of these two catalysts, the base wash of the support seems to have no effect on the particle size obtained after Pt deposition.

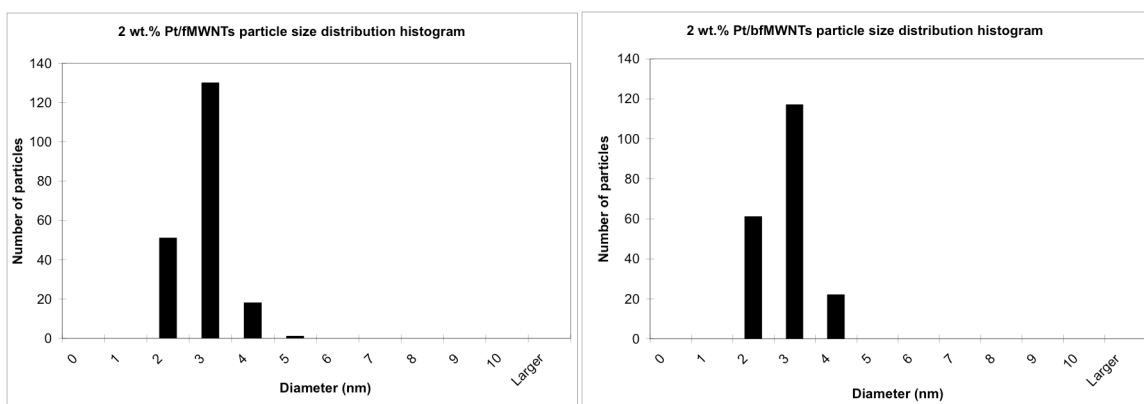


Figure 5.8. Particle size distribution histograms for 2 wt.% Pt/fMWCNTs-I (left) and 2 wt.% Pt/bfMWCNTs-I (right).

This result, combined with the conclusions drawn from the elemental analyses, suggests that after removal of the oxidation debris, the concentration of surface groups remains sufficient to ensure that a high metal dispersion is obtained. Parenthetically, differences can be observed between this and the previously shown particle size distribution histogram of a different Pt/fMWCNTs sample. These differences can be attributed to the degree of variability inherent to the catalyst preparation and/or the catalyst analysis (TEM not being a bulk technique makes the latter more likely). Nevertheless, given that the differences between the histograms obtained for different batches of the same catalyst are exiguous (their maxima differ ~ 1 nm), valid comparisons can be made between

histograms obtained from different formulations as long as their particle size distributions diverge conspicuously.

Finally, the effect of removing the oxidation debris on the performance of the resulting catalyst was investigated. Figure 5.9 compares the activity of 2 wt.% Pt/bfMWCNTs in NO reduction with propene with that of 2 wt.% Pt/fMWCNTs.

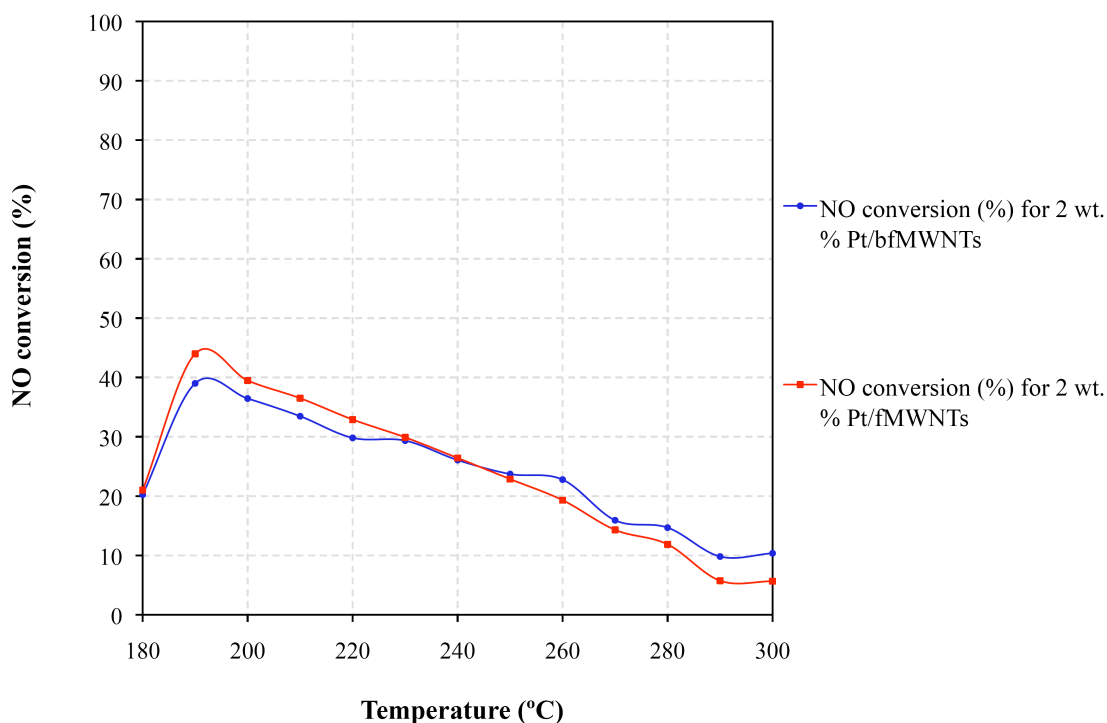


Figure 5.9. Combined plot comparing the performance of 2 wt.% Pt/fMWCNTs with that of 2 wt.% Pt/bfMWCNTs in NO reduction with propene.

From this comparison it is apparent that both catalysts show fairly similar deNO_x activities. This is to be expected, given that the characterization of these catalysts revealed no significant differences between them.

5.4.3. Effect of the reductant concentration.

Experiments were performed in order to determine the effect of the propene concentration on catalyst performance. Figure 5.10 is a combined plot comparing the performance of a 2 wt.% Pt/fMWCNTs-P catalyst under different propene:NO ratios.

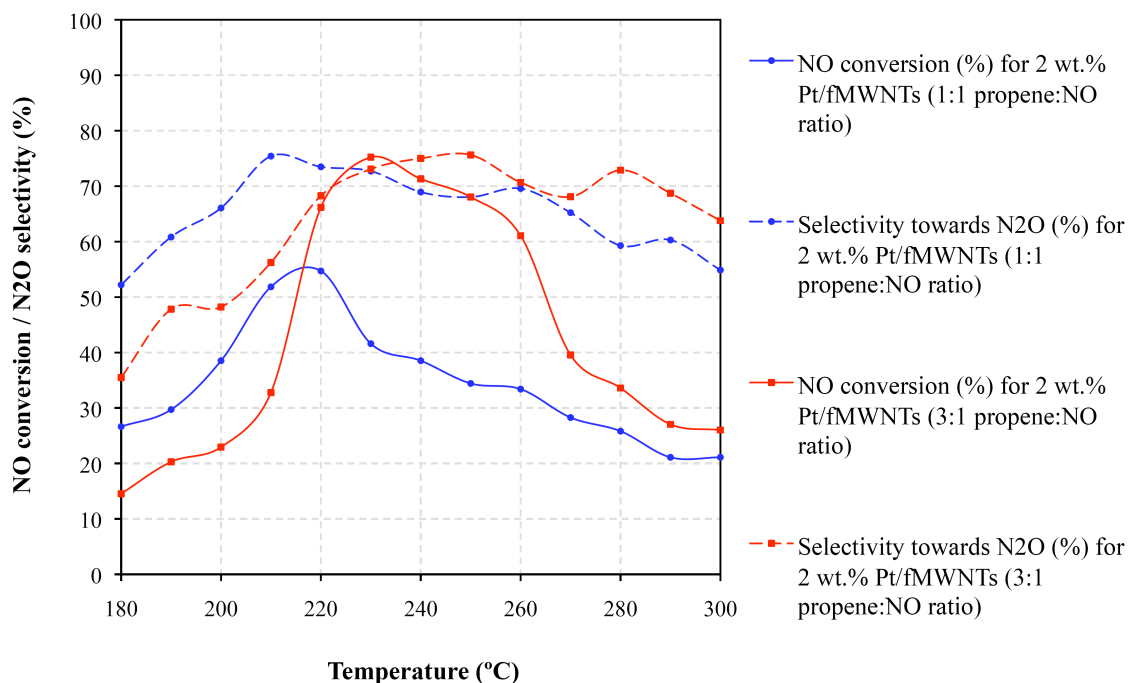


Figure 5.10. Combined plot comparing the performance of 2 wt.% Pt/fMWCNTs-P in NO reduction with propene under different propene:NO ratios. Feed composition: 500 ppm NO, 500 or 1500 ppm C₃H₆, 10 % O₂ and 10 % H₂O, balance nitrogen.

It can be clearly observed that although the selectivity to N₂O is almost totally independent of the propene concentration, the deNO_x activity increases considerably upon tripling the propene:NO mole ratio. This effect is not unexpected, given that NO reduction by propene competes with the total oxidation of the latter by oxygen. Therefore, any increase in propene concentration should lead to a higher amount of propene available for NO reduction. Simultaneously, the deNO_x activity also shows a

slight temperature shift toward higher temperatures (*ca.* 10 °C), which is consistent with an increase in the light-off temperature of the hydrocarbon caused by the increase in concentration of the latter (see section 5.5 below).

5.4.4. Effect of promotion with Rh and/or Ir.

In addition to Pt, bimetallic Pt-containing catalysts of the type Pt-Rh [44,87] and Pt-Ir [89,177-179] have been reported to be active in NO_x reduction with hydrocarbons. With this in mind, and taking into account our findings regarding the effects of the catalyst support and the catalyst preparation method on deNO_x performance, Pt/fMWNTs, Pt-Rh/fMWNTs and Pt-Ir/fMWNTs catalysts with 2 wt.% total metal loading (and 1:1 metal-to-metal weight ratio in bimetallic formulations) were prepared *via* impregnation. Figure 5.11, which compares the performance of these three materials, illustrates how the monometallic catalyst shows a higher NO conversion than the bimetallic preparations.

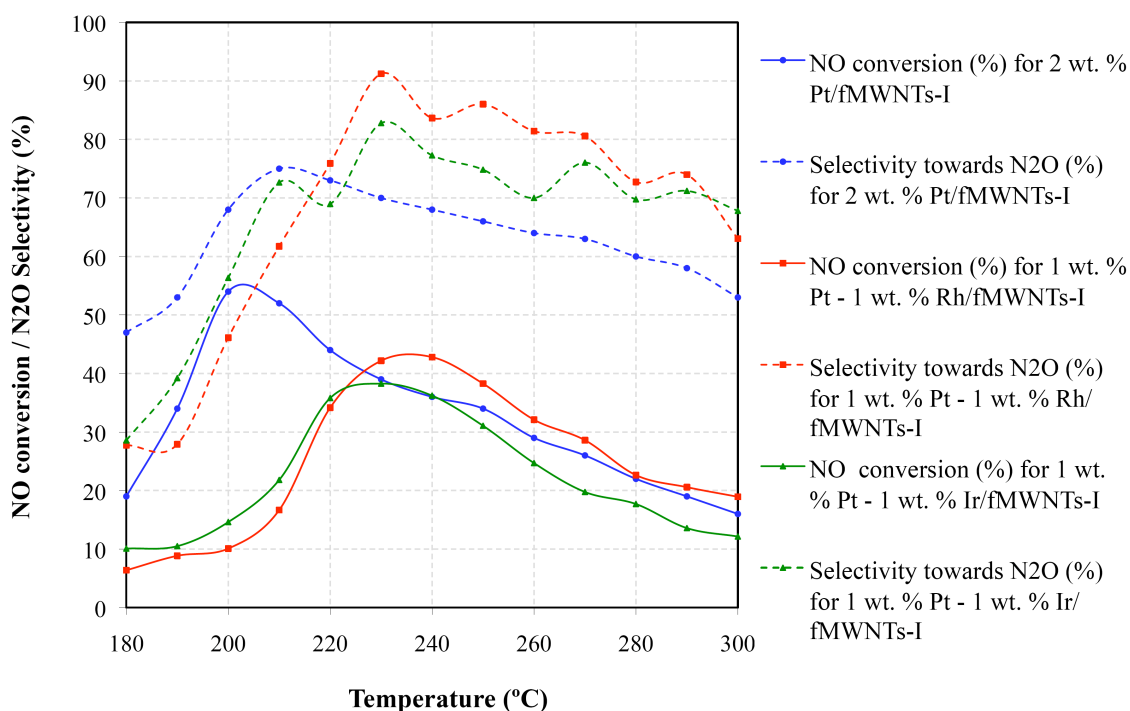


Figure 5.11. Combined plot comparing the performance of 2 wt.% Pt/fMWNTs-I, 1 wt.% Pt – 1 wt.% Rh/fMWNTs-I and 1 wt.% Pt – 1 wt.% Ir/fMWNTs-I in NO reduction with propene.

Additionally, the temperature at which the monometallic catalyst shows its maximum activity is *ca.* 30 °C lower than that of the bimetallic catalysts and *ca.* 50 °C lower than that of a 1:1:1 trimetallic preparation with the same total metal loading (not shown). Further, given that the same trends were observed when the formulations were prepared by the polyol method or when pristine MWCNTs were used as catalyst support, this behavior is clearly metal-dependent. The latter in turn suggests that the inferior catalytic performance shown by multimetallic catalysts can be attributed to the degree in which the HC-SCR reactants (propene in particular) are adsorbed on Rh and Ir vis-à-vis Pt (*vide infra*).

Figure 5.11 shows that although the Pt-Rh/fMWCNTs catalyst represents the bimetallic formulation with the best NO reduction activity, its performance is inferior to that of the corresponding Pt-only catalyst. However, since all our bimetallic formulations had been prepared aiming for a 1:1 weight ratio between the two metallic components, the effect of the metal ratio on deNO_x activity was of interest. A loading study was performed in which two Pt rich Pt-Rh catalysts with a 2 wt.% total metal loading were prepared using fMWCNTs as the support and impregnation as the preparation method. One of these catalysts had a 3:1 Pt to Rh weight ratio, while in the other these metals were in a 9:1 proportion. Figure 5.12 compares the deNO_x activity of the Pt-Rh catalysts with that of the corresponding Pt-only catalyst.

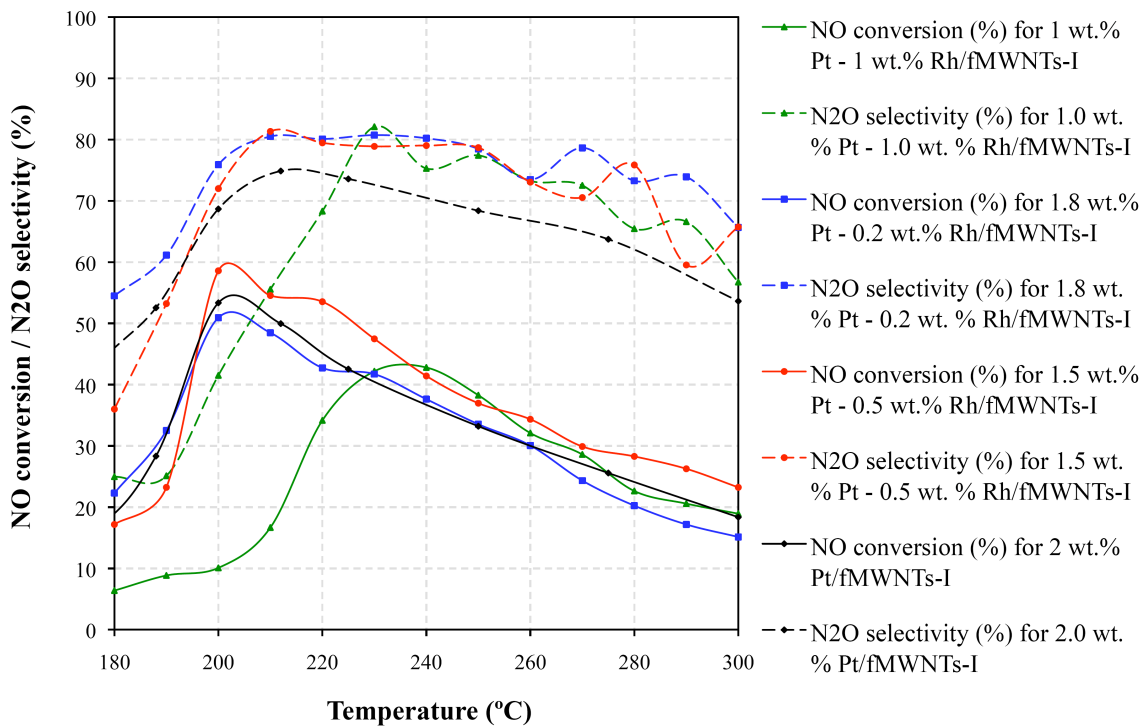


Figure 5.12. Combined plot comparing the performance of Pt/fMWCNTs-I to that of Pt-Rh/fMWCNTs-I with different Pt:Rh ratios in NO reduction with propene.

From this figure, it is apparent that the catalyst with a 3:1 Pt:Rh ratio shows improved behavior compared to that of the Pt-only catalyst and represents the most active formulation prepared in the project. Table 5.2 summarizes and compares the reactor data for selected Pt-only and Pt-Rh catalysts.

Table 5.2. NO conversion data for selected Pt and Pt-Rh catalysts.

Catalyst ¹	T _{max} (°C)	Conv. to N ₂ at T _{max} (%)	Conv. to N ₂ O at T _{max} (%)	Conv. to NO ₂ at T _{max} (%)	NO conv. FWHM ² (°C)	TOF ³ at T _{max} (10 ⁻³ s ⁻¹)
Pt/MWCNTs-I	225	30.5	18.4	4.0	75	8.9
Pt/fMWCNTs-I	205	33.0	20.4	1.7	80	6.8
Pt/fMWCNTs-P	220	32.4	22.3	17.4	87	13.0
1:1 Pt-Rh/fMWCNTs-I	235	24.9	17.9	0.8	65	5.6
3:1 Pt-Rh/fMWCNTs-I	200	35.2	23.4	1.4	75	7.9
9:1 Pt-Rh/fMWCNTs-I	200	28.4	21.5	7.6	85	6.6

¹2.0 wt.% total metal loading for each catalyst.

²Full Width at Half Maximum.

³Turn Over Frequency defined as the number of NO molecules converted to N₂ and N₂O per surface precious metal atom per second.

It is important to note that the turnover frequencies (TOFs) reported in this table were calculated using the median particle diameter of particles observable under TEM (>1 nm). Since the existence of sub-nanometer particles has been proven by means of STEM (see Chapter 6) and all of the calculated TOFs fall within a very narrow range, these values should be approached with caution. As an incidental disclaimer, in heterogeneous catalysis TOFs can be misleading when it comes to measuring the effectiveness of a catalyst, since it is possible for a formulation to have a high TOF and a low catalytic activity. Indeed, in catalysts with low surface area per unit volume (i.e., few catalytically active surface sites) this is often the case, which is why the use of activity-selectivity plots is a more appropriate medium to illustrate the catalytic performance of a given formulation [180].

Figure 5.13 shows the particle size distribution histograms of the three Pt-Rh catalysts. These histograms were acquired and compared in order to determine whether catalyst performance was influenced by particle size.

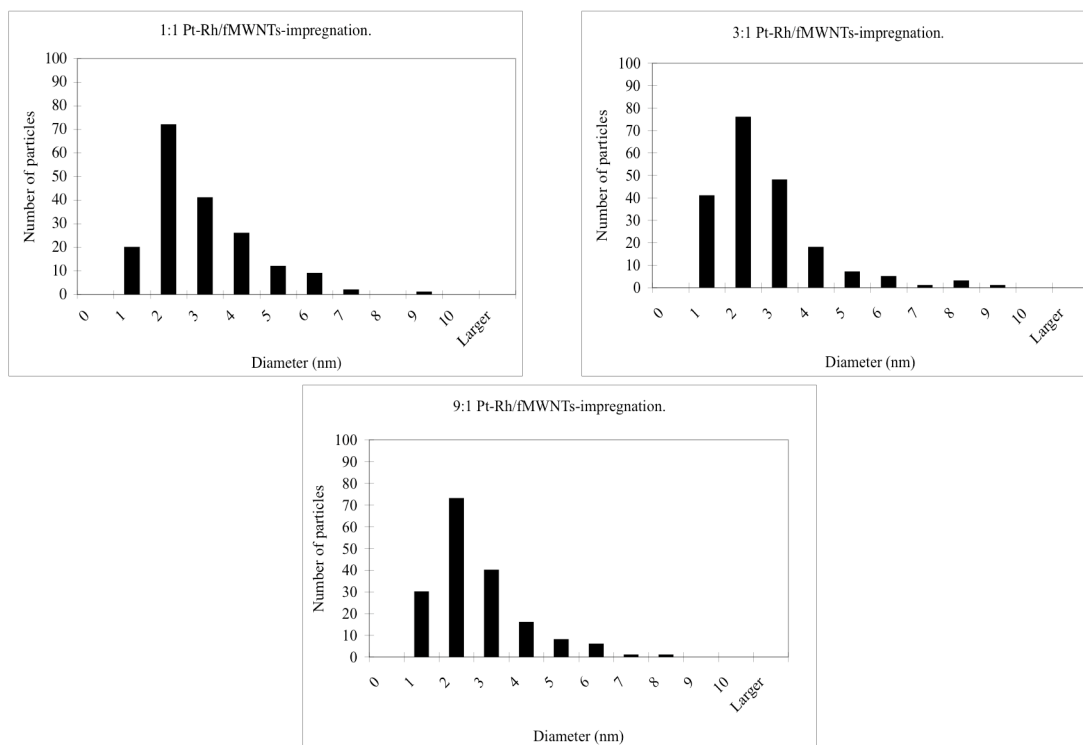


Figure 5.13. Particle size distribution histograms for 1.0 wt.% Pt – 1.0 wt.% Rh/fMWCNTs-I (left), 1.5 wt.% Pt – 0.5 wt.% Rh/fMWCNTs-I (center) and 1.8 wt.% Pt – 0.2 wt.% Rh/fMWCNTs-I (right).

In all three cases, the particle size distribution was centered on particles between 2 and 3 nm in diameter and, in general, the histograms look quite similar. This suggests that the deNO_x activity of Pt-Rh/fMWCNTs catalysts depends largely on the ratio in which the metals are present (without categorically ruling out the influence of the metal dispersion on catalytic activity). This observation is consistent with a literature report, in which a 0.75 wt.% Pt – 0.25 wt.% Rh/Al₂O₃ catalyst was found to show the highest activity for NO conversion (~60 % at 250 °C) in a series of Pt-Rh catalysts with different Pt:Rh ratios [44]. However, this reference also reports an improvement in N₂ selectivity for the 3:1 Pt-Rh catalyst compared to that of the corresponding Pt-only formulation. Regrettably, such an improvement is not observed for fMWCNTs-based catalysts.

In the aforementioned literature report, the authors neglect to discuss the fundamental reason why a catalyst with a 3:1 Pt-Rh alloy as the active phase can outperform a Pt-only formulation in NO reduction with propene. However, a hypothesis is offered to explain the superior performance of the 3:1 Pt-Rh catalyst vis-à-vis 1:1 Pt-Rh and 1:3 Pt-Rh formulations with the same total metal loading. Firstly, these workers claim that the hydrocarbon can follow two reaction paths in the HC-SCR reaction, since it can either be directly oxidized into CO₂, or be partially oxidized into carbonaceous radicals which can then proceed to react with NO_x to yield N₂ [181,182]. Thereafter, the authors conclude that an excess of Rh favors the former path over the latter, which results in a decrease in deNO_x activity. In our work, spectroscopic and adsorption studies were carried out in an attempt to elucidate the role of Rh in the promotion of Pt-only CNTs-based formulations. The results of these studies are covered in the following chapter.

Finally, Figure 5.14 shows the particle size distribution histograms of the 2 wt.% Pt/fMWCNTs-I and the 1.5 wt.% Pt – 0.5 wt.% Rh/fMWCNTs-I catalysts both before and after these catalysts were screened.

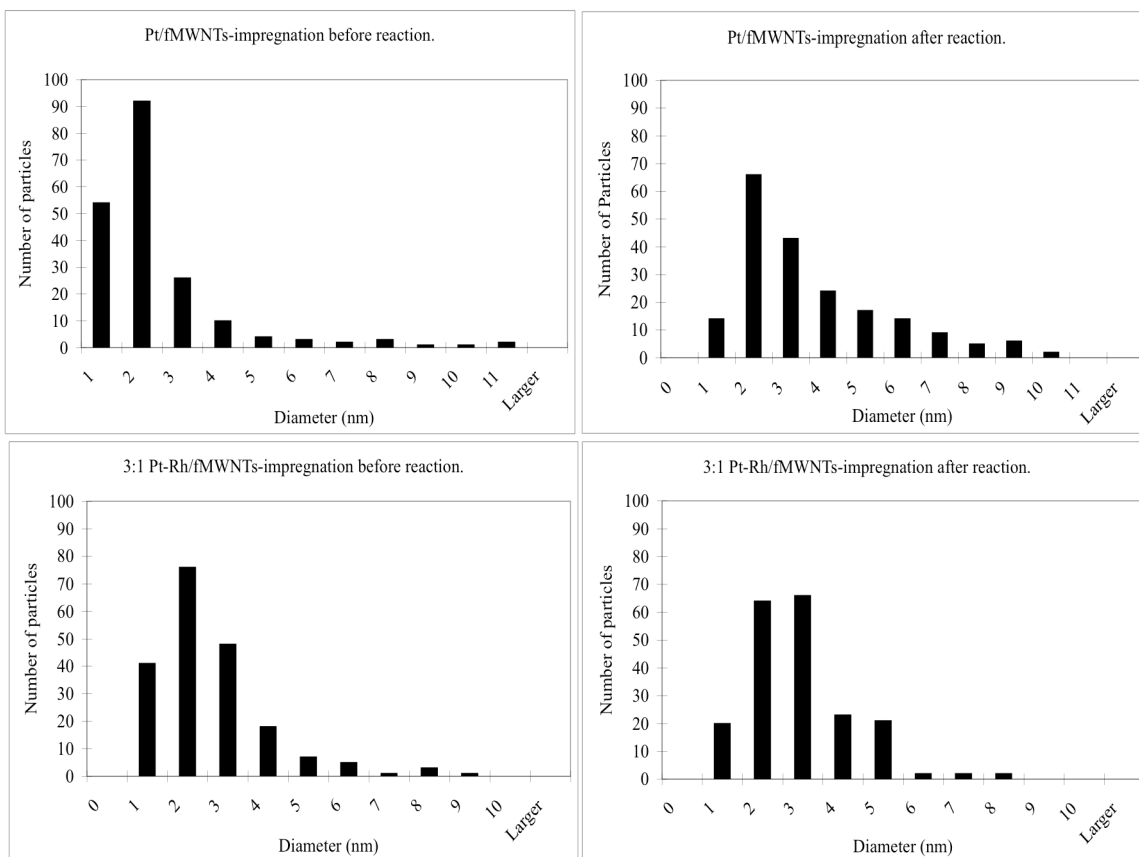


Figure 5.14. Particle size distribution histograms for fresh 2 wt.% Pt/fMWCNTs-I (top left), 2 wt.% Pt/fMWCNTs-I after exposure for ~12 h to reaction conditions (top right), fresh 1.5 wt.% Pt – 0.5 wt.% Rh/fMWCNTs (bottom left) and 1.5 wt.% Pt – 0.5 wt.% Rh/fMWCNTs after exposure for ~12 h to reaction conditions (bottom right).

A comparison between these histograms permits an assessment of the extent of metal particle growth resulting from exposure to the reaction conditions. Although the particle size distributions of the used catalysts seem to have shifted towards larger particles, these shifts would correspond to a particle growth of only 1-2 nm. This can be deemed to be a negligible growth, given the fact that the shift is within the range of the analytical error (*vide supra*). Further, particle growth was found to be very similar for both the mono and the bimetallic catalyst.

With the aim of further optimizing the 1.5 wt.% Pt – 0.5 wt.% Rh/fMWCNTs catalyst (the best formulation found in our work), an alternative preparation method was attempted based on a recent patent [183] describing the preparation of Pt-Rh three-way catalysts. In this method, the support is first dispersed in water and the appropriate amount of ethanolamine platinum (IV) hexahydroxide is added to the resulting suspension. The pH is adjusted to 6.0 with dilute aqueous ammonia solution to precipitate the Pt. After this, the appropriate amount of $\text{Rh}(\text{NO}_3)_3$ is added and the pH is adjusted to 7.0 to precipitate the Rh. Finally, the suspension is centrifuged, the supernatant decanted, and the solid dried. Following this procedure, two catalyst batches were produced: one was tested for deNO_x activity as-prepared, while the other was exposed to a flow of H₂ at 400 °C for 3 h (a reduction step not included in the patent) prior to testing. Figure 5.15 shows the deNO_x performance of these two catalysts and compares it with that of a catalyst prepared *via* impregnation.

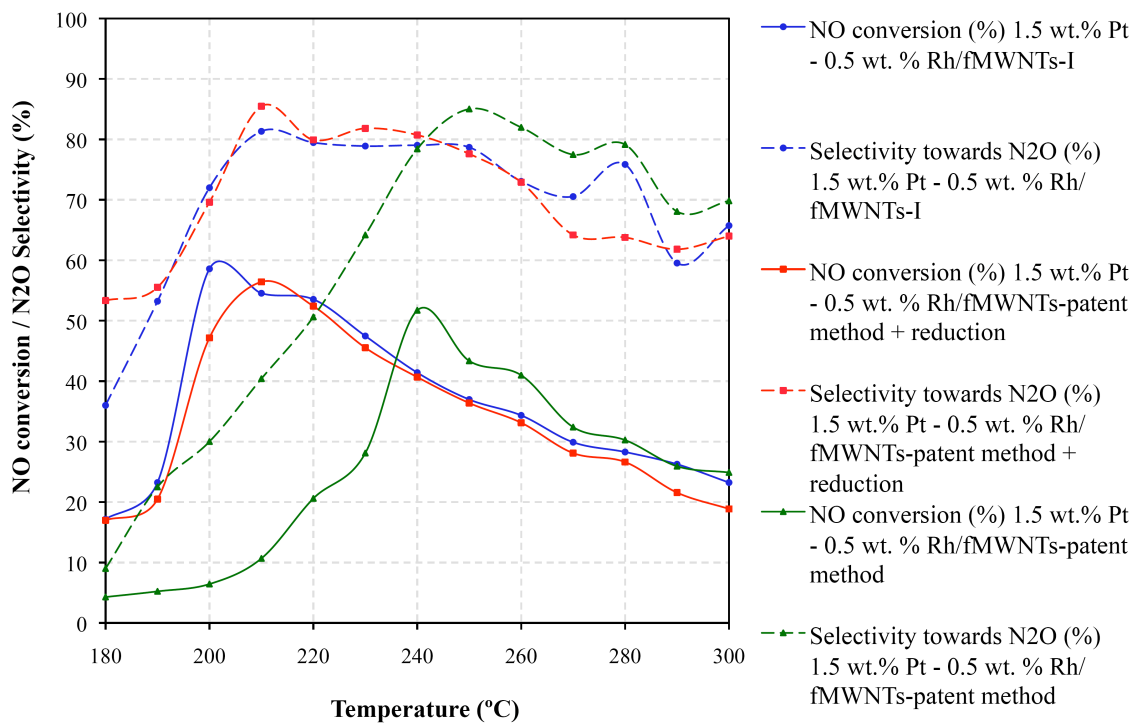


Figure 5.15. Combined plot showing the performance of three 1.5 wt.% Pt – 0.5 wt.% Rh/fMWCNTs catalysts prepared by different methods in NO reduction with propene.

As can be seen from the figure, neither of these newly prepared catalysts surpassed the NO reduction performance of the catalyst previously prepared by impregnation. However, it is interesting to note that of the two catalysts prepared by the patent method, only the one that was reduced showed an activity similar to that of the catalyst prepared by impregnation. On the other hand, the deNO_x activity shown by the unreduced catalyst went from almost zero across the whole temperature range to that shown in Figure 5.15 after a couple of hours under reaction conditions. This suggests that a slow *in situ* reduction of the Pt was taking place, which in turn indicates that Pt is required to be in the metallic state to catalyze the HC-SCR reaction.

5.4.5. Sodium promotion.

The effects of Na⁺ addition on the performance of Pt/Al₂O₃ HC-SCR catalysts have been reported in the literature [184,185]. These effects, which include not only an increase in the deNO_x activity but also an improvement in catalyst selectivity towards N₂ when propene is used as the reductant, are thought to have their origin in the electrostatic field induced by the sodium cation, which strengthens the Pt-electron acceptor (NO and O₂) bonds while weakening the Pt-electron donor (C₃H₆) bonds, as well as weakening the N-O bond in adsorbed NO molecules [186]. Based on these reports, the promoting effect of Na⁺ was studied for Pt/fMWCNTs and Pt-Rh/fMWCNTs catalysts. Three Pt-Na/fMWCNTs catalysts with different Pt:Na weight ratios (2:1, 2:5 and 2:10) were prepared by a method involving two sequential impregnations followed by Na precursor decomposition under He and Pt reduction under H₂ [184]. These catalysts were then tested for deNO_x activity using propene as reductant. Of these, only the 2:10 catalyst showed a promising performance (Figure 5.16). This can be rationalized on the basis that while adsorption of both oxygen and NO is enhanced by Na⁺ promotion, oxygen adsorption is favored since it is a stronger electron acceptor than NO. Therefore, for a given Pt loading and reductant concentration, the sodium loading has to be sufficiently high to enhance NO adsorption, while ensuring that oxygen adsorption is not taken to a regime at which the catalyst is poisoned [185]. As shown in Figure 5.16, the 2 wt.% Pt – 10 wt.% Na/fMWCNTs catalyst shows a NO conversion of between 20 and 30% over the 150 to 300 °C temperature range.

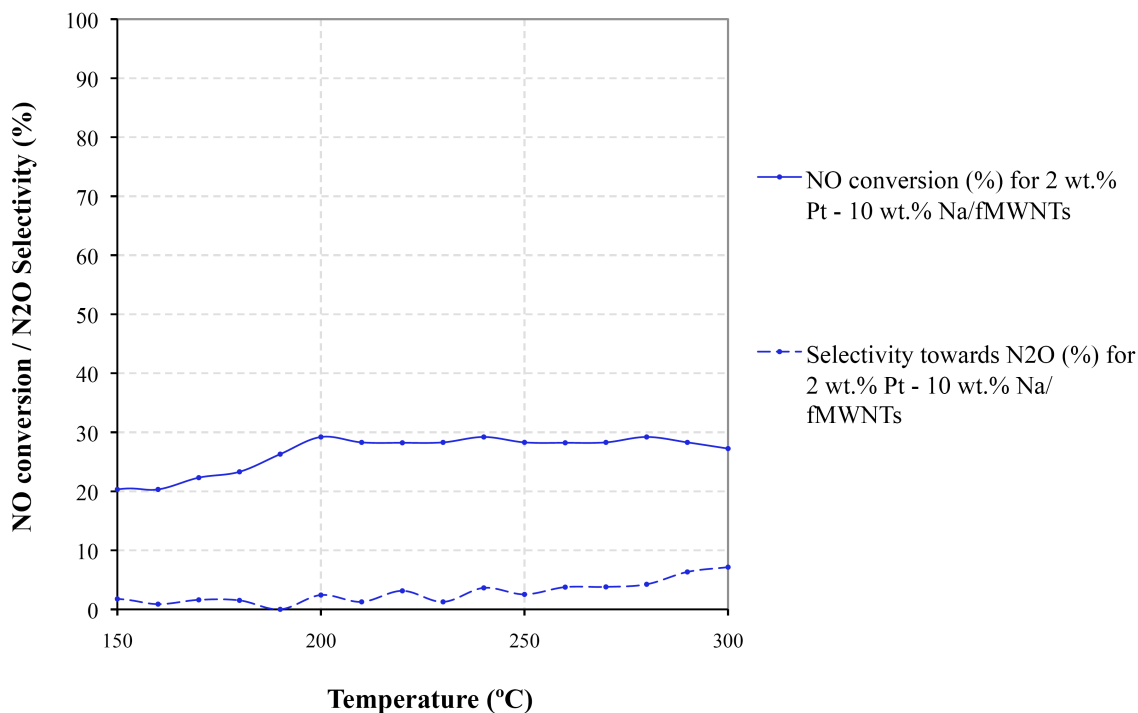


Figure 5.16. Plot showing the performance of 2 wt.% Pt – 10 wt.% Na/fMWCNTs-I, 2 wt.% Pt – 1 wt.% Na/fMWCNTs-I and 2 wt.% Pt – 5 wt.% Na/fMWCNTs-I in NO reduction with propene.

Further, the NO reduction product seems to be almost exclusively N₂. The deNO_x activity shown by this catalyst is comparable to that reported in the literature for Pt-Na/Al₂O₃ catalysts with similar Pt:Na ratios. However, the N₂-selectivity shown by the 2 wt.% Pt – 10 wt.% Na/fMWCNTs catalyst is considerably superior to that shown by both unpromoted Pt/fMWCNTs and Na⁺-promoted Pt/Al₂O₃ catalysts.

Two alternative ways of preparing a 2 wt.% Pt – 10 wt.% Na/fMWCNTs catalyst were also attempted: 1) Pt and Na precursors were impregnated onto the support simultaneously before being reduced with H₂, and 2) the Pt precursor was impregnated and reduced before the Na precursor was impregnated and decomposed. Unfortunately, the resulting catalysts showed disappointingly low NO reduction activity. TEM-EDS measurements performed in an attempt to understand the influence of the catalyst

preparation method on the observed catalyst behavior are discussed in the following chapter.

The method that yielded the best performing Pt-Na catalyst was also used to prepare a 1 wt.% Pt – 1 wt.% Rh – 10 wt.% Na/fMWCNTs catalyst. However, when tested, it showed rather poor NO reduction activity. This result was not completely unexpected, since it has been reported in the literature that Rh catalysts are inhibited by the presence of sodium. This is likely due to the fact that, contrary to the case of Pt, propene is not as strongly adsorbed on Rh as oxygen. Therefore, an excessive promotion of oxygen adsorption due to the presence of sodium leads to the inhibition of propene adsorption and oxidation [187].

5.4.6. Examination of alternative metals and metal promoters.

In order to study whether metals other than Rh and Ir could improve deNO_x activity and/or selectivity, a number of catalysts in which Pt was alloyed with alternative metals were prepared and tested. The support and preparation method for these catalysts was the same in all cases; *viz.*, fMWCNTs and impregnation, respectively. Pd, Co and Ag were alloyed with Pt in a 1:1 weight ratio, however, the performance of these catalysts in the 180-300 °C temperature range proved to be considerably inferior to that shown by the corresponding Pt-only catalyst.

Further, given that Ag/Al₂O₃ has been reported to be one of the most active catalysts for NO_x reduction by hydrocarbons [188], a Ag/fMWCNTs catalyst was prepared *via* the impregnation method. Since it is believed that Ag⁰ is the catalytically active phase in this reaction and the use of fMWCNTs as support should keep the metal in a more reduced state (as compared to oxidic supports), the preparation and screening of this catalyst was of particular interest. Unfortunately, this catalyst showed little or no activity in the 180-300 °C temperature range, independent of the reductant used (propene, decane and ethanol were tested).

Finally, since it has also been reported in the literature [189,190] that the addition of Rh to Ag/Al₂O₃ catalysts induces a significant improvement in deNO_x performance, a 1.8 wt.% Ag – 0.2 wt.% Rh/fMWCNTs catalyst was prepared and tested. However, the catalytic behavior of the material was also disappointing, regardless of the reductant used.

5.5. Kinetic studies.

Experiments were performed in order to determine relevant kinetic parameters (activation energies and reaction orders) for NO reduction with propene catalyzed by the two MWCNTs-based formulations with the most promising deNO_x performance: 2 wt.% Pt/fMWCNTs and 1.5 wt.% Pt – 0.5 wt.% Rh/fMWCNTs. The results of these studies are condensed in Table 5.3.

Table 5.3. Kinetic data for 2 wt.% Pt/fMWCNTs and 1.5 wt.% Pt – 0.5 wt.% Rh/fMWCNTs.

Catalyst	Apparent activation energy (kJ/mol)	Reaction order in NO		Reaction order in C ₃ H ₆	
		190 °C	200 °C	190 °C	200 °C
2 wt.%Pt/fMWCNTs	57±4	0.21	0.21	-0.31	0.64
1.5 wt.% - 0.5 wt.% Rh/fMWCNTs	58±8	0.13	0.28	-0.32	-0.46*

*0.39 at 205 °C.

Several conclusions can be drawn from these data. First, the activation energy values are lower than those reported in the literature for Pt/Al₂O₃ (91 kJ/mol) [153], Pt-CeO₂/Al₂O₃ (182 kJ/mol) [191] and Pt-beta-coated cordierite monoliths (72±11 kJ/mol) [16]. Bearing in mind the improved performance of MWCNTs-based catalysts compared to that of formulations involving oxidic supports, this result is not unexpected. Also unsurprising were the more scattered activation energy values measured for the bimetallic catalyst compared to those of the monometallic formulation, given that in the former, the metal particles may cover the whole spectrum of Pt:Rh ratios, effectively behaving as a collection of catalysts and increasing the complexity of the system.

The observed reaction kinetics reflect, among other factors, the effect of temperature on the adsorption of reactants on the active sites of the catalyst and the reaction orders for propene shown in Table 5.3 offer a good example of this. Negative reaction orders for C_3H_6 at 190 °C signify that at low temperatures the surface of the catalyst is covered, and therefore poisoned, by propene. As the temperature increases and approaches the light-off temperature of the reductant, the reaction orders for propene become positive, indicating the availability of active sites made possible by the oxidation of the alkene. These findings are also consistent with the results reported in Figure 5.10, which show a shift in the peak NO_x conversion to higher temperature upon increasing the propene concentration.

In conclusion, several factors have been found to have a positive effect on the low temperature HC-SCR performance shown by MWCNTs-based formulations. These factors include the use of fMWCNTs as catalyst support, impregnation as the catalyst preparation method and a 3:1 Pt-Rh alloy as the catalytically active phase. Further, the use of high C: NO_x ratios has been found to further increase the maximum NO_x conversion shown by these catalysts. Finally, it has been determined that the activation energies shown by MWCNTs-based formulations towards the HC-SCR reaction are among the lowest reported in the literature, which is consistent with their improved de NO_x performance in the low temperature regime.

Chapter 6. Probing Structure-activity Relationships in HC-SCR Catalysts.

6.1. Introduction.

Heterogeneous catalysis is, by definition, a surface phenomenon. Thus, the outcome of a heterogeneously catalyzed reaction is highly dependent on the nature of the catalytic surface. It is therefore important not only to be cognizant of the attributes of a catalyst under study, but to probe the relationship such attributes have with catalytic performance. Indeed, empirically elucidating relations between catalyst composition, metal particle size and morphology, support acidity and porosity on the one hand, and catalytic performance on the other, is immensely useful during the development and the optimization of a catalyst.

A variety of methods are available to probe these structure-activity relationships, such as microscopy, fluorescence, diffraction, adsorption and reaction techniques [192]. However, spectroscopic techniques, in which a catalyst is excited and its response to the excitation is studied, have proven to yield particularly valuable information in this regard. This is especially true for techniques in which the particles or radiation emitted by the catalyst come from the first ten atomic layers of the sample, since surface specific information is obtained. Unfortunately, these surface sensitive techniques possess an intrinsic drawback, i.e., the fact that analyses must be performed in ultra high vacuum, which precludes the probing of the surface under reaction conditions. However, in order to address the latter issue, adsorption and reaction techniques can be used to complement surface sensitive spectroscopic techniques. Indeed, all surface characterization methods have both advantages and limitations and therefore, a successful research strategy should involve the combination of several techniques as a means to obtain the most meaningful information possible.

With this in mind, MWCNTs-based lean deNO_x catalysts were submitted to a variety of spectroscopic and adsorption techniques in an attempt to gain fundamental insights which might aid in the understanding and further improvement of these formulations. Among the analytical methods used throughout this work, three spectroscopic techniques were

instrumental in studying structure-activity relations: Energy Dispersive Spectroscopy (EDS), X-ray Photoelectron Spectroscopy (XPS) and X-ray Absorption Spectroscopy (XAS).

EDS allows for the elemental analysis of samples being observed under the electron microscope. This is possible given the fact that matter emits X-rays when bombarded with electrons and the energy of these X-rays is characteristic for the emitting atom. Thus, the X-ray fluorescence caused by the electron beam in a TEM allows for the composition of a sample to be determined with remarkable spatial resolution [193,194]. In this work, TEM-EDS and STEM-EDS analyses were used not only to study the elemental composition of microscopic regions and individual nanoparticles in HC-SCR catalysts, but also to study the distribution of catalytically active components and promoters with respect to each other *via* elemental mapping.

All photoemission spectroscopies are based on the photoelectric effect, a phenomenon in which the adsorption of a photon by an atom causes the latter to eject an electron. In XPS, X-ray photons are used to cause this ejection. Measuring the kinetic energy of the emitted photoelectrons allows for the calculation of their binding energy. Since a set of binding energies is characteristic for an element, XPS can be used to analyze sample composition. Further, due to the fact that the energy of electrons is slightly dependent on the chemical state of the atom, the calculated binding energies can also afford chemical information, such as the coordination environment and the oxidation state of a given atom [195-197]. Therefore, the oxidation state of the metallic phase in HC-SCR catalysts was investigated in some detail throughout this work by means of XPS.

When an atom is irradiated with X-rays, absorption takes place and a photoelectron is produced when the energy of the incident radiation matches the binding energy of an electron within the atom. Thus, X-ray absorption spectra show a series of edges corresponding to the binding energies of all the electrons in the atom. However, if the emitting atom is in a lattice, the photoelectron (which has both particle and wave character) can be scattered back by a neighboring atom. The scattered wave then

constructively or destructively interferes with the outgoing primary wave, which modulates X-ray absorption and causes the spectrum to show fine structure near the adsorption edge. Depending on the proximity to the absorption edge, the analysis of this fine structure affords discrete pieces of information about the surface under study. Thus, X-ray Adsorption Fine Structure (XAFS) is divided into X-ray Absorption Near Edge Structure (XANES) and Extended X-ray Absorption Fine Structure (EXAFS). The former allows the distinction between different oxidation states based on the position of the absorption edge, while the latter provides details about the coordination environment of the adsorbing atom [198,199]. In this work, XAFS was applied to the study of HC-SCR catalysts in an attempt to obtain information regarding the oxidation state as well as the distance, number and type of neighbors of the metal atoms.

As mentioned in the previous chapter, a degree of support acidity has been found to increase the maximum NO_x conversion achieved by MWCNTs-based HC-SCR catalysts, as well as decreasing the temperature at which this maximum is reached. Thus, in addition to the aforementioned spectroscopic techniques, acidity measurements based on the Temperature Programmed Desorption (TPD) of ammonia were performed to further probe the relationship between support acidity and catalyst performance. TPD analyses are based on three main premises: 1) adsorption minimizes the energy of the adsorbate molecules through the formation of chemical bonds with a surface; 2) if an adsorbate-surface complex is heated, the energy provided to the system will cause the adsorbate molecules to desorb; and 3) the desorption temperature is a good indicator of the strength of the adsorbate-surface bonds.

Finally, in the previous chapter it was mentioned that the mechanism through which HC-SCR performance is improved by the use of a 3:1 Pt-Rh alloy as the active phase remained to be elucidated. Given that the adsorption of C_3H_6 appears to precede its combustion, it could be hypothesized that the role of the alloy is to optimize the adsorption of the hydrocarbon. Thus, the TPD of C_3H_6 on fMWCNTs-based catalysts was also investigated as a means to probe this hypothesis.

6.2. Experimental methods.

6.2.1. Elemental analysis under the Transmission Electron Microscope.

TEM-EDS and STEM-EDS analyses were carried out either by converging the beam in TEM mode or using the 1 nm analytic probe in STEM mode. For elemental mapping, sample preparation consisted of lightly dusting catalyst powder onto a 200 mesh lacey carbon-copper grid. Spectrum images were then obtained in STEM mode using the EmiSpec. Inc., EsVision software.

6.2.2. Temperature Programmed Desorption (TPD) experiments.

TPD experiments were performed using a Micromeritics AutoChem II 2920 system. In C₃H₆-TPD experiments, the catalysts were first heated to 300 °C under He flow, reduced with H₂ at this temperature for 30 min and then cooled to room temperature under flowing He. The reduced catalysts were then exposed to a flow of 2 % C₃H₆ in He for 1 h and then purged with He for 30 min prior to ramping the temperature to 500 °C at a rate of 10 °C/min under He flow. The evolution of desorbed gases during the temperature ramp was followed using a Pfeiffer OmniStar mass spectrometer. The parent ion of propene (m/z=41) was followed along with several other representative ions (m/z=26, 27, 29, 40 and 42). The same procedure was followed in NH₃-TPD experiments, except for the fact that samples were degassed at 300 °C for 30 min under He flow instead of being reduced, the ammonia concentration was 5 % NH₃ in He and the masses analyzed corresponded to the parent ion of ammonia (m/z=17), along with ions corresponding to m/z=16, 15 and 14.

6.2.3. X-ray Photoelectron Spectroscopy (XPS) analyses.

XPS analyses were performed on a PHI 5600 LS instrument, using an Al K α X-ray radiation source. The analysis area was 1 × 3 mm and the C 1s line (285.0 eV) was employed as a binding energy standard.

6.2.4. X-ray Absorption Fine Structure measurements.

Catalysts and Pt references (including Pt⁰ foil, PtO₂, and Pt(acac)₂) were evaluated by XANES at Brookhaven National Laboratory. Catalysts were re-reduced in an *in situ* flow

cell in flowing H₂ (100 ccm) and He (300 ccm) at 300 °C and held for 30 min in flowing H₂. XANES spectra were recorded in transmission mode at the National Synchrotron Light Source (NSLS) at Brookhaven National Laboratory, Upton, New York, Beamline X18-b. The beamline was equipped with a Si (111) channel cut monochromator. A crystal detuning procedure was used to help remove harmonic content from the beam and make the relative response of the incident and transmission detectors more linear. The X-ray flux for the beamline was on the order of 1×10¹⁰ photons per second at 100 mA and 2.8 GeV, and the usable energy range at X-18b is from 5.8 to 40 keV. XANES spectra were recorded near the Pt L_{III} edge (11.5637 keV). Sample thickness was determined by calculating the amount in grams per square centimeter of sample, w_D, by utilizing the thickness equation:

$$w_D = \ln(I_0/I_t) / \sum[(m/r)_j w_j] \quad (6.1)$$

where m/r is the total cross section (absorption coefficient/density) of element “j” in the sample at the absorption edge of the EXAFS element under study in cm²/g, w_j is the weight fraction of element j in the sample, and ln(I₀/I_t) was taken over a typical range of 1 – 2.5. An average value of w_D from inputting both values was employed. Based on the calculation for w_D, and the cross-sectional area of the pellet, the grams were calculated. Boron nitride was utilized to dilute the sample, such that the wafer could be self-supported. Smooth wafers, free of pinholes, were pressed and loaded into the *in situ* XAS flow cell, and the treatment gas was directed to the sample area. The cell was purged for a long duration of time with a high flow rate of inert gas to ensure removal of air, prior to the re-reduction treatment. For each XANES analysis, a linear combination of reference spectra for Pt⁰ (Pt foil) and Pt(II) (Pt(acac)₂) was used to fit the spectra for catalysts after the reduction treatment using the WinXAS software [200]. The spectra did not exhibit any contribution from Pt(IV) oxide (i.e., PtO₂).

6.2.5. Diffuse Reflectance Infrared Fourier Transform Spectroscopy (DRIFTS) analyses.

A Nicolet Nexus 870 FTIR system with a DRIFTS cell was employed. In a typical experiment, the sample was diluted with either KBr or silicon and loaded into a DRIFTS

cell with windows whose composition matched the diluent. The sample was then exposed to a flow equivalent to 500 ppm NO₂ in N₂ and the spectrum was acquired.

Experimental methods for particle size analysis *via* H₂ chemisorption and TEM observations have already been described in Chapter 4.

6.3. TEM-EDS and STEM-EDS studies.

As mentioned in the previous chapter, the presence of sub-nanometer particles in MWCNTs-based catalysts has been proven by means of STEM-EDS. The first indication of the existence of these particles was found during the analysis of a 1 wt.% Pt – 1 wt.% Ir/fMWCNTs-I catalyst *via* TEM, when it was noticed that several parts of the sample exhibited a “spotted” appearance. Given that these “spots” could actually be clusters of just a few metal atoms, more detailed STEM studies were subsequently performed. Tellingly, when these regions were analyzed *via* EDS, peaks corresponding to the deposited metals were observed. Figure 6.1 shows the TEM micrograph, the STEM micrograph (under contrast mode) and the EDS spectrum of one of these regions.

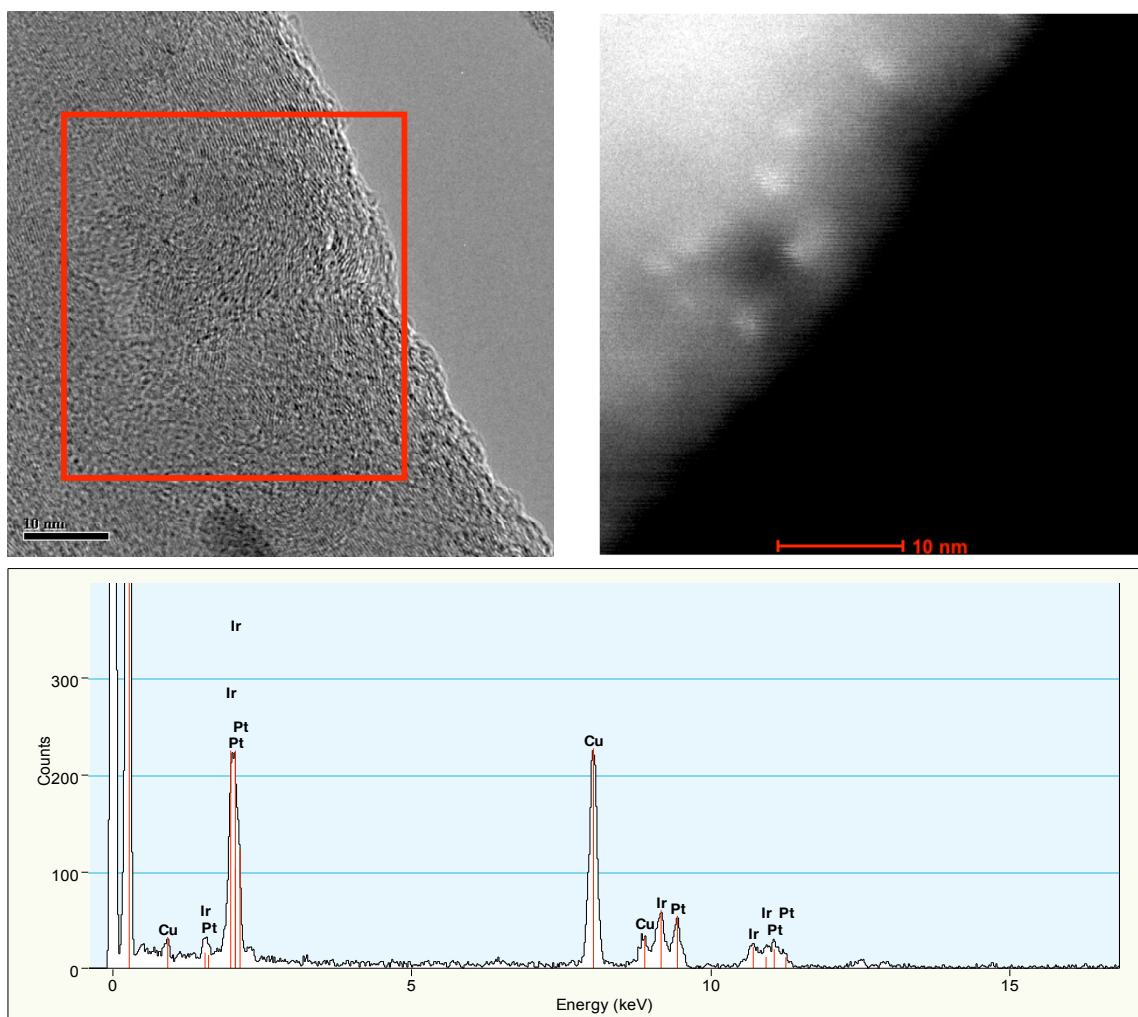


Figure 6.1. TEM micrograph of Pt-Ir/fMWCNTs-I (upper left), STEM (under contrast mode) micrograph of approximately the same region of the sample (upper right) and EDS spectrum showing peaks corresponding to both Pt and Ir (bottom).

These results confirm the presence of small metal clusters. However, whether these clusters were mono or bimetallic in the case of bimetallic catalysts had yet to be determined. In order to verify whether it is possible to establish the elemental composition of particles of approximately 1 nm in diameter by means of EDS, a 2 wt.% Pt/fMWCNTs-I catalyst was first analyzed *via* STEM-EDS. Figure 6.2 shows a STEM

micrograph of this sample, along with the energy-dispersive X-ray spectrum of the region indicated by the red square.

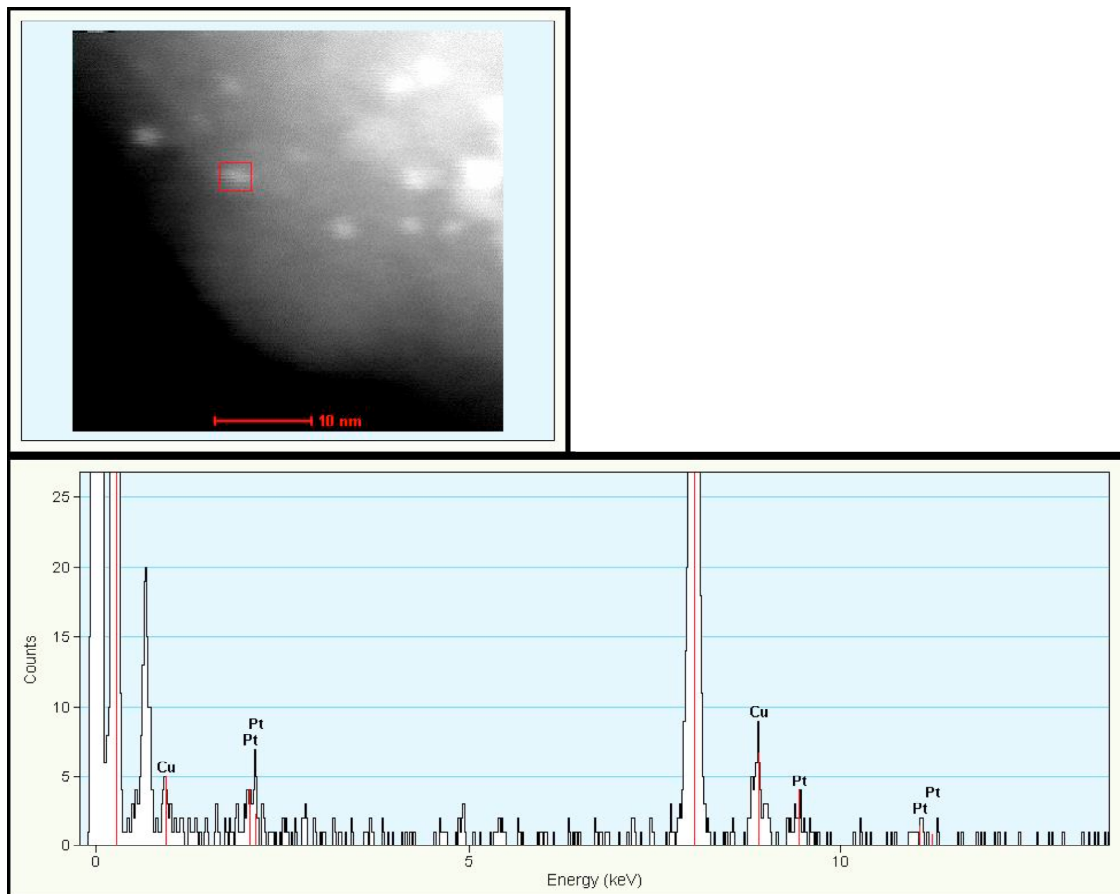


Figure 6.2. STEM micrograph of 2 wt.% Pt/fMWCNTs-I and EDS spectrum of the region highlighted in the micrograph.

This figure confirms that it is indeed possible to use STEM-EDS in order to determine the elemental composition of small particles (<2 nm), at least in monometallic catalysts. Thus, analyses were then focused on the 1 wt.% Pt – 1 wt.% Rh/fMWCNTs-I bimetallic catalyst. Figure 6.3 shows a STEM micrograph of this catalyst and the EDS spectrum of the highlighted region.

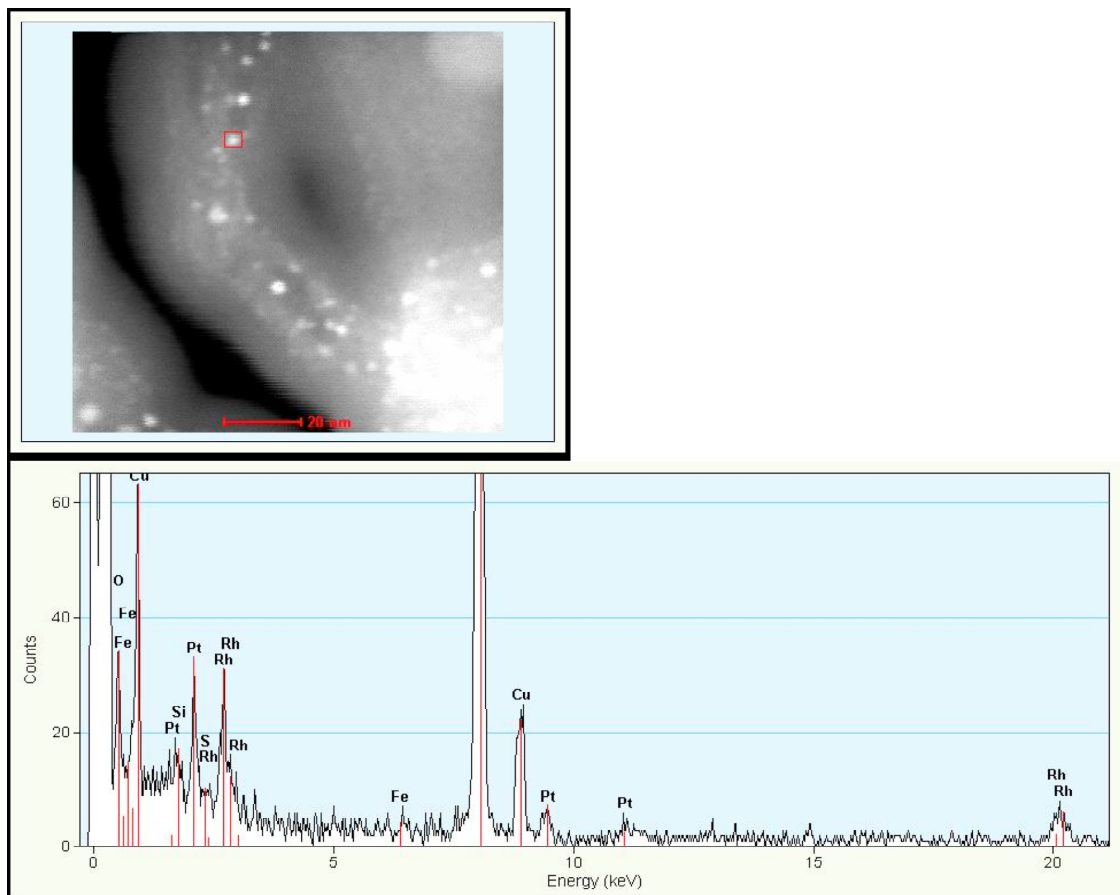


Figure 6.3. STEM micrograph of 1 wt.% Pt - 1 wt.% Rh/fMWCNTs-I and EDS spectrum of the highlighted region.

The figure confirms that for the Pt-Rh bimetallic catalysts, particles as small as 1 nm are true Pt-Rh alloys, which is consistent with the shape of the deNO_x curves shown by these formulations. However, given that TEM is not a bulk technique and that only a small number of bimetallic particles were analyzed, these results are not conclusive with respect to whether the Pt:Rh ratio is fixed at the stoichiometric value in all particles, as opposed to varying from one particle to the next. It is also worth noting that for the bimetallic catalysts, STEM observations are in agreement with the particle size distribution histograms determined from TEM data.

In the scientific literature, two main variables have been invoked when trying to rationalize the catalytic performance of Pt HC-SCR catalysts: metal dispersion and support acidity. Burch [47] and Demicheli [170] have both concluded that high metal dispersion leads to less active catalysts in terms of turnover frequencies (TOFs). However, Denton *et al.* [171] have shown that lower dispersions do not translate into higher NO_x conversions due to the fact that decreasing dispersion results in less (if more active) available sites. Thus, NO_x conversion seems to be independent of metal dispersion [66]. On the other hand, the acidity of the support has been found to be crucial to NO_x conversion and instrumental in the optimization of HC-SCR catalysts (see section 6.4.1 below).

As mentioned in the previous chapter, TEM-EDS measurements were also performed in an attempt to understand the influence of the catalyst preparation method on the performance of Na⁺-promoted MWCNTs-based catalysts. In general, two main features were observed in all Na⁺-containing samples: 1) large MWCNTs aggregates that, when analyzed *via* EDS, were shown to contain Pt and a significant amount of sodium, and 2) regions in which small bundles of MWCNTs (or even individual MWCNTs) resembling the appearance of sodium-free catalysts and confirmed to be free of sodium *via* EDS. Representative micrographs of these two types of regions in the 2 wt.% Pt – 10 wt.% Na/fMWCNTs-I catalyst are shown in Figure 6.4 and Figure 6.5, respectively.

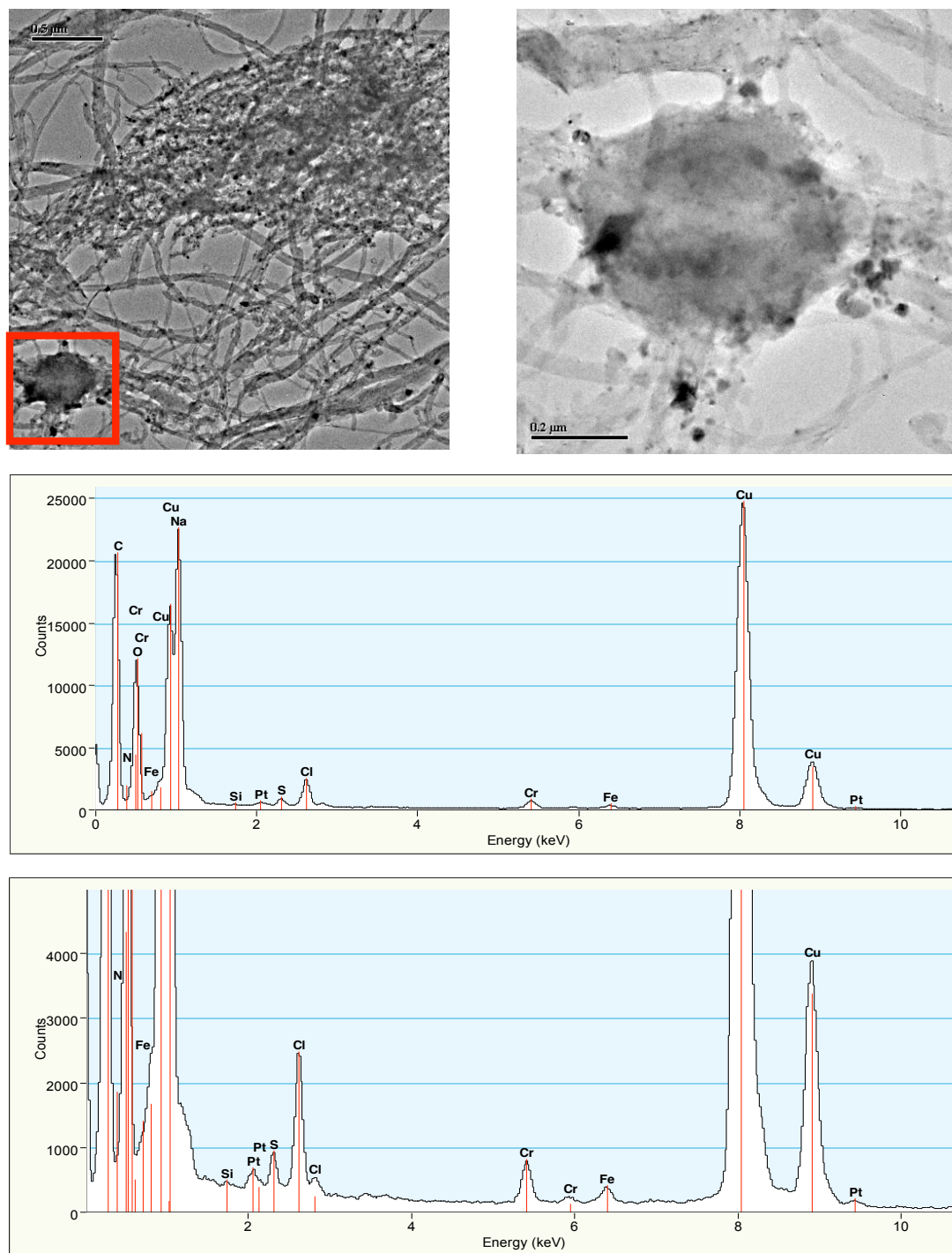


Figure 6.4. TEM micrograph of a region containing a MWCNTs aggregate (left) within a 2 wt.% Pt – 10 wt.% Na/fMWCNTs-I catalyst, a close-up of the highlighted area (right), EDS spectrum of the highlighted area (top) and a close-up of the low intensity peaks of the spectrum (bottom).

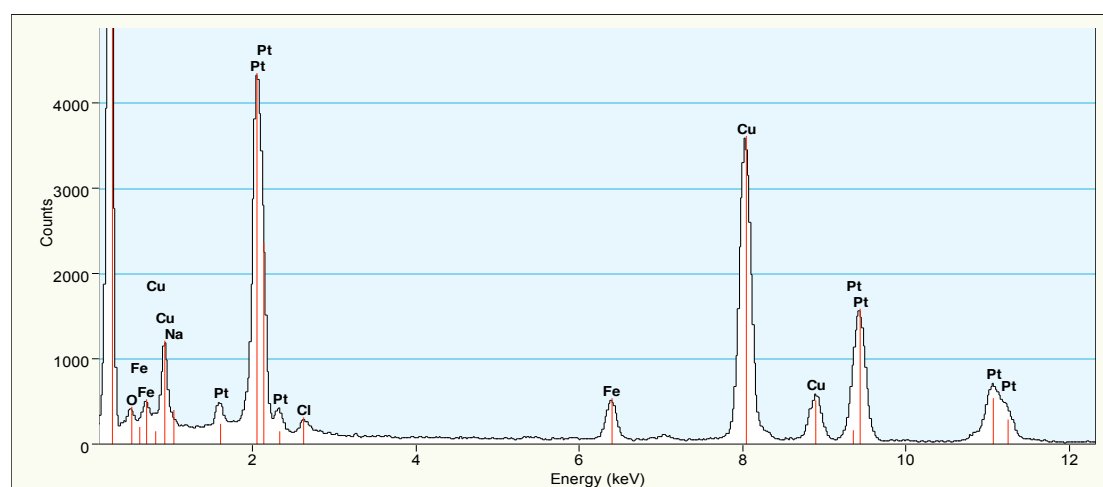
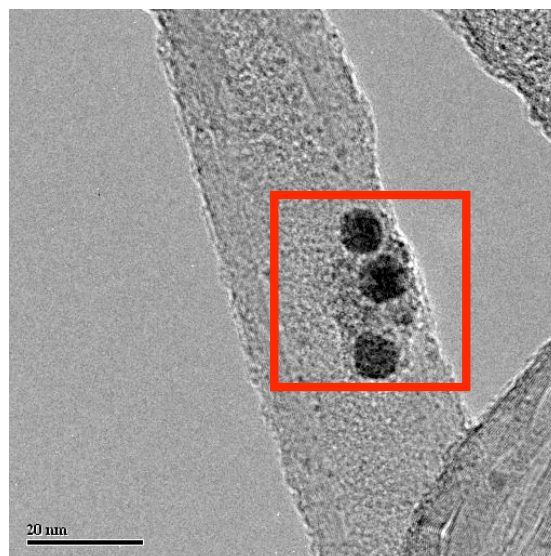


Figure 6.5. TEM micrograph of a region containing well dispersed MWCNTs within a 2 wt.% Pt – 10 wt.% Na/fMWCNTs-I catalyst and EDS spectrum of the highlighted area.

Since these two features were observed in all Pt-Na catalysts analyzed by TEM, the effect of the catalyst preparation method on catalyst performance cannot be explained on the basis of TEM data. There is also an apparent contradiction between the observations made with the electron microscope and the catalytic behavior of the 2 wt.% Pt – 10 wt.% Na/fMWCNTs-I catalyst: if indeed this catalyst has sodium-free regions, a higher selectivity towards N_2O , closer to the one observed for sodium-free catalysts, would be

expected. In fact, it can be argued that these sodium-free regions are actually a product of the TEM sample preparation method, in which the material is dispersed by bath sonication for 5 min in a volatile organic solvent; i.e., agglomeration of the Na⁺ phase may occur during this process. Consequently, an alternative sample preparation method was used in subsequent STEM experiments performed to further probe the effect of the preparation method on catalyst performance within Na⁺-promoted catalysts (see section 6.7 below).

6.4. TPD studies.

6.4.1. NH₃-TPD.

As shown in the preceding chapter, a degree of support acidity has been found to improve the deNO_x performance of MWCNTs-based HC-SCR formulations in two distinct ways: 1) by increasing the maximum NO_x conversion achieved by the catalysts; and 2) by decreasing the temperature at which this maximum is reached.

This phenomenon has previously been observed for HC-SCR formulations with oxidic and carbonaceous supports by other authors, most notably García-Cortés *et al.* [29]. These workers, based on results of Mass Spectroscopy - Temperature Programmed Desorption (MS-TPD) experiments in which C₃H₆ was used as the probe molecule, suggested that support acidity impacts hydrocarbon oxidation, which in turn determines the level of activity and the temperature window for the deNO_x reaction. This appears to be consistent with the results of Niwa *et al.* These authors, through ammonia MS-TPD measurements, found that Brønsted acid sites play an important role in the cracking of hydrocarbons [201-203].

Thus, the MS-TPD of NH₃ was performed on pristine and functionalized MWCNTs in an effort to probe their acidity. The results of these experiments are shown in Figure 6.6.

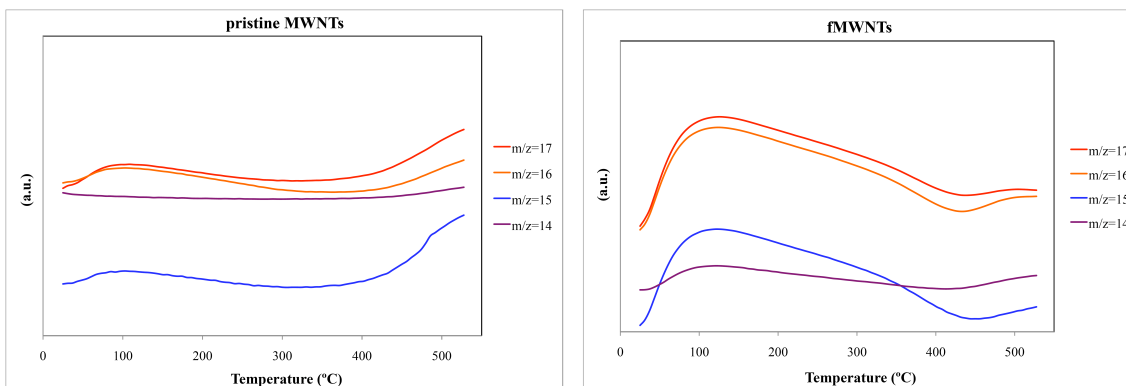


Figure 6.6. NH₃-MS-TPD profiles of pristine MWCNTs (left) and fMWCNTs (right).

Although these measurements are qualitative, the considerably higher maximum shown by the main NH₃-desorption peak on fMWCNTs clearly shows that fMWCNTs contain more acid sites than pristine MWCNTs. Further, it seems that the acid sites on fMWCNTs are slightly stronger, judging from the temperature at which the main NH₃-desorption peak shows its maximum (~115 °C for fMWCNTs vs. ~100 °C for pristine MWCNTs). Since increased acidity is believed to promote the cracking of the hydrocarbon and the temperature at which HC-SCR catalysts display their NO_x conversion maxima is known to be coupled to hydrocarbon light-off, the higher acidity of fMWCNTs with respect to MWCNTs can explain why 2 wt.% Pt/fMWCNTs shows a higher NO_x conversion maximum at lower temperatures than 2 wt.% Pt/MWCNTs.

6.4.2. C₃H₆-TPD.

Given that the adsorption of the hydrocarbon is a pre-requisite for combustion, these acidity studies were complemented with C₃H₆-TPD measurements on fMWCNTs-based catalysts. This was done in an attempt to investigate whether the use of a 3:1 Pt-Rh alloy as the active phase improves HC-SCR activity *via* enhancing the adsorption of C₃H₆ (without taking the latter to a regime in which the catalysts is poisoned by the hydrocarbon). Indeed, catalysts with a higher Pt:Rh ratio seem to be prone to some degree of deactivation, judging from their decreased NO_x conversion maximum and from the shift of T_{max} (which is coupled to the hydrocarbon light-off) to higher temperatures.

Further, C₃H₆-TPD measurements were also performed on bare supports (MWCNTs and fMWCNTs) for comparison purposes. On one hand, a comparison between the C₃H₆-TPD of fMWCNTs and PGMs/fMWCNTs could potentially provide information concerning different adsorption sites (the support vs. the metal), whereas a comparison between the C₃H₆-TPD and the NH₃-TPD of the bare supports could provide valuable information with respect to the inherent acidity of the carriers. The latter is particularly important, since Lercher and co-workers have concluded that acidity measurements are dependent on the probe molecule used [204].

Figure 6.7 shows the MS signals corresponding to both molecular and fragmentation species observed during C₃H₆-TPD on representative PGMs/MWCNTs catalysts, as well as on the bare MWCNTs and fMWCNTs supports. In order to account for the fragmentation of propene inside the mass spectrometer, three masses with perfectly differentiated signal contributions were chosen to represent molecular propene ($m/z=40$, 41 and 42) and the same was done to represent fragmentation species ($m/z=26$, 27 and 29).

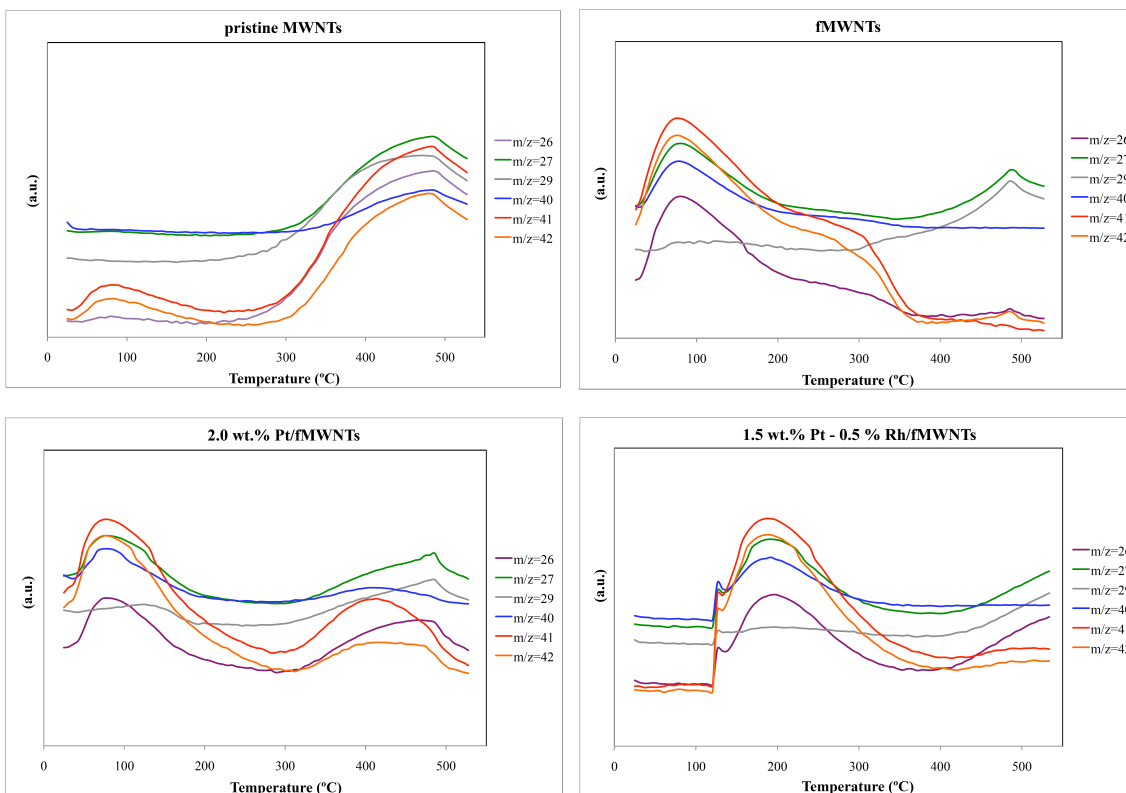


Figure 6.7. C_3H_6 -MS-TPD profiles of pristine MWCNTs (top left), fMWCNTs (top right), 2 wt.% Pt/fMWCNTs (bottom left) and 1.5 wt.% Pt – 0.5 wt.% Rh/fMWCNTs (bottom right).

From the figure, it appears that propene and/or oligomers of propene are strongly adsorbed on pristine MWCNTs (these species desorbing at temperatures in excess of 300 °C), although a small amount of weakly adsorbed species is also observed. In contrast, the adsorption of weakly bound propene seems to be favored on fMWCNTs, which also show the ability to strongly adsorb a small amount of the alkene. In effect, pristine MWCNTs seem to be able to form stronger surface-adsorbate bonds with propene and propene-derived species than fMWCNTs. Arguably, the reason for the latter is the very effective π - π stacking that the aromatic outer wall of MWCNTs is known to establish with unsaturated species [205-207], which appears to be disrupted when the MWCNTs are functionalized.

When the profiles shown by fMWCNTs and 2 wt.% Pt/fMWCNTs are compared, it seems clear that adsorption takes place both on the metal and on the support, judging from the strongly adsorbed species (whose desorption occurs above 300 °C) which are present on Pt/fMWCNTs and absent on fMWCNTs.

Tellingly, a comparison between the TPD profiles shown by 2 wt.% Pt/fMWCNTs and 1.5 wt.% Pt – 0.5 wt.% Rh/fMWCNTs clearly indicates that stronger adsorption complexes are produced on the bimetallic catalyst. All experimental conditions being identical, the reason for this can be safely attributed to the presence of Rh and to its unique ability to strongly adsorb propene and propene-derived species. This unique ability of Rh is also indicated by a comparison between the C₃H₆-TPD profiles of the 3:1 Pt-Rh/fMWCNTs catalyst with those of the bare fMWCNTs support. Indeed, the temperature at which the desorption of the most weakly bound species reaches its maximum shifts by more than 100 °C to higher temperatures on the bimetallic catalyst, a phenomenon not seen on the monometallic formulation.

Furthermore, it appears to be the case that the metal represents the main site from which adspecies desorb in the alloy catalyst. The latter is evidenced by the absence in the 3:1 Pt-Rh/fMWCNTs TPD profiles of the desorption peaks with maxima at approximately 100 °C shown by fMWCNTs. If adspecies desorbed from both the support and the metal, the resulting TPD profiles would show two distinct peaks with maxima around 100 and 200 °C. It seems to be the case that although adsorption takes place both on the carrier and on the catalytically active phase, support adspecies tend to migrate to the metal (the shoulder shown by the desorption peak of the bimetallic catalysts may be indicative of adspecies in the metal-support interface). Arguably, this reverse spillover of propene (which has been proposed previously by García-Cortés *et al.* for Pt-based HC-SCR catalysts [29]), coupled to the ability of Rh to strongly adsorb C₃H₆, causes a higher concentration of hydrocarbonaceous species to be present on the bi-metallic catalyst at the temperature of maximum NO_x conversion (200 °C), which in turn may account for the improved deNO_x performance shown by 1.5 wt.% - 0.5 wt.% Rh/fMWCNTs with respect to 2 wt.% Pt/fMWCNTs. This is consistent with the less than ideal performance of the 1 wt.% Pt –

1 wt.% Rh/fMWCNTs (in which the high Rh loading appears to take the hydrocarbon adsorption to a regime in which deactivation starts being observed). Parenthetically, an analogous deactivation mechanism has been proposed for Pt/Ba/Al₂O₃ NO_x storage-reduction traps, in which NO_x desorbed from the support and the Ba phase was determined to undergo reverse spillover onto the Pt surface, effectively inhibiting the oxidation of propene and increasing the light-off temperature for CO₂ production [208].

Finally, the similarities between the C₃H₆-TPD and the NH₃-TPD profiles of the bare supports confirm that fMWCNTs are more Brønsted acidic than MWCNTs, independent of the probe molecule used.

6.5. XPS studies.

An additional factor which may influence the NO_x reduction activities of supported metal catalysts, but which to date has not been widely considered, is the oxidation state of the metal. Given that a more reduced PGM surface displays a lower amount of oxygen adatoms (and thus a higher amount of available Pt sites on which NO_x and C₃H₆ can adsorb), catalysts in which the metal is kept in a more metallic state are expected to exhibit improved deNO_x performance. Therefore, in this work four representative catalysts (2 wt.% Pt/Al₂O₃, 2 wt.% Pt/MWCNTs, 2 wt.% Pt/fMWCNTs and 1.5 wt.% Pt – 0.5 wt.% Rh/fMWCNTs) were analyzed *via* XPS in order to investigate the electronic state of the metals present. It is well known that as Pt particles become smaller, they show an increasing tendency to exist as the oxide, PtO. Thus, two different binding energies were expected in the X-ray photoelectron spectrum of each catalyst: 1) for large particles (>1 nm), a binding energy corresponding to Pt in its metallic state (Pt⁰); and 2) for small particles (<1 nm), a binding energy corresponding to PtO (Pt²⁺) [209]. Unfortunately, the total metal loadings of the catalysts proved to be too low for XPS to quantify the amount of Pt present in each oxidation state. Consequently, model catalysts with higher metal loadings were prepared and analyzed.

Given that the metal particle size can greatly influence the degree of PtO formation, the metal dispersions of catalysts between which a comparison is to be made should be as

close as possible. Therefore, as a first step, a metal loading was chosen which would allow similar dispersions on MWCNTs, fMWCNTs and Al₂O₃ supports. Three Pt/Al₂O₃ reference catalysts with different loadings (5 wt.%, 10 wt.% and 20 wt.%) were prepared (by impregnation) and their loadings were confirmed by XRF. Table 6.1 shows the metal dispersion and average Pt particle size of the catalysts, determined *via* H₂-chemisorption, and compares them with the 2 wt.% Pt/Al₂O₃ formulation.

Table 6.1. Metal dispersion and average particle size of model Pt/Al₂O₃ reference catalysts.

Catalyst	Dispersion (%)	Average particle size (nm)
2 wt.% Pt/Al ₂ O ₃	100.0	1.0
5 wt.% Pt/Al ₂ O ₃	77.7	1.5
10 wt.% Pt/Al ₂ O ₃	57.4	2.1
20 wt.% Pt/Al ₂ O ₃	14.8	8.0

Taking these values into account, and the fact that for MWCNTs-based catalysts the average particle size is consistently close to 2.0 nm, the 10 wt.% total metal loading was chosen and three representative catalysts (Pt/MWCNTs, Pt/fMWCNTs and 3:1 Pt-Rh/fMWCNTs) were prepared *via* impregnation targeting this loading. The particle size distribution histograms of these three MWCNTs-based catalysts, along with that of the Al₂O₃-supported catalyst (all shown in Figure 6.8), were then obtained by means of TEM.

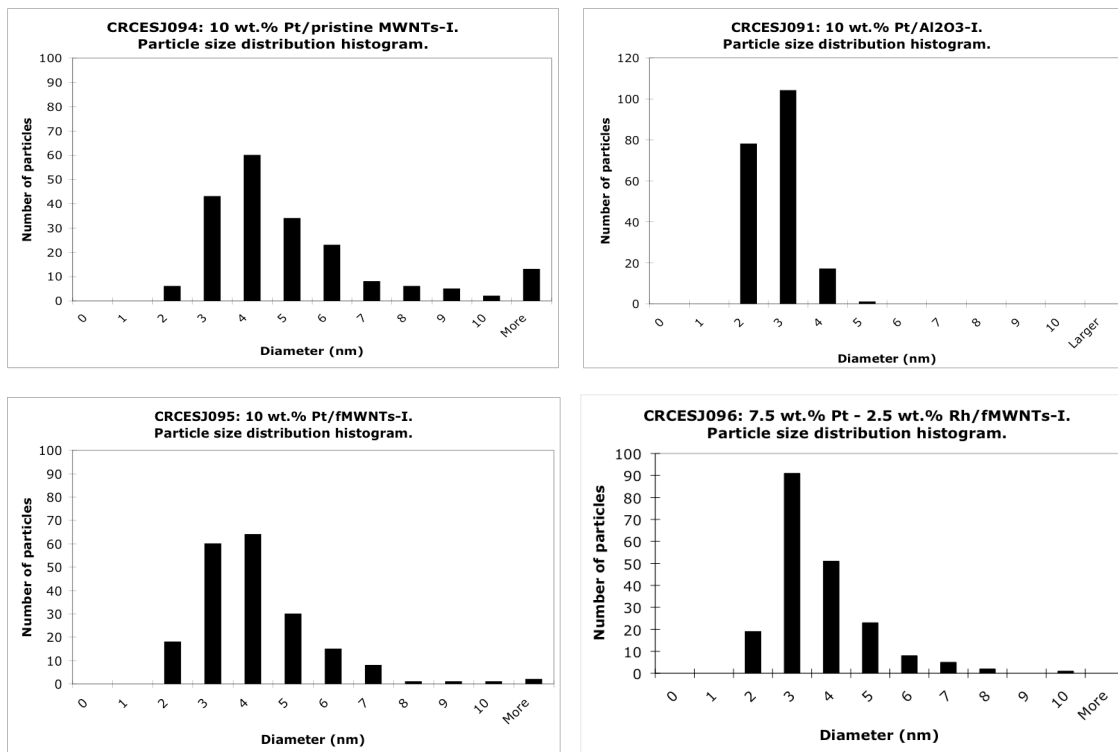


Figure 6.8. Particle size distribution histograms for 10 wt.% Pt/Al₂O₃ (top left), 10 wt.% Pt/MWCNTs (top right), 10 wt.% Pt/fMWCNTs (bottom left) and 7.5 wt.% Pt – 2.5 wt.% Rh/fMWCNTs (bottom right) (200 particles measured per histogram).

As can be seen from Figure 6.8, all the particle size distribution histograms have their maxima in the 3-5 nm range. This validated the use of these catalysts for the XPS studies, which were subsequently carried out at an outside laboratory (RBD Enterprises, Bend, OR). Figure 6.9 shows an expanded view of the Pt 4d region in the XPS spectrum of the 10 wt.% Pt/Al₂O₃ reference catalyst.

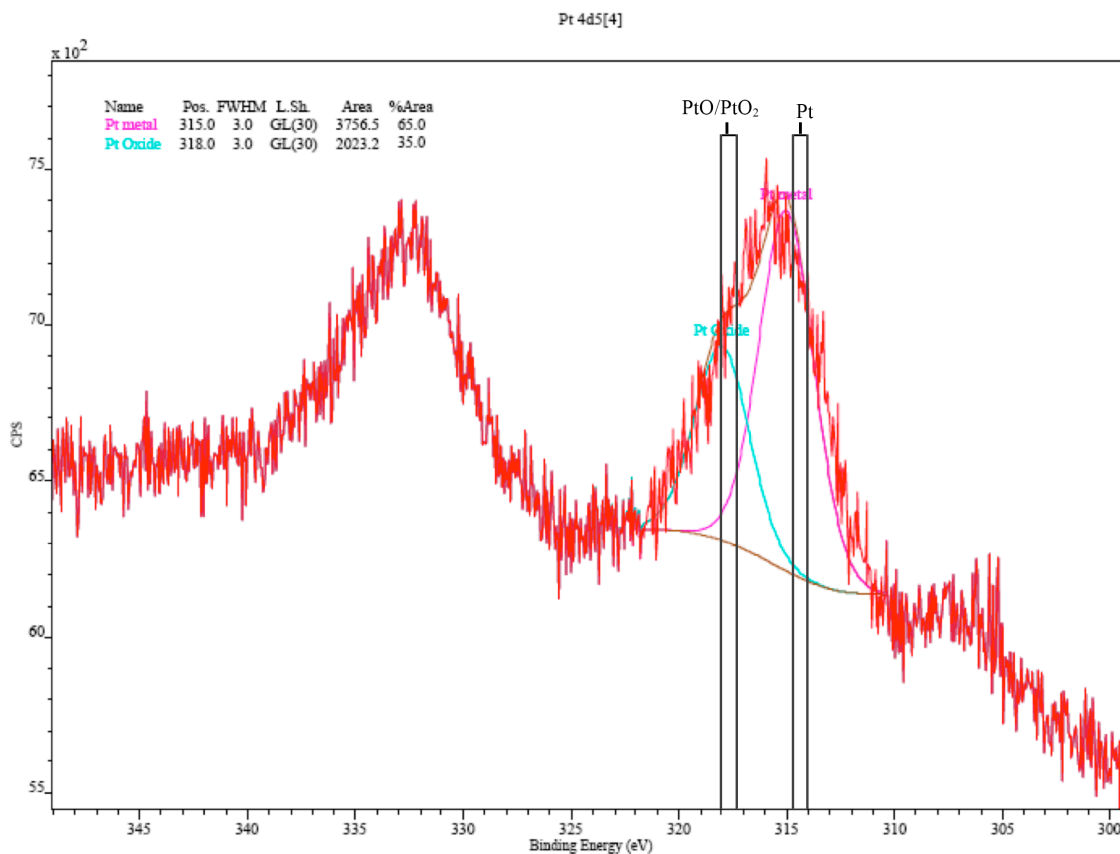


Figure 6.9. Expanded view of the Pt 4d region in the XPS spectrum of the 10 wt.% Pt/Al₂O₃ reference catalyst. The ranges shown in the spectrum correspond to those of the Pt 4d_{5/2} peak (right peak in the spectrum) as reported in the X-ray Photoelectron Spectroscopy Database of the National Institute of Standards and Technology (NIST) [140].

Given that analysis of the main Pt peak (4f) was rendered impractical due to interference from the Al 2p peak, peak fitting was performed on the Pt 4d_{5/2} peak. As shown in Figure 6.9, the resulting fit indicates that approximately two-thirds of the analyzed Pt is in the metallic form while the remaining third is present as the oxide. Given the low signal intensity of this peak, the fitting results should be viewed with caution. Nevertheless, they provide a clear indication that a considerable fraction of the Pt is present in the oxidized form when alumina is used as the support.

Figure 6.10 compares the Pt 4f peak of Pt/MWCNTs, Pt/fMWCNTs and 3:1 Pt-Rh/fMWCNTs.

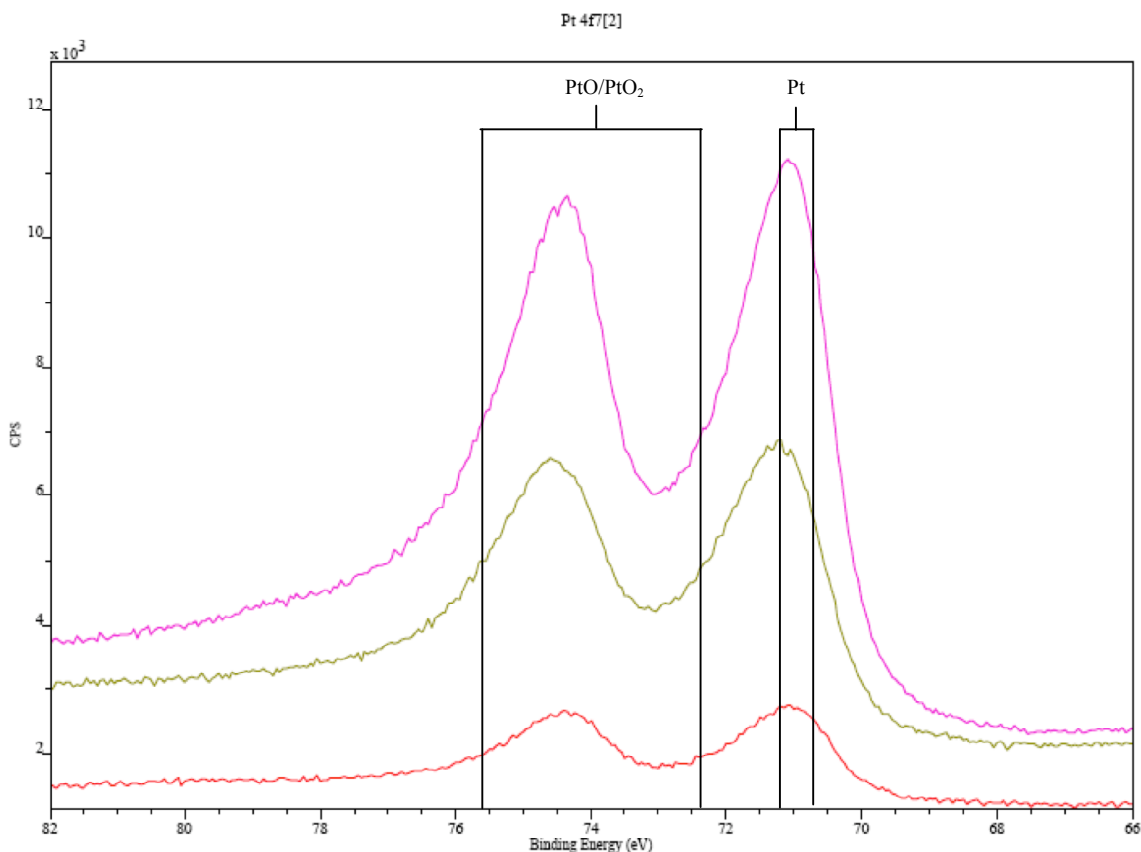


Figure 6.10. Combined plot showing an expanded view of the Pt 4f region in the XPS spectra of 10 wt.% Pt/fMWCNTs (top), 7.5 wt.% Pt – 2.5 wt.% Rh/fMWCNTs (middle) and 10 wt.% Pt/MWCNTs (bottom) catalysts. The ranges shown in the spectrum correspond to those of the Pt 4f_{7/2} peak (right peak in the spectrum) as reported in the X-ray Photoelectron Spectroscopy Database of the National Institute of Standards and Technology (NIST) [140].

As can be seen from the figure, the intensity of the peaks, which represents the amount of Pt analyzed, follows the order Pt/fMWCNTs > Pt-Rh/fMWCNTs > Pt/MWCNTs. Taking into account that XPS is typically only able to analyze the 4-5 outermost atomic layers within a sample, this ordering is consistent with the metal dispersions in the catalysts as

indicated by TEM. Further, in all cases the fitting of the $4f_{7/2}$ peak (the right peak in the spin-orbit doublets in Figure 6.10 for which the binding energy ranges are shown) indicated the presence of very little platinum oxide, if any at all (estimated at $\leq 5\%$ for each catalyst). This seems to be in agreement with the rationalization concerning the improved deNO_x activity shown by MWCNTs-based catalysts compared to the activities shown by catalysts with oxidic supports; namely, that Pt is kept in a more reduced state in the former.

To further ensure that the oxidation state of the metal is indeed a support effect and not a particle size effect, the XPS analysis of an Al₂O₃-based catalyst with a considerably lower metal dispersion was performed. A 20 wt.% Pt/Al₂O₃ catalyst was prepared, having a metal dispersion of $\sim 15\%$ according to H₂-chemisorption. In contrast, the three original model catalysts were determined to have dispersions of $\sim 60\%$ by the same method. Reassuringly, when the 20 wt.% Pt/Al₂O₃ catalyst was analyzed *via* XPS, its spectrum (not shown) appeared to be very similar to that of the original 10 wt.% Al₂O₃-based model catalyst; i.e., *ca.* one-third of the Pt was present as the oxide. This corroborates the hypothesis that MWCNTs stabilize the metal in a more reduced state, a desired effect given that metallic Pt is believed to be the active phase in the HC-SCR reaction.

Given that the amount of PtO is too low to be quantified in all MWCNTs-based catalysts, the XPS results also suggest that the effect that both Rh and the use of MWCNTs versus fMWCNTs have on the oxidation state of Pt is either negligible or nil.

Finally, it is important to mention that during the preparation of the alumina-based formulations, the metal precursor was decomposed to Pt metal by the calcination (under air) of the green catalysts at 400 °C for 2.5 hours. This is in contrast to the way in which Pt metal particles were produced when MWCNTs were used as the catalyst support (reduction under 10 % H₂ in He at 350 °C for 3.5 hours). In order to probe whether the preparation method had any influence in the oxidation state of the metal, a 10 wt.% Pt/Al₂O₃ model catalyst was prepared by a method involving sequential impregnations followed by H₂ reduction. After confirming its Pt loading by means of XRF and

determining its average Pt particle size to be ~ 2.0 nm by means of H_2 chemisorption, this model catalyst was analyzed by XPS. Figure 6.11 shows an expanded view of the Pt 4f and the Al 2p region in the XPS spectrum of the 10 wt.% Pt/ Al_2O_3 catalyst prepared with H_2 reduction.

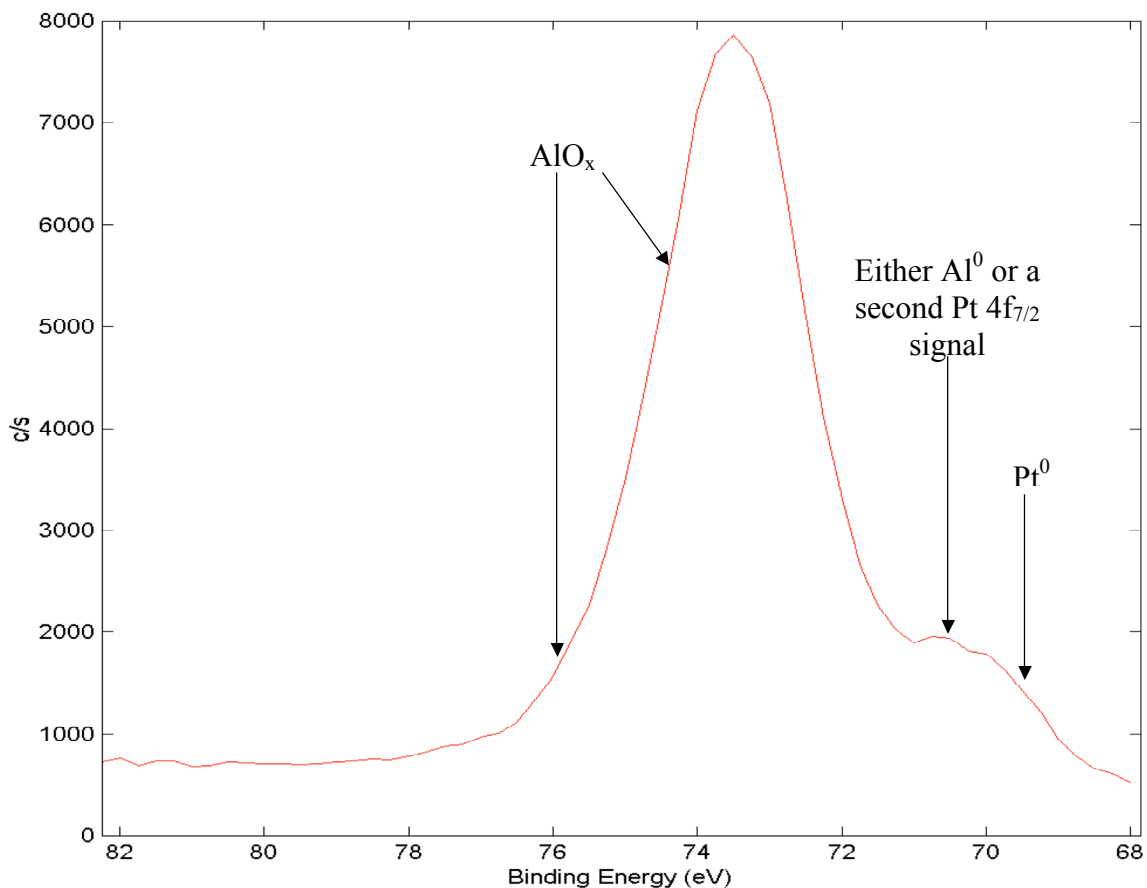


Figure 6.11. Expanded view of the Pt 4f and the Al 2p region in the XPS spectrum of 10 wt.% Pt/ Al_2O_3 prepared by impregnation followed by H_2 reduction.

As shown in Figure 6.11, besides proving the presence of both metallic Pt and oxidized Al, the Pt 4f / Al 2p signal provides evidence for either another form of Pt or the presence of metallic Al. Given the unlikelihood of Al being present in the metallic form, XPS suggests that at least a fraction of the Pt is oxidized. Peak fitting of the Pt 4d_{5/2} signal (not

shown) also suggests the presence of two different forms of Pt; however, the results proved less than conclusive due to the rather symmetric nature of the peak. Consequently, X-ray Absorption Near Edge Structure (XANES) measurements on catalysts whose preparation included a H₂-reduction step were performed at Brookhaven National Laboratory, with the aim of further probing the effect of the support on the Pt oxidation state.

6.6. X-ray Absorption Fine Structure (XAFS) studies.

In an attempt to further probe the effect of the catalyst support on the oxidation state of Pt, XANES studies were performed on three representative samples, namely 2 wt.% Pt/fMWCNTs, 1.5 wt.% Pt – 0.5 wt.% Rh/fMWCNTs and 2 wt.% Pt/Al₂O₃. All three samples were prepared by the same method (impregnation followed by H₂-reduction) and determined to have comparable metal dispersions (~66 %) in order to ensure that the oxidation state of the metal was solely dependent on the catalysts support. In scouting experiments, the catalysts were re-reduced *in situ* under a flow of 25 % H₂ in He at 300 °C for 30 min prior to XANES measurements. The results of these studies (summarized in Table 6.2) indicate that a higher fraction of Pt is in the reduced state in the alumina-supported formulation.

Table 6.2. XANES quantification of Pt present in different oxidation states (% of total Pt analyzed) calculated using a linear combination of reference spectra for Pt⁰ (Pt foil) and Pt(II) (Pt(acac)₂) to fit the sample spectra over the range 11.535 – 11.615 keV. No contribution for Pt(IV) (PtO₂) was observed.

Sample	Pt ⁰	Pt ²⁺
2 wt.% Pt/fMWCNTs	76.7	23.3
1.5 wt.% Pt – 0.5 wt.% Rh/fMWCNTs	89.6	10.4
2 wt.% Pt/Al ₂ O ₃	95.9	4.1

Although these results seems to be in direct disagreement with those of XPS measurements which have suggested Pt to be more reduced in MWCNTs-supported catalysts (*vide supra*), the inconsistency can be attributed to the reduction step performed

before XANES analyses (no such step was taken prior to XPS measurements). Therefore, XAFS studies under an oxidative atmosphere closely resembling that found under real HC-SCR operating conditions (10 % O₂) were deemed necessary in order to effectively use this technique to investigate the effect of the catalyst support on the oxidation state of Pt. Unfortunately, the execution of the latter studies was scheduled past the deadline for the submission of this dissertation, and thus the results were unavailable at the time the document was finalized.

6.7. Elemental mapping.

A set of elemental maps were acquired in order to gain further understanding of the most promising catalyst compositions identified in this work; i.e., the 1.5 wt.% Pt – 0.5 wt.% Rh/fMWCNTs and the 2 wt.% Pt – 10 wt.% Na/fMWCNTs catalysts. To this end, the samples were first imaged with the electron microscope under the transmission mode to find representative regions. Once this was done, the microscope was switched to the scanning transmission mode under which the chosen region was simultaneously scanned and analyzed *via* EDS. After the scan was complete, the raw data were processed into intensity maps in which the brightness of a given pixel corresponds to the concentration of a particular element in that region of the sample.

For the 1.5 wt.% Pt – 0.5 wt.% Rh/fMWCNTs catalyst, the main focus was on determining the location of Pt and Rh with respect to each other. Figure 6.12 shows the carbon, platinum and rhodium maps of a 1.5 wt.% - 0.5 wt.% Rh/fMWCNTs catalyst, along with the STEM micrograph in which the mapped region is highlighted, and a composite image of the three elemental maps.

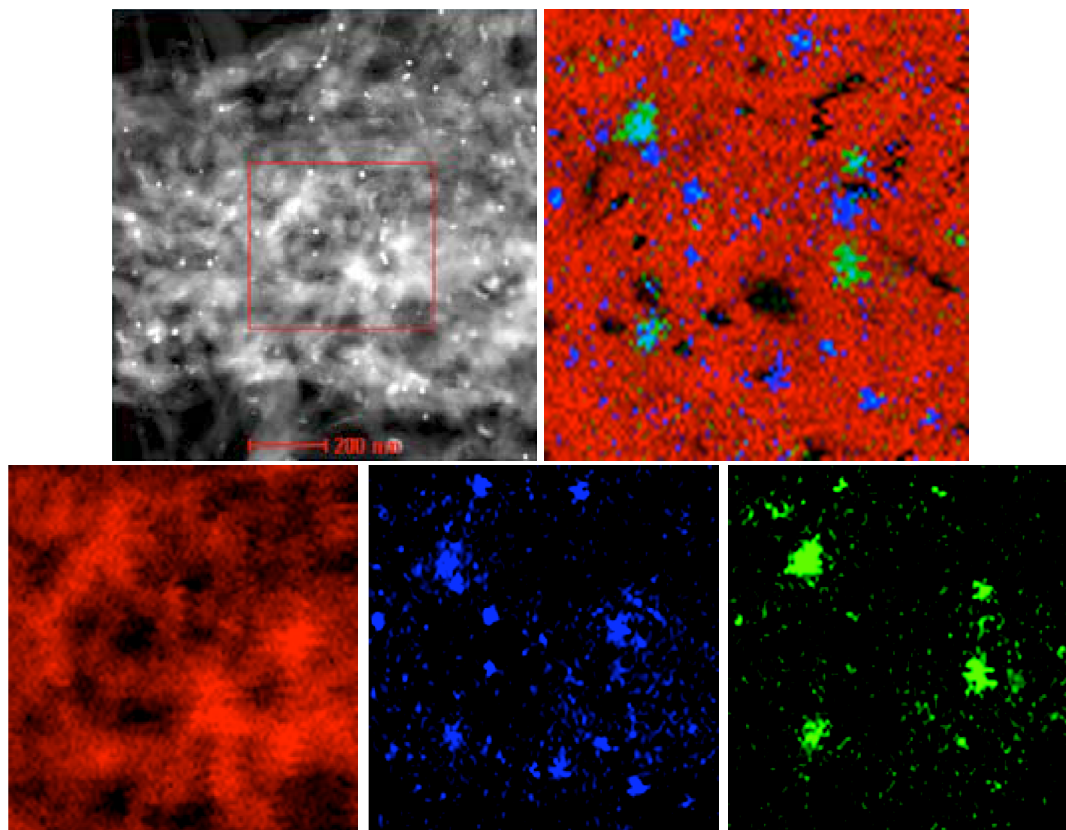


Figure 6.12. STEM micrograph (top row, left) of a 1.5 wt.% Pt – 0.5 wt.% Rh/fMWCNTs catalyst; elemental maps (bottom row) for carbon (red), platinum (blue) and rhodium (green); and a composite image of all three elemental maps (top row, right). The maps were taken from the highlighted region in the STEM micrograph.

Both the shape of the activity curves and previously executed STEM-EDS analyses (*vide supra*) have suggested Pt and Rh to be truly alloyed (even in particles as small as 2 nm) and, as can be seen in the figure, this fact was confirmed in the bulk material by an elemental map taken of a region of $\sim 1 \mu\text{m}^2$. In order to correctly interpret these elemental maps, it is important to remember that a transmission electron microscope compresses a three-dimensional space into a two-dimensional image. Therefore, superimposed small precious metal particles should not be mistaken to be a single large particle. As can be seen in Figure 6.12, there are both Pt-rich and Rh-rich regions in the bulk material; i.e.,

the distribution of these two metals throughout the support is not homogeneous. This is unsurprising, given the preparation method of this bimetallic catalyst. Indeed, the latter makes it reasonable to expect the resulting metal particles to cover the entire spectrum of Pt:Rh ratios.

For the 2 wt.% Pt – 10 wt.% Na/fMWCNTs catalyst, emphasis was placed on determining the location of Pt and Na with respect to each other in an effort to rationalize the crucial effect that the preparation method exerts on catalyst performance. Figure 6.13 summarizes the three different preparation methods used to synthesize the 2 wt.% Pt – 10 wt.% Na/fMWCNTs catalyst, along with a STEM micrograph in which the mapped region is highlighted, and the corresponding carbon, platinum, and sodium elemental maps.

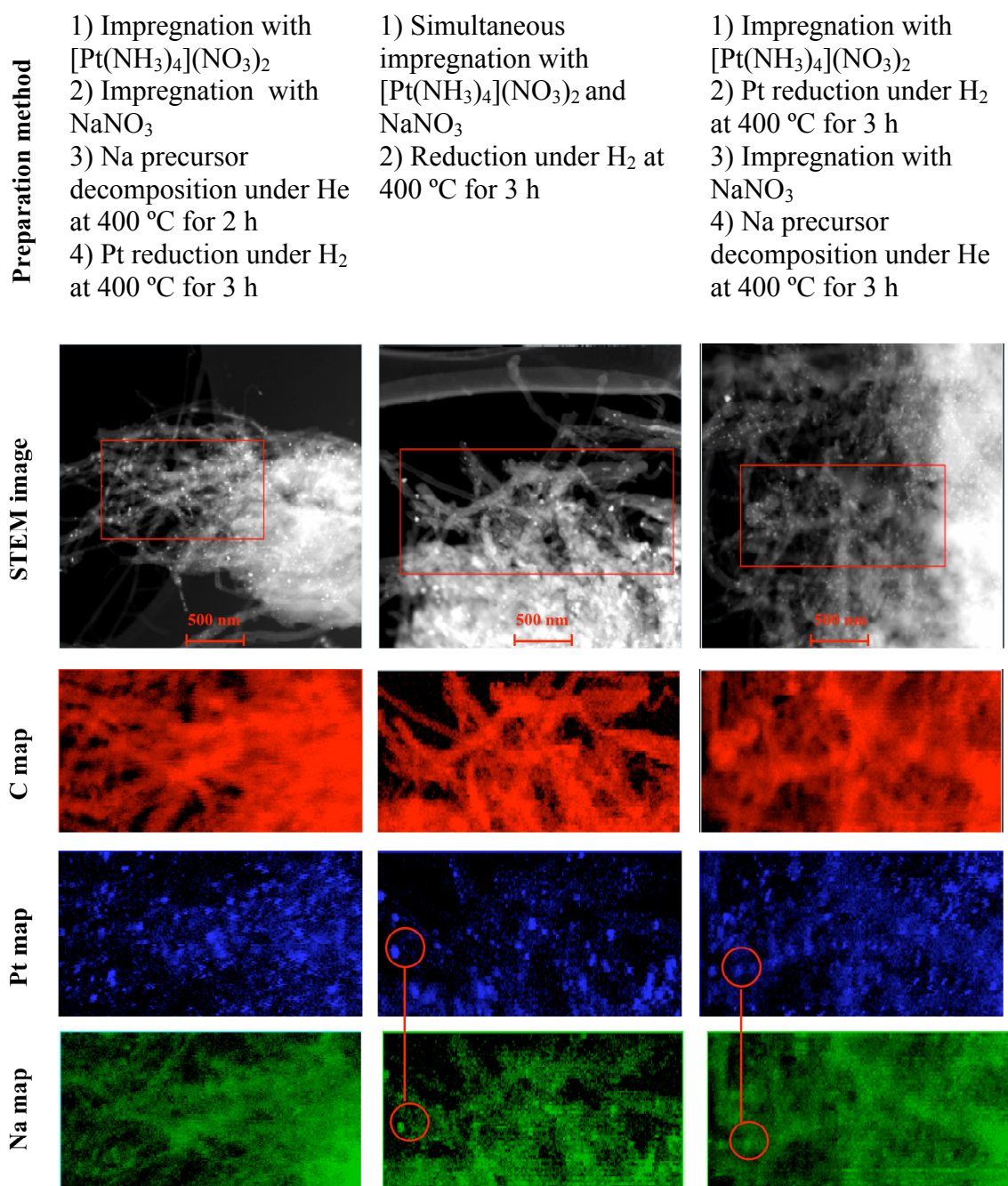


Figure 6.13. Carbon, platinum and sodium maps of three 2 wt.% Pt – 10 wt.% Na/fMWCNTs catalysts prepared by different preparation methods (the mapped region corresponds to the highlighted rectangles in the STEM micrographs).

In past TEM-EDS experiments, parts of the sample containing well-dispersed MWCNTs appeared to be Na-free. Given that this may have resulted from the use of a sample preparation method involving the dispersion of the sample in an organic solvent, this time a dry-mounting technique was used to load the sample onto the TEM grid (a less invasive method). Further, to ensure that the mapped regions were representative, the analyzed regions contained both well-dispersed MWCNTs and bulk-like material (as highlighted by the red rectangles on the STEM micrographs in Figure 6.13).

Taking into account that the catalyst represented by the left column (henceforth sample A) was the only one showing promising performance, the maps were analyzed in an effort to rationalize the observed differences in catalyst properties. Comparing the Pt map in the left column with that in the middle column (henceforth sample B), the former seems to have a better Pt dispersion than the latter. Indeed, given that Na^+ was present in large excess, simultaneous impregnation should lead to most of the ion exchange sites on the fMWCNTs support being occupied by Na^+ , which would be expected to result in a poor Pt dispersion. Thus, impregnating Pt before Na leads to a superior Pt dispersion, which might explain the improved deNO_x activity of the resulting catalyst.

Another feature of note is that the Na map in the right column (henceforth sample C) shows areas of high Na concentration that seem to match the location of Pt in the corresponding Pt map. This may explain the improved performance of sample A with respect to that represented by sample C, given that one could argue that carrying out sodium precursor impregnation/decomposition after Pt impregnation/reduction would cause Pt to be covered by a layer of Na^+ , which might deactivate the Pt. Interestingly, this Pt-Na match is also observed in sample B, while it appears to be absent from sample A. With regards to the manner in which such deactivation might occur, two explanations are offered: 1) a Na coating would prevent the HC-SCR reactants from reaching the Pt surface; and 2) due to the close location of the metals with respect to one other, the promoting effect of Na^+ in the inactive catalysts may be considerably higher than that in the active catalyst. Indeed, several authors have established that the Na-loading window

in which promotional effects are observed is fairly narrow, since the sodium loading has to be sufficiently high to enhance NO adsorption, while ensuring that oxygen adsorption is not taken to a regime at which the catalyst is poisoned [184,185]. The latter may be occurring in the catalysts that show poor deNO_x activity.

XPS studies were subsequently performed at an outside laboratory (EAG, Sunnyvale, CA) in an attempt to determine the reason behind the lack of activity shown by samples B and C. Indeed, in the inactive catalysts, XPS should either show the catalyst surface to be enriched with Na (if deactivation occurred *via* the coating of Pt with Na) or a change in the Pt binding energy (if deactivation was caused by the proximity of the metals). The results of these measurements are shown in Tables 6.3 and 6.4.

Table 6.3. Atomic concentrations (%) determined *via* XPS.

Sample	C	N	O	F	Na	S	Cl	Pt
A	82.7	0.4	8.7	0.5	7.4	<0.1	<0.1	0.09
B	83.6	0.4	8.3	0.5	6.9	0.1	<0.1	0.10
C	75.8	0.5	12.6	0.6	10.4	<0.1	<0.1	0.09

Table 6.4. XPS quantification of Pt present in different oxidation states (% of total Pt analyzed) calculated from Pt 4f peak fitting.

Sample	Pt ⁰	Pt in intermediate state	PtO
A	10	58	32
B	7	47	46
C	7	54	39

Although these XPS results do not show the surface concentration of Na to be consistently higher in the inactive catalysts (see Table 6.3), the chemical state of Pt in the different samples is particularly interesting. First, it seems clear that the presence of Na causes a significant fraction (>30 %) of Pt to be present in the form of PtO; as stated above, in Na-free MWCNTs-based catalysts the amount of Pt oxides has been determined to be <5 %. Further, XPS peaks at binding energy values intermediate between that of Pt metal and PtO have been found to be the most prominent feature in the XPS spectra of Na-promoted catalysts (see Table 6.4). Figure 6.14 is shown as an example of the latter.

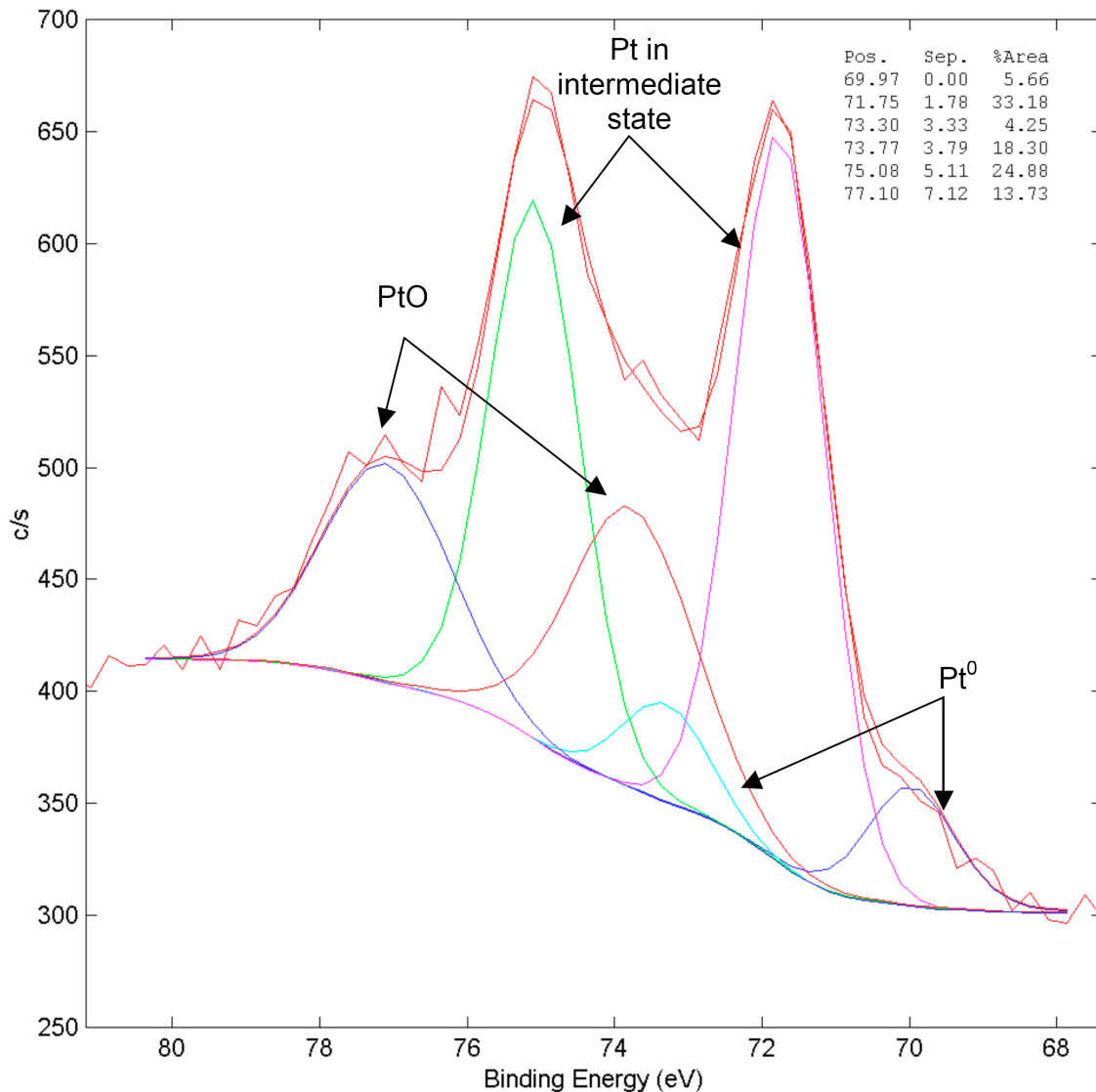


Figure 6.14. Pt 4f region in the XPS spectrum of 2 wt.% - 10 wt.% Na/fMWCNTs (sample A).

It can be argued that the electrostatic field induced by the alkali cation causes most of the Pt to be in this intermediate (promoted) chemical state [210]. In turn, the comparatively higher fraction of metallic Pt and promoted Pt over PtO observed for sample A, may help to explain its superior activity as compared to the other Na-promoted catalysts.

6.8. DRIFTS studies.

DRIFTS studies were attempted with the aim of identifying HC-SCR reaction surface intermediates, as well as establishing their location (i.e., whether they were adsorbed on the metal or on the support). Taking into account the fact that MWCNTs are strongly IR-absorbing materials, prior to analysis a series of catalyst dilutions in KBr were prepared. Given that surface species resulting from the adsorption of NO_2 on Pt are known to possess relatively intense IR bands (compared to typical HC-SCR reaction surface intermediates), the diluted catalysts (contained in a cell equipped with KBr windows) were first exposed to a flow of 500 ppm NO_2 in N_2 . However, although some peaks were observed, it was determined that they corresponded to KBr-adsorbed NO_2 species. Therefore, a decision was made to use silicon in place of KBr, both for the cell window and as the diluent. Unfortunately, even when these changes were made and several experimental parameters essayed, the signal-to-noise ratio remained unacceptably low. On this basis we conclude that there is no realistic prospect of obtaining meaningful DRIFTS spectra on these MWCNTs-based catalysts.

To summarize the findings in this chapter, the oxidation state of the metal can be invoked to explain the enhanced HC-SCR activity observed when MWCNTs-based materials are used as the support material as opposed to alumina. Further, it seems that the activity improvement observed when functionalized (as opposed to pristine) MWCNTs are used as the support is due to the cracking and subsequent partial oxidation of the hydrocarbon being facilitated by the increased acidity of fMWCNTs. Finally, the use of a 3:1 Pt-Rh alloy as the active phase improves HC-SCR activity *via* enhancing the adsorption of C_3H_6 without taking the latter to a regime in which the catalyst is poisoned by the hydrocarbon.

Chapter 7. Mechanistic Studies on HC-SCR Catalysts.

7.1. Introduction.

Supported PGMs are among the best low temperature HC-SCR catalysts found to date, given their ability to show high conversion levels, their hydrothermal stability and their resistance to poisons. However, these materials also show two important drawbacks, namely a narrow temperature window of operation and an objectionably high selectivity towards N_2O . In an attempt to gain fundamental insights that might help to address these limitations, the HC-SCR reaction mechanism on PGM-catalysts has been zealously investigated. Indeed, a survey of the scientific literature pertaining to this topic can prove befuddling, given the great variation within the experimental parameters used in the various studies, the results obtained and the conclusions drawn. Nevertheless, it is possible to find recurrent motifs that allow the proposed mechanisms to be classified into two distinct categories: those involving NO decomposition and subsequent oxygen removal by the hydrocarbon reductant and those involving the formation of C-N bonds. Within this chapter, these two types of mechanism will be reviewed in some detail prior to presenting the results of mechanistic studies performed on Pt/fMWCNTs.

7.1.1. Mechanisms involving NO decomposition followed by HC-assisted surface reduction.

This is undoubtedly the most straightforward mechanism proposed for the HC-SCR reaction. It was first proposed by Burch *et al.* in 1994 [47] and it avers that NO dissociatively adsorbs on reduced Pt sites forming nitrogen and oxygen adatoms. N_{ads} species can then combine and produce N_2 , or react with weakly adsorbed NO and yield N_2O . The hydrocarbon subsequently reacts with O_{ads} (clean off step) to afford combustion products along with reduced Pt sites, thus closing the catalytic cycle [211]. This mechanism is shown schematically in Figure 7.1.

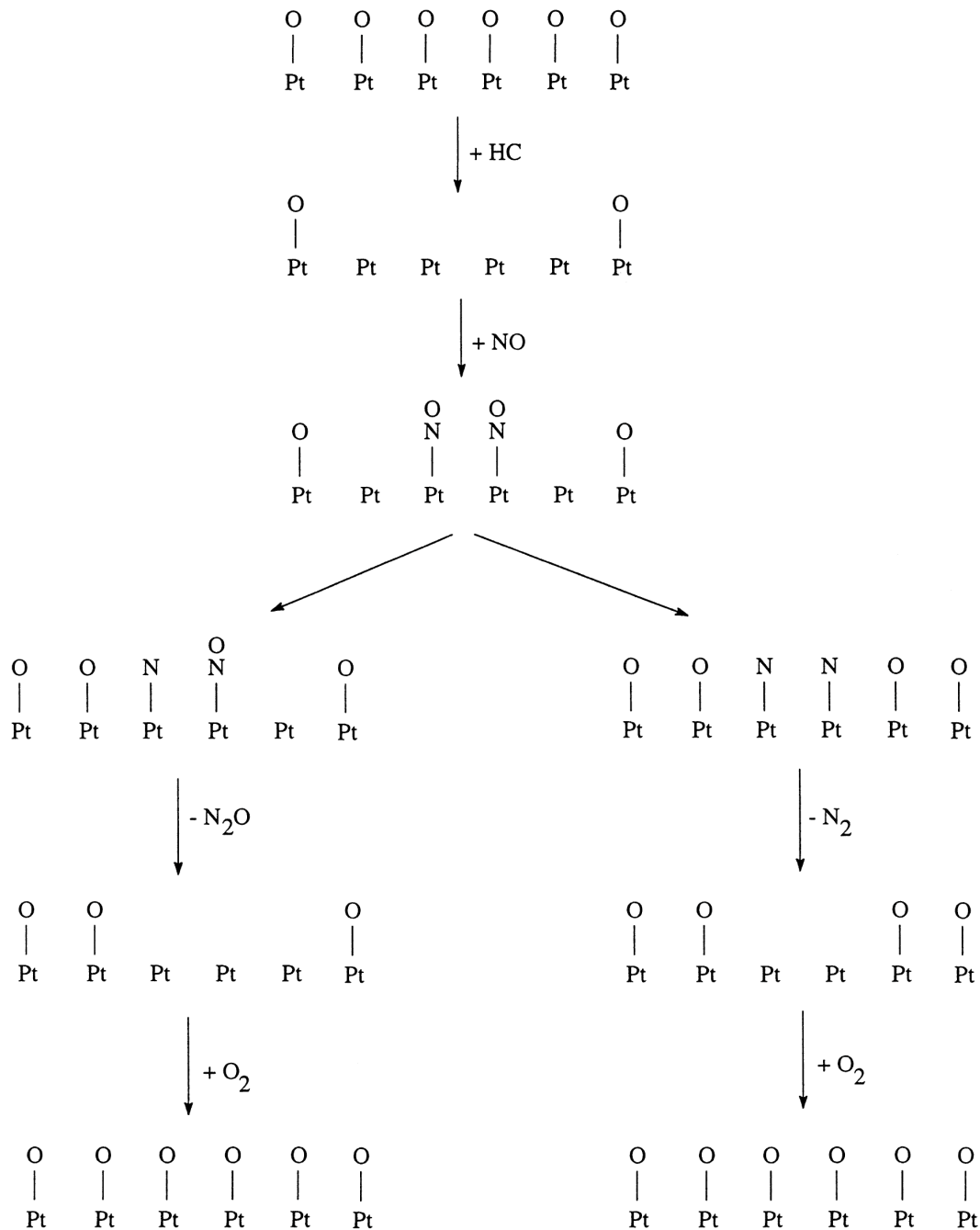


Figure 7.1. Schematic HC-SCR redox mechanism over a Pt surface. Reprinted from Catalysis Today, Vol. 46, V.I. Pârvulescu, P. Grange, B. Delmon, Catalytic removal of NO, Pages No. 233-316, Copyright (1998), with permission from Elsevier.

Both the NO conversion and the N₂ selectivity curves shown by Pt catalysts can be explained by this mechanism. Arguably, the former owes its shape to the competition between NO and O₂ for adsorption sites (low temperatures favor NO dissociation while high temperatures make Pt oxidation more likely), while the latter is due to NO dissociation being faster at higher temperatures (which makes the combination of two nitrogen adatoms to form N₂ more probable than the combination of N_{ads} and NO_{ads} to yield N₂O).

Evidence supporting this mechanism comes from different kinds of experiments, although some of the most cogent data have been obtained through transient Temporal Analysis of Products (TAP) and Steady-State Isotopic Transient Kinetic Analysis (SSITKA) [47,53,212,213].

Transient TAP reactor experiments have shown that when a reduced Pt surface is exposed to NO, a concomitant evolution of N₂ is observed. However, no O₂ is produced, arguably because O_{ads} species resulting from the dissociation of NO start poisoning the catalyst surface, which is eventually completely oxidized and deactivated towards NO dissociation. Tellingly, when a reductant is introduced in the system in the absence of gas phase oxygen, NO dissociation resumes. The lack of direct interaction between NO and the reductant was confirmed by changing the time interval between the introduction of these reagents. Interestingly, experiments performed with different reductants (H₂, CO and C₃H₆) showed that the use of propene shows only a small increase in the N₂ yield. According to Burch and co-workers, this proves that most of the N₂ is produced through the dissociation of NO, which is promoted by the higher reducing power of the hydrocarbon. However, a small contribution from a carbon-assisted NO decomposition [*sic*] mechanism is also invoked to explain the increase in the N₂-make observed when C₃H₆ is used as the reductant. Finally, in order to probe whether volatile organic intermediates are involved in the HC-SCR reaction, the time between the introduction of the reagents (C₃H₆, O₂ and NO) was changed. No difference in the N₂ yield was observed and thus, it was concluded that this type of intermediate does not play a significant role in the reaction.

The important matter of the N₂O-formation has also been addressed by Burch *et al.* through SSITKA experiments in which the use of ¹⁵NO suggested that N₂ is formed from two different surface species (N_{ads} and NO_{ads}), while N₂O is formed by two identical ones (NO_{ads} and NO_{ads}). Further, it has been proposed that the combination of N_{ads} and NO_{ads} results in a transition state chemically (not electronically) equivalent to N₂O. This transition state results in the desorption of N₂ *via* the weakening of the two Pt-N bonds and the strengthening of the Pt-O bond. According to Burch, given that the desorption of N₂O occurs through a similar process involving two NO_{ads} species, whether N₂ or N₂O is desorbed depends only on the probability of Pt-N bond breaking *vs.* Pt-O bond forming. In other words, a pseudo-absorbed form of N₂O (which would not be in equilibrium with gaseous N₂O) may be an intermediate in the formation of gas phase N₂ at low temperatures. This is in agreement with the fact that N₂O decomposition is slow at low temperatures on Pt catalysts (especially when there is a high competition for adsorption sites and in the presence of water) [83,214,215].

Other kinetic data, such as the power law order of reaction with respect to oxygen and the hydrocarbon are also consistent with a mechanism in which Pt is in a reduced state [216-218]. Indeed, C₃H₆ adsorption occurs even under a large excess of oxygen, thereby keeping Pt completely reduced. The latter has been confirmed by experiments in which CO₂ evolution is observed subsequent to the elimination of the hydrocarbon from the system.

Although several authors have rejected this mechanism [216-222], Burch claims that all of the objections presented by these workers are open to alternative interpretations and that based on their results, a NO decomposition mechanism can not be excluded as a major contributor to the HC-SCR reaction on catalysts with PGMs as the active phase.

7.1.2. Mechanisms involving the formation of C-N bonds.

Most authors opposing the NO decomposition mechanism are proponents of mechanisms in which the hydrocarbon reductant reacts with oxygen adatoms (produced *via* the dissociative adsorption of O₂) to yield surface oxygenated intermediates, which can then

react selectively with adsorbed or gas phase NO_x to produce the HC-SCR reaction products [219]. The main evidence for these mechanisms comes from the detection of hydrocarbon-derived surface intermediates *via* infrared spectroscopy, although the reactions of model organic compounds on HC-SCR catalysts have also been adduced. Mechanisms involving the formation of C-N bonds can be further classified depending on the nature of the intermediate deemed crucial for the occurrence of the net HC-SCR reaction. Fortunately, most mechanisms fall into one of two main categories: those involving cyanide (-CN) or isocyanate (-NCO) surface species as an intermediate; and those involving organo-nitro and related adspecies.

7.1.2.1. Mechanisms involving cyanide or isocyanate species as an intermediate.

Bamwenda, Captain and Amiridis can be counted amongst the principal proponents of a mechanism involving -CN and -NCO species as the critical intermediates. As early as 1994, based on the results of Diffuse Reflectance Infrared Fourier Transform Spectroscopy (DRIFTS) studies, Bamwenda *et al.* [223] started developing a mechanistic scheme in which adsorbed propene (or a derivative thereof) forms an oxygenated organic complex after interacting with oxygen. This complex can then undergo one of two transformations: 1) it can react with surface or gaseous oxygen to yield combustion products; or 2) it can react with adsorbed NO_x species to form an intermediate that eventually fragments into -CN or -NCO. According to these authors, -NCO species can then react with adsorbed NO_x or oxygen to produce another complex whose rearrangement yields N_2 , N_2O , CO, CO_2 and O_2 . This mechanistic scheme is shown in Figure 7.2. Interestingly, Bamwenda and co-workers also observed a qualitative relationship between the amount of N-containing adspecies detected *via* FTIR and the NO reduction rate [162,223].

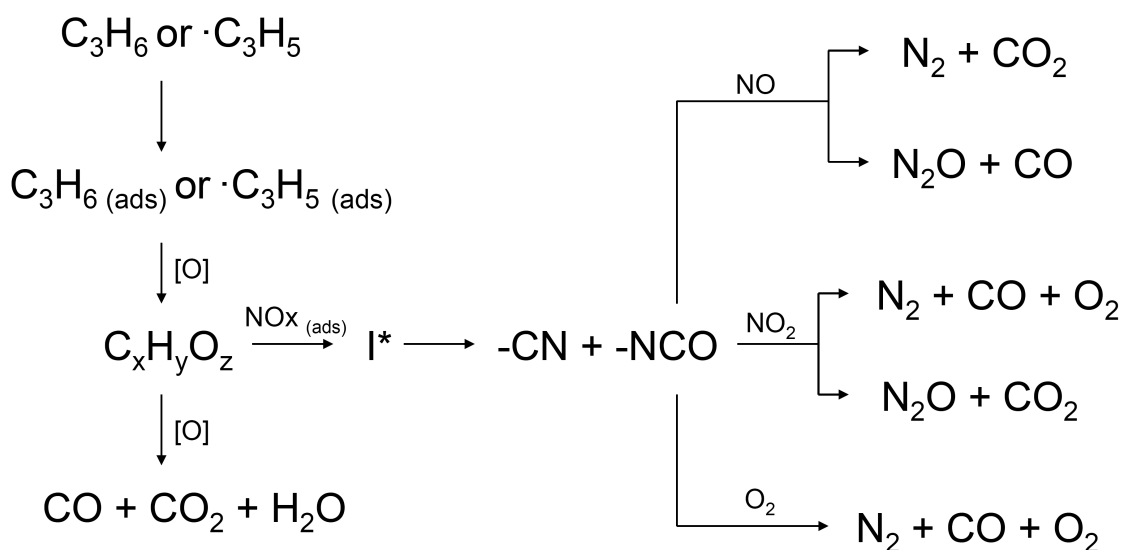


Figure 7.2. Mechanistic scheme for the HC-SCR of NO_x as proposed by Bamwenda (I* represents and excited intermediate).

Captain and Amiridis also detected the presence of –CN and –NCO adspecies on both Pt/Al₂O₃ and Pt/SiO₂ catalysts under HC-SCR reaction conditions through *in situ* FTIR spectroscopy. However, these authors also found differences in the way in which these two catalysts behave. On Pt/Al₂O₃, –NCO species formed by the reaction between a hydrocarbon derivative and gaseous or weakly adsorbed NO_x, were found to be reactive towards NO, NO₂ and O₂. Further, isocyanate species formed in dry conditions hydrolyzed to NH₃ when water was introduced to the system. Since it is possible for the resulting NH₃ to selectively reduce NO_x, the authors concluded that –NCO species are potential intermediates in the HC-SCR reaction both in the absence and in the presence of water. On the other hand, –CN species were deemed to be spectators due to the fact that they were found to be inert towards NO, NO₂ and O₂ [48]. Results of FTIR studies performed by Schießer *et al.* are in agreement with the role assigned to –NCO and –CN species by Captain and Amiridis. However, Schießer and co-workers furthered the results of these researchers by successfully coupling FTIR observations with catalytic activity measurements and by investigating the origin of cyanide and isocyanate species in depth.

Indeed, Schießer has proposed that the formation of –NCO occurs by the reaction of NO with CO formed *via* the partial oxidation of C₃H₆. In turn, the oxidation of the resulting isocyanate species by NO_x yields N₂ and/or N₂O, while their reduction produces inert cyanide groups [49]. In subsequent studies performed on Pt/SiO₂ by Captain and Amiridis, surface isocyanate species were not detected, although cyanide surface species were observed. These workers proposed that cyanide species were formed by the reaction of NO with an activated surface hydrocarbon. Further, it was found that the reaction of the resulting –CN species with NO_x formed N₂, N₂O, and CO₂, while their reaction with O₂ yielded N₂ and CO₂ [224]. Thus, on Pt/SiO₂, –CN was deemed the potential HC-SCR reaction intermediate. The mechanistic proposal of Captain and Amiridis is illustrated in Figure 7.3.

Reactions on Pt/Al ₂ O ₃	Reactions in common	Reactions on Pt/SiO ₂
	$C_3H_6 + * \longrightarrow C_xH_y^*$	
	$C_xH_y^* + O_2 \longrightarrow I^*$	
$I^* + NO + O_2 \longrightarrow NCO^*$		$I^* + NO \longrightarrow CN^*$
	$C_xH_y + NO \longrightarrow CN^*$	
	$I^* + O_2 \longrightarrow CO_2 + H_2O$	
$NCO^* + NO_x \longrightarrow N_2 + N_2O + CO_2$		$CN^* + NO_x \longrightarrow N_2 + N_2O + CO_2$
$NCO^* + O_2 \longrightarrow N_2 + CO_2$		$CN^* + O_2 \longrightarrow N_2 + CO_2$

Figure 7.3. Mechanistic scheme for the HC-SCR of NO_x on Pt/Al₂O₃ and Pt/SiO₂ catalysts as proposed by Captain and Amiridis (I* represents an activated hydrocarbon intermediate and * represents an adsorbed species).

This type of mechanism has been thoroughly reviewed by Burch *et al.* [53,225], who have presented a series of objections. First and foremost, these authors claim that the very

detection of these species *via* IR spectroscopy proves that they are not real intermediates, since a true intermediate would react milliseconds after its formation. With respect to the work of Captain and Amiridis on Pt/Al₂O₃, Burch finds several other factors that suggest that –NCO species are not an important intermediate in the HC-SCR reaction. Indeed, Burch argues that: 1) the rate of reaction of –NCO species with NO under typical HC-SCR conditions (<500 ppm NO) might be too slow; 2) if –NCO species mainly reside on the support, then they cannot easily participate in the HC-SCR reaction; and 3) no definitive correlation between the intensity of the isocyanate band and NO conversion has been established [226]. He also claims that the hydrolysis reaction that isocyanate species are known to undergo [227,228] make the lifetime of these species too short, although he concedes that the formation of NH_x species may play a role depending on their rate of combustion under large oxygen excess. Nevertheless, in spite of all these objections, Burch also notes that it is difficult to unequivocally exclude these species as potential intermediates. Considering the work of Captain and Amiridis on Pt/SiO₂, Burch has also expressed dissent. Indeed, he claims that the fact that the withdrawal of the HC-SCR reagents from the system causes the evolution of N₂ and N₂O to cease almost instantaneously while the surface –CN concentration takes several minutes to decay to zero raises doubts about the participation of cyanide species in the HC-SCR reaction. Finally, this author has also claimed that since the reaction kinetics are almost unaffected by the catalyst support, it seems that neither –CN nor –NCO have a major role in the reaction mechanism.

As already mentioned above, the use of model organic compounds has also been used to probe the HC-SCR reaction mechanism. For instance, Obuchi *et al.* have found that t-butyl nitrile N-oxide (tBuCNO) can easily isomerize to t-butyl isocyanate (tBuNCO) on bare alumina. The latter then decomposes to CO₂ and t-butylamine, which in turn forms N₂ in the presence of NO₂. Thus, these authors have concluded that once intermediates like t-butylamine are formed, their conversion to HC-SCR reaction products is relatively straightforward [229].

7.1.2.2. Mechanisms involving organo-nitro or related species as an intermediate.

Some other authors have proposed that the HC-SCR reaction proceeds *via* the intermediacy of nitro and nitrite adspecies. Indeed, Tanaka *et al.* have detected these species on a Pt/SiO₂ catalyst during the HC-SCR reaction through the use of IR spectroscopy. Tellingly, these species were found to rapidly react with NO₂ and O₂ to yield N₂ and N₂O. Further, experiments with pure compounds such as nitromethane and n-butyl nitrite confirmed that these reagents can indeed react and form N₂ and N₂O at rates similar to those shown by the HC-SCR reaction [230].

Joubert and co-workers have found some evidence suggesting that the formation of organo-nitro compounds is an initial step in the formation of HC-SCR reaction products [231,232]. Indeed, through Gas Chromatography – Mass Spectrometry (GC-MS) studies in which three different nitro compounds were used (1- and 2-nitropropane and 2-methyl-2-nitropropane), these authors were able to prove that the hydrolysis of these molecules under HC-SCR conditions afforded NO_x, N₂O, N₂ and CO₂. Of particular interest to the researchers was the observation that the N₂O-make was highly dependent on the degree of substitution of the carbon immediately adjacent to the nitro group, following the order 1- nitropropane > 2-nitropropane >> 2-methyl-2-nitropropane. Further, when the products of the HC-SCR reaction were trapped and analyzed *via* GC-MS, Joubert *et al.* found nitriles, nitro and nitroso compounds. These observations led the workers to invoke liquid-phase mechanisms previously reported by Nef [233] (see Figure 7.4) and others [234] to explain the formation of N₂O. However, Burch has also reviewed this proposal and concluded that the occurrence of these complicated reaction schemes under HC-SCR conditions is still uncertain and thus requires further evidence.

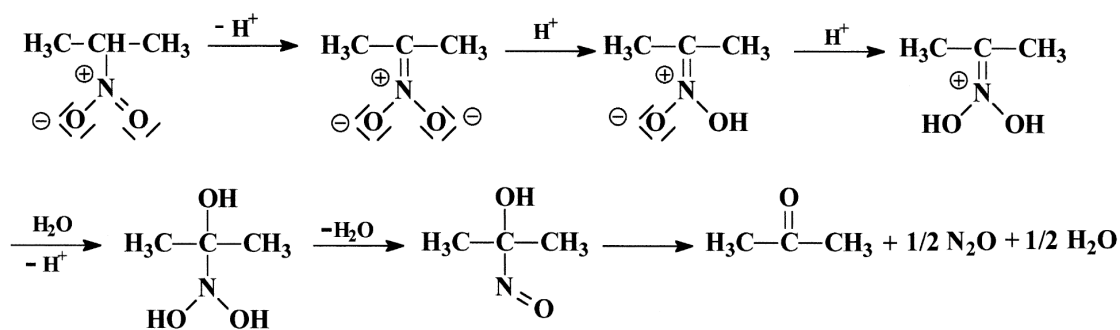


Figure 7.4. Mechanism of N₂O production via 2-nitropropane hydrolysis as proposed by Nef. Reprinted from Applied Catalysis B: Environmental, Vol. 23, E. Joubert, T. Bertin, J.C. Ménézo, J. Barbier, N₂O formation during organic nitro compounds' hydrolysis on platinum based catalysts, Pages No. L83-L87, Copyright (1999), with permission from Elsevier.

In summary, the HC-SCR mechanism on PGM-containing catalysts is an actively investigated and highly debated topic. To further complicate matters, it is recognized by most authors that the experimental conditions, as well as the nature and the state of the catalyst, may have an important role in determining the type of mechanism that is followed. Moreover, almost all workers agree on the fact that it is possible for several mechanisms to operate simultaneously. Indeed, Nikolopoulos *et al.* have found kinetic evidence which led them to conclude that a NO decomposition mechanism and a mechanism involving a C-N-type intermediate may operate in parallel [235].

In recent years, a new mechanistic model that may help to resolve this lingering controversy has started to emerge. In effect, this approach reconciles the mechanism involving NO decomposition followed by HC-assisted surface reduction with the mechanisms involving carbon and nitrogen-containing intermediates by claiming that the clean off step can be effectively accomplished by C_xH_yO_zN_w species [236]. Further, these new types of mechanisms have been proposed based on experimental evidence obtained through techniques alternative to infrared spectroscopy, addressing one of the main

objections presented against schemes involving nitrogen-containing organic intermediates. Most notably, García-Cortés *et al.* have recently reported a mechanism involving partially oxidized intermediates (whose combustion by gaseous O₂ constitutes the clean off step) based on the study of reaction transients [237].

A transient is created by switching one gas out of a reactant stream and replacing it with an equal volume and flow of an inert gas, while keeping both temperature and pressure constant. By tracking the concentration of the reactants and products before, during and after the formation of the transient, insight on the nature, concentration and reactivity of surface species can be gained. Relevant information can also be gathered from the reverse switch, i.e. substituting a reagent for an inert gas. Indeed, the reaction mechanism can be probed in considerable detail by submitting the various HC-SCR reactants to this methodology and performing the experiments at temperatures slightly below and above that of maximum NO_x conversion (T_{max}).

In our work, attempts to elucidate the mechanism of operation of MWCNTs-based catalysts were first made by applying DRIFTS with the aim of identifying reactive surface intermediates. Unfortunately, due to the low signal-to-noise ratio caused by the high absorbance of MWCNTs in the infrared, these efforts were fruitless. Taking this into account, along with the already mentioned objections against the use of infrared spectroscopy in the study of the HC-SCR reaction, the application of the transient technique was chosen as a viable alternative to the investigation of the mechanism of operation of MWCNTs-based formulations.

7.2. Experimental methods.

7.2.1. Transient experiments.

Experiments were performed in a horizontal tubular quartz reactor (5 mm internal diameter). The catalyst (34.5 mg) was packed into a ~1 cm bed between plugs of quartz wool. The gas mixture flowing through the catalyst bed consisted of 2350 ppm NO, 2350 ppm C₃H₆ and 10 % O₂ balanced with He. The gas flows were regulated with mass flow controllers (0.1 mL/min sensitivity) and the total flow rate was kept at 300 cm³/min

(STP), corresponding to a $W/F = 0.002 \text{ g} \cdot \text{h} \cdot \text{dm}^{-3}$. A four-way electro valve allowed for the switching of a reactant gas for an equal flow of an inert gas (1 % Ar in He) and vice versa, while a high precision regulation valve and two high sensitivity pressure transducers allowed for the switches to be performed without a concomitant pressure variation in the system. Temperature was kept constant using a controller with a sensitivity of $0.1 \text{ }^\circ\text{C}/\text{min}$ and two thermocouples (one of which was embedded in the upstream quartz wool plug while the other was kept between the reactor and the furnace). The outlet gases were continuously analyzed using a Pfeiffer OmniStar mass spectrometer with a residence time of 10 ms.

In a typical experiment, a gas mixture containing the reactant gases is flowed through the catalyst bed and the temperature is slowly increased until both the NO and C_3H_6 conversion levels are deemed satisfactory (as a means to ensure the operation of the reactor in a differential manner, conversion levels were kept between 10 and 25 %). In order to avoid the build-up of unreactive spectator species, the reactant to inert gas switch is performed immediately after ensuring that steady state conditions have been attained. Likewise, the reverse switch is performed promptly after the new steady state conditions are reached. Finally, the temperature of the reactor is increased until the C_3H_6 conversion is quantitative and the switches are then repeated at this temperature. In this manner, $\text{NO}/\text{C}_3\text{H}_6/\text{O}_2 \rightarrow \text{Ar}/\text{C}_3\text{H}_6/\text{O}_2$, $\text{Ar}/\text{C}_3\text{H}_6/\text{O}_2 \rightarrow \text{NO}/\text{C}_3\text{H}_6/\text{O}_2$, $\text{NO}/\text{C}_3\text{H}_6/\text{O}_2 \rightarrow \text{NO}/\text{Ar}/\text{O}_2$, $\text{NO}/\text{Ar}/\text{O}_2 \rightarrow \text{NO}/\text{C}_3\text{H}_6/\text{O}_2$, $\text{NO}/\text{C}_3\text{H}_6/\text{O}_2 \rightarrow \text{NO}/\text{C}_3\text{H}_6/\text{Ar}$ and $\text{NO}/\text{C}_3\text{H}_6/\text{Ar} \rightarrow \text{NO}/\text{C}_3\text{H}_6/\text{O}_2$ switches were performed both below and above the temperature of maximum NO reduction activity (T_{max}), which was determined to be $280 \text{ }^\circ\text{C}$. This contrasts with results obtained in previous microreactor tests (see Table 5.2), in which the temperature of maximum NO conversion (T_{max}) was found to be $205 \text{ }^\circ\text{C}$ for the same Pt/fMWCNTs catalyst. This shift of T_{max} to considerably higher temperatures can be ascribed to a substantial increase in the effective space velocity. Indeed, although the experiment was designed in order to set the space velocity at $50,000 \text{ h}^{-1}$ (*vide supra*), the transient experiments were performed using significantly lower amounts of catalyst (~30 times smaller than the amount used in previous reactor runs), which made the measurement and control of both temperature and space velocity difficult. Nevertheless,

all of the experiments were performed using the same conditions, which allowed for reliable data to be obtained from these experiments.

Mass spectrometry was used to follow the switches and the subsequent relaxation of the system, as well as to measure conversion levels and ensure steady state conditions. Prior to its use, experimental quadrupole cracking patterns were obtained for all the gases (reactants and products) involved, in order to determine the contribution of each species to the relevant m/z signals. A series of equations was then used to yield semi-quantitative values for gases of interest: NO, C₃H₆, O₂, N₂O, NO₂, CO₂ and Ar. Ultimately, to simplify the analysis of the transient profiles, these semi-quantitative values were normalized between 0 and 1.

7.3. Transient experiments.

7.3.1. Transient experiments below T_{max} (260 °C).

7.3.1.1. NO/C₃H₆/O₂ → Ar/C₃H₆/O₂ switch.

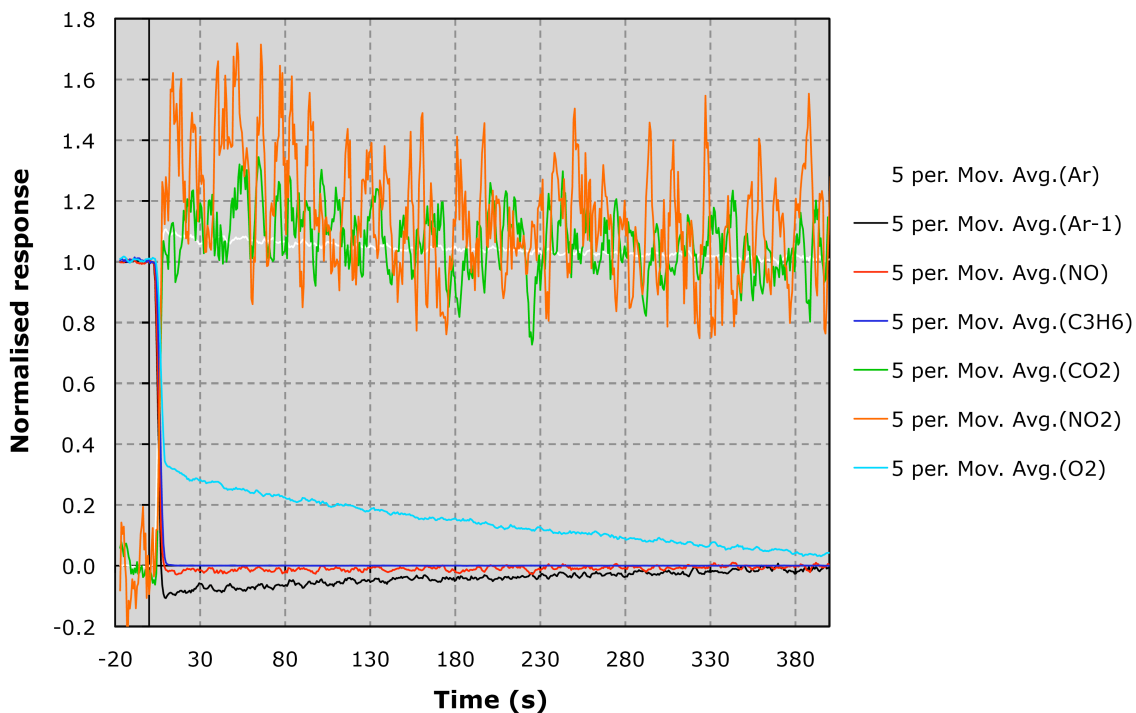


Figure 7.5. NO/C₃H₆/O₂ → Ar/C₃H₆/O₂ switch performed at 260 °C.

The first noticeable feature in the transient profiles corresponding to this switch is the closeness with which the NO signal follows that of Ar* ($Ar^*=1-Ar$), which is attributed to the fact that under reaction conditions the amount of NO reversibly adsorbed on the catalyst surface is practically nil. The fall in the C₃H₆ profile can be explained by its reaction with oxygen (as well as with any residual NO), as evidenced by the corresponding increase in the CO₂ concentration; this increase confirms that under SCR conditions hydrocarbon combustion is disfavored in spite of the vast oxygen excess. Indeed, this explanation is consistent with the delay of the hydrocarbon profile with respect to the NO signal, since the continuation of the NO reduction reaction is partially to blame for the slowness with which the O_{ads} species (necessary in the combustion reaction) are known to be produced and/or react with adsorbed hydrocarbon species [238]. The shape of the O₂ profile seems to agree with these observations, since in the few seconds that follow the switch, gas phase oxygen is most likely involved in three processes: 1) increased hydrocarbon combustion; 2) reaction with partially oxidized hydrocarbon species (C_xH_yO_zN_w); and 3) dissociative adsorption on vacant sites that become available immediately after NO is removed. Eventually, as steady state is approached and both the number of available sites and the amount of C_xH_yO_zN_w intermediates decrease, the new surface equilibrium is slowly established and the rate of oxygen consumption decelerates.

With regards to the NO₂ profile, both its noisiness and the striking similarities it has with the CO₂ signal point to the NO₂ profile being an artifact of CO₂ interference. Indeed, if the amount of NO₂ being produced prior to the elimination of NO from the system is small to begin with (as would be expected from the reaction conditions), the switch should only cause a negligible drop in the amount of NO₂ that reaches the MS. Thus, the contribution of other gases to the m/z=46 MS signal (however small), becomes important (specially if the interfering gases are present in a relatively high concentration, as is the case with CO₂). The shape of the CO₂ signals corresponding to m/z=22, 28 and 44 (data not shown) is consistent with this explanation.

7.3.1.2. $Ar/C_3H_6/O_2 \rightarrow NO/C_3H_6/O_2$ switch.

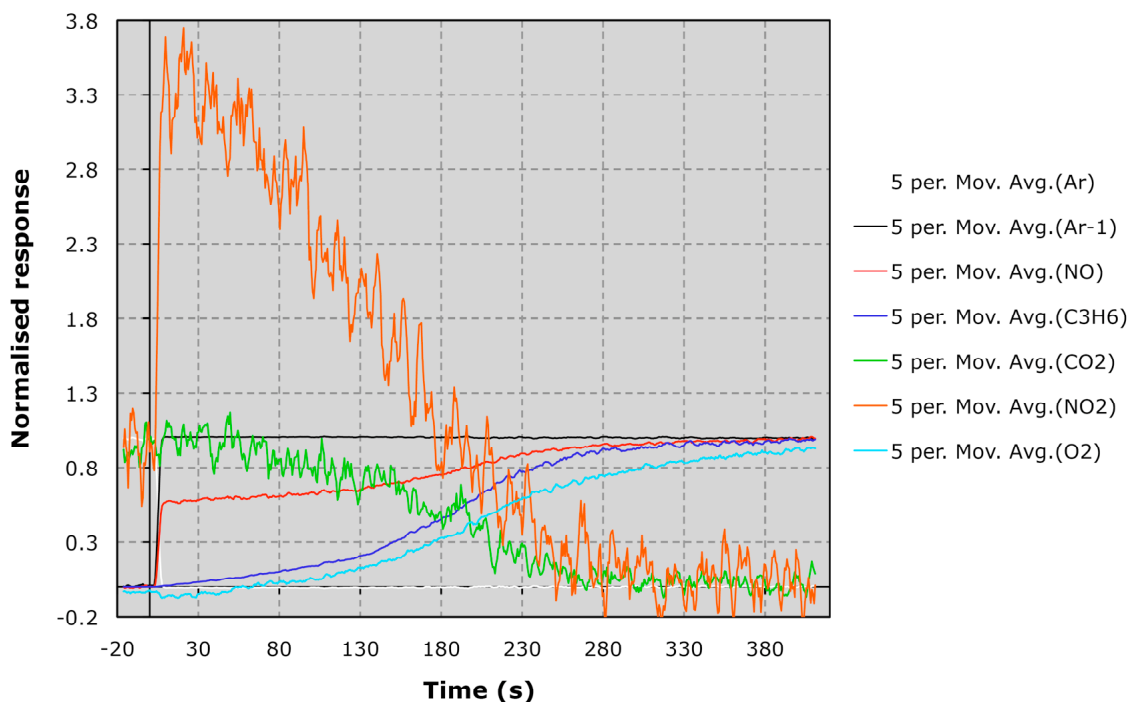


Figure 7.6. $Ar/C_3H_6/O_2 \rightarrow NO/C_3H_6/O_2$ switch performed at 260 °C.

For this particular switch, the outstanding trait is the very high maximum shown by the NO_2 profile. Evidently, when gas phase NO is reintroduced to the system, it immediately starts combining with O_{ads} species (with which the catalyst surface has become enriched in the absence of NO) to produce NO_2 . However, the NO profile also shows a sharp increase in the first couple of seconds following the switch, indicating that the oxidation of NO into NO_2 is not quantitative. After this initial surge, the NO signal then proceeds to follow a more gradual increase to the steady state concentration. Tellingly, C_3H_6 , O_2 and CO_2 signals also approach the steady state in a gradual fashion. From these curves, it is obvious that the direct reaction of C_3H_6 with oxygen continues for a considerable amount of time after the switch is made. Approximately 4 min after the switch, NO is no longer engaged in the production of NO_2 , at which point the combustion of the hydrocarbon is inhibited (the surface oxygen having been largely consumed) and NO reduction resumes. These observations suggest a model in which NO adsorption prevails over O_2 adsorption, which is in accordance with the selectivity of the system.

Finally, the counterintuitive initial and final steady state levels shown by the NO₂ profile must be addressed, since they seem to suggest that the amount of NO₂ being produced is less in the presence of NO than in its absence. This paradox can be satisfactorily explained by invoking, once again, the interference of CO₂ with the NO₂ signal.

7.3.1.3. NO/C₃H₆/O₂ → NO/Ar/O₂ switch.

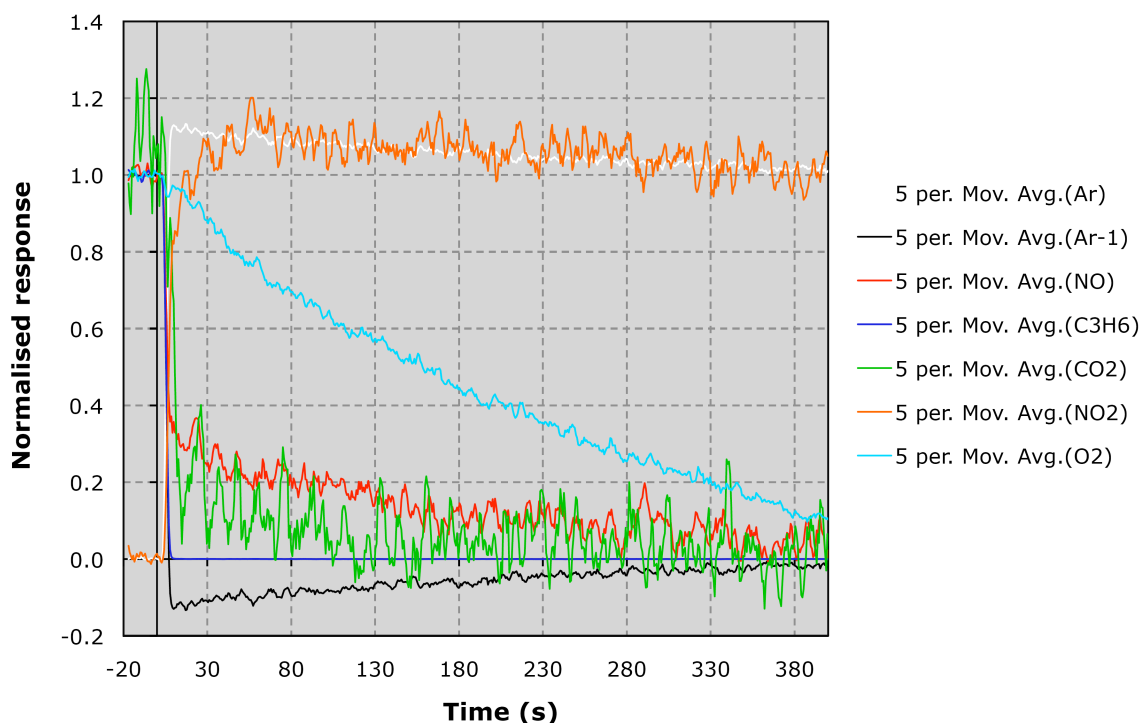


Figure 7.7. NO/C₃H₆/O₂ → NO/Ar/O₂ switch performed at 260 °C.

Below the temperature of maximum NO reduction activity, the elimination of the hydrocarbon reductant from the system is followed by a drastic drop in both the C₃H₆ and the CO₂ signals. In the case of C₃H₆, the immediate fall of the profile to steady state levels reveals the amount of hydrocarbon reversibly adsorbed on the catalyst surface to be practically zero. As for CO₂, the fact that the signal does not reach steady state levels right away suggests the presence of a residual amount of C₃H₆-derived species which continues to be oxidized after the hydrocarbon is withdrawn from the gas phase. It is worth noting that although hydrocarbon combustion continues for a short period of time

after the switch, the surface of the catalyst immediately starts experiencing oxygen enrichment, reflected in the gradual fall in the O_2 profile. Parenthetically, the initial surge experienced by the NO_2 signal indicates the presence of O_{ads} species on the catalyst surface prior to the switch, but the fact that the latter signal quickly reaches steady state levels while the O_2 profile does so in a much more gradual manner points to an oxygen enrichment of the catalyst surface subsequent to the exchange. Indeed, the NO profile is consistent with a surface covered mostly by NO_{ads} and C_3H_6 -derived species. After the exchange, NO continues to be reduced by the latter, while it also starts to undergo oxidation to NO_2 . The occurrence of both reactions, and the speed with which the second occurs, accounts for the initial decrease in the NO signal, while the slow consumption of the C_3H_6 -derived species to yield vacant sites on which NO can adsorb explains the long delay incurred before the system reaches steady state. Finally, it is apparent that the amount of NO_2 produced at steady state is significant, since the overall amount of NO decreases (while an increase would be expected based solely on the elimination of C_3H_6 from the system and the consequent interruption of the NO reduction reaction).

7.3.1.4. $\text{NO}/\text{Ar}/\text{O}_2 \rightarrow \text{NO}/\text{C}_3\text{H}_6/\text{O}_2$ switch.

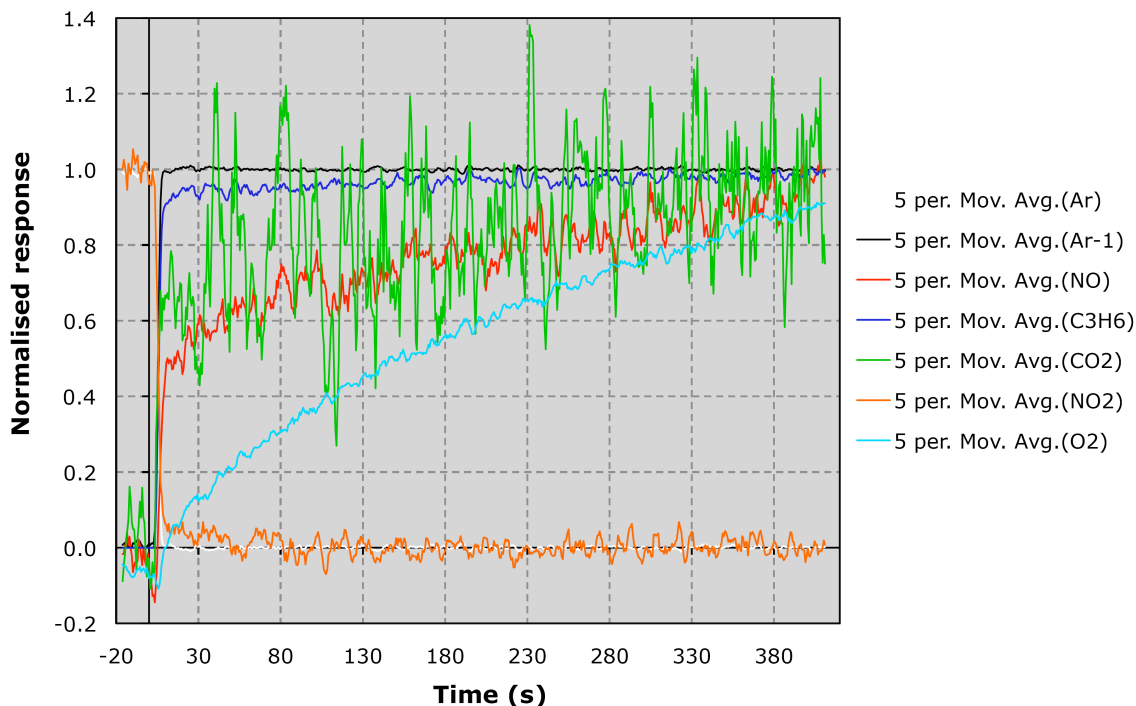


Figure 7.8. $\text{NO}/\text{Ar}/\text{O}_2 \rightarrow \text{NO}/\text{C}_3\text{H}_6/\text{O}_2$ switch performed at 260°C .

When the hydrocarbon reductant is reintroduced to the system, the C_3H_6 profile follows two different kinetics, the faster one being represented by a spike subsequent to the switch which exhibits a slight delay with respect to Ar^* . Associated with this spike is a rise in the CO_2 profile. These observations are consistent with a model in which prior to the switch, the surface of the catalyst is covered with O_{ads} . At first sight, the shapes of both NO and O_2 profiles seem to be counterintuitive. One might expect a gradual fall in the NO profile and a sudden drop in the O_2 signal caused by the resumption of NO reduction and C_3H_6 combustion, respectively. The sharp drop of the NO_2 signal might provide an explanation. Indeed, if the amount of NO_2 being produced prior to the switch is significant, a considerable rise in both the NO and O_2 profiles would be expected upon introduction of the hydrocarbon. This rise is evidently large enough to overwhelm the drop in gas phase NO and O_2 concentration resulting from the recommencement of the NO reduction and C_3H_6 combustion reactions.

7.3.1.5. $\text{NO}/\text{C}_3\text{H}_6/\text{O}_2 \rightarrow \text{NO}/\text{C}_3\text{H}_6/\text{Ar}$ switch.

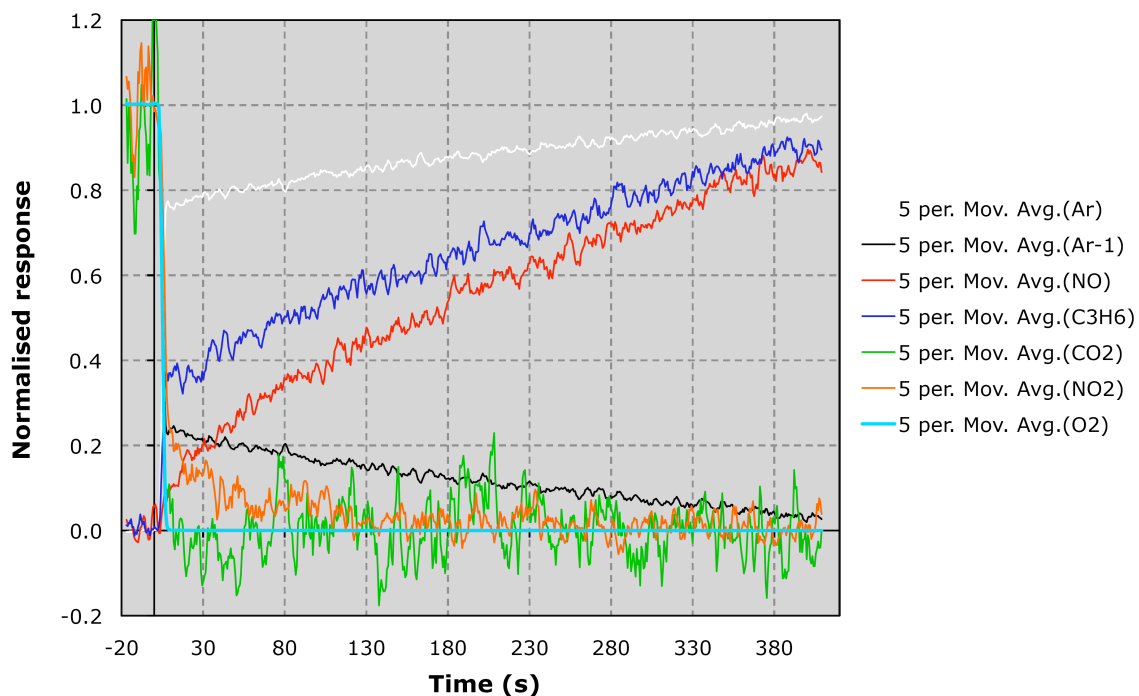


Figure 7.9. $\text{NO}/\text{C}_3\text{H}_6/\text{O}_2 \rightarrow \text{NO}/\text{C}_3\text{H}_6/\text{Ar}$ switch performed at 260°C .

The first noticeable feature in this particular switch is the time the Ar signal requires to reach stability. Indeed, it is worth noting that this feature is consistently observed in every switch in which O₂ is substituted by Ar, just as an initial spike over steady state levels in the oxygen signal is consistently observed when O₂ is reintroduced to the system (*vide infra*). These features are not completely unexpected, since the relative concentration of oxygen with respect to the other exchanged gases (NO and C₃H₆) is considerably (~40x) higher and this has an appreciable impact on the amount of time the system requires to attain stability after the switch. Nevertheless, given the fact that this affects all signals equally, the use of these profiles can still yield relevant information as long as this intrinsic experimental shortcoming is factored into their interpretation. The plummeting of the O₂ signal indicates that, as for NO and C₃H₆, the amount of oxygen reversibly adsorbed on the surface of the catalyst is essentially zero. Further, the sudden drop that the NO₂ and CO₂ profiles experience immediately after oxygen is withdrawn from the

stream suggests either that the amount of oxygen irreversibly adsorbed on the catalyst surface also is negligible or that the oxidation reactions that produce these products involve gas phase oxygen as opposed to oxygen adatoms. Interestingly, the fall in the NO₂ signal is slightly delayed with respect to that of CO₂, just as the initial rise in the NO signal is delayed with respect to that of C₃H₆. This not only confirms that the kinetics of the hydrocarbon combustion reaction are faster than those of NO oxidation, but also suggests that in the absence of the latter reaction the NO and C₃H₆ profiles would not be offset; as it is, they are very similar in appearance. This, in turn, suggests that both NO and C₃H₆ are involved in the production of partially oxidized hydrocarbon species crucial for the occurrence of the HC-SCR reaction, as has been suggested by other authors [44,237].

7.3.1.6. *NO/C₃H₆/Ar → NO/C₃H₆/O₂ switch.*

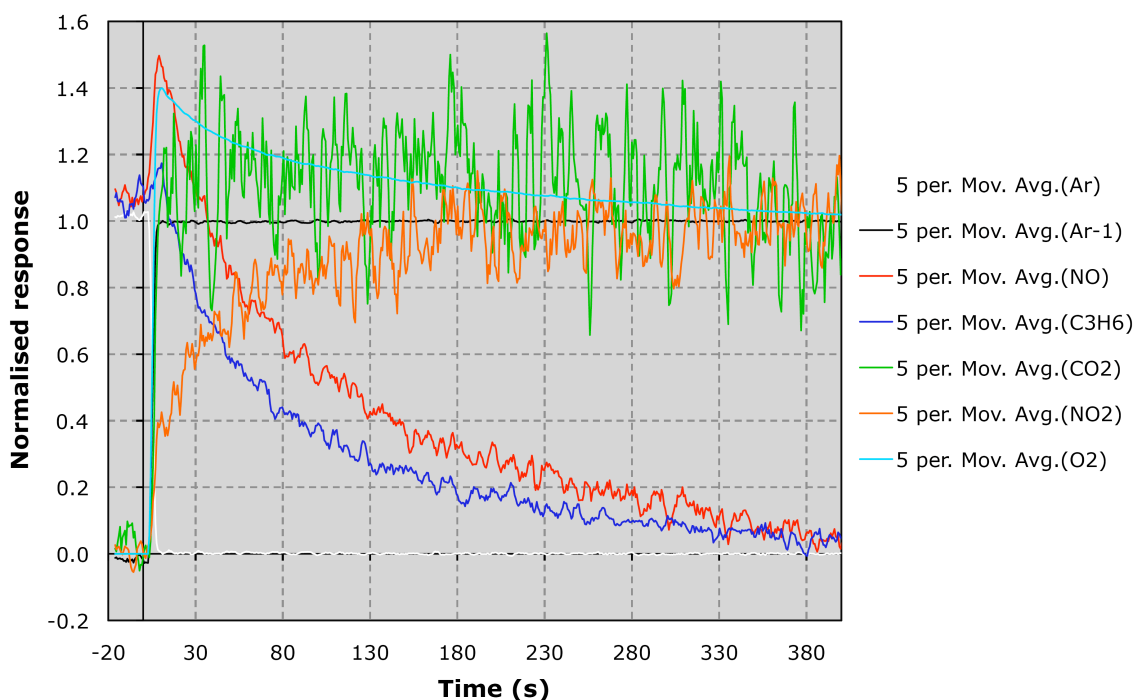


Figure 7.10. NO/C₃H₆/Ar → NO/C₃H₆/O₂ switch performed at 260 °C.

In essence, all of the observations made for the switch in which O₂ is eliminated from the feed are confirmed when this reactant is reintroduced to the gas stream. As stated above, the initial spike above steady state levels experienced by all reactants immediately after the switch is attributed to the system's response to the pressure drop that accompanies the exchange. It is important to note, however, that a rise above steady state levels has been observed by other authors [237] for the oxygen signal alone, the spike being attributed to the inability of O₂ to adsorb or react immediately after the switch. Thus, for the particular case of oxygen, a potential contribution of the aforementioned phenomenon to the signal's maximum cannot be ruled out. The difference in the kinetics of hydrocarbon combustion (fast reaction) and NO oxidation (slower reaction) is clearly shown by the fast rise of the CO₂ signal and the comparatively slow rise of the NO₂ profiles. Further, the different maxima shown by the NO and the C₃H₆ signals can also be attributed to the dissimilar rates of the oxidation reactions in which these two gases are involved. Finally, the similarities between the NO and C₃H₆ profiles once again suggest their participation in the production of new partially oxidized hydrocarbon species over vacant Pt sites made available by the combustion reaction.

7.3.2. Transient experiments above T_{max} (300 °C).

7.3.2.1. $\text{NO}/\text{C}_3\text{H}_6/\text{O}_2 \rightarrow \text{Ar}/\text{C}_3\text{H}_6/\text{O}_2$ switch.

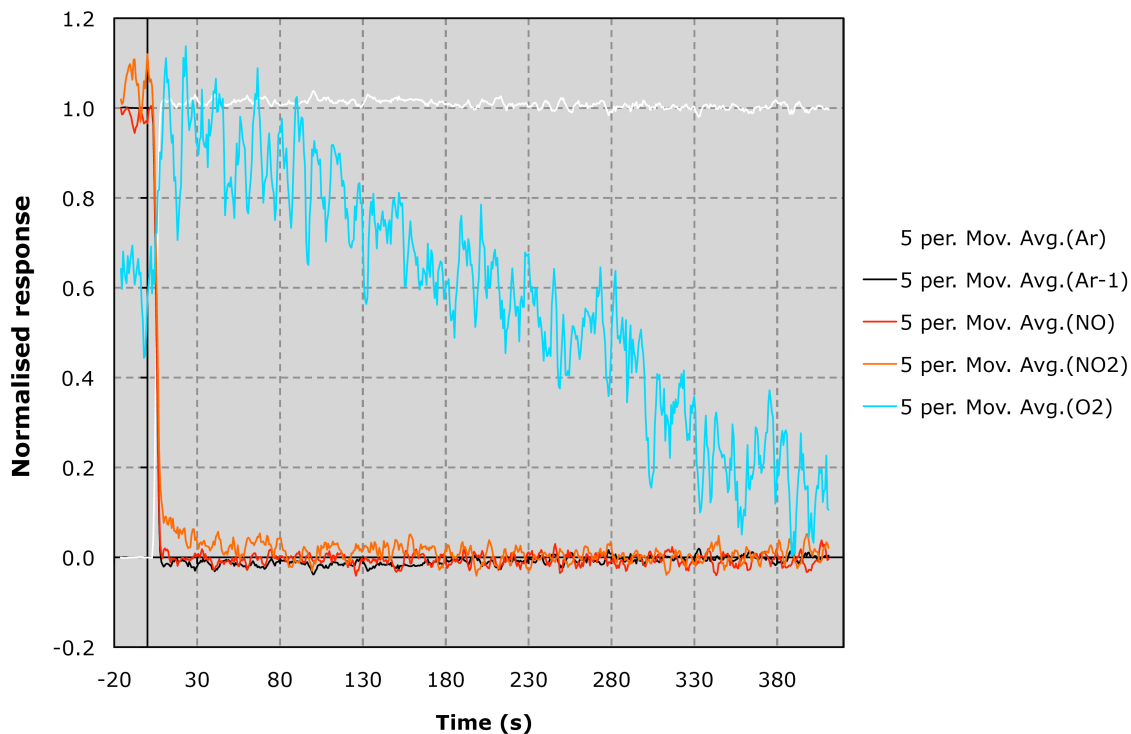


Figure 7.11. $\text{NO}/\text{C}_3\text{H}_6/\text{O}_2 \rightarrow \text{Ar}/\text{C}_3\text{H}_6/\text{O}_2$ switch performed at 300 °C.

Given that hydrocarbon consumption is quantitative at this temperature, both the C_3H_6 and the CO_2 profiles are omitted (the initial and final steady states being the same, the normalization yields nothing but noise). The same could be said with regards to the O_2 signal, which shows no significant change. As soon as NO is eliminated from the stream both the NO and NO_2 signals immediately decline, although the NO_2 signal is slightly delayed with respect to that of NO. These observations are consistent with a model in which prior to the switch, NO is adsorbed on the catalyst surface and undergoing both reduction and oxidation, although hydrocarbon combustion is the prevalent reaction. Indeed, the lack of variation in the O_2 signal indicates that the amount of NO_2 being produced prior to the switch is negligible.

7.3.2.2. $\text{Ar}/\text{C}_3\text{H}_6/\text{O}_2 \rightarrow \text{NO}/\text{C}_3\text{H}_6/\text{O}_2$ switch.

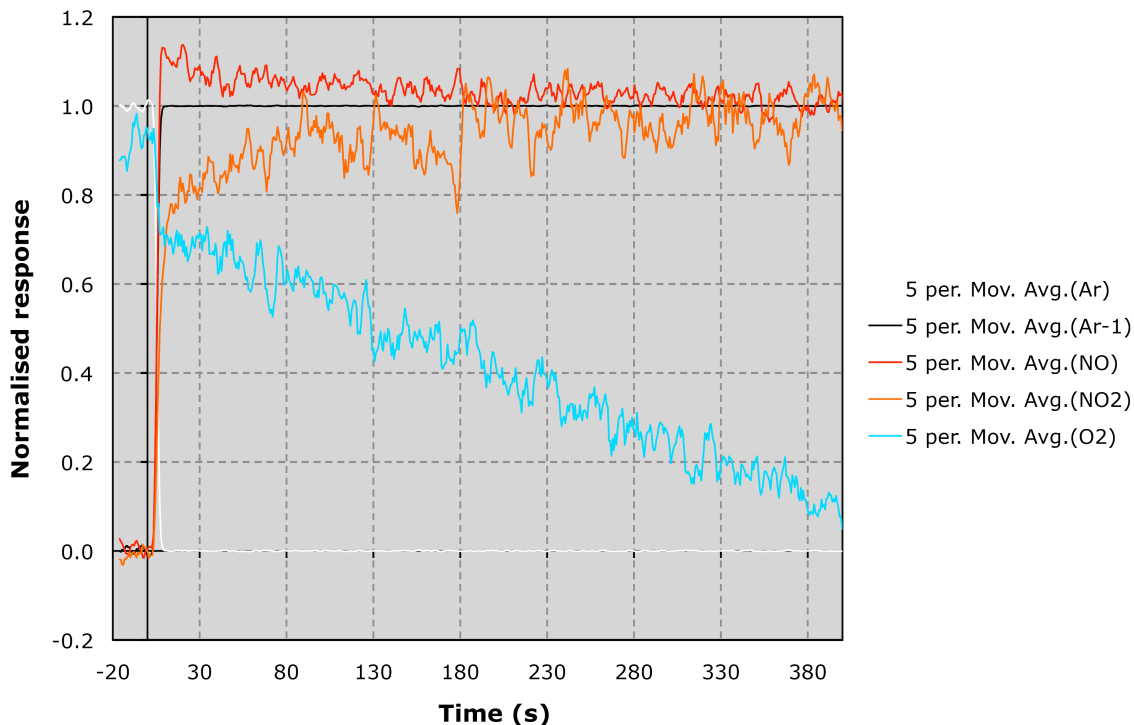


Figure 7.12. $\text{Ar}/\text{C}_3\text{H}_6/\text{O}_2 \rightarrow \text{NO}/\text{C}_3\text{H}_6/\text{O}_2$ switch performed at 300 °C.

The C_3H_6 , CO_2 and O_2 profiles are omitted from the switch in which NO is reintroduced to the system for the same reasons they were left out from the switch in which NO was withdrawn (*vide supra*). Considering the NO and NO_2 profiles, a sharp rise in both signals is observed immediately after the exchange. In the case of NO, this rise surpasses the final steady state level and then slowly decays to the latter, while the NO_2 signal shows an initial surge followed by a more gradual increase to its steady state level. Evidently, after the exchange NO instantly starts being oxidized to NO_2 , which is consistent with a model in which the catalyst surface is oxygen-rich prior to the switch. The occurrence of NO oxidation can also explain the gradual fall of the NO signal after the latter reaches its initial maximum, although a contribution from the slow recommencement of the NO reduction reaction cannot be ruled out.

7.3.2.3. $\text{NO}/\text{C}_3\text{H}_6/\text{O}_2 \rightarrow \text{NO}/\text{Ar}/\text{O}_2$ switch.

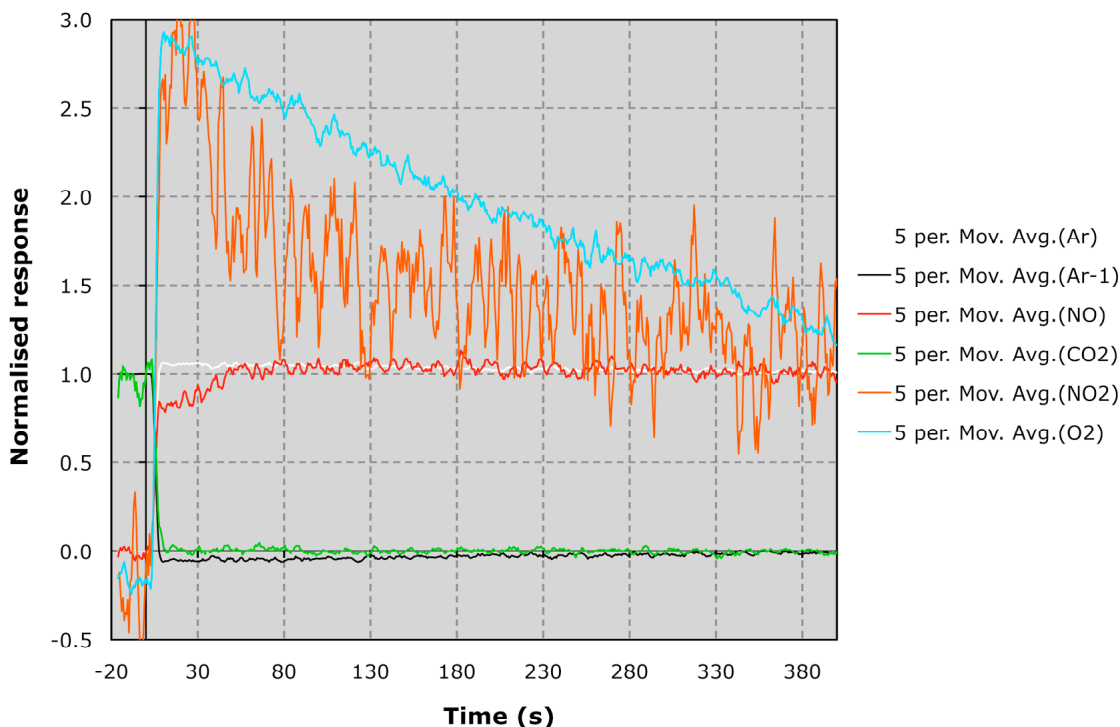


Figure 7.13. $\text{NO}/\text{C}_3\text{H}_6/\text{O}_2 \rightarrow \text{NO}/\text{Ar}/\text{O}_2$ switch performed at 300 °C.

The soaring of both NO_2 and O_2 signals above steady state levels immediately after the elimination of C_3H_6 from the gas phase is the most conspicuous element within this switch. The rise of these two signals is accompanied by a plunge in the CO_2 profile, which is indicative of a very low surface concentration of combustible species prior to the switch. Both the noisiness of the NO_2 signal and the almost instantaneous rise of the NO profile to steady state levels suggest that only a small fraction of the newly available O_2 becomes involved in NO oxidation. Instead, it is apparent that after an initial surge in the concentration of oxygen in the gas phase, dissociative adsorption (a slow process) becomes the most prevalent route for O_2 consumption, as evidenced by the gradual drop of both the oxygen and the NO_2 signals to steady state levels.

7.3.2.4. $\text{NO}/\text{Ar}/\text{O}_2 \rightarrow \text{NO}/\text{C}_3\text{H}_6/\text{O}_2$ switch.

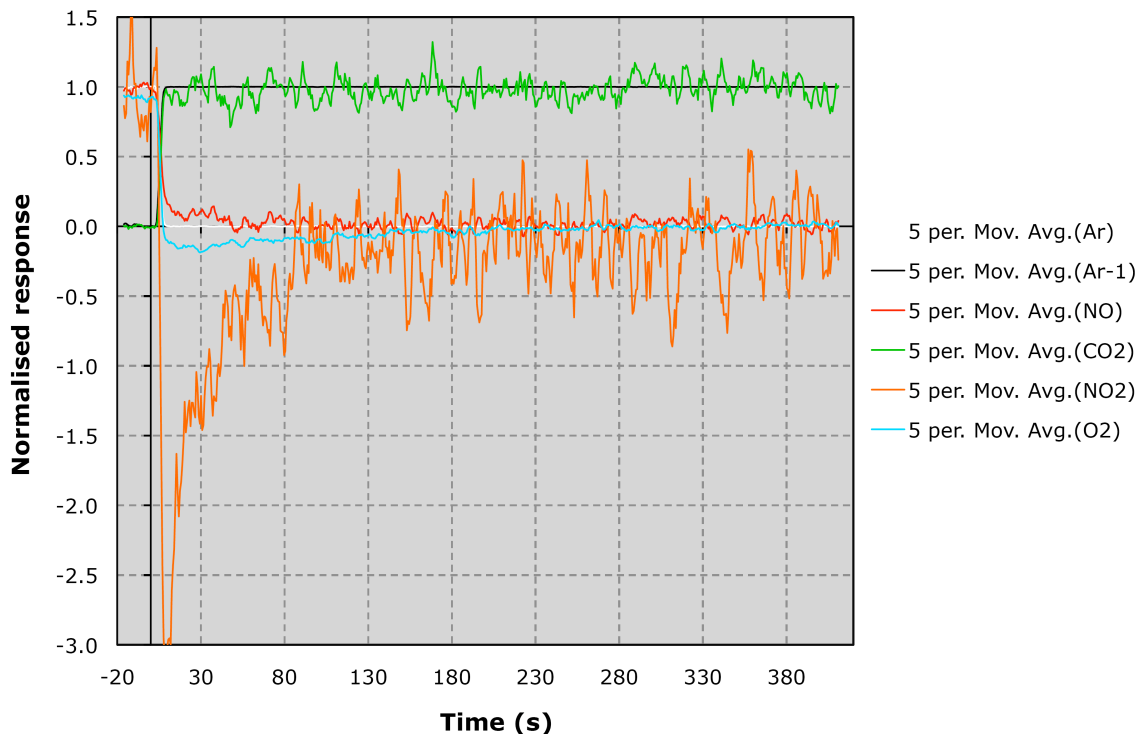


Figure 7.14. $\text{NO}/\text{Ar}/\text{O}_2 \rightarrow \text{NO}/\text{C}_3\text{H}_6/\text{O}_2$ switch performed at 300 °C.

In this particular switch, the reintroduction of C_3H_6 to the system is accompanied by a dramatic decrease in the NO_2 profile to levels considerably lower than those corresponding to the final steady state. Only the reaction of the hydrocarbon with NO_2 could account for such an immediate plunge in the NO_2 signal. Indeed, the swift rise of the CO_2 profile signals the instantaneous recommencement of the C_3H_6 combustion reaction, as does the shape of the oxygen profile. Finally, the rapid drop of the NO signal to steady state levels points to the resumption of NO reduction.

7.3.2.5. $\text{NO}/\text{C}_3\text{H}_6/\text{O}_2 \rightarrow \text{NO}/\text{C}_3\text{H}_6/\text{Ar}$ switch.

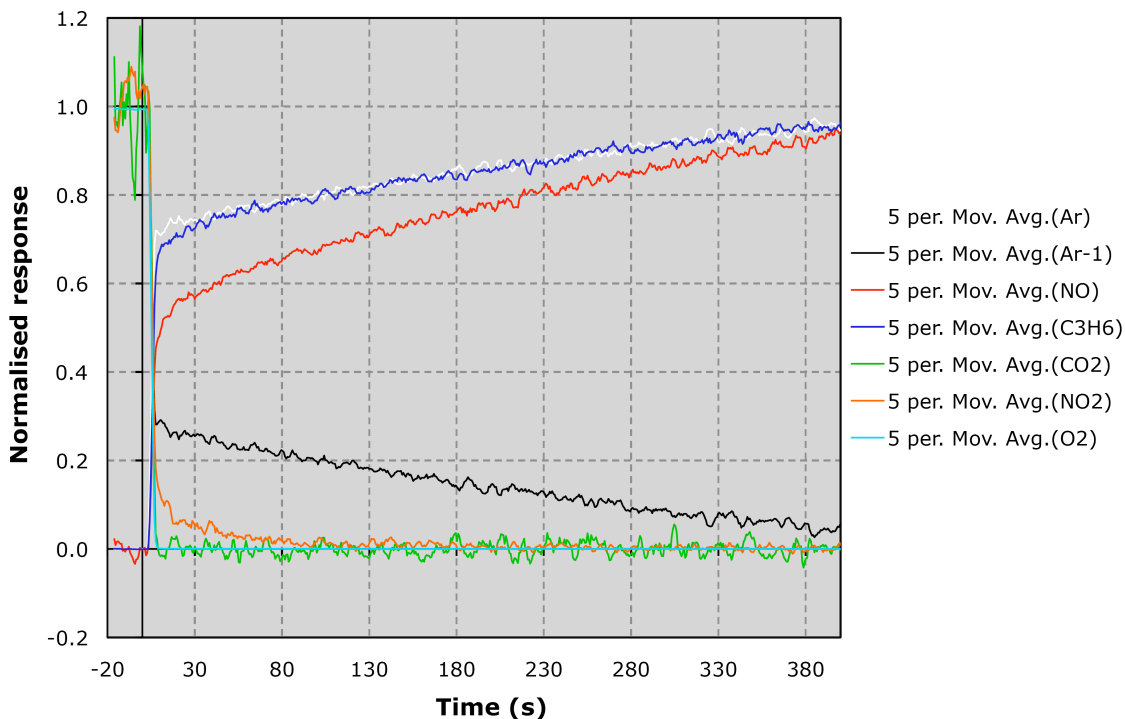


Figure 7.15. $\text{NO}/\text{C}_3\text{H}_6/\text{O}_2 \rightarrow \text{NO}/\text{C}_3\text{H}_6/\text{Ar}$ switch performed at 300 °C.

As observed in previous switches in which O_2 is the exchanged reactant, the Ar signal requires a considerable amount of time to achieve stability. This particular feature has already been accounted for (*vide supra*). The immediate fall to steady state levels shown by the O_2 and the CO_2 signals after the exchange points to a surface which prior to the switch has a low coverage of both reversibly adsorbed oxygen and combustible C_3H_6 -derived species. Further, the delay of the NO_2 signal with respect to the CO_2 profile suggests that the occurrence of NO oxidation outlasts the combustion of the hydrocarbon subsequent to the switch. The latter is consistent with the delay of the NO signal with respect to the C_3H_6 profile.

7.3.2.6. $NO/C_3H_6/Ar \rightarrow NO/C_3H_6/O_2$ switch.

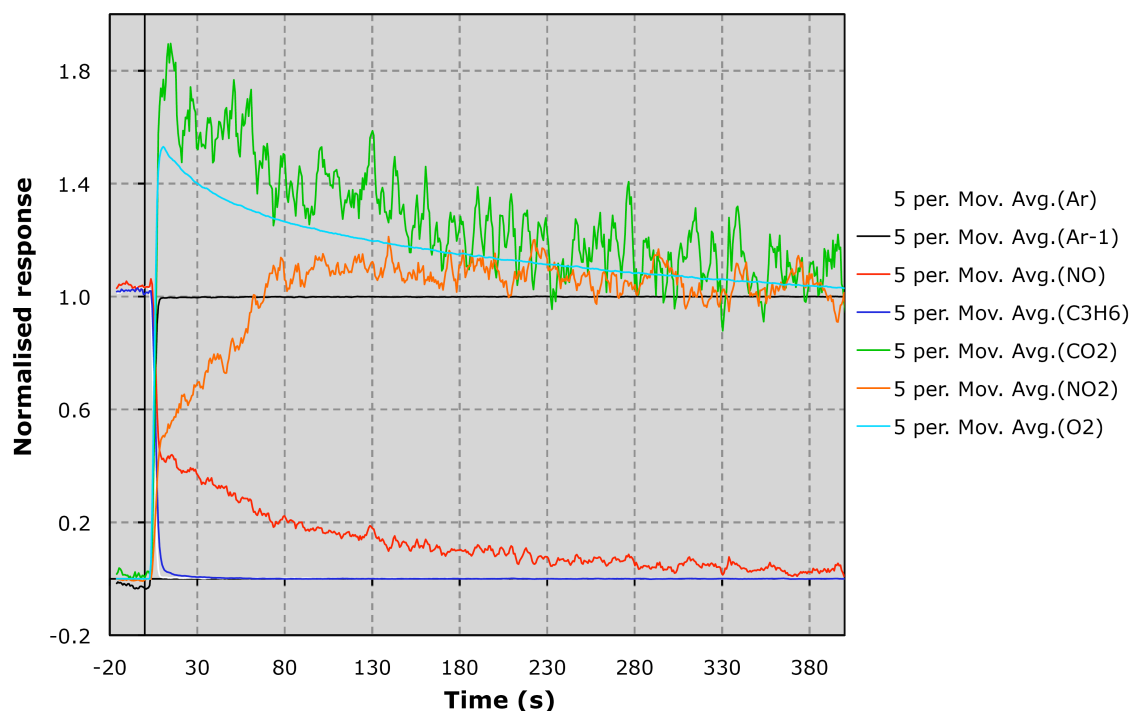


Figure 7.16. $NO/C_3H_6/Ar \rightarrow NO/C_3H_6/O_2$ switch performed at 300 °C.

While the withdrawal of O_2 yields fairly similar profiles below and above T_{max} , the system shows vastly different responses when oxygen is reintroduced to it at different temperatures. The drop of the C_3H_6 signal to the steady state levels immediately after the exchange, the initial spike above steady state levels in the CO_2 profile and its subsequent gradual decay to stationary values are all indications of a surface that had become enriched with carbonaceous species prior to the switch. Nevertheless, as the initial rise in the NO_2 profile and the concomitant fall in the NO signal show, the catalyst surface also has a relatively high concentration of NO_{ads} species that quickly react with oxygen to yield NO_2 . While the initial response shown by all signals has already been accounted for, a contribution from the response of the system to the reintroduction of a reactant whose concentration vastly exceeds that of any other species cannot be neglected. With the exception of the hydrocarbon, all of the species seem to follow two distinctly

different kinetics as they attain steady state. After an initially drastic rise or drop, most species then approach steady state in a more gradual fashion, presumably due to the resumption of the NO reduction reaction.

7.4. The state of the catalyst surface.

During heterogeneous catalysis, the adsorption (either molecular or dissociative) of at least one of the reactants is a prerequisite for catalysis to occur. Once adsorption has taken place, the resulting adsorbed species can then react with other adsorbed species or with reactants in the gas phase. Probing the state of a catalyst at a given temperature is complicated by the different rates at which the different species adsorb and react. However, it is possible to compound a picture of a catalyst surface in steady state since, by definition, an equilibrium between the aforementioned phenomena must be established at this condition. Indeed, it is through the disruption of this equilibrium that reaction transients allow for the state of the catalyst to be elucidated.

Therefore, the first condition that must be met to perform a transient mechanistic study is to ensure the catalysts is operating at equilibrium, i.e., displaying a constant reaction rate. For continuous tubular (plug-flow) reactors like the one used in this work, the reaction rate can be assumed constant over the catalyst bed length only at low conversion levels [239]. Thus, at the temperature of maximum activity (T_{\max}), the very high conversion of reactants into products precludes the use of transients to probe the state of the catalyst surface. However, this state can be interpolated from the state of the catalyst at temperatures above and below T_{\max} . It is therefore necessary to consider all the possible adsorptions and reactions that can take place on the catalyst surface before discussing which of these are favored at a particular temperature.

The HC-SCR reaction in its simplest form involves three reactants (O_2 , NO and C_3H_6), each one exhibiting different degrees of complexity in its adsorption on a clean Pt surface. The only route for O_2 to adsorb on Pt is dissociatively, oxygen adatoms being the only possible outcome. NO can undergo both molecular and dissociative adsorption, which generate NO_{ads} or nitrogen and oxygen adatoms, respectively. C_3H_6 can also

follow both adsorption paths, but the higher number of atoms in this molecule make possible for it to display a variety of cracking patterns when dissociatively adsorbing, thus increasing the number of potential resulting species. For convenience, these hydrocarbon-derived species can be given the general formula C_xH_y .

The catalyst surface can therefore contain nitrogen and oxygen adatoms, as well as NO_{ads} and C_xH_y species. Further, these species can react with each other to yield adsorbed HC-SCR reaction products (CO_2 , H_2O , N_2 , N_2O or NO_2) and/or intermediates (C_xH_y , $C_xH_yO_z$ or $C_xH_yO_zN_w$) that need to undergo additional reactions before evolving into these reaction products. Alternatively, the adsorbed species can react with gas phase reactants and even with desorbed products, giving the system a tantalizing complexity. Fortunately, the systematic application of the transient technique (in which only one reactant is withdrawn or reintroduced at a time) can greatly simplify the analysis of the catalyst state at a given temperature.

7.4.1. The state of the Pt/fMWCNTs catalyst below T_{max} .

The most relevant insight gained through experiments performed below the temperature of maximum activity is that at this temperature NO adsorption is favored over O_2 adsorption. In light of this, the low concentration of oxygen adatoms in the catalyst surface points to the fact that although NO may undergo both molecular and dissociative adsorptions, the former is clearly favored. These experiments also show that, at this temperature, the Pt surface is rich in C_3H_6 -derived species (C_xH_y). Thus, the most prevalent species on the catalyst surface should be C_xH_y and NO_{ads} species, as well as their reaction product: partially oxidized hydrocarbon species ($C_xH_yO_zN_w$). Given the fact that the presence of oxygen is required for the HC-SCR reaction to occur and that the surface coverage by O_{ads} is low, it seems that these adsorbed species need to react with gas phase oxygen in order to become HC-SCR reaction products. Indeed, the latter appears to be the favored reaction at this temperature. However, $C_xH_yO_zN_w$ species appear to follow two distinct reaction paths: one leading to the production of N_2 , the other to the production of N_2O . Since oxygen adatoms are believed to be involved in the

production of NO₂, a low surface concentration of O_{ads} species is also consistent with the almost negligible amount of NO₂ observed at temperatures below T_{max}.

7.4.2. The state of the Pt/fMWCNTs catalyst above T_{max}.

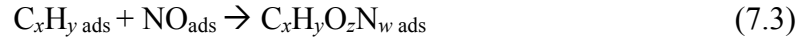
Above the temperature of maximum activity, oxygen adsorption is favored over NO adsorption, which has several consequences. First and foremost, the catalyst surface becomes enriched with oxygen adatoms. Obviously, this favors the occurrence of oxidation reactions which C_xH_y and NO_{ads} species undergo to produce CO₂ and NO₂, respectively. These oxidation reactions show very fast kinetics. This considerably reduces the surface concentration of C_xH_y and NO_{ads} species that can react and produce partially oxidized hydrocarbon species (C_xH_yO_zN_w), which in turn hinders the occurrence of the HC-SCR reaction. The amount of surface C_xH_y species is further reduced by their reaction with NO₂, which is also known to follow fast kinetics.

7.4.3. The state of the Pt/fMWCNTs catalyst at T_{max}.

According to Obuchi *et al.*, at the temperature of maximum activity, the amount of partially oxidized hydrocarbon intermediates should also reach a maximum [44]. Therefore, at T_{max}, the surface of the catalyst must show a maximum with respect to the adsorption of both C₃H₆ and NO and/or the fastest reaction kinetics between C_xH_y and NO_{ads} to yield C_xH_yO_zN_w intermediates. This is consistent with the results of XPS studies in which at T_{max} Pt was found to be both in the metallic state and as Pt²⁺ [209]. Indeed, Pt sites in which partially oxidized hydrocarbon species are adsorbed should bear a charge, while metallic Pt sites should be generated when C_xH_yO_zN_w species react with gas phase oxygen to yield HC-SCR products.

7.5. Mechanistic conclusions.

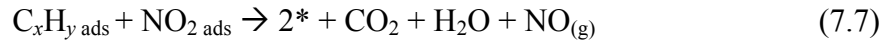
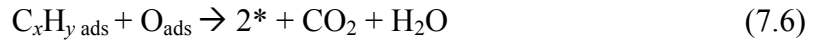
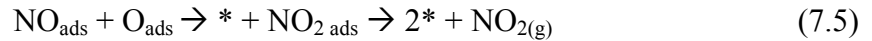
Mechanistic studies were undertaken in an attempt to gain fundamental insights which may inform further improvements to Pt/fWMTNs as a low temperature HC-SCR catalyst. Taking the results into account, the prevalence of four main reactions would amount to the ideal HC-SCR reaction cycle:



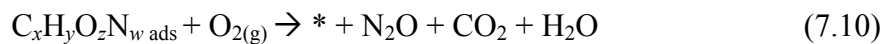
although it is possible for some of the redox reactions proposed by Burch *et al.* to occur simultaneously without negatively impacting the performance of the catalyst:



The exclusive occurrence of reactions (7.1)-(7.6) would maximize the degree to which the hydrocarbon achieves the complete reduction of NO_x , thus optimizing both the de NO_x activity and the selectivity towards N_2 shown by a supported PGM HC-SCR catalyst. However, a series of undesired reactions also seems to take place:



Reactions (7.5)-(7.7) are favored when O_2 adsorption prevails over NO adsorption (above T_{max}) and their occurrence has a negative impact on the de NO_x activity shown by the catalyst. Thus, there is a vested interest in minimizing the incidence of these last three reactions. Furthermore, in order to improve N_2 -selectivity, the occurrence of other reactions, which may also be taking place, should be avoided as well:



As mentioned in the second chapter of this dissertation, several workers have reported that although supported Rh catalysts require higher temperatures to achieve lower NO_x conversion maxima when compared to similar Pt catalysts, formulations with Rh as the active phase display wider activity windows of operation and show better N_2 -selectivity across the whole temperature range. Thus, the use of Pt-Rh/fMWCNTs alloy catalysts was investigated in an attempt to develop a formulation showing a high conversion maximum at low temperature accompanied by a wide activity window and improved N_2 -selectivity. A 1.5 wt.% Pt – 0.5 wt.% Rh/fMWCNTs catalyst was found to be quite promising, although its selectivity towards N_2O is disappointingly similar to that of the monometallic catalyst. The latter, though unfortunate, might provide valuable mechanistic clues, as proven by C_3H_6 -TPD measurements performed on the mono- and the bimetallic catalysts, as well as on bare MWCNTs and fMWCNTs supports (see previous chapter). First, it appears from the TPD profiles that a reverse spillover step involving the migration of C_3H_6 and/or C_3H_6 -derived species from the support to the metal is taking place. Second, it is clear that hydrocarbonaceous species bind more strongly to the Pt-Rh alloy than they do to Pt alone. Based on these observations, it seems that the study of reaction transients on Rh and Pt-Rh alloy HC-SCR catalysts could yield additional insights on the HC-SCR reaction mechanism on supported PGM catalysts.

Chapter 8. Preparation, Characterization and Testing of Monolithic HC-SCR MWCNTs-based Catalysts.

8.1. Introduction.

In the late 1960s, stimulated by regulations limiting automobile emissions introduced in the state of California, the car industry began to research and develop pollution abatement technologies for auto-exhausts. The U.S. Clean Air Act of 1970 expedited this process, forcing automakers to not only develop active, selective and durable catalysts able to curb automotive contaminants, but to provide for the incorporation of these formulations into the already complex makeup of internal combustion engine vehicles. The answer was found in the introduction of catalytic mufflers into the auto-exhaust line [240]. However, this approach involved a series of engineering challenges. First and foremost, it was essential to minimize the backpressure caused by the presence of a catalytic reactor in order to avoid negatively impacting engine performance. Further, it was necessary to endow catalysts with the sturdiness necessary for them to retain their physical integrity in the extreme environment of the exhaust.

When trying to solve the problem of housing a catalyst in the exhaust, one of the first proposals was to utilize alumina spheres (~1/6 in. in diameter) as the carrier for both stabilizers and precious metals, the latter being the catalytically active component. Catalysts had been traditionally manufactured in this form for years, so the packing of these “beads” into a reactor bed to be placed downstream of the engine and right before the acoustic muffler appeared to be the logical answer. In time, it was observed that the attrition experienced by the alumina particles in these beaded formulations unacceptably undermined the durability of the catalysts, which prompted the search for alternatives.

The answer was found in monolith reactors with parallel open channels whose cross-section looks like (and thus is called) a honeycomb. The name suggests the shape of the channels to be hexagonal, although they may be triangular, square or circular. Since mechanical strength and resistance to thermal shock are indispensable, ceramic was the material of choice from the onset of the monolithic honeycomb catalyst era. Cordierite (a

ceramic material with the approximate composition $2\text{MgO} \cdot 5\text{SiO}_2 \cdot 2\text{Al}_2\text{O}_3$) quickly became an industry staple due to its very low thermal expansion. Nevertheless, metal monoliths were also developed, mostly in the form of rolls of corrugated sheets of stainless steel. Besides their chemical composition, the dimensions of the monoliths were also found to be critical to achieve both a satisfactory performance and an adequate durability. Thus, to increase the geometric surface area available for the occurrence of mass transfer-controlled reactions, ceramic monoliths are typically made to have at least 300-400 cells per square inch (cpsi) in their cross-section, with wall thicknesses of *ca.* 0.15 mm and channels around 1.5 mm in diameter, corresponding to a $\sim 70\%$ open frontal area. Metal monoliths tend to incorporate thinner walls, which allow for greater cell densities (>400 cpsi) and open frontal areas of $\sim 90\%$ [2].

The catalytically active phase is introduced to these monoliths *via* standard techniques known as washcoating. One approach involves the preparation of slurry containing a high surface area support (typically γ -alumina) as well as additives (precious metals, promoters, stabilizers, etc.) into which the ceramic monolith is plunged. This slurry covers and bonds to the porous ceramic surface of the monolith, which is then dried and calcined in air at around $500\text{ }^\circ\text{C}$ to guarantee a satisfactory adherence between washcoat and monolith. An alternative method used to manufacture a honeycomb catalyst is to first washcoat the monolith with the bare alumina support, and subsequently submerge the resulting washcoated honeycomb into impregnating solutions containing the additives. Given that an excessively thick washcoat can lead to mass transfer limitations and an extremely thin washcoat is prone to be deactivated by the deposition of contaminants, the thickness of the washcoat is the result of a compromise and typically averages $\sim 30\text{ }\mu\text{m}$.

In our work, monolithic catalysts with fMWCNTs as the high surface area support and PGMs as the catalytically active phase were prepared and tested on a diesel engine for activity in the HC-SCR reaction. As mentioned in Chapter 2, MWCNTs possess an exceptional advantage over other support materials in heterogeneous catalysts, namely, the ability to be grown on substrates of complex shape. Thus, the *in situ* growth of MWCNTs on the inner channels of a stainless steel monolith was investigated as the first step in the

preparation of PGMs/fMWCNTs/metal monolith catalysts. Additional work was performed to address the issue of metal monolith-grown MWCNT functionalization, as well as the subsequent deposition of PGMs onto the resulting fMWCNTs. Finally, the resulting monolithic catalysts were tested so the effects of temperature, space velocity and C:NO_x ratio of the exhaust on catalytic performance could be assessed.

8.2. Experimental methods.

8.2.1. Growth of MWCNTs on a metal monolith.

A stainless steel 300 cpsi metal monolith (DCL, Inc., Toronto, ON) of cylindrical shape ($r=4$ cm, $h=10$ cm, $V=0.41$ L) was packed into a fused quartz horizontal reactor and placed in an electric furnace. Argon was flowed through the metal monolith while the temperature of the reactor was raised to 800 °C. Once this temperature was reached, the flow of argon was switched to a flow of 10 % H₂ in Ar and a saturated solution of ferrocene in xylenes was fed into the reactor for 1 h. The system was then allowed to cool to room temperature under an inert atmosphere. The reactor was then turned around and the run was repeated to ensure MWCNT growth throughout the entire inside of the monolith. On average, two runs yielded 7.7 g of metal monolith-supported MWCNTs.

8.2.2. Functionalization of metal monolith-grown MWCNTs with 0.5 % NO₂ in N₂.

A stainless steel 300 cpsi metal monolith coated with MWCNTs was packed into a fused quartz horizontal reactor placed in an electric furnace. Nitrogen was flowed through the metal monolith while the temperature of the reactor was raised to 300 °C. Once this temperature was reached, the flow of nitrogen was switched to 0.5 % NO₂ in N₂ and the flow maintained for 1 h. The system was then allowed to cool to room temperature under inert atmosphere. The reactor was then turned around and the run was repeated to ensure MWCNT functionalization throughout the entire inside of the monolith.

8.2.3. PGM deposition on NO₂-functionalized monolith-grown MWCNTs via the polyol method.

The appropriate amount of metal precursor(s) (H₂PtCl₆ · 6H₂O or H₂PtCl₆ · 6H₂O and RhNO₃) was dissolved in ethylene glycol and the resulting solution was stirred for 15

min. A NO₂-functionalized MWCNTs-coated 300 cpsi stainless steel monolith was then dipped in the solution and the stirring continued for 15 min. The system was then heated to 160 °C and kept at this temperature for 1.5 h, after which the monolith was turned upside down and the temperature maintained at 160 °C for a further 1.5 h. The monolith was then drained, dried, washed with deionized water, and dried again. Using this method, both a monometallic and a bimetallic monolithic catalyst were prepared. The monometallic catalyst was determined to contain 58 g Pt/cuft, whereas the bimetallic catalyst was found to contain 69 g 3:1 Pt-Rh/cuft.

8.2.4. Scanning Transmission Electron Microscopy (SEM) analysis.

Prior to analysis, samples were submitted to a standard gold coating procedure. SEM observations were performed using a Hitachi-S2700 instrument equipped with a LaB₆ electron gun working at 15 KeV.

8.2.5. Determination of the precious metal content of PGM/NO₂-fMWCNTs/metal monolith catalysts.

To determine the precious metal density of PGM/NO₂-fMWCNTs/metal monolith catalysts, the filtrate and washings from the preparations were collected, analyzed *via* PIXE, and the amount of metal successfully deposited was calculated by difference. Prior to PIXE analysis, the samples were poured into an 8 mL Teflon cup and covered with a Kapton film through which the sample was irradiated.

8.2.6. Testing of monolithic catalysts in a diesel engine.

Tests were conducted at Oak Ridge National Laboratory, in the Fuels, Engines, and Emissions Research Center. A Mercedes OM668 4-cylinder, 1.7-liter common-rail diesel engine was coupled to a motoring DC dynamometer. The engine, which is a 1999 model used in the Mercedes A170 in Europe, has a bore and stroke of 80 mm and 84 mm respectively, and it has a rated power output of 66kW (89 hp) at 4200 rpm. Modifications to the engine included the addition of an electronic intake throttle, an electronically controlled high flow exhaust gas recirculation (EGR) valve (in lieu of the stock vacuum-operated valve), and an EGR cooler [241]. Additionally, the factory engine control

module was replaced with a rapid development engine controller based on a dSpace® MicroAutoBox. This rapid development system (RDS) was developed in partnership with Ricardo, Inc., and provides complete control over all engine electronics, including timing, duration, and number of fuel injection events, fuel rail pressure, intake throttle, EGR valve, and turbocharger wastegate.

Temperature sweep experiments were performed by increasing the engine load in stepwise fashion at fixed engine speed (1500 rpm). No EGR was employed. The catalyst volume was 0.41 L. Experiments were conducted at gas hourly space velocities (GHSVs) of either 30,000 or 50,000 h⁻¹; to obtain the desired exhaust gas flows, a slipstream was taken from the main exhaust flow. In the experiments propene was used as the reductant, supplied externally from a gas cylinder. The propene was injected at a distance of ~15" upstream of the catalyst face, in a turbulent area immediately downstream of the split in the exhaust to the slipstream. The mixed gas passed through an elbow and expansion cone (from 2.5" pipe to 3.5" pipe) prior to the catalyst. To monitor the temperature across the catalyst, thermocouples were placed approximately 2" from the front catalyst face and about 1.5" from the catalyst face on the downstream side.

Dual conventional emissions benches were used for raw exhaust sampling. These benches use California Analytical Instruments® (CAI) non-dispersive infrared (NDIR) analyzers for carbon monoxide (CO) and carbon dioxide (CO₂), heated chemiluminescence detectors (HCLD) for NO_x, and heated flame ionization detectors (HFID) for total hydrocarbons (HC). A Nicolet Rega 7000 Fourier Transform InfraRed (FTIR) analyzer was used for quantifying nitrous oxide (N₂O) in the diluted exhaust.

feed concentrations varied with engine set point, however, measured concentrations typically fell within the following ranges: 100-1000 ppm for NO, 0-100 ppm for NO₂, 6-13 % for CO₂, 0-1400 ppm for CO, 25-90 ppm for HC, and 5-14 % for H₂O.

The experimental methods used for TEM, TEM-EDS, TGA, XPS, porosity and surface analyses have already been described in Chapter 3.

8.3. Preparation and characterization of monolithic catalysts.

8.3.1. Growth of MWCNTs on a metal monolith.

In order to verify the feasibility of supporting MWCNTs on automotive monoliths, the growth of MWCNTs was attempted on a commercial 3" x 4" metallic monolith (300 cpsi, obtained from DCL Int. Inc.). In a typical experiment, the monolith was placed inside a nanotube synthesis reactor, consisting of a quartz tube reactor surrounded by a tube furnace. After purging the system with inert gas, a solution of ferrocene in xylenes was continuously introduced at a rate of 13 mL/hr via a syringe pump into a pre-heat section maintained at 200 °C. The xylenes/ferrocene vapors produced in this pre-heater were carried into the main part of the reactor, maintained 800 °C, by a flow of 10 % H₂/N₂. The walls of the monolith provide a surface on which MWCNTs grow perpendicularly in parallel alignment. At the end of the run, the system was allowed to cool to room temperature and the monolith recovered and weighed. The weight of the grown MWCNTs was then calculated by subtracting the weight of the monolith prior to the run and averaged 7.7 g. Visual inspection revealed the presence of a continuous and apparently uniform coating of MWCNTs on the monolith. SEM measurements were subsequently performed in order to characterize the morphology of the supported MWCNTs. Figure 8.1 shows a photograph of the coated monolith and a SEM image of the MWCNT coating which reveals the high degree of nanotube alignment.

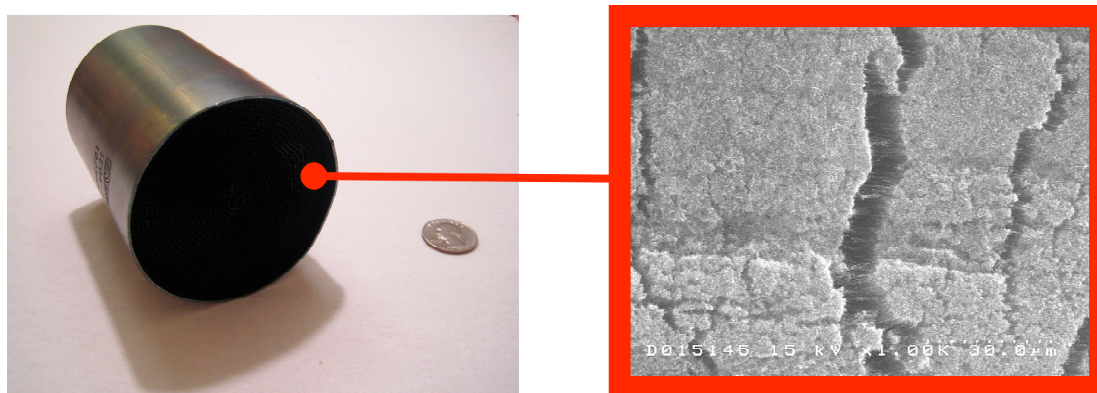


Figure 8.1. Photograph of a metal monolith coated with MWCNTs and SEM image of the MWCNTs showing their alignment.

8.3.2. Precious metal deposition on monolith-grown MWCNTs.

The most promising low temperature HC-SCR formulations prepared in this project utilized functionalized multi-walled carbon nanotubes (fMWCNTs) as the catalyst support and impregnation as the preparation method. However, it proved possible to prepare catalysts of fairly comparable performance using a polyol method for precious metal deposition and/or by using pristine MWCNTs as the support (at low Pt loadings). This is particularly fortunate when trying to deposit precious metals on metal monolith-grown MWCNTs, given that any attempt to functionalize the supported nanotubes with mineral acids would corrode the monolith, thus compromising its physical integrity. Further, the use of the impregnation method is discouraged since the evaporation of the solvent would lead to a gradient in the PGM precursor concentration and result in poor metal dispersion. Therefore, the effectiveness of the polyol method to deposit Pt particles on untreated monolith-grown MWCNTs was investigated, since this approach would eliminate the need for MWCNT functionalization.

A recently published modified polyol method [242] was first followed. This method involves dissolving chloroplatinic acid (CPA) in ethylene glycol (EG) and heating the resulting solution in order to reduce the metal and produce a colloid, which is then put in contact with the support (monolith-grown MWCNTs in this case). However, when this method was attempted, a problem immediately arose: the colloidal particles tended to aggregate and precipitate from the suspension. Given that this would negatively affect the Pt particle size of the product, it was decided to place the CPA in EG solution in contact with the support before carrying out the reduction. By so doing, colloidal Pt particles might be anchored by the support as soon as they formed, avoiding their aggregation and improving the metal dispersion in the final product. Unfortunately, the problem described above persisted, indicating that although Pt particles were forming, they were not being deposited on the support. Indeed, when the metal loading of the products of these two preparations was determined by means of PIXE, the Pt content was considerably below that targeted. In an attempt to confirm the conclusions gathered from the PIXE analyses, some of the scraped material was observed under the transmission

electron microscope. As can be seen in Figure 8.2, some relatively large particles (~ 20 nm in diameter) were observed and confirmed to be Pt by means of TEM-EDS.

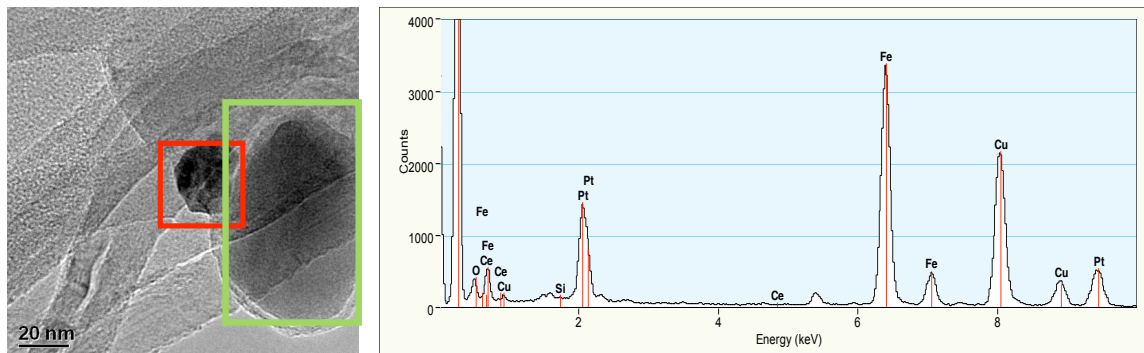


Figure 8.2. TEM image of a Pt/MWCNTs/metal monolith catalyst and EDS spectrum of the area highlighted in red. An iron particle (the catalyst used in the production of the MWCNTs) is highlighted in green.

Particles as small as 2 nm in diameter were also observed (see Figure 8.3), but their size impeded their elemental analysis by means of TEM-EDS. In general, however, relatively few Pt particles were found, consistent with the elemental analysis results.

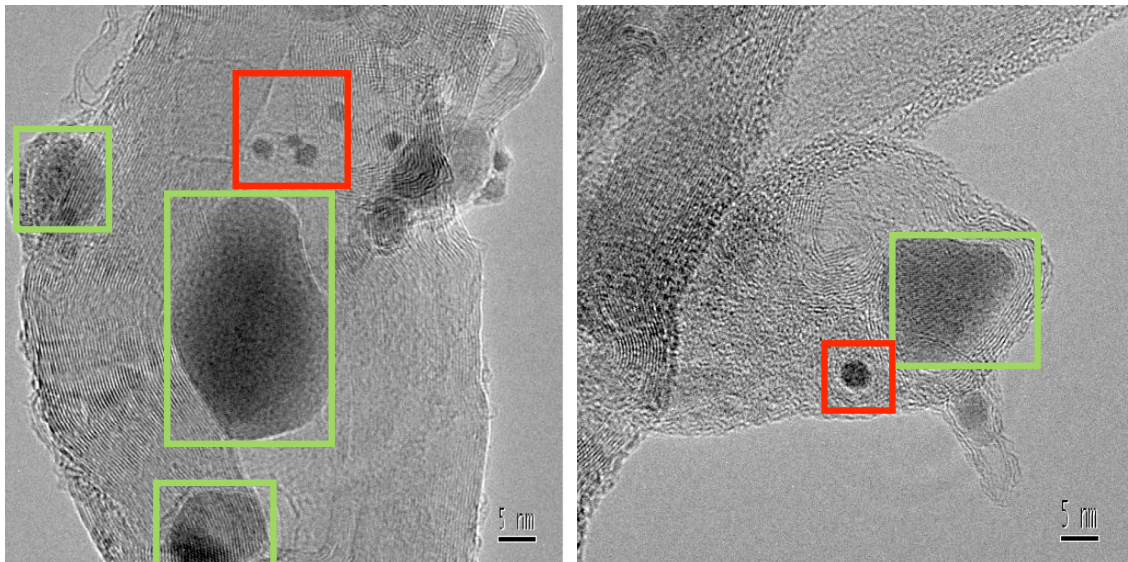


Figure 8.3. TEM image of a Pt/MWCNTs/metal monolith catalyst showing both Pt metal particles of 2-5 nm in diameter (red) and iron catalyst particles remaining from the MWCNT synthesis (green).

Evidently, acid activation of the MWCNTs is a prerequisite for the deposition of high concentrations of Pt particles on nanotubes *via* the polyol method, as has been reported by some researchers [169]. Acid activation introduces functionalities which can anchor Pt ions prior to their reduction, thus facilitating metal deposition and improving the dispersion at high Pt loadings.

8.3.3. Activation of monolith-grown MWCNTs.

In Chapter 5, it has been shown that the use of functionalized MWCNTs as catalyst support yields formulations with improved HC-SCR performance. Further, as described above, activation of the MWCNT support is necessary to obtain precious metals deposition on the surface of the monolith-tethered MWCNTs. With this in mind and without forgetting that the use of mineral acids would be detrimental to the metal monolith, the surface modification of the monolith-grown MWCNTs was attempted using alternative methods. A first attempt was made to activate MWCNTs with the use of an oxygen plasma. Unfortunately, this process was found to be generally ineffective.

A second attempt was made following a recent report in the literature concerning the use of polyethyleneimine (PEI) as a functionalizing agent for MWCNTs [242], in which a three-step approach was used to prepare a Pt/fMWCNTs/metal monolith catalyst. The first step involved the adsorption of PEI on the surface of the MWCNTs as a means to functionalize them. In the second step, the PEI-fMWCNTs/metal monolith was contacted with an aqueous CPA solution, aiming for the anchoring of the Pt to the functionalities introduced in the first step. In the third and last step, H₂ was flowed through the device at 350 °C, trying to accomplish both the reduction of the metal and the elimination of the PEI. Unfortunately, during the anchoring step the formation of a black precipitate could be observed, again suggesting that although Pt particles were formed, the particles failed to deposit on the surface of the MWCNTs. Several variations of this method were essayed in an attempt to achieve deposition of the Pt particles, however, the problem persisted.

Scouting experiments examining the adsorption of a variety of alternative surfactants including glycolic acid, octadecyl trimethyl ammonium bromide, sodium dodecyl sulfate and sodium dodecyl benzene sulfonate were also performed in an attempt to functionalize the MWCNTs without the use of mineral acids. Unfortunately, these experiments also proved unsuccessful.

In view of this, the use of NO₂ was investigated as a means to functionalize the monolith-grown MWCNTs prior to Pt deposition by the polyol method. Preliminary TGA studies were performed in order to determine the feasibility of this nanotube activation method. In these experiments, pristine MWCNTs were exposed to a flow of 0.5 % NO₂ in N₂, ramped to a given temperature at a rate of 5 °C/min and kept at this temperature for 3 or 6 h. Figure 8.4 shows the results of these experiments.

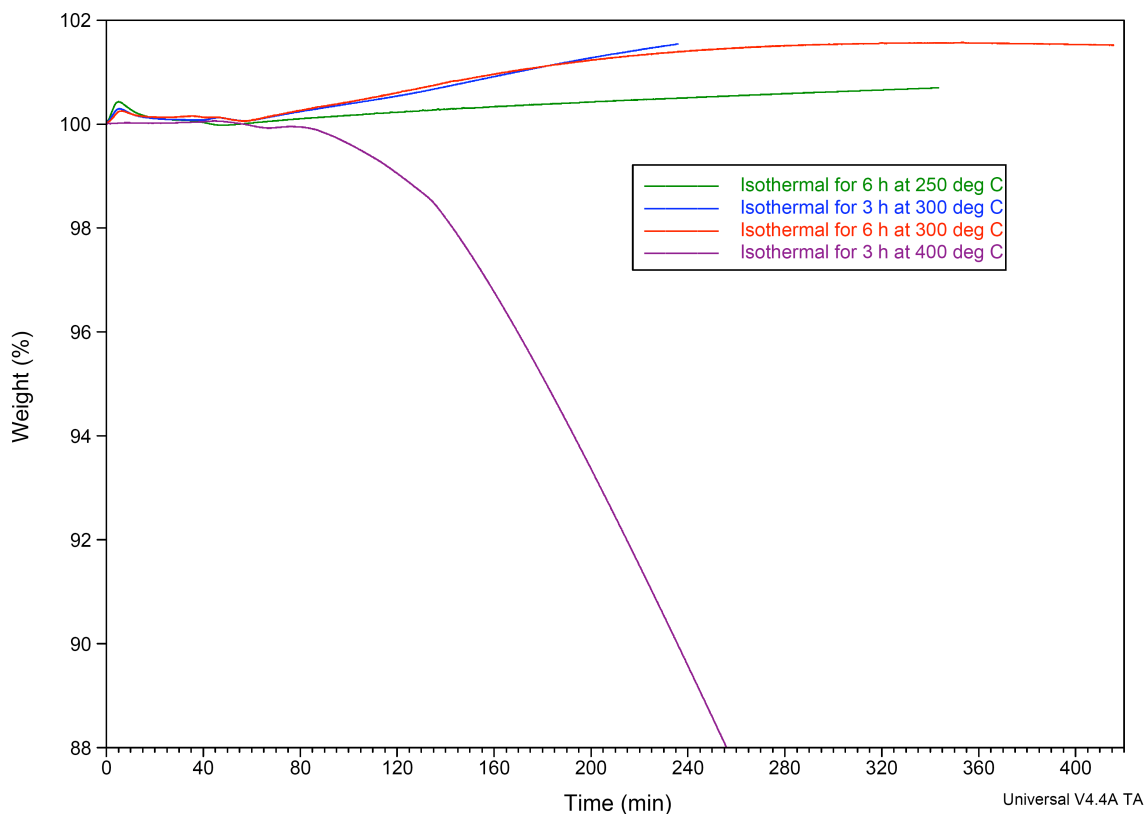


Figure 8.4. Combined TGA plot of MWCNTs thermally treated under a flow of 0.5 % NO₂ balance N₂ (all samples were initially ramped to the indicated temperature at a rate of 5 °C/min).

From the figure, it can be seen that the treatment at 400 °C is too aggressive, leading to an unacceptable weight loss in the MWCNTs. On the other hand, when this temperature was reduced to 250 °C the material experienced a moderate weight gain (~1 %), consistent with nanotube functionalization. In an attempt to increase the latter, pristine MWCNTs were then treated at 300 °C and the sample showed a weight gain of *ca.* 1.5 % after 3 h (no further weight gain was observed when the treatment was prolonged). In an attempt to confirm the latter result and in order to characterize the resulting material, several grams of pristine MWCNTs were submitted to the same treatment (a flow of 0.5 % NO₂ in N₂ at 300 °C for 3 h). Table 8.1 shows the surface properties of the resulting NO₂-fMWCNTs and compares them to those of pristine MWCNTs and fMWCNTs obtained by activation methods involving the use of mineral acids.

Table 8.1. Surface properties of pristine MWCNTs, acid treated MWCNTs and NO₂-treated MWCNTs.

Sample / treatment	Surface area (m ² /g)	Pore volume (cm ³ /g)
As synthesized nanotubes	42.1	0.182
HNO ₃ -treated (4 h reflux)	51.2	0.160
1:1 H ₂ SO ₄ -HNO ₃ -treated (2 h bath sonication)	46.5	0.182
1:1 H ₂ SO ₄ -HNO ₃ -treated (4 h reflux)	59.2	0.272
0.5 % NO ₂ -treated (3 h at 300 °C)	51.6	0.199

As the table shows, in terms of the surface area and the pore volume of the resulting product, a treatment involving the use of NO₂ is comparable to treatments involving reflux in HNO₃ or bath sonication in a 1:1 H₂SO₄-HNO₃ mixture.

The elemental analysis (by combustion) of the NO₂-treated MWCNTs was attempted, however, no valuable information could be withdrawn from the results. The latter is due to the fact that in this method the oxygen concentration is calculated by difference and the calculation is complicated by the weight gain caused by the formation of the ash (iron oxide formed from the residual catalytic particles used in the MWCNTs synthesis). Thus, the elemental analysis of NO₂-fMWCNTs was performed *via* an alternative technique, namely, XPS. Indeed, NO₂-fMWCNTs were submitted for an XPS study of the type previously performed on pristine and acid treated MWCNTs (see section 3.4). These measurements provided information not only on the surface elemental composition of NO₂-fMWCNTs, but also on the nature of the functional groups introduced by the NO₂ treatment. Figure 8.5 shows the O 1s region within the XPS spectra of NO₂-fMWCNTs, while Table 8.2 shows their atomic surface composition and Table 8.3 shows the amount of oxygen present in different chemical states. For comparison purposes, pristine and acid treated MWCNTs have also been included in Tables 8.2 and 8.3 (binding energy assignments were based on both the X-ray Photoelectron Spectroscopy Database of the National Institute of Standards and Technology (NIST) [140] and previous literature reports [141,142]).

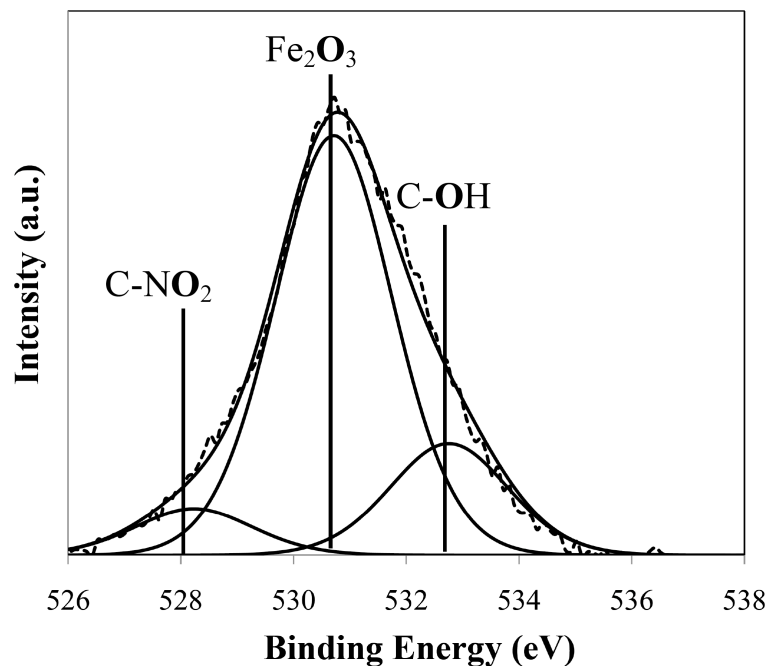


Figure 8.5. O 1s region in the XPS spectrum of NO₂-fMWCNTs.

Table 8.2. Elemental surface analysis (by XPS) of pristine, NO₂-treated and acid-treated MWCNTs.

Sample / treatment	at.%C from C 1s	at.%N from N 1s	at.%S from S 2p	at.%O from O 1s
As synthesized nanotubes	95.2	0.3	-	4.5
0.5 % NO ₂ -treated (3 h at 300 °C)	91.4	0.6	-	8.0
1:1 H ₂ SO ₄ -HNO ₃ -treated (4 h reflux)	84.6	0.7	0.1	14.6

Table 8.3. XPS quantification of oxygen present in different chemical states (% of total oxygen analyzed) calculated from O 1s peak fitting.

Sample / treatment	Fe ₂ O ₃	C-NO ₂	C-OH	-C=O	C-OQ-R(H)
As synthesized nanotubes	64.5	-	35.5	-	-
0.5 % NO ₂ -treated (3 h at 300 °C)	72.6	8.0	19.4	-	-
1:1 H ₂ SO ₄ -HNO ₃ -treated (4 h reflux)	18.4	2.8	-	50.9	27.9

As Table 8.2 shows, the NO₂ treatment causes an increase in the O and N content of the nanotubes and a concomitant decrease in their C content. This points to the introduction of O and N containing functional groups to the nanotube surface. A comparison between the surface composition of MWCNTs functionalized with NO₂ and with 1:1 H₂SO₄-HNO₃ shows the latter treatment to achieve a higher degree of functionalization, which is unsurprising given the relative aggressiveness of the treatments.

From the data presented in Table 8.3, the effect of NO₂ on the nanotubes, particularly with respect to the nature of the functionalities introduced by the acid treatment can be inferred. First, judging from the higher amount of oxygen present as iron oxide, NO₂ can be deemed capable of opening the nanotube tips, thus exposing and subsequently oxidizing residual iron particles from MWCNTs synthesis. However, this increase in Fe₂O₃ can also be due to NO₂ causing a diminution in the amount of -OH present at the surface, which would augment the contribution of oxygen in Fe₂O₃ towards the total. In turn, the partial elimination of -OH groups can be attributed to the fact that these functionalities are present in defect sites on pristine MWCNTs, which would be more reactive towards a strong oxidizing agent such as NO₂. Finally, it appears that the favored products of NO₂ oxidation are MWCNT-tethered nitro groups, which may be introduced to the nanotube surface at the expense of -OH functionalities.

Encouraged by these results, a MWCNTs-coated metal monolith was then submitted to the same conditions to obtain metal monolith-grown NO₂-functionalized multiwalled

carbon nanotubes (NO₂-fMWCNTs) onto which the deposition of Pt by the polyol method was subsequently attempted. Reassuringly, during the course of the metal deposition no colloidal particles could be seen precipitating from the suspension, suggesting the successful deposition of Pt onto the monolith-grown NO₂-fMWCNTs. In order to confirm that the metal deposition had indeed taken place, a small amount of carbonaceous material was scrapped from the monolith and observed under the TEM. Figure 8.6 and Figure 8.7 show TEM micrographs for a Pt/NO₂-fMWCNTs/metal monolith and a 3:1 Pt-Rh/NO₂-fMWCNTs/metal monolith catalyst, respectively.

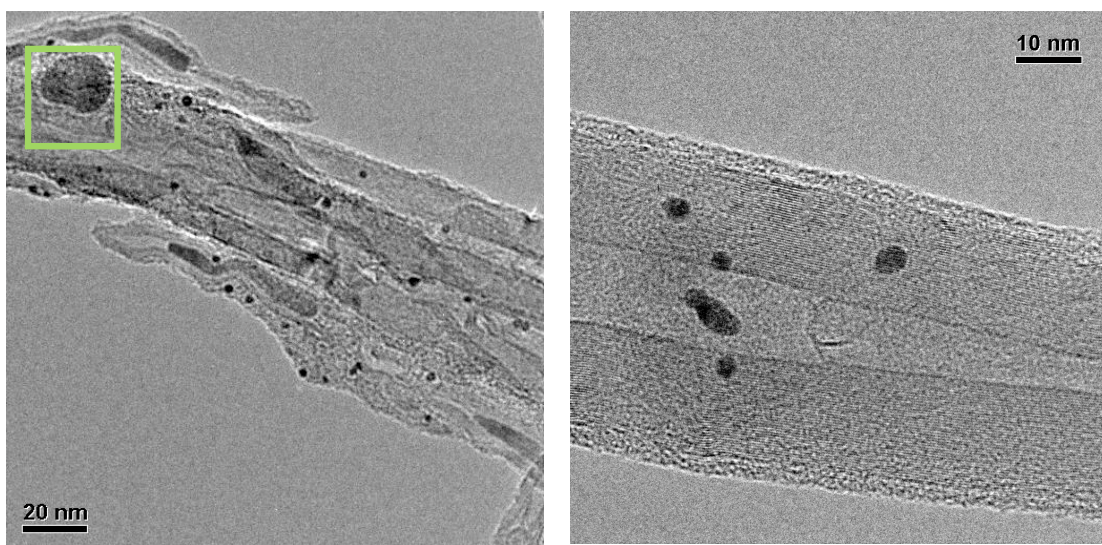


Figure 8.6. TEM micrographs of Pt/NO₂-fMWCNTs/metal monolith (an iron catalyst particle remaining from the MWCNT synthesis is highlighted in green).

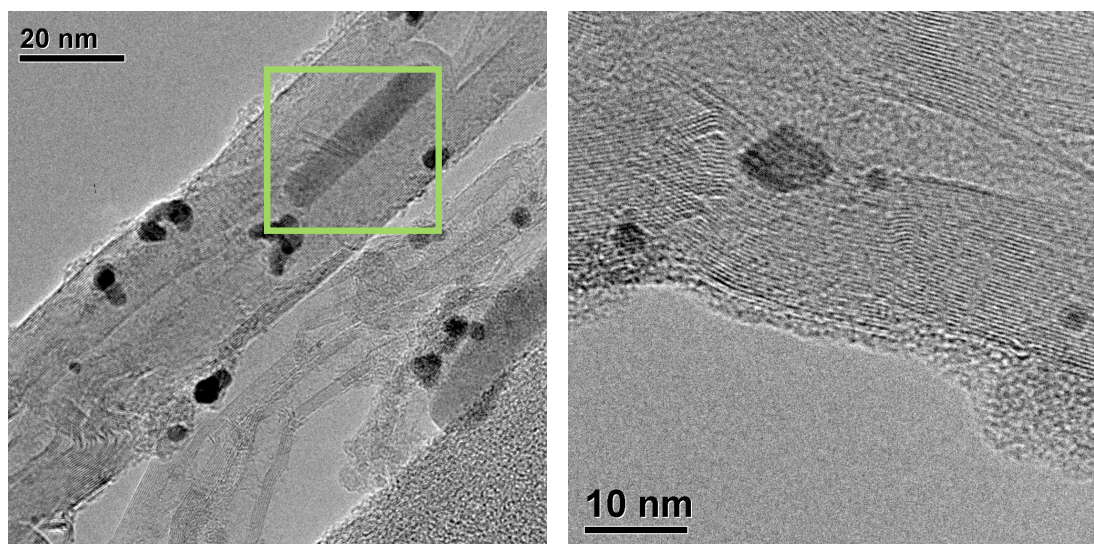


Figure 8.7. TEM micrographs of 3:1 Pt-Rh/NO₂-fMWCNTs/metal monolith (an iron catalyst particle remaining from the MWCNT synthesis is highlighted in green).

From the figures, it is evident that in both cases metal deposition onto the monolith-grown NO₂-fMWCNTs indeed took place and that particles of *ca.* 5 nm in diameter were produced. Finally, in order to quantify the amount of metal successfully deposited, the washings of each preparation were analyzed *via* PIXE and the amount of metal deposited was calculated by difference. By this method, the monometallic catalyst was determined to contain 58 g Pt/cuft, whereas the bimetallic catalyst was found to contain 69 g 3:1 Pt-Rh/cuft.

8.4. Engine tests.

8.4.1. Pt/NO₂-fMWCNTs/metal monolith catalyst.

Engine tests on the monolith catalysts were performed at Oak Ridge National Laboratory, using a 4-cylinder, 1.7-liter common-rail diesel engine coupled to a motoring DC dynamometer. Details of the experimental set-up have been described in the experimental methods section of this chapter (*vide supra*). To expedite the testing, and to provide a comparison with microreactor data collected on the powder catalyst samples, propene was used as the reductant, supplied externally from a gas cylinder. Figures 8.8 and 8.9

summarize the results of experiments in which the average catalyst temperature was varied at constant space velocity (corresponding to $30,000 \text{ h}^{-1}$ and $50,000 \text{ h}^{-1}$, respectively) using a fixed C:NO_x ratio of 8.

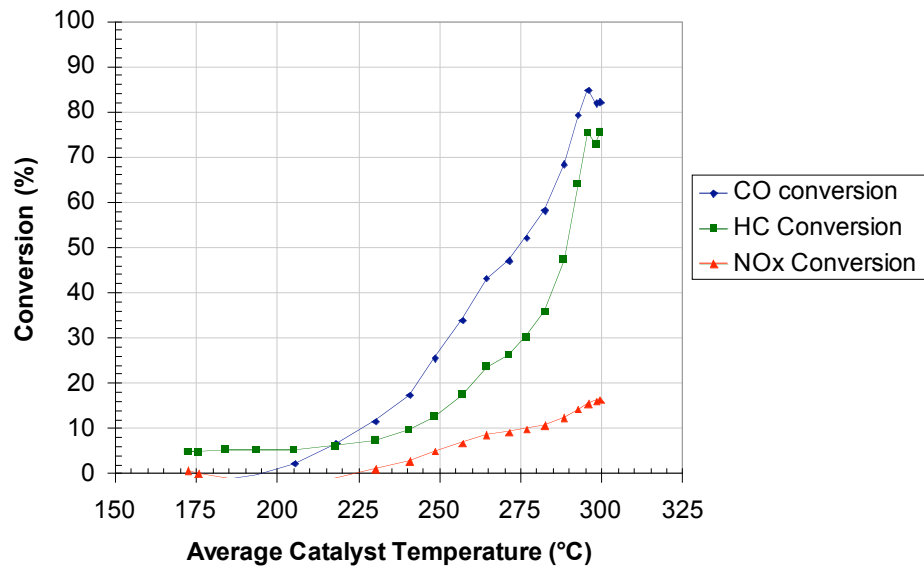


Figure 8.8. Results of temperature sweep for Pt/NO₂-fMWCNTs/metal monolith catalyst. GHSV = $30,000 \text{ h}^{-1}$, C:NO_x = 8:1.

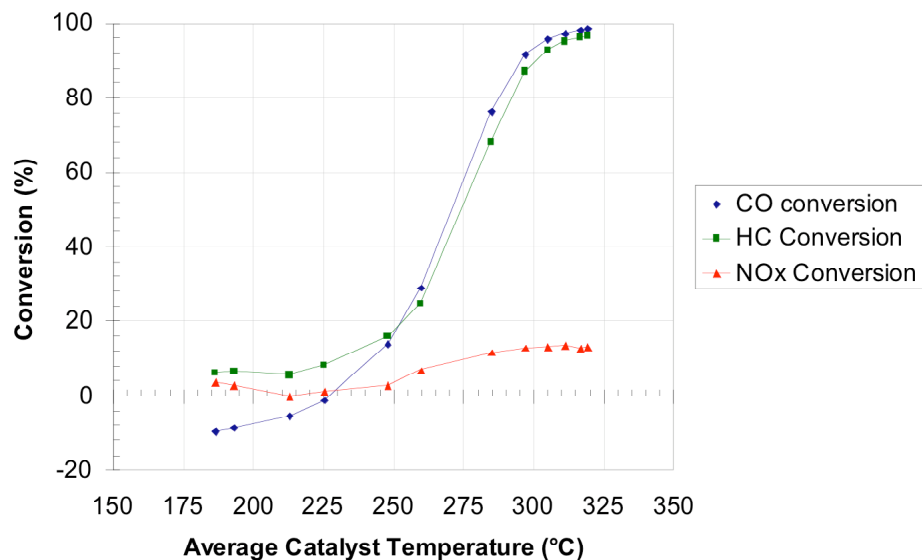


Figure 8.9. Results of temperature sweep for Pt/NO₂-fMWCNTs/metal monolith catalyst. GHSV = 50,000 h⁻¹, C:NO_x = 8:1.

From these results it is apparent that while the catalyst is moderately active for the conversion of CO and hydrocarbons (the latter being mostly propene), the NO_x reduction activity is low. Rather surprisingly, NO_x conversion increases with temperature up to 300 °C, this having been fixed as the maximum operating temperature of the catalyst (in order to avoid any possible thermal damage). This contrasts with results obtained in microreactor tests (see Table 5.2), in which the temperature of maximum NO conversion (T_{max}) was found to fall in the range 205-225 °C for MWCNT-supported Pt catalysts. Direct comparison of the results of powder and monolith catalyst tests are hampered by the considerable difference in effective space velocity used in the two types of test. In the latter case, the GHSV is calculated on the basis of the entire monolith volume and the effective GHSV is therefore much higher than for a powder catalyst sample; this alone may explain the difference in NO_x reduction activity. Additionally, there are several other possible factors that may contribute to the high T_{max} value: (i) the actual Pt loading may be lower than indicated by chemical analysis of the filtrate and washings resulting from the catalyst preparation (a low concentration of catalytically active sites would be

expected to result in a shift in the HC, CO and NO_x light-off curves to higher temperature); (ii) the bulk Pt dispersion might be worse than indicated by TEM, which would again represent a low concentration of active sites; and (iii) the catalyst might have been inhibited by components in the exhaust gas. Note that in the case of (i), a low Pt loading would also result in low NO_x conversion. In the case of a poor Pt dispersion, the NO_x conversion would not necessarily be decreased according to literature data [29,66,75,170]; however, a shift in the T_{max} to higher temperature might be expected, given that that this is tied to the light-off temperature of the hydrocarbon reductant. As regards the exhaust gas composition, while this was inevitably somewhat different to the feed used in the microreactor experiments, it seems unlikely that this alone could produce such a significant deviation in results. In order to address these issues, post mortem analyses were performed on the Pt and Pt-Rh monolith catalysts used in this study in an attempt to directly assess metal dispersions.

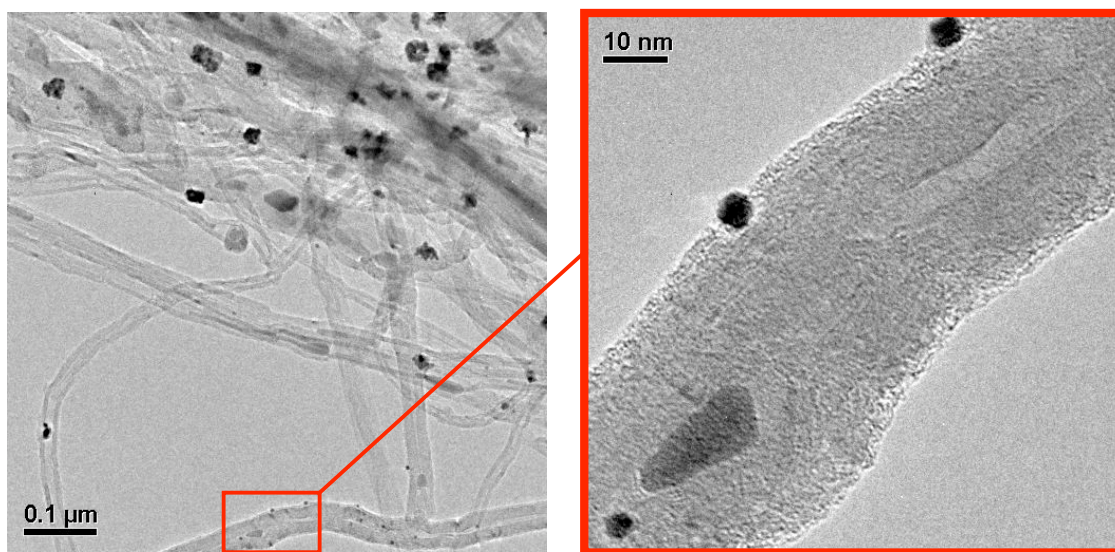


Figure 8.10. Low magnification TEM micrograph of post-mortem Pt/NO₂-fMWCNTs/metal monolith (left) and a close-up of the highlighted area (right).

Interestingly, the particle size distribution within the post-mortem monolithic catalysts appeared to be bimodal, most particles showing diameters around 5 and 20 nm (similar observations were made on both the monometallic and the bimetallic catalysts). It appears that during engine testing the catalysts experience some degree of sintering. As

stated above, this could potentially increase the light-off temperature of the hydrocarbon, which would in turn contribute to the shift of T_{\max} to higher temperatures.

Finally, it should be noted that although the propene was injected in a turbulent area upstream of the catalyst, mixing may have been less than optimal. While this would not be expected to shift the T_{\max} , it would negatively affect the NO_x conversion.

Comparison of the data in Figures 8.8 and 8.9 reveals that increasing the space velocity from $30,000 \text{ h}^{-1}$ to $50,000 \text{ h}^{-1}$ had only a minor effect on the NO_x , HC and CO conversion. NO_x conversion peaked at around 17 % at the lower GHSV and 13.5 % at the higher value, while the CO and HC light-off appeared slightly better at $50,000 \text{ h}^{-1}$ (as reflected in the temperature required for 50 % conversion); the differences were small, however, and may be due to a slight shift in the operating conditions. The relatively low NO_x conversion hampered the measurement of accurate product selectivities; however, based on N_2O concentrations measured by FT-IR (data not shown) the selectivity to N_2O fell in the range ~35-100 %.

8.4.2. 3:1 Pt-Rh/ NO_2 -fMWCNTs/metal monolith catalyst.

The results of temperature sweep experiments performed using the 3:1 Pt-Rh/ NO_2 -fMWCNTs/metal monolith catalyst are summarized in Figures 8.11 and 8.12. As before, space velocities of $30,000 \text{ h}^{-1}$ and $50,000 \text{ h}^{-1}$ were employed, respectively, at a fixed C: NO_x value of 8.

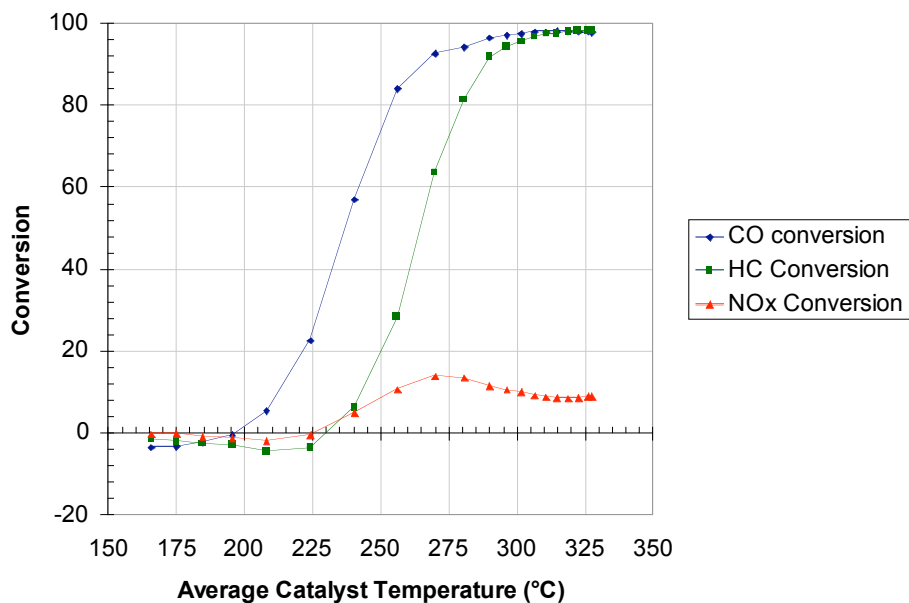


Figure 8.11. Results of temperature sweep for 3:1 Pt-Rh/NO₂-fMWCNTs/metal monolith catalyst. GHSV = 30,000 h⁻¹, C:NO_x = 8:1.

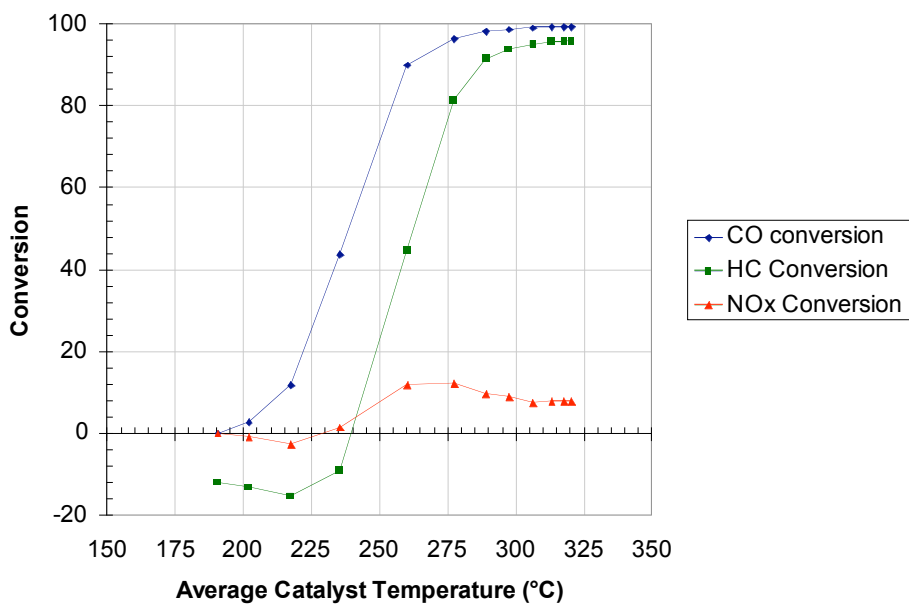


Figure 8.12. Results of temperature sweep for 3:1 Pt-Rh/NO₂-fMWCNTs/metal monolith catalyst. GHSV = 50,000 h⁻¹, C:NO_x = 8:1.

As found for the Pt catalyst, the temperature of maximum NO_x conversion for the 3:1 Pt-Rh catalyst is shifted significantly relative to the earlier microreactor tests. From Figures 8.11 and 8.12 a T_{max} of ~270 °C is apparent, as compared to the T_{max} of 200 °C reported in Table 5.2. In comparison to the Pt catalyst, the Pt-Rh analogue showed slightly higher activity for CO and HC oxidation at both space velocities examined, while the NO_x conversion was comparable.

In order to investigate the effect of the reductant:NO_x ratio on catalyst performance, runs were conducted at fixed inlet temperature (270 °C) and space velocity (50,000 h⁻¹). As shown in Figure 8.13, increasing the C:NO_x ratio resulted in a progressive increase in NO_x conversion up to a maximum value of 18 %, obtained at a C:NO_x ratio of 17. Also of note is the observation that above a C:NO_x ratio of ~14 the HC and CO conversions started to decline; this is likely due to the fact that at such high C:NO_x ratios the catalyst surface is mainly covered by hydrocarbons, thereby preventing the adsorption of sufficient oxygen for efficient CO and HC oxidation.

Figure 8.14 shows the N₂O concentration measured during the foregoing experiment. Of note is that the N₂O make declines at high C:NO_x ratios, even as the NO_x conversion is increasing. This would suggest that high hydrocarbon surface coverage inhibits N₂O formation, which might therefore provide a means of mitigating N₂O emissions during HC-SCR over this catalyst (albeit at increased fuel penalty). However, based on the data in Figure 8.14, the calculated N₂O selectivity ranges from 40 % to 100 %, which is comparable to that observed for the corresponding powder catalyst in earlier microreactor experiments in which a C/NO_x=1 was used. Thus, no C:NO_x ratio effect on N₂O selectivity is evinced by this particular experiment.

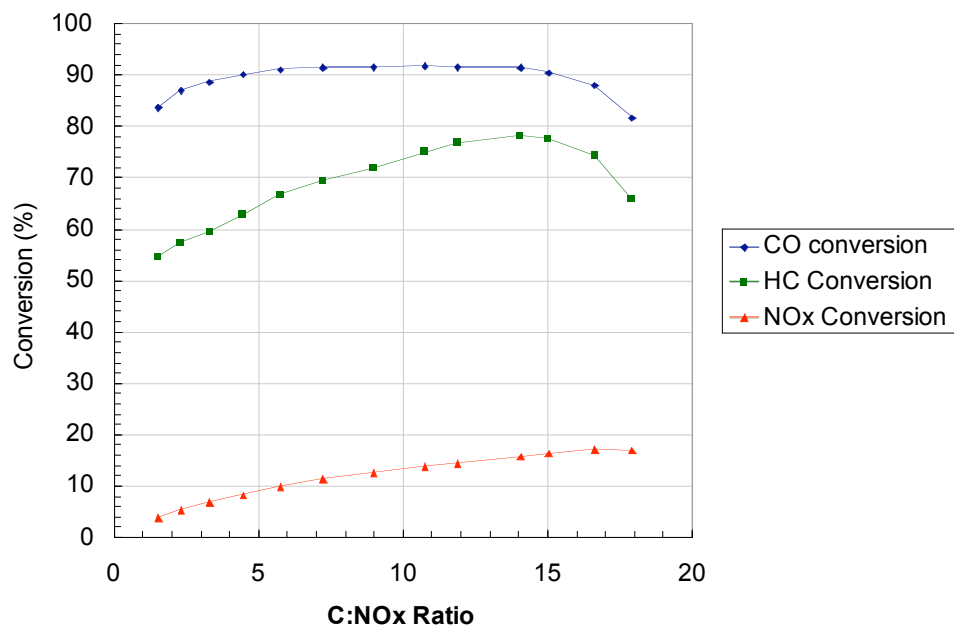


Figure 8.13. Results of C:NO_x sweep for 3:1 Pt-Rh/NO₂-fMWCNTs/metal monolith catalyst. GHSV = 50,000 h⁻¹, T = 270-290 °C.

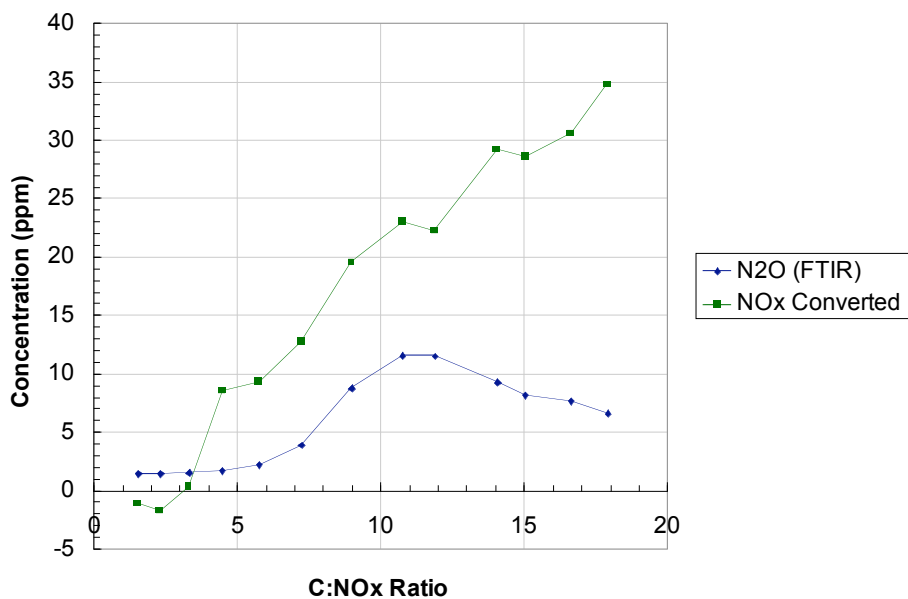


Figure 8.14. N₂O make during C:NO_x sweep for 3:1 Pt-Rh/NO₂-fMWCNTs/metal monolith catalyst. GHSV = 50,000 h⁻¹, T = 270-290 °C.

In summary, the results of engine tests reveal that the monolithic Pt and Pt-Rh catalysts are fairly active for the oxidation of CO and hydrocarbons, while NO_x reduction activity was found to be rather low; this fact can be largely attributed to the very high effective space velocities used, although others factors may play a role. For the Pt-Rh catalyst NO_x conversion increased with increasing C:NO_x ratio up to a limiting value at C:NO_x = 17. Of interest is the finding that the N₂O make declines at high C:NO_x ratios, even as the NO_x conversion is increasing. This suggests that high hydrocarbon surface coverage inhibits N₂O formation.

Finally, it is worth addressing the issue of catalyst architecture. For both the Pt and Pt-Rh catalysts studied, the metal loadings (58 g/cuft and 69 g/cuft, respectively) are in the range typically employed for diesel oxidation catalysts (DOCs) used on LDD vehicles. However, due to the low density of the MWCNTs support, the loading of MWCNTs on the monolith (7 g for the 0.41 L monolith, equivalent to 17 g/L) is much lower than the washcoat loading of a typical DOC or HC-SCR catalyst (~100 g/L). This has two main consequences: (i) it necessitates the use of high metal loadings on the MWCNTs support (10.8 wt.% and 12.5 wt.%, respectively, for the Pt and Pt-Rh catalysts), which will tend to result in sub-optimal metal dispersions (in comparison with those possible at lower metal loadings); and (ii) the low MWCNT loading will tend to diminish the direct involvement of the support in catalysis (e.g., as compared to the powder catalyst samples tested earlier in this work). These considerations highlight the potential disadvantages of employing a conventional metal monolith as the catalyst substrate. A better approach may be to form the MWCNTs into a rigid, self-supporting foam monolith, as done for activated carbon in certain environmental applications [243]. This should eliminate the above drawbacks, potentially improving catalyst performance.

In conclusion, monolithic catalysts have been prepared by growing MWCNTs on metallic monoliths, activating the monolith-grown MWCNTs with NO₂ and depositing precious metals *via* an *in situ* chemical reduction process. Engine tests performed on the resulting monolithic Pt and Pt-Rh catalysts revealed the latter to be fairly active for the oxidation

of CO and hydrocarbons, while NO_x reduction activity was found to be rather low. The can be largely attributed to the very high effective space velocities used, although other factors may also contribute.

Chapter 9. Concluding Remarks.

The Selective Catalytic Reduction of NO_x using hydrocarbon reductants has been investigated over MWCNTs supported PGM catalysts. MWCNTs-supported formulations have been found to exhibit higher NO_x conversion maxima at lower temperatures than catalysts incorporating oxidic supports. This has been tentatively attributed to the more reduced state in which the metallic phase is kept by MWCNTs, although additional XANES measurements under realistic HC-SCR conditions (an oxidative atmosphere) are required to verify this hypothesis. Further, the functionalization of the MWCNT support prior to the deposition of precious metals has been found to improve the HC-SCR performance of MWCNTs-based catalysts. This has been assigned to the fact that functionalization increases the Brønsted acidity of the carrier, which in turn enhances the partial oxidation of the hydrocarbon. The use of a 3:1 Pt-Rh alloy as the catalytically active phase can further improve the performance of fMWCNTs-supported formulations by optimizing hydrocarbon adsorption. Indeed, 1.5 wt.% Pt – 0.5 wt.% Rh/fMWCNTs is the catalyst which displays the most promising low temperature HC-SCR performance found in this work.

The HC-SCR reaction mechanism on MWCNTs-based catalysts has been investigated by performing transient, kinetic and adsorption studies on Pt/fMWCNTs. Results indicate that the reaction includes a reverse spill-over step in which hydrocarbonaceous species migrate from the catalyst support to the metal. Further, it appears that the reaction involves $\text{C}_x\text{H}_y\text{O}_z\text{N}_w$ intermediates whose reaction with gas phase oxygen yields the HC-SCR reaction products. However, comparative studies on Rh and Pt-Rh catalysts could yield additional insights on the HC-SCR reaction mechanism on supported PGM formulations.

A route to the monolithic MWCNTs-based HC-SCR catalysts has been devised and the resulting catalysts have been tested on a diesel engine. Engine tests have shown the monolithic catalysts to be active for both CO and hydrocarbon oxidation, although less so for NO_x reduction. Since the cause of the latter can be the low loading of MWCNTs on

the monoliths, this issue can be approached through studies on the monolithic catalyst architecture. Indeed, the use of a self-supporting MWCNTs monolith could be investigated as a means to increase the involvement of the MWCNT support in catalysis.

Finally, studying the long-term thermal deactivation and the resistance to poisons of MWCNTs-based catalysts would provide valuable information vis-à-vis their durability and further inform the feasibility of commercially implementing this technology.

Appendix – List of Abbreviations.

AC: activated carbon.

AES: atomic emission spectroscopy.

ATRIR: attenuated total reflectance infrared.

BET: Brunnauer-Emmett-Teller.

bfMWCNTs: base-washed functionalized multi-walled carbon nanotubes.

CAAA: clean air act amendments.

CNT: carbon nanotube.

CPA: chloroplatinic acid ($\text{H}_2\text{PtCl}_6 \cdot 6\text{H}_2\text{O}$).

CVD: chemical vapor deposition.

DOC: diesel oxidation catalyst.

DPF: diesel particulate filter.

DRIFTS: diffuse reflectance infrared Fourier transform spectroscopy.

DWCNT: double-walled carbon nanotube.

EDS: energy dispersive X-ray spectroscopy.

EG: ethylene glycol.

EXAFS: extended X-ray absorption fine structure.

fMWNCTs: functionalized multi-walled carbon nanotubes.

FTIR: Fourier transform infrared.

FTP: federal test procedure.

FWHM: full width at half maximum.

GHSV: gas hourly space velocity.

GWP: global warming potential.

HC: hydrocarbon.

HC-SCR: selective catalytic reduction of NO_x with hydrocarbon reductants.

HT: high temperature.

-I: impregnation (used after a given catalyst name to denote that the formulation has been prepared *via* impregnation).

ICP: inductively coupled plasma.

LDD: light duty diesel.

LT: low temperature.

MS: mass spectrometry.

MWCNTs: multi-walled carbon nanotubes.

NH₃-SCR: selective catalytic reduction of NO_x with ammonia as reductant.

NO₂-fMWCNTs: multi-walled carbon nanotubes functionalized with NO₂.

NO_x: nitrogen oxides (NO and NO₂).

-P: polyol (used after a given catalyst name to denote that the formulation has been prepared *via* the polyol method).

PGMs: platinum group metals (Ru, Rh, Pd, Os, Ir, Pt).

PIXE: proton-induced X-ray emission.

PM: particulate matter.

SCR: selective catalytic reduction.

STEM: scanning transmission electron microscopy *or* scanning transmission electron microscope.

STP: standard temperature and pressure (20 °C, 1 atm).

SWCNT: single-walled carbon nanotube.

TCD: thermal conductivity detector.

TEM: transmission electron microscopy *or* transmission electron microscope.

TGA: thermogravimetric analysis.

TOF: turnover frequency.

TPD: temperature programmed desorption.

TWC: three-way catalyst.

WHSV: weight hourly space velocity.

W/F: weight over flow.

XAFS: X-ray absorption fine structure.

XANES: X-ray absorption near edge structure.

XAS: X-ray absorption spectroscopy.

XPS: X-ray photoelectron spectroscopy.

XRF: X-ray fluorescence.

References.

- [1] J.N. Armor, in: J.N. Armor (Ed.), Environmental Catalysis, American Chemical Society. Washington, DC, 1994.
- [2] R.H. Heck, R.J. Farrauto, Catalytic Air Pollution Control. Commercial Technology, 2nd ed., John Wiley & Sons, Inc., New York, 2002.
- [3] M.V. Twigg, U.S. Patent 7,141,226 B2, 2006
- [4] G. Centi, A. Galli, B. Montanari, S. Perathoner, A. Vaccaria, Catal. Today 35 (1997) 113.
- [5] G. Centi, L. Dall'Olio, S. Perathoner, J. Catal. 194 (2000) 130.
- [6] F. Kapteijn, J. Rodriguez-Mirasol, J.A. Moulijn, Appl. Catal. B 9 (1996) 25.
- [7] <http://www.epa.gov/air/emissions/nox.htm>
- [8] L.L. Sloss, N.K. Hjaimarsson, H.N. Soud, L.M. Campbell, D.K. Stone, G.S. Shareef, T. Emmel, M. Maibodi, C.D. Livengood, J. Markussen, Nitrogen Oxides Control Technology Fact Book, Noyes Data Co., Park Ridge, USA, 1992.
- [9] H. Rodhe, C. Johansson, Impact of anthropogenic activities on the global N₂ cycle, IVL 3568, Stockholm, Sweden, IVL Swedish Environmental Research Institute.
- [10] R. Atkinson, in: A.Y. Watson, R.R. Bates, D. Kennedy (Eds.), Air Pollution, The Automobile and Public Health, National Academy Press. Washington, DC, 1988.
- [11] J. Dunmore, in: A. Cutrera (Ed.), European Environmental Yearbook 1987, Milan, 1987.
- [12] J.N. Armor, Appl. Catal. B 1 (1992) 221.
- [13] T. Shuihua, G. Lizhen, L. Baochun, L. He, Z. Liangfu, Y. Zuolong, J. Nat. Gas Chem. 10 (2001) 196.
- [14] V.I. Pârvulescu, P. Grange, B. Delmon, Catal. Today 46 (1998) 233.
- [15] M. Kavanaugh, Atmos. Environ. 21 (1987) 463.
- [16] A. Bueno-López, M.J. Illán-Gómez, C. Salinas-Martínez de Lecea, Appl. Catal. A 302 (2006) 244.
- [17] <http://www.meca.org>
- [18] <http://www.dieselnet.com/standards/us/ld.php>
- [19] http://www.dieselnet.com/standards/us/ld_t2.php

- [20] <http://www.dieselnet.com/standards/cycles/ftp75.html>
- [21] M. Iwamoto, Proc. of meeting of Catalytic Technology for Removal of nitrogen monoxide, Tokyo, 1990.
- [22] M. Iwamoto, H. Yahiro, Y. Yuu, S. Shundo, N. Mizuno, Shokubai 32 (1990) 430.
- [23] W. Held, A. Konig, T. Richter, L. Ruppe, SAE paper 900496 (1990).
- [24] R.H. Heck, R.J. Farrauto, Appl. Catal. A 221 (2001) 443.
- [25] M. Crocker, S. Eckhoff, A. Fukumoto, T. Matsumoto, R. Bending, P. Duggleby, Lean NOx catalysis for mobile source emission abatement, CATL-022, 223rd ACS National Meeting, San Diego, 2001.
- [26] C. Enderle, C. Schön, T. Ried, W. Müller, L. Ruwisch, M. Kögel, S. Franschek, T. Kreuzer, E. Lox, SAE 2003-01-1161.
- [27] B. Damson, J. Rudelt, J. Oesterle, G. Gaiser, SAE 2003-01-1165.
- [28] T. Maunula, Y. Kintaichi, M. Inaba, M. Haneda, K. Sato, H. Hamada, Appl. Catal. B 15 (1998) 291.
- [29] J.M. García-Cortés, J. Pérez-Ramírez, M.J. Illán-Gómez, F. Kapteijn, J.A. Moulijn, C. Salinas-Martínez de Lecea, Appl. Catal. B 30 (2001) 399.
- [30] M.F.R. Pereira, J.L. Figueiredo, J.J.M. Orfao, P. Serp, P. Kalck, Y. Kihn, Carbon 42 (2004) 2807.
- [31] A. Giroir-Fendler, P. Denton, A. Boreave, H. Praliaud, M. Primet, Top. Catal. 16 (2001) 237.
- [32] S. Ringler, P. Girard, G. Maire, S. Hilaire, G. Roussy, F. Garin, Appl. Catal. B 20 (1999) 219.
- [33] M. Iwamoto, H. Hamada, Catal. Today 10 (1991) 57.
- [34] J.S. Ritscher, U.S. Patent 4,297,328, 1981.
- [35] W. Held, DE3642018, 1987.
- [36] H. Hamada, Y. Kintaichi, M. Sasaki, T. Ito, M. Tabata, Appl. Catal. 64 (1990) L1.
- [37] H. Hamada, Y. Kintaichi, M. Sasaki, T. Ito, Appl. Catal. 70 (1991) L1.
- [38] H. Hamada, Y. Kintaichi, M. Tabata, M. Sasaki, T. Ito, Chem. Lett. 20 (1991) 2179.
- [39] S. Sato, H. Hirabayashi, H. Yahiro, N. Mizuno, M. Iwamoto, Catal. Lett. 12 (1992) 193.
- [40] T. Tabata, M. Kokitsu, O. Okada, Catal. Today 22 (1994) 147.

- [41] C.N. Montrcuil, M. Shelef, *Appl. Catal. B* 1 (1993) 1.
- [42] E. Kikuchi, K. Yogo, S. Tanaka, M. Abe, *Chem. Lett.* 20 (1991) 1063.
- [43] M. Konno, T. Chikahisa, T. Murayama, M. Iwamoto, *Society of Automotive Engineering* (1992) Paper No. 920091.
- [44] A. Obuchi, A. Ohi, M. Nakamura, A. Ogata, K. Mizuno, H. Ohuchi, *Appl. Catal. B* 2 (1993) 71.
- [45] H.K. Shin, H. Hirabayashi, H. Yahiro, M. Watanabe, M. Iwamoto, *Catal. Today* 26 (1995) 13.
- [46] R. Wunsch, G. Gund, W. Weisweiler, B. Krutzsch, K.E. Haak, G. Wenninger, F. Wirbeleit, *SAE Trans. Section 4* (No. 962004) (1996) 1892.
- [47] R. Burch, P.J. Millington, A.P. Walker, *Appl. Catal. B* 4 (1994) 65.
- [48] D.K. Captain, M.D. Amiridis, *J. Catal.* 184 (1999) 377.
- [49] W. Schiesser, H. Vinek, A. Jentys, *Appl. Catal. B* 33 (2001) 263.
- [50] M.D. Amiridis, T. Zhang, R.J. Farrauto, *Appl. Catal. B* 10 (1996) 203.
- [51] W. Gruenert, H. Papp, C. Rottlaender, M. Baerns, *Chem. Tech. (Leipzig)* 47 (1995) 205.
- [52] R. Burch, P.J. Millington, *Catal. Today* 29 (1996) 37.
- [53] R. Burch, J.P. Breen, F.C. Meunier, *Appl. Catal. B* 39 (2002) 283.
- [54] F.C. Meunier, J.P. Breen, V. Zuzaniuk, M. Olsson, J.R.H. Ross, *J. Catal.* 187 (1999) 493.
- [55] N. Bogdanchikova, F.C. Meunier, M. Avalos-Borja, J.P. Breen, A. Pestryakov, *Appl. Catal. B* 36 (2002) 287.
- [56] K.A. Bethke, H.H. Kung, *J. Catal.* 172 (1997) 93.
- [57] K.-I. Shimizu, J. Shibata, H. Yoshida, A. Satsuma, T. Hattori, *Appl. Catal. B* 30 (2001) 151.
- [58] K.L. Roberts, M.D. Amiridis, *Ind. Eng. Chem. Res* 36 (1997) 3528.
- [59] D.K. Captain, K.L. Roberts, M.D. Amiridis, *Catal. Today* 42 (1998) 93.
- [60] M. Iwamoto, H. Yahiro, H.K. Shin, M. Watanabe, J. Guo, M. Konno, T. Chikahisa, T. Murayama, *Appl. Catal. B* 5 (1994) L1.
- [61] M. Sasaki, H. Hamada, Y. Kintaichi, T. Ito, *Catal. Lett.* 15 (1992) 297.
- [62] H. Hirabayashi, H. Yahiro, N. Mizuno, M. Iwamoto, *Chem. Lett.* 21 (1992) 2235.

- [63] R. Burch, D. Ottery, *Appl. Catal. B* 9 (1996) L19.
- [64] H. Yahiro, H. Hirabayashi, H.K. Shin, N. Mizuno, M. Iwamoto, *Trans. Mater. Res. Soc. Jpn.* 18A (1994) 409.
- [65] G. Zhang, Y. Yamaguchi, H. Kawakami, T. Suzuki, *Appl. Catal. B* 1 (1992) L15.
- [66] J.M. García-Cortés, M.J. Illán-Gómez, A. Linares-Solano, C. Salinas-Martínez de Lecea, *Appl. Catal. B* 25 (2000) 39.
- [67] J.M. García-Cortés, M.J. Illán-Gómez, A. Linares-Solano, C. Salinas-Martínez de Lecea, *Stud. Surf. Sci. Catal.* 130 (2000) 1427.
- [68] J. Pérez-Ramírez, J.M. García-Cortés, F. Kapteijn, M.J. Illán-Gómez, A. Ribera, C. Salinas-Martínez de Lecea, J.A. Moulijn, *Appl. Catal. B* 25 (2000) 191.
- [69] K.O. Haj, S. Ziyade, M. Ziyad, F. Garin, *Appl. Catal. B* 37 (2002) 49.
- [70] E. Iojoiu, P. Gelin, H. Praliaud, M. Primet, *Appl. Catal. A* 263 (2004) 39.
- [71] S. Nojima, K. Iida, N. Kobayashi, *Nippon Kagaku Kaishi* (2001) 27.
- [72] R. Burch, P.J. Millington, *Catal. Today* 26 (1995) 185.
- [73] R. Burch, T.C. Watling, *Appl. Catal. B* 11 (1997) 207.
- [74] M. Inaba, Y. Kintaichi, H. Hamada, *Catal. Lett.* 36 (1996) 223.
- [75] J.H. Lee, H.H. Kung, *Catal. Lett.* 51 (1998) 1.
- [76] R. Burch, T.C. Watling, *Catal. Lett.* 37 (1996) 51.
- [77] R. Burch, J.A. Sullivan, T.C. Watling, *Catal. Today* 42 (1998) 13.
- [78] R. Burch, T.C. Watling, *Catal. Lett.* 43 (1997) 19.
- [79] R. Burch, T.C. Watling, *Appl. Catal. B* 17 (1998) 131.
- [80] R. Burch, D. Ottery, *Appl. Catal. B* 13 (1997) 105.
- [81] E. Seker, E. Gulari, *J. Catal.* 194 (2000) 4.
- [82] M.D. Amiridis, K.L. Roberts, C.J. Pereira, *Appl. Catal. B* 14 (1997) 203.
- [83] G.R. Bamwenda, A. Obuchi, A. Ogata, J. Oi, S. Kushiya, K. Mizuno, *J. Mol. Catal. A: Chem.* 126 (1997) 151.
- [84] T.I. Halkides, D.I. Kondarides, X.E. Verykios, *Catal. Today* 73 (2002) 213.
- [85] A. Fritz, V. Pitchon, *Appl. Catal. B* 13 (1997) 1.
- [86] K.S. Oh, S.I. Woo, *Appl. Surf. Sci.* 254 (2007) 677.
- [87] N. Ishikawa, JP2000140644, 2000
- [88] M. Crocker, unpublished results.

- [89] A. Takami, T. Takemoto, H. Iwakuni, K. Yamada, M. Shigetsu, K. Komatsu, *Catal. Today* 35 (1997) 75.
- [90] K.C.C. Kharas, U.S. Patent 5,977,012, 1999
- [91] K.C.C. Kharas, U.S. Patent 6,087,295, 2000
- [92] M. Monthieux, V.L. Kuznetsov, *Carbon* 44 (2006) 1621.
- [93] S. Iijima, *Nature* 354 (1991) 56.
- [94] S. Subramoney, *Adv. Mater.* 10 (1998) 1157.
- [95] M.M.J. Treacy, T.W. Ebbesen, J.M. Gibson, *Nature* 381 (1996) 678.
- [96] E.W. Wong, P.E. Sheehan, C.M. Lieber, *Science* 277 (1997) 1971.
- [97] J.-P. Salvetat, A.J. Kulik, J.-M. Bonard, G.A.D. Briggs, T. Stoeckli, K. Metenier, S. Bonnamy, F. Beguin, N.A. Burnham, L. Forro, *Adv. Mater.* 11 (1999) 161.
- [98] J.H. Hafner, C.L. Cheung, A.T. Woolley, C.M. Lieber, *Prog. Biophys. Mol. Biol.* 77 (2001) 73.
- [99] M. Guthold, M. Falvo, W.G. Matthews, S. Paulson, J. Mullin, S. Lord, D. Erie, S. Washburn, R. Superfine, J.F.P. Brooks, R.M. Taylor, *J. Mol. Graph. Model.* 17 (1999) 187.
- [100] B.Q. Wei, R. Vajtai, P.M. Ajayan, *Appl. Phys. Lett.* 79 (2001) 1172.
- [101] E. Frackowiak, F. Béguin, *Carbon* 39 (2001) 937.
- [102] F.L. Darkrim, P. Malbrunot, G.P. Tartaglia, *Int. J. Hydrogen Energy* 27 (2002) 193.
- [103] V.V. Simonyan, J.K. Johnson, *J. Alloys Comp.* 330-332 (2002) 659.
- [104] E. Frackowiak, F. Béguin, *Carbon* 40 (2002) 1775.
- [105] A.S. Kotosonov, *JETP Lett.* 70 (1999) 476.
- [106] F. Tsui, L. Jin, O. Zhou, *Appl. Phys. Lett.* 76 (2000) 1452.
- [107] K. Tsukagoshi, B.W. Alphenaar, H. Ago, *Nature* 401 (1999) 572.
- [108] P. Chen, X. Wu, X. Sun, J. Lin, W. Ji, K.L. Tan, *Phys. Rev. Lett.* 82 (1999) 2548.
- [109] S. Curran, A.P. Davey, J. Coleman, A. Dalton, B. McCarthy, S. Maier, A. Drury, D. Gray, M. Brennan, K. Ryder, M.L. de la Chapelle, C. Journet, P. Bernier, H.J. Byrne, D. Carroll, P.M. Ajayan, S. Lefrant, W. Blau, *Synth. Met.* 103 (1999) 2559.
- [110] Z. Jin, X. Sun, G. Xu, S.H. Goh, W. Ji, *Chem. Phys. Lett.* 318 (2000) 505.
- [111] Y.-P. Sun, B. Zhou, K. Henbest, K. Fu, W. Huang, Y. Lin, S. Taylor, D.L. Carroll, *Chem. Phys. Lett.* 351 (2002) 349.

- [112] Z. Jin, L. Huang, S. Hong Goh, G. Xu, W. Ji, *Chem. Phys. Lett.* 352 (2002) 328.
- [113] V. Lordi, N. Yao, J. Wei, *Chem. Mater.* 13 (2001) 733.
- [114] Z.L. Liu, L.M. Gan, L. Hong, W.X. Chen, J.Y. Lee, *J. Power Sources* 139 (2005) 73.
- [115] B. Coq, J. Marc Planeix, V. Brotons, *Appl. Catal. A* 173 (1998) 175.
- [116] S.C. Tsang, Y.K. Chen, R.M. Lago, M.L.H. Green, *Fullerenes and Fullerene Nanostructures*, Proceedings International Winterschool on Electronic Properties of Novel Materials, Kirchberg, 1996.
- [117] Z.L. Liu, X.H. Lin, J.Y. Lee, W. Zhang, M. Han, L.M. Gan, *Langmuir* 18 (2002) 4054.
- [118] W.Z. Li, C.H. Liang, J.S. Qiu, W.J. Zhou, H.M. Han, Z.B. Wei, G.Q. Sun, Q. Xin, *Carbon* 40 (2002) 791.
- [119] T. Matsumoto, T. Komatsu, K. Arai, T. Yamazaki, M. Kijima, H. Shimizu, Y. Takasawa, J. Nakamura, *Chem. Commun.* (2004) 840.
- [120] M.J. Illán-Gómez, E. Raymundo-Pinero, A. García-García, A. Linares-Solano, C. Salinas-Martínez de Lecea, *Appl. Catal. B* 20 (1999) 267.
- [121] R. Andrews, D. Jacques, A.M. Rao, F. Derbyshire, D. Qian, X. Fan, E.C. Dickey, J. Chen, *Chem. Phys. Lett.* 303 (1999) 467.
- [122] J. Zhang, H.L. Zou, Q. Qing, Y.L. Yang, Q.W. Li, Z.F. Liu, X.Y. Guo, Z.L. Du, *J. Phys. Chem. B* 107 (2003) 3712.
- [123] J. Liu, A.G. Rinzler, H. Dai, J.H. Hafner, R.K. Bradley, P.J. Boul, A. Lu, T. Iverson, K. Shelimov, C.B. Huffman, F. Rodriguez-Macias, Y.-S. Shon, T.R. Lee, D.T. Colbert, R.E. Smalley, *Science* 280 (1998) 1253.
- [124] S.C. Tsang, P.J.F. Harris, M.L.H. Green, *Nature* 362 (1993) 520.
- [125] P.M. Ajayan, T.W. Ebbesen, T. Ichihashi, S. Iijima, K. Tanigaki, H. Hiura, *Nature* 362 (1993) 522.
- [126] A. Kuznetsova, D.B. Mawhinney, V. Naumenko, J.T. Yates, J. Liu, R.E. Smalley, *Chem. Phys. Lett.* 321 (2000) 292.
- [127] A. Kuznetsova, I. Popova, J.T. Yates, M.J. Bronikowski, C.B. Huffman, J. Liu, R.E. Smalley, H.H. Hwu, J.G. Chen, *J. Am. Chem. Soc.* 123 (2001) 10699.

- [128] L. Qingwen, Y. Hao, Y. Yinchun, Z. Jin, L. Zhongfan, *J. Phys. Chem. B* 106 (2002) 11085.
- [129] R.Q. Yu, L.W. Chen, Q.P. Liu, J.Y. Lin, K.L. Tan, S.C. Ng, H.S.O. Chan, G.Q. Xu, T.S.A. Hor, *Chem. Mater.* 10 (1998) 718.
- [130] S.C. Tsang, Y.K. Chen, P.J.F. Harris, M.L.H. Green, *Nature* 372 (1994) 159.
- [131] Y. Xing, *J. Phys. Chem. B* 108 (2004) 19255.
- [132] K. Esumi, M. Ishigami, A. Nakajima, K. Sawada, H. Honda, *Carbon* 34 (1996) 279.
- [133] K. Dai, L. Shi, J. Fang, Y. Zhang, *Mater. Sci. Eng., A* 465 (2007) 283.
- [134] C. Whitaker, I. Uber, F. ForoHar, W. Koppes, Abstract of papers 231st ACS National Meeting, Atlanta, 2006.
- [135] F. Peng, L. Zhang, H. Wang, P. Lv, H. Yu, *Carbon* 43 (2005) 2405.
- [136] I.I. Salame, T.J. Badosz, *J. Colloid Interface Sci.* 240 (2001) 252.
- [137] M.S.P. Shaffer, X. Fan, A.H. Windle, *Carbon* 36 (1998) 1603.
- [138] L. Liu, Y. Qin, Z.-X. Guo, D. Zhu, *Carbon* 41 (2003) 331.
- [139] N. Hung, I. Anoshkin, A. Dementjev, D. Katorov, E. Rakov, *Inorg. Mater.* 44 (2008) 219.
- [140] <http://srdata.nist.gov/xps/>
- [141] V. Datsyuk, M. Kalyva, K. Papagelis, J. Parthenios, D. Tasis, A. Siokou, I. Kallitsis, C. Galiotis, *Carbon* 46 (2008) 833.
- [142] U. Zielke, K.J. Hüttinger, W.P. Hoffman, *Carbon* 34 (1996) 983.
- [143] W.Z. Li, C.H. Liang, W.J. Zhou, J.S. Qiu, H.Q. Li, G.Q. Sun, Q. Xin, *Carbon* 42 (2004) 436.
- [144] Z.H. Zhou, S.L. Wang, W.J. Zhou, G.X. Wang, L.H. Jiang, W.Z. Li, S.Q. Song, J.G. Liu, G.Q. Sun, Q. Xin, *Chem. Commun.* (2003) 394.
- [145] *MRS Bull.* 24 (1989) 29.
- [146] K.-Y. Chan, J. Ding, J. Ren, S. Cheng, K.Y. Tsang, *J. Mater. Chem.* 14 (2004) 505.
- [147] W.-X. Chen, J.Y. Lee, Z. Liu, *Mater. Lett.* 58 (2004) 3166.
- [148] J.T.G. Overbeek, *Adv. Colloid Interface Sci.* 15 (1982) 251.
- [149] T. Sugimoto, *Adv. Colloid Interface Sci.* 28 (1987) 6.
- [150] F. Fievet, F. Vincent, J. Lagier, B. Dumont, *J. Mater. Chem.* 3 (1993) 627.

- [151] J. Garcia, H.T. Gomes, P. Serp, P. Kalck, J.L. Figueiredo, J.L. Faria, *Catal. Today* 102 (2005) 101.
- [152] F.M. Dautzenberg, in: S.A. Bradley, M.J. Gattuso, R.J. Bertolacini (Eds.), *Characterization and Catalyst Development: An Iterative Approach*, ACS Symposium Series, Vol. 411, 1989.
- [153] B. Ioan, A. Miyazaki, K.I. Aika, *Appl. Catal. B* 59 (2005) 71.
- [154] A. Obuchi, I. Kaneko, J. Oi, A. Ohi, A. Ogata, G.R. Bamwenda, S. Kushiya, *Appl. Catal. B* 15 (1998) 37.
- [155] J.H. Li, J.M. Hao, L.X. Fu, T.L. Zhu, *Top. Catal.* 30-31 (2004) 81.
- [156] C.H. Li, K.F. Yao, J. Liang, *Carbon* 41 (2003) 858.
- [157] H. Hamada, Y. Kintaichi, M. Sasaki, T. Ito, *Appl. Catal. A* 75 (1991) L1.
- [158] R. Burch, *Catal. Today* 35 (1997) 27.
- [159] H. Hamada, *Catal. Today* 22 (1994) 21.
- [160] H.H. Ingelsten, M. Skoglundh, E. Fridell, *Appl. Catal. B* 41 (2003) 287.
- [161] G. Zhang, T. Yamaguchi, H. Kawakami, T. Suzuki, *Appl. Catal. B* 1 (1992) L15.
- [162] G.R. Bamwenda, a. Ogata, a. Obuchi, J. Oi, K. Mizuno, J. Skrzypek, *Appl. Catal. B* 6 (1995) 311.
- [163] K.S. Oh, S.I. Woo, *Catal. Lett.* 110 (2006) 247.
- [164] F. Figueras, B. Coq, E. Ensuque, D. Tachon, G. Delahay, *Catal. Today* 42 (1998) 117.
- [165] A. Satsuma, K. Yamada, T. Mori, M. Niwa, T. Hattori, Y. Murakami, *Catal. Lett.* 31 (1995) 367.
- [166] O.V. Metelkina, V.V. Lunin, V.A. Sadykov, S.A. Beloshapkin, G.M. Alikina, E.V. Lunina, O.O. Parenago, *Pet. Chem.* 40 (2000) 90.
- [167] K. Kawabata, H. Yoshimatsu, K. Fujiwara, T. Yabuki, A. Osaka, A. Miura, J. *Mater. Sci.* 34 (1999) 2529.
- [168] F. Figueras, J.L. Flores, G. Delahay, A. Giroir-Fendler, A. Bourane, J.M. Clacens, A. Desmartin-Chomel, C. Lehaut-Burnouf, *J. Catal.* 232 (2005) 27.
- [169] W.Z. Li, C.H. Liang, W.J. Zhou, J.S. Qiu, Z.H. Zhou, G.Q. Sun, Q. Xin, *J. Phys. Chem. B* 107 (2003) 6292.

- [170] M.C. Demicheli, L.C. Hoang, J.C. Ménézo, J. Barbier, M. Pinabiau-Carlier, Appl. Catal. A 97 (1993) L11.
- [171] P. Denton, A. Giroir-Fendler, H. Praliaud, M. Primet, J. Catal. 189 (2000) 410.
- [172] E. Xue, K. Seshan, J.R.H. Ross, Appl. Catal. B 11 (1996) 65.
- [173] K. Otto, H.C. Yao, J. Catal. 66 (1980) 229.
- [174] J. Kaspar, C. de Leitenburg, P. Fornasiero, A. Trovarelli, M. Graziani, J. Catal. 146 (1994) 136.
- [175] X. Xu, D.W. Goodman, Catal. Lett. 24 (1994) 31.
- [176] R. Verdejo, S. Lamoriniere, B. Cottam, A. Bismarck, M. Shaffer, Chem. Commun. (2007) 513.
- [177] H. Iwakuni, A. Takami, K. Komatsu, Stud. Surf. Sci. Catal. 121 (1999) 251.
- [178] A. Takami, T. Takemoto, H. Iwakuni, F. Saito, K. Komatsu, Society of Automotive Engineers 950746 (1995).
- [179] M. Shigetsu, A. Takami, M. Kyougoku, H. Iwakuni, F. Saito, K. Komatsu, Matsuda Giho 13 (1995) 30.
- [180] M. Bowker, The Basis and Applications of Heterogeneous Catalysis, Oxford University Press, New York, 1998.
- [181] A. Obuchi, A. Ogata, K. Mizuno, A. Ohi, M. Nakamura, H. Ohuchi, J. Chem. Soc., Chem. Commun. (1992) 247.
- [182] A. Obuchi, M. Nakamura, A. Ogata, K. Mizuno, A. Ohi, H. Ohuchi, J. Chem. Soc., Chem. Commun. (1992) 1150.
- [183] L. Mussmann, EP1138382, 2001.
- [184] I.V. Yentekakis, V. Tellou, G. Botzolaki, I.A. Rapakousios, Appl. Catal. B 56 (2005) 229.
- [185] P. Vernoux, A.Y. Leinekugel-Le-Cocq, F. Gaillard, J. Catal. 219 (2003) 247.
- [186] N.D. Lang, J.K. Holloway, J.K. Norskov, Surf. Sci. 150 (1985) 24.
- [187] N. Macleod, J. Isaac, R.M. Lambert, Appl. Catal. B 33 (2001) 335.
- [188] E.F. Iliopoulou, A.P. Evdou, A.A. Lemonidou, I.A. Vasalos, Appl. Catal. A 274 (2004) 179.
- [189] K. Sato, T. Yoshinari, Y. Kintaichi, M. Haneda, H. Hamada, Catal. Commun. 4 (2003) 315.

- [190] K. Sato, T. Yoshinari, Y. Kintaichi, M. Haneda, H. Hamada, *Appl. Catal. B* 44 (2003) 67.
- [191] J.A. Botas, M.A. Gutiérrez-Ortiz, M.P. González-Marcos, J.A. González-Marcos, J.R. González-Velasco, *Appl. Catal. B* 32 (2001) 243.
- [192] J.W. Niemantsverdriet, *Spectroscopy in Catalysis: an Introduction*, VCH, New York, 1993.
- [193] L.C. Feldman, J.W. Mayer, *Fundamentals of Surface Science and Thin Film Analysis*, North-Holland, Amsterdam, 1986.
- [194] H. Dexpert, E. Freund, E. Lesage, J.P. Lynch, *Metal-Support and Metal-Additive Effects in Catalysis*, Elsevier, Amsterdam, 1982.
- [195] G. Ertl, J. Küppers, *Low Energy Electrons and Surface Chemistry*, VHC, Weinheim, 1885.
- [196] P.K. Ghosh, *Introduction to Photoelectron Spectroscopy*, Wiley, New York, 1983.
- [197] D. Briggs, M.P. Seah, *Practical Surface Analysis by Auger and X-ray Photoelectron Spectroscopy*, Wiley, New York, 1978.
- [198] A. Bianconi, L. Incoccia, S. Stipcich, *EXAFS and Near Edge Structure*, Springer, Berlin, 1983.
- [199] D.C. Koningsberger, R. Prins, *X-ray Absorption*, Wiley, New York, 1987.
- [200] T. Ressler, *WinXAS 97, Version 1.0*, 1997.
- [201] K. Suzuki, T. Noda, N. Katada, M. Niwa, *J. Catal.* 250 (2007) 151.
- [202] N. Katada, T. Tsubaki, M. Niwa, *Appl. Catal. A* 340 (2008) 76.
- [203] M. Niwa, S. Nishikawa, N. Katada, *Microporous Mesoporous Mater.* 82 (2005) 105.
- [204] J.A. Lercher, C. Gründling, G. Eder-Mirth, *Catal. Today* 27 (1996) 353.
- [205] W. Feng, A. Fujii, M. Ozaki, K. Yoshino, *Carbon* 43 (2005) 2501.
- [206] Y. Zhang, S. Yuan, W. Zhou, J. Xu, Y. Li, *J. Nanosci. Nanotechnol.* 7 (2007) 2366.
- [207] C. Zhou, Q. Zhuang, J. Qian, X. Li, Z. Han, *Chem. Lett.* 37 (2008) 254.
- [208] J.A. Anderson, B. Bachiller-Baeza, M. Fernández-García, *Phys. Chem. Chem. Phys.* 5 (2003) 4418.
- [209] J.M. García-Cortés, J. Pérez-Ramírez, J.N. Rouzaud, A.R. Vaccaro, M.J. Illán-Gómez, C. Salinas-Martínez de Lecea, *J. Catal.* 218 (2003) 111.

- [210] G. Prelazzi, U. Bardi, A. Santucci, *Appl. Surf. Sci.* 62 (1992) 277.
- [211] M.D. Amiridis, C. Mihut, M. Maciejewski, A. Baiker, *Top. Catal.* 28 (2004) 141.
- [212] R. Burch, J.A. Sullivan, *J. Catal.* 182 (1999) 489.
- [213] J.A. Sullivan, R. Burch, A.A. Shestov, *Chem. Eng. Res. Des.* 78 (2000) 947.
- [214] A. Obuchi, A. Ogata, H. Takahashi, J. Oi, G.R. Bamwenda, K. Mizuno, *Catal. Today* 29 (1996) 103.
- [215] J. Oi, A. Obuchi, G.R. Bamwenda, A. Ogata, H. Yagita, S. Kushiyama, K. Mizuno, *Appl. Catal. B* 12 (1997) 277.
- [216] S. Nojima, K. Iida, N. Kobayashi, *Shokubai* 40 (1998) 372.
- [217] C. Wogerbauer, M. Maciejewski, A. Baiker, U. Gobel, *Proceedings of the Fifth International Congress on Catalysis and Automotive Pollution Control, Brussels, Belgium, 12–14 April 2000, Topics in Catalysis, Vols. 16/17, Kluwer Academic Publishers/Plenum Press, 2001.*
- [218] R. Burch, T.C. Watling, in: N. Kruse, A. Frennet, J.M. Bastin (Eds.), *Studies in Surface Science and Catalysis: Catalysis and Automotive Pollution Control IV, Vol. 116, Elsevier. Amsterdam, 1998.*
- [219] C. Rottlander, R. Andorf, C. Plog, B. Krutzsch, M. Baerns, *Appl. Catal. B* 11 (1996) 49.
- [220] S. Lacombe, J.H.B.J. Hoebink, G.B. Marin, *Appl. Catal. B* 12 (1997) 207.
- [221] V. Pitchon, A. Fritz, *J. Catal.* 186 (1999) 64.
- [222] W.H. Chen, H. Lu, C.M. Pradier, J. Paul, A. Flodstrom, *J. Catal.* 172 (1997) 3.
- [223] G.R. Bamwenda, A. Obuchi, A. Ogata, K. Mizuno, *Chem. Lett.* (1994) 2109.
- [224] D.K. Captain, M.D. Amiridis, *J. Catal.* 194 (2000) 222.
- [225] R. Burch, *Cat. Rev.* 46 (2004) 271.
- [226] V.A. Matyshak, O.V. Krylov, *Catal. Today* 25 (1995) 1.
- [227] F. Radtke, R.A. Koepfel, E.G. Minardi, A. Baiker, *J. Catal.* 167 (1997) 127.
- [228] A.D. Cowan, N.W. Cant, B.S. Haynes, P.F. Nelson, *J. Catal.* 176 (1998) 329.
- [229] A. Obuchi, C. Wogerbauer, R. Koppel, A. Baiker, *Appl. Catal. B* 19 (1998) 9.
- [230] T. Tanaka, T. Okuhara, M. Misono, *Appl. Catal. B* 4 (1994) L1.
- [231] E. Joubert, T. Bertin, J.C. Ménézo, J. Barbier, *Appl. Catal. B* 23 (1999) L83.
- [232] E. Joubert, J.C. Ménézo, D. Duprez, J. Barbier, *Top. Catal.* 16 (2001) 225.

- [233] J.U. Nef, in: J. March (Ed.), *Advanced Organic Chemistry, Reactions, Mechanisms and Structures*, 4th ed., Wiley-Interscience, Wiley, New York, 1992.
- [234] J. March, *Advanced Organic Chemistry*, Wiley-Interscience, New York, 1992.
- [235] A.A. Nikolopoulos, E.S. Stergioula, E.A. Efthimiadis, I.A. Vasalos, *Catal. Today* 54 (1999) 439.
- [236] O. Gorce, F. Baudin, C. Thomas, P. Da Costa, G. Djega-Mariadassou, *Appl. Catal. B* 54 (2004) 69.
- [237] J.M. García-Cortés, M.J. Illán-Gómez, C. Salinas-Martínez de Lecea, *Appl. Catal. B* 74 (2007) 313.
- [238] R. Burch, T.C. Watling, *J. Catal.* 169 (1997) 45.
- [239] F. Kapteijn, R.J. Berger, J.A. Moulijn, in: G. Ertl, H. Knözinger, F. Schüth, J. Weitkamp (Eds.), *Handbook of heterogenous catalysis*, 2nd ed., Wiley-VCH, Weinheim, 2008.
- [240] J.M. Thomas, W.J. Thomas, *Principles and practice of heterogeneous catalysis*, VHC Publishers, Inc., New York, 1997.
- [241] J. Parks, B. West, M. Swartz, S. Huff, SAE 2008-01-0448.
- [242] I. Kvande, S. Briskeby, M. Tsytkin, M. Rønning, S. Sunde, R. Tunold, D. Chen, *Top. Catal.* 45 (2007) 81.
- [243] B. Crittenden, A. Patton, C. Jouin, S. Perera, S. Tennison, J.A.B. Echevarria, *Adsorption* 11 (2005) 537.

VITA

Eduardo Santillan-Jimenez.

Personal Information.

Place of birth: San Luis Potosí, Mexico.

Date of birth: October 27, 1980.

Education.

Universidad Autónoma de San Luis Potosí.

San Luis Potosí, S.L.P. Mexico.

Bachelor of Science Degree in Chemistry (2003).

University of Kentucky.

Center for Applied Energy Research / Department of Chemistry.

Lexington, KY U.S.A.

Doctoral studies (2004-2008).

Advisor: Prof. Mark Crocker. Co-advisor: Prof. David Atwood.

University of Alicante.

Department of Inorganic Chemistry. Carbon Materials and Environment Group.

Alicante, Spain.

Dissertation studies (January-April 2008).

Advisor: Prof. Concepción Salinas Martínez de Lecea.

Awards and scholarships.

Consejo Nacional de Ciencia y Tecnología.

Graduate Studies Abroad Scholarship (2004-2008).

University of Kentucky Graduate School.

Teaching Assistantship (2004-2005).

University of Kentucky Center for Applied Energy Research.

Research Assistantship (2005-2008).

University of Kentucky Graduate School.

Dissertation Enhancement Award to fund a research stay at the University of Alicante (2007).

Publications.

1. Shengming Liu , Pingrong Wei , Yuzhong Wang , Eduardo Santillan-Jimenez , Ronald C Bakus, II, David A Atwood. *Use of a structurally characterized molecular cluster to form $Yb_3Al_5O_{12}$ under ambient conditions.* Main Group Chemistry. Volume 4, Number 1 / March 2005. Pages 3-10.

2. J. Link Shumaker, Czarena Crofcheck, S. Adam Tackett, Eduardo Santillan-Jimenez, Mark Crocker. *Biodiesel production from soybean oil using calcined Li-Al layered double hydroxide catalysts*. *Catalysis Letters*. Volume 115, Numbers 1-2 / May 2007. Pages 56-61.
3. J. Link Shumaker, C. Crofcheck, S. Adam Tackett, Eduardo Santillan-Jimenez, Tonya Morgan, Yaying Ji, Mark Crocker, Todd J. Toops. *Biodiesel synthesis using calcined layered double hydroxide catalysts*. *Applied Catalysis B: Environmental*. Volume 82, Issues 1-2 / July 2008. Pages 120-130.

Conference proceedings.

1. J.L. Shumaker, C. Crofcheck, S.A. Tackett, E. Santillan-Jimenez, M. Crocker. *Biodiesel synthesis from soybean oil using calcined Li-Al layered double hydroxide catalysts*. Europacat VIII, August 26-31, 2007, Turku, Finland, Paper O12-5.
2. J.L. Shumaker, S.A. Tackett, E. Santillan-Jimenez, C. Crofcheck, M. Crocker. *Heterogeneous Catalysts for Biodiesel Production Derived From Layered Double Hydroxides*. 19th Annual Michigan Catalysis Society Spring Symposium, Dearborn, MI, May 10, 2007.
3. J.L. Shumaker, S.A. Tackett, E. Santillan-Jimenez, C. Crofcheck, M. Crocker. *Development of Heterogeneous Catalysts for Biodiesel Production*. Tri-State Catalysis Society Fall Symposium, Lexington, KY, September 13, 2006.
4. E. Santillan-Jimenez, M. Crocker, J.E. Parks II, C. Salinas Martínez de Lecea. *Carbon nanotube supported metal catalysts for NO_x reduction using hydrocarbon reductants*. 5th International Conference on Environmental Catalysis. Belfast, Northern Ireland, August 31 – September 3, 2008.